INTEGRATED SEISMIC MONITORING TECHNIQUES FOR SCALABLE AND HIGH-RESOLUTION PERMAFROST CHARACTERIZATION

by

Ahmad Tourei

A thesis submitted to the Faculty and the Board of Trustees of the Colorado School of Mines in partial fulfillment of the requirements for the degree of Doctor of Philosophy (Hydrologic Science and Engineering).

Golden, Colorado

Date ____________________________

Signed: ____________________________

Ahmad Tourei

Signed: ____________________________

Dr. Eileen Martin
Thesis Advisor

Signed: ____________________________

Dr. John Hole
Thesis Co-advisor

Golden, Colorado

Date ____________________________

Signed: ____________________________

Dr. Eric Anderson
Associate Professor and Director
Hydrologic Science and Engineering

ABSTRACT

Permafrost plays a critical role in the Arctic's climate system, and its degradation poses major challenges to environmental stability as the Arctic experiences particularly strong responses to climate change. Permafrost is often highly heterogeneous, yet its fine-scale degradation processes remain poorly understood. Given the limitations of individual site characterization methods, a combination of geophysical and geotechnical techniques is needed to constrain the thermal, hydrological, and mechanical properties of permafrost.

This dissertation develops a scalable framework for characterization of permafrost heterogeneity by integrating active multichannel geophysical techniques with passive distributed fiber-optic sensing and unsupervised machine learning. The first part of this work focuses on field investigations conducted near Utqiaġvik, Alaska, where active-source multichannel analysis of surface waves (MASW), electrical resistivity tomography (ERT), borehole temperature sensing, and validating core samples are combined to constrain the lateral and vertical variability of permafrost. While inversion non-uniqueness remains a challenge, joint interpretation of seismic and electrical results improves model reliability by resolving key permafrost features such as ice-rich and cryopeg layers. It also quantifies the long-term impacts of civil infrastructure on active-layer thickening and subsurface heterogeneity. However, repeating these surveys in remote Arctic regions is logistically challenging and risks disturbing the cryosphere, highlighting the need for non-invasive passive monitoring approaches that can provide repeatable permafrost degradation assessments.

The second part of this research addresses data management challenges in large-scale distributed acoustic sensing (DAS) for passive monitoring by introducing a convolutional autoencoder framework for unsupervised anomaly detection. The algorithm filters and retains segments containing meaningful geophysical signals, enabling significant data storage reduction and continuous event detection without labeled training data. Initially developed for mining-induced seismicity monitoring, the approach is extended to passive permafrost characterization in Utqiaġvik, where naturally occurring cryoseismic events are identified and utilized as a new source of energy for permafrost imaging. Inverted shear-wave velocities demonstrate the feasibility of non-invasive permafrost imaging by revealing ice-rich permafrost layers. Collectively, the results establish a field-deployable, data-driven sensing framework for tracking permafrost degradation. The methods developed here may broadly be transferable to other domains, including environmental fiber-optic sensing, geohazard assessment, and energy infrastructure, where scalable, high-resolution seismic monitoring is essential.

TABLE OF CONTENTS

LIST OF FIGURES

LIST OF TABLES

ACKNOWLEDGMENTS

I would like to thank my advisor, Eileen Martin, for cultivating a student with a nontraditional background and for encouraging curiosity, creativity, and independent thinking at every step. Thank you, Eileen, for trusting me when I was an excited geotechnical engineer eager to explore new geophysical methods while still learning their foundations, and for being such a wonderful mentor. I truly cannot imagine receiving more support than I did from you. Your patience, guidance, and enthusiasm have shaped my research and my confidence as a scientist. Also, thank you for creating an atmosphere where students are inspired to pursue their own research ideas, encouraged to get connected with others beyond the university, and supported in guiding junior students along the way.

I am deeply grateful to John Hole, my co-advisor at Virginia Tech, for his constant encouragement and for our thoughtful scientific, personal, and life discussions over the years. Thank you, John, for explaining complex topics in simple ways that made everything feel approachable. I also sincerely appreciate the valuable input and feedback from my committee members, Ge Jin, Matt Siegfried, and Gabe Walton, whose thoughtful questions, comments, and perspectives greatly strengthened this work.

I thank the National Science Foundation (NSF) for supporting the majority of my research, and the U.S. Department of Energy (DOE) for their support through the Geothermal INTERN program, which broadened my perspective and introduced me to the intersection of research and industry. I also thank the Center to Advance the Science of Exploration to Reclamation in Mining (CASERM) for funding parts of this work that led to the development of open-source software now available to the broader research community. I am grateful to the Geological Society of America (GSA) for the grant that supported my permafrost research, as well as to the Rocky Mountain Association of Geologists (RMAG) Foundation, Environmental and Engineering Geophysical Society (EEGS) Foundation, and the U.S. Permafrost Association (USPA) for the recognition and scholarships.

In addition to my advisors and committee members, I greatly benefited from thoughtful discussions with Hydrologic Science and Engineering and Geophysics faculty, including Roel Snieder, Jeff Sharagge, Brandon Dugan, Paul Sava, Dave Benson, and Kamini Singha. I am thankful for the technical support and inspiring seminars provided by the Center for Wave Phenomena (CWP) at Mines, which helped shape my research direction and skills. I am also grateful to Vladimir Romanovsky for providing the annual temperature profiles for northern Alaska, which informed the introduction of this dissertation. I'd like to especially thank Derrick Chambers for being a mentor and friend, and for spending countless hours helping me develop next-level coding skills that have greatly benefited my research.

I am grateful to have collaborated with and learned from brilliant scientists and engineers whose feedback and friendship made this journey enjoyable. I want to thank Gabriel Rocha dos Santos, Xiaohang Ji, Alexander Ankamah, Sergei Rybakov, Hafiz Issah, Shihao Yuan, Nikhil Punithan, Tomas Snyder, Aaron Girard, Ahmed Ahmed, Adesh Pandey, Ashish Kumar, Nick Dorogy, Levi Cass, Aleksei Titov, Armin Asadi, Mehrdad Imani, and many others.

Most importantly, I could not have carried out this work without the unwavering love, patience, and support of my friends and family throughout these years. I am deeply grateful to my sister, Elham, for always standing by me and supporting me through every stage of my education abroad, and to my brother-in-law, Omid, whose early chemistry lessons set me on the path to entering an accredited college. To my loved ones, thank you for being there through every challenge, every late night, and every moment of doubt. Your encouragement has meant more than words can express.

To those whose presence and faith carried me farther than I could have walked alone.

CHAPTER 1 INTRODUCTION

Site characterization forms the foundation of geotechnical, geophysical, and environmental investigations. It underpins the design, construction, performance assessment, and long-term monitoring of engineered systems built on the ground. Understanding subsurface conditions, including stratigraphy, stiffness, and thermal or hydrological states, is crucial for predicting ground behavior under both static and dynamic loading. Traditional geotechnical site investigations relied on point-based in-situ tests and discrete sampling, which, while providing direct measurements of material properties, often fail to capture spatial variability across complex geological settings (Elkateb et al., 2011; Pfaffhuber et al., 2020). In contrast, geophysical methods often offer distributed, continuous profiling of subsurface properties but yield indirect measurements that require inversion and further validation due to their inherent non-uniqueness. Consequently, it is crucial to recognize and acknowledge the assumptions and limitations of each method and interpret their results within an integrated framework to achieve a more comprehensive understanding of subsurface conditions.

Characterizing and understanding the subsurface in cold regions presents additional scientific and engineering challenges due to the inherent spatial and temporal complexity of the subsurface. Permafrost, which refers to any ground material that remains below 0 °C for at least two consecutive years, is a coupled thermo-hydro-mechanical medium in which variations in ice content, temperature, salinity, and moisture can generate highly heterogeneous and dynamic ground conditions. Accurate monitoring of these processes is vital for assessing the stability of Arctic infrastructure and understanding feedback mechanisms between the cryosphere and the climate system (Hjort et al., 2022). However, no single sensing or sampling method can fully resolve the multifaceted characteristics of permafrost due to the inherent limitations of each technique. For example, seismic methods are effective for delineating frozen and unfrozen zones but are relatively insensitive to salinity variations that can influence ice–water phase boundaries (Dou, 2015; Wu et al., 2017). In contrast, electrical and electromagnetic techniques provide valuable information about saline and unfrozen features such as cryopegs and taliks, complementing seismic observations (Ekimova et al., 2025; Oldenborger & LeBlanc, 2018).

Moreover, conventional site characterization approaches are constrained by limited spatial coverage and temporal continuity, making it difficult to capture the evolving nature of frozen ground across scales–from centimeter-scale ice lenses to kilometer-scale landscape features and to fully understand long-term processes. For instance, the interaction between permafrost and civil infrastructure is an inherently time-dependent problem that unfolds over a broad range of temporal scales–from diurnal freeze–thaw cycles to multi-decadal and even glacial–interglacial climate oscillations. For the timescales most relevant to typical civil engineering design and asset management (approximately 30–50 years), understanding both short-term variability and long-term trends is critical for assessing infrastructure resilience (Grussing, 2013). Therefore, continuous and spatially extensive monitoring techniques are required to capture the evolution of permafrost and its coupling with built systems (Chen et al., 2020; Liu et al., 2010). Remote sensing technologies such as Interferometric Synthetic Aperture Radar (InSAR) (Liu et al., 2010; Zwieback et al., 2024), radar altimetry (Zakharova et al., 2014), and laser altimetry (Bryant et al., 2025; Michaelides et al., 2021) have shown strong potential for detecting surface deformation associated with permafrost thaw and subsidence over regional scales. These satellite-based techniques provide invaluable large-scale observations but are limited in their ability to resolve subsurface processes. InSAR, for example, primarily measures surface displacement in the line-of-sight direction and cannot directly distinguish the underlying thermo-hydrological or mechanical mechanisms driving the deformation (Yang et al., 2020). Its sensitivity to environmental factors such as snow cover, vegetation, and temporal decorrelation also may restrict its applicability in Arctic tundra regions, where rapid seasonal changes can degrade signal coherence (Zhang et al., 2022).

Recent advances in geophysical sensing technologies, such as distributed fiber-optic systems, now enable continuous, high-resolution observations of seismic, strain, and temperature conditions in permafrost (Wagner et al., 2018). While these developments have revolutionized passive monitoring capabilities, they also generate massive data volumes that challenge traditional processing and interpretation workflows. Therefore, leveraging data-driven and artificial intelligence (AI)-based approaches provides solutions for efficiently extracting meaningful patterns, detecting anomalies, and translating large-scale sensing data into actionable insights about permafrost dynamics.

1.1 Integrated Monitoring Approach

Accurate site characterization in challenging environments often requires combining multiple monitoring techniques. Traditional geotechnical in-situ tests (e.g., Standard Penetration Test and Cone Penetration Test) provide direct information on soil properties but only at discrete borehole locations. Boreholes are typically spaced far apart (often tens to hundreds of meters), which risks missing important spatial variability in subsurface conditions (USGS, 2023). By contrast, as noted earlier, geophysical surveys (such as seismic-, electrical-, or radar-based methods) offer continuous or distributed profiling of subsurface properties between boreholes, but they yield indirect measurements that must be inferred through inversion. Such geophysical inversions are inherently nonunique–for example, multiple different shear-wave velocity (Vs) profiles can fit the same surface-wave dispersion data equally well (Foti et al., 2009). This ambiguity means that geophysical results alone, while spatially extensive, can suffer from uncertainty in interpretation.

To overcome these limitations, an integrated monitoring approach leverages the complementary strengths of geotechnical and geophysical data. Point measurements from boreholes serve as ground truth constraints to guide and calibrate geophysical inversions, thereby reducing non-uniqueness, while the geophysical measurements fill in the continuous spatial detail between sparse boreholes (USGS, 2023) Several studies have demonstrated that combining multiple characterization techniques yields a more robust understanding of the subsurface than any single method alone (Braga & Gama, 2024; Chen et al., 2021; Olayanju et al., 2017). Integrating multichannel geophysical and geoelectrical methods with selective geotechnical sampling may yield improved interpretation accuracy, which is particularly valuable in heterogeneous ground conditions where neither boreholes nor geophysics alone can capture the full complexity.

1.2 Multichannel Analysis of Surface Waves and Electrical Resistivity Tomography

The Multichannel Analysis of Surface Waves (MASW) method is a seismic technique that utilizes the dispersive properties of surface waves–primarily Rayleigh and, in certain configurations, Love waves–to infer the near-surface Vs structure (Park et al., 1999a). Surface waves represent the most energetic components of seismic signals generated by near-surface sources and recorded at the ground surface, with Rayleigh waves involving both radial and vertical particle motion, and Love waves exhibiting a horizontal shear motion confined to the near-surface layers. Because their propagation velocities are frequency-dependent and governed by the elastic moduli and density distribution with depth, analysis of surface-wave dispersion provides a robust means of estimating Vs profiles. In MASW, the phase velocity of each frequency component is extracted from multichannel seismic records and inverted through a nonlinear least-squares or global optimization algorithm to derive the shear-wave velocity–depth function (Park et al., 1999a).

For permafrost characterization, MASW is particularly valuable because it provides information on the mechanical stiffness of the subsurface derived from Vs measurements. Higher shear-wave velocities can indicate either mechanically stronger lithologic units or frozen, ice-rich soils where ice bonding increases stiffness and wave propagation speed. Conversely, lower velocities may signify thawed, unconsolidated, or water-saturated zones with reduced shear strength (Ji et al., 2024; Liew et al., 2022). Compared to geotechnical methods, MASW can offer a non-destructive, rapid, and spatially continuous means of subsurface characterization, making it especially advantageous for permafrost studies in remote and environmentally sensitive Arctic regions (Evangelista & Santucci de Magistris, 2015).

Electrical Resistivity Tomography (ERT) is a geoelectrical imaging technique that characterizes the subsurface by measuring the spatial distribution of electrical resistivity (Daily et al., 2005). It operates by injecting a known electric current into the ground through a pair of electrodes and recording the resulting potential differences at other electrodes along the profile. The apparent resistivity derived from these measurements reflects the integrated response of the subsurface materials, which is then inverted to produce a two- or three-dimensional resistivity model.

Because electrical resistivity is strongly influenced by factors such as pore-water salinity, temperature, and soil texture, ERT is particularly sensitive to the hydrothermal state of frozen ground (Piolat et al., 2024). In permafrost environments, high resistivity values typically correspond to frozen, ice-rich materials, whereas low resistivity zones indicate thawed or saline layers such as cryopegs or taliks (Yoshikawa et al., 2004). The inversion of ERT data involves solving a nonlinear optimization problem constrained by regularization terms that balance data misfit and model smoothness, allowing the recovery of resistivity contrasts with depth. Advances in multi-electrode arrays, high-precision instrumentation, and time-lapse ERT techniques enable detailed monitoring of freeze–thaw dynamics, active-layer thickness, and permafrost degradation over seasonal to decadal timescales (Herring et al., 2023). When combined with complementary datasets such as seismic velocity profiles or temperature logs, ERT provides a powerful means to constrain the thermal and hydrological structure of permafrost and to evaluate coupled processes affecting ground stability and infrastructure performance in cold-region settings. However, both MASW and ERT results are inherently non-unique due to the ill-posed nature of the inversion process, where multiple subsurface resistivity distributions can explain the same measured data within acceptable error limits. Therefore, the interpretation of these geophysical and geoelectrical models must be guided by independent geological information, borehole data, or complementary geophysical measurements to ensure physically realistic and geologically consistent results.

1.3 Global Warming and Permafrost Degradation

Permafrost is distributed across approximately 25% of the land surface in the northern hemisphere and is highly sensitive to atmospheric temperature variation primarily caused by global warming (Biskaborn et al., 2019; Lantuit et al., 2012). The Arctic average annual surface temperature has increased by 3.1 °C from 1971 to 2019, which is three times faster than the global rate (AMAP, 2021; IPCC, 2021; Rantanen et al., 2022). In Utqiaġvik (the study area of this dissertation, formerly known as Barrow), Alaska, the average annual air temperature has risen over 4 °C since 1980, and recent decades have seen Arctic Alaska's permafrost warm by 1-3 °C (Nicolsky et al., 2017; Thoman & Walsh, 2019). As illustrated in Figure 1.1, the effects of global warming are particularly pronounced in the Arctic due to Arctic amplification–a feedback process in which the loss of reflective sea ice increases the absorption of solar radiation by darker ocean waters, thereby accelerating regional warming (Yao et al., 2021). Rising air temperatures lead to the thawing of permafrost, thickening of the active layer, and the release of previously trapped greenhouse gases, including carbon dioxide and methane (Koven et al., 2011). This release reinforces global warming, creating a positive feedback loop that further destabilizes permafrost and amplifies the impacts of climate change on Arctic landscapes.

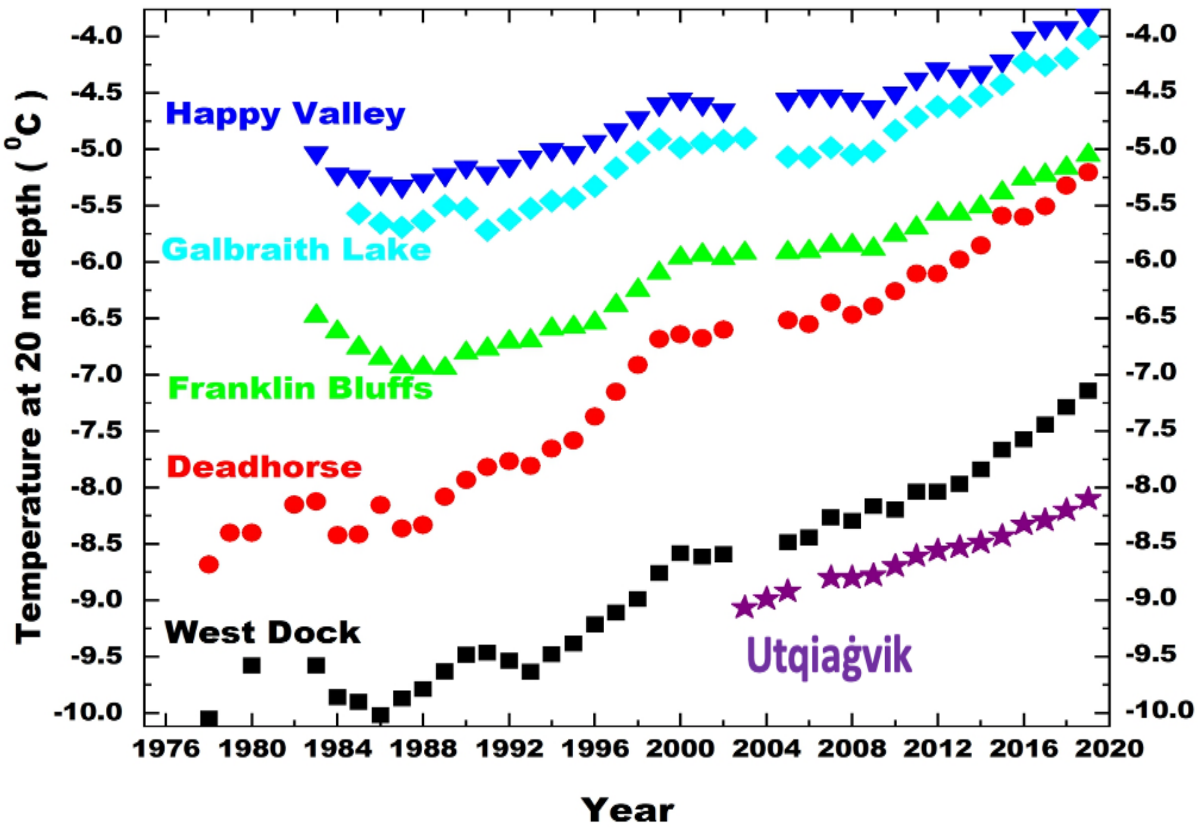

Figure 1.1 Time series of temperatures at the 20 m depth in northern Alaska. Modified from Osterkamp (2003) based on Romanovsky et al. (2020).

Permafrost often exhibits a highly heterogeneous structure resulting from variations in thermal, hydrological, and cryogenic processes. This complexity arises from fine-scale spatial variations in properties such as temperature, ice content, and moisture distribution. As illustrated in Figure 1.2, permafrost may contain diverse features such as ice lenses, ice wedges, ice-rich zones, and unfrozen saline layers known as cryopeg. Understanding the spatial heterogeneity of permafrost in Arctic tundra is important for studying geomorphological and ecosystem variations under climate change, as well as potential engineering impacts (Schneider von Deimling et al., 2021).

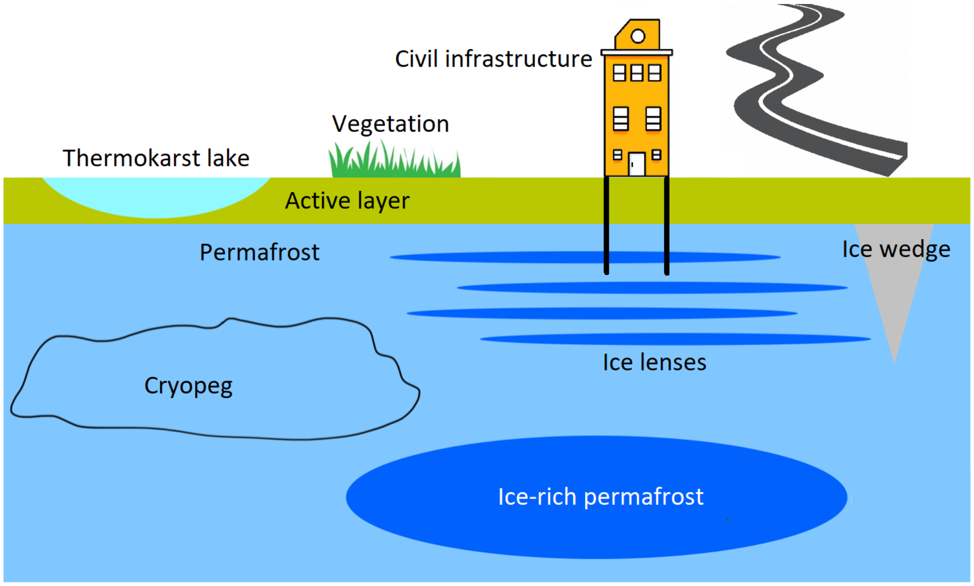

Figure 1.2 Schematic profile of permafrost.

Increasing temperature in the high-latitude permafrost regions leads to permafrost degradation, which includes permafrost warming, active layer thickening, and thaw-related hazards such as the development of taliks, land subsidence, and thermokarst in low-lying areas, mass wasting on slopes, and thermal erosion and abrasion along riverbanks and coasts (Hjort et al., 2022). Global warming causes contaminated and industrial sites in regions of stable permafrost to thaw, posing a significant environmental threat (Langer et al., 2023). Permafrost degradation drives serious changes in local geomorphology, hydrology, vegetation, wildlife dynamics, and greenhouse gas emissions (Hjort et al., 2022; Streletskiy et al., 2015). Permafrost exhibits vastly variable properties between thawed and frozen states due to the phase change of water, impacting its strength and bearing capacity, which can lead to infrastructure failure (Hjort et al., 2022). The interaction between permafrost and civil infrastructure contributes to permafrost degradation and increases construction and maintenance costs (Streletskiy et al., 2012, 2015). Indeed, climate-driven permafrost degradation has caused costly damage in Arctic communities – for example, maintenance and repair costs for public infrastructure in Alaska are projected to increase by an estimated \$3.6–6.1 billion by 2030 (and \$5.6–7.6 billion by 2080) as permafrost continues to warm (Liew et al., 2022).

While existing research primarily focuses on the influence of degrading permafrost on infrastructure, it is crucial to consider the impact of civil infrastructure on permafrost. As shown in Figure 1.3, various forms of infrastructure, such as pile foundations, pipelines, and landfills, are constructed on permafrost that is gradually warming and degrading. Different foundations and architecture introduce thermal and physical impacts that can disturb the natural environment and alter adjacent tundra ecosystems (Walker et al., 2022). As climate change continues, the vulnerability of both civil infrastructure and permafrost systems grows, necessitating detailed knowledge of risk exposure in current and future infrastructure areas (Hjort et al., 2022; Melvin et al., 2017). Understanding the influence of civil infrastructure on degrading permafrost allows for a realistic risk assessment.

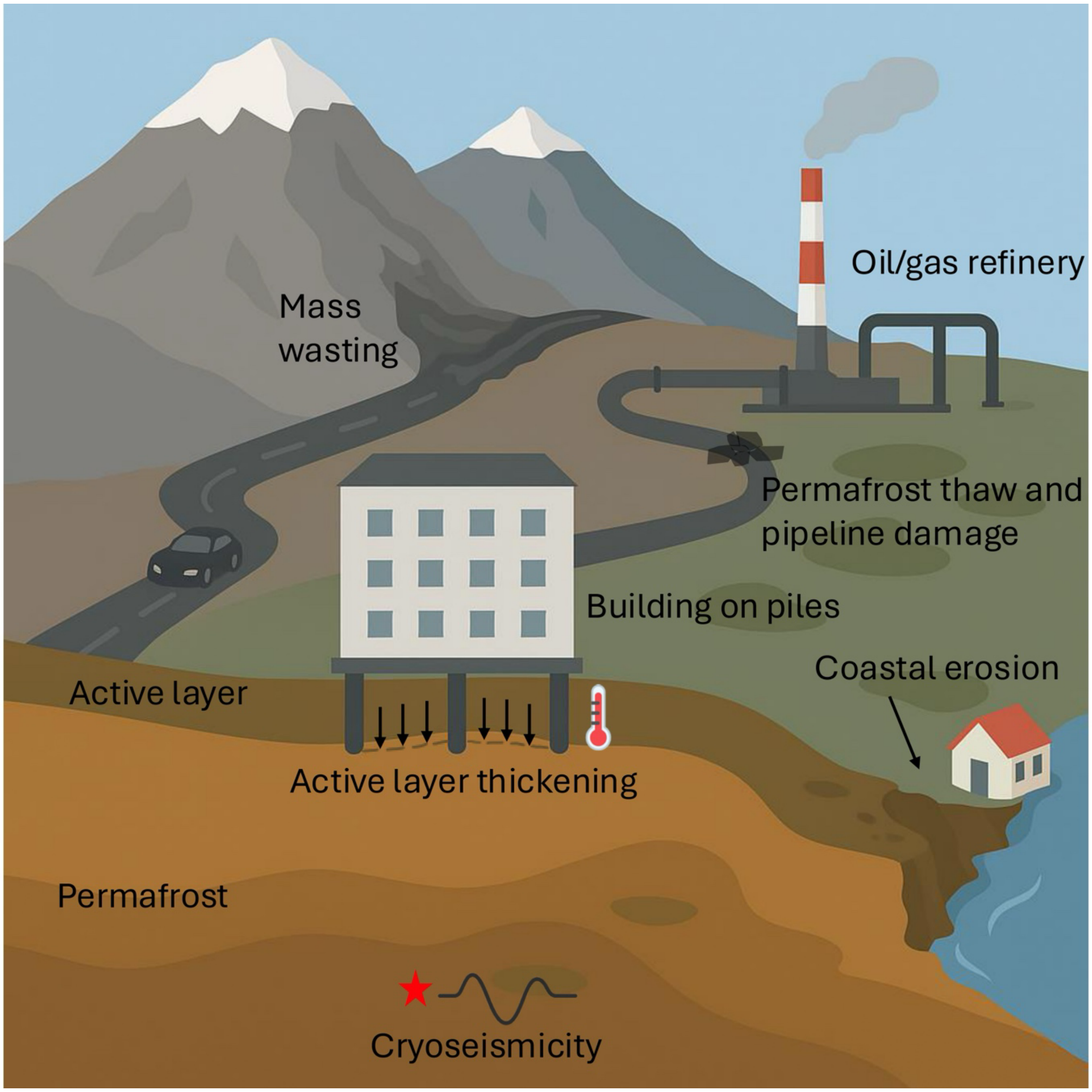

Figure 1.3 Conceptual illustration of permafrost degradation processes and their impacts on civil infrastructure and landscapes in cold regions. Adopted from Hjort et al. (2022).

1.4 Distributed Fiber-Optic Sensing

Distributed Fiber Optic Sensing (DFOS) encompasses a suite of technologies that utilize intrinsic light scattering within optical fibers to detect and quantify physical changes along the fiber length. When a laser pulse propagates through an optical fiber, a small portion of the light is scattered back toward the source due to microscopic inhomogeneities in the glass core (Hartog, 2017). Most of this backscattered light maintains the same wavelength as the incident pulse (Rayleigh scattering), while a smaller fraction exhibits wavelength shifts caused by inelastic scattering phenomena (Raman and Brillouin scattering), as shown in Figure 1.4. The frequency shift associated with Brillouin scattering is directly related to strain in the fiber, resulting from either mechanical deformation or thermal expansion, whereas the intensity ratio between Stokes and anti-Stokes components in Raman scattering is primarily sensitive to temperature variations (Ferdinand, 2014).

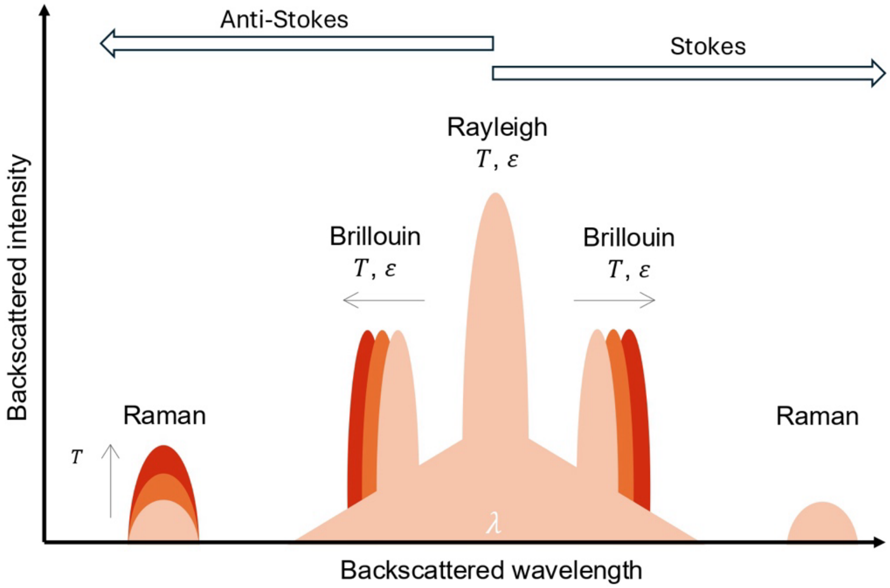

Figure 1.4 Different optical scattering for DFOS based on temperature and strain sensitivity. Adapted from Ferdinand (2014).

DFOS technologies are broadly categorized into three primary types: Distributed Strain Sensing (DSS), Distributed Temperature Sensing (DTS), and Distributed Acoustic Sensing (DAS). Each system employs an interrogator unit (IU) to emit laser pulses and measure the returning backscattered signal, allowing spatially continuous measurements along the entire fiber length. DSS systems, typically based on Brillouin or Rayleigh scattering, are used for low-frequency or quasi-static strain measurements and are sensitive to both mechanical and thermally induced strain. DTS systems, relying on Raman scattering, are designed to measure temperature distributions with high spatial resolution. DAS systems, in contrast, often utilize coherent Rayleigh backscatter to record dynamic strain or vibration over a broad frequency range (e.g., 0.01 to 50,000 Hz, but lower frequencies are possible), making them particularly suitable for seismic, acoustic, and structural monitoring applications.

For permafrost monitoring, DFOS technologies offer unique advantages for observing the coupled thermal–mechanical processes that govern frozen-ground dynamics. DTS provides continuous thermal profiling to detect active-layer thickening, freeze–thaw transitions, and localized talik development, while

DAS enables the detection of seismic velocity variations and small-scale cryoseismic events associated with freezing, thawing, and ground movement. These systems enable passive, long-term, high-resolution monitoring of permafrost temperature and seismic behavior over kilometer-scale distances, providing insights into the stability of Arctic infrastructure and the progression of climate-driven permafrost degradation.

1.5 Deep Learning-Based Methods for Scalable Seismic Monitoring

DAS technology has enabled the acquisition of spatially and temporally dense seismic data, enhancing monitoring applications such as hydrofracturing (Binder & Chakraborty, 2019; Saw et al., 2025), offshore seismicity (Shi et al., 2025), permafrost dynamics (Cheng et al., 2022), and mining-induced seismicity (Chambers et al., 2025; Chambers & Shragge, 2023), among others. Unlike traditional seismic networks, which rely on sparse arrays of seismic stations, DAS leverages photonics technology to transform fiber-optic cables into high-resolution seismic sensors (Lindsey et al., 2021). The spatially and temporally dense DAS data enable the detection of subtle seismic events that might otherwise go unnoticed with conventional monitoring systems.

However, this data richness comes at a cost: kilometer-scale arrays can generate several terabytes of data per day, creating substantial challenges for storage, processing, and real-time analysis. These challenges are further compounded in passive monitoring studies, where the lack of labeled training data limits the applicability of supervised machine learning approaches. Moreover, DAS deployments often occur in environments where broadband seismic arrays were previously infeasible, and where the full spectrum of event types–ranging from seismicity and cryoseismic activity to anthropogenic noise and instrument artifacts–is not known a priori. In such cases, manual exploratory analysis of DAS data quickly becomes impractical, both in terms of time and computational resources. Therefore, the development of automated tools capable of detecting various anomalies such as seismic events, traffic noise, and instrument noise, is essential for the efficient storage, processing, and interpretation of DAS data.

Unsupervised autoencoder (AE) techniques can play a crucial role in identifying anomalies in DAS data. Convolutional AE is a class of neural networks designed to learn outliers within the compressed representations of high-dimensional data. They have gained prominence in anomaly detection tasks due to their capability to effectively capture essential waveform characteristics (Mousavi et al., 2019; Neloy & Turgeon, 2024). AE has also demonstrated strong performance in denoising seismic data, enhancing the detection and characterization of seismic events (Jiang et al., 2022; Shi et al., 2025). Chien et al. (2023) demonstrated the potential of autoencoder-based approaches for unsupervised classification of DAS seismic signals by combining a convolutional autoencoder with a Gaussian mixture model clustering to categorize injection-related seismicity in a geothermal setting. However, their framework was designed primarily for signal classification rather than anomaly detection, relied on an additional clustering step, and was tailored to a specific geothermal application. In contrast, our approach enables direct anomaly detection without clustering and is designed to be more generalizable across diverse DAS monitoring environments.

1.6 Research Objectives and Dissertation Outline

The primary objective of this study is to integrate multiple monitoring techniques to improve the interpretation and characterization of permafrost heterogeneity. A particular emphasis is placed on MASW and assessing how this monitoring approach can be made scalable through the application of the DAS technology. To support this objective, this study also develops and applies lightweight, computationally efficient anomaly detection algorithms for DAS data, enabling effective data reduction and facilitating the identification of signals that can be used for permafrost monitoring.

This dissertation presents the development and application of scalable site characterization techniques for permafrost monitoring. Chapter 2 investigates how the active MASW technique can be applied for permafrost characterization and presents an integrated framework that combines MASW (seismic) with ERT (geoelectrical), borehole core sampling (geotechnical), and borehole temperature logging (thermal sensing) to evaluate their combined interpretive value for permafrost heterogeneity characterization. Chapter 3 introduces a computationally efficient autoencoder-based deep learning framework for anomaly detection in large-scale DAS data to enhance mining-induced seismicity monitoring, with its generalizability demonstrated using a three-year continuous permafrost dataset collected in Utqiaġvik, Alaska. Building on this framework, Chapter 4 applies the autoencoder model to improve DAS data management and to detect cryoseismic events in the Utqiaġvik dataset as new sources of energy for imaging, which are subsequently leveraged for permafrost characterization. The dissertation concludes with Chapter 5, which synthesizes the findings, discusses broader implications for Arctic infrastructure and environmental monitoring, and outlines directions for future research in scalable site characterization.

CHAPTER 2 CHARACTERIZING PERMAFROST HETEROGENEITY AND DEGRADATION THROUGH INTEGRATED ACTIVE GEOPHYSICAL, GEOELECTRICAL, GEOTECHNICAL, AND TEMPERATURE SENSING

Reproduced from a paper published with open access in the Journal of Geophysical Research–Earth Surface[1].

Ahmad Tourei[2], Xiaohang Ji[3], Gabriel Fernando Rocha dos Santos[4], Rafal Czarny[4], Sergei Rybakov[5], Ziyi Wang[3], Matthew Hallissey[3], Eileen Martin[2], Ming Xiao[3], Tieyuan Zhu[4], Dmitry Nicolsky[5], Anne Jensen[6]

2.1 Abstract

Subsurface processes significantly influence surface dynamics in permafrost regions, necessitating the utilization of diverse geophysical methods to reliably constrain permafrost characteristics. This research uses multiple geophysical techniques to explore the spatial variability of permafrost in undisturbed tundra and its degradation in disturbed tundra in Utqiaġvik (formerly known as Barrow), Alaska. Here, we integrate multiple quantitative techniques, including multichannel analysis of surface waves (MASW), electrical resistivity tomography (ERT), and ground temperature sensing to qualitatively study heterogeneity in permafrost's geophysical characteristics. MASW results reveal active layer shear wave velocities (Vs) between 240 and 370 m/s, and permafrost Vs between 450 and 1700 m/s, typically showing a low-high-low velocity pattern. Additionally, we find an inverse relationship between in-situ Vs and ground temperature measurements. The Vs profiles, along with electrical resistivity profiles, reveal cryostructures such as cryopeg and ice-rich zones in the permafrost layer. The integrated results of MASW and ERT provide valuable information for characterizing permafrost heterogeneity and cryostructure. Corroboration of these geophysical observations with permafrost core samples' stratigraphy and salinity measurements further validates these findings. This combination of geophysical and temperature sensing methods, along with permafrost core sampling, confirms a robust approach to assessing permafrost's spatial variability in coastal environments. Our results also indicate that civil

---

[1] Reproduced with permission of JGR: Earth Surface. Tourei, A., Ji, X., Rocha dos Santos, G., Czarny, R., Rybakov, S., Wang, Z., ... & Jensen, A. (2024). Mapping permafrost variability and degradation using seismic surface waves, electrical resistivity, and temperature sensing: A case study in Arctic Alaska. *Journal of Geophysical Research: Earth Surface*, 129(3), e2023JF007352.

[2] Hydrologic Science and Engineering Program, Colorado School of Mines, Golden, CO, USA

[3] Department of Civil and Environmental Engineering, The Pennsylvania State University, State College, PA, USA

[4] Department of Geosciences, The Pennsylvania State University, State College, PA, USA

[5] Geophysical Institute, University of Alaska Fairbanks, Fairbanks, AK, USA

[6] Department of Anthropology, University of Alaska Fairbanks, Fairbanks, AK, USA

infrastructure systems such as gravel roads and pile foundations affect permafrost by thickening the active layer, lowering the Vs, and reducing heterogeneity. We show how the resulting Vs profiles can be used to estimate key parameters for designing buildings in permafrost regions and maintaining existing infrastructure in polar regions.

2.2 Introduction

2.2.1 Global Warming Impacts on Permafrost Degradation and Ground Thermal Regime

Permafrost research often focuses primarily on ground temperature due to its direct effect on physical and biogeochemical soil processes, but permafrost is also affected by air temperature, snow cover, soil moisture, vegetation cover, and soil properties (Lantuit et al., 2012; Smith et al., 2022). In-situ monitoring using thermistors and thermocouples has shown that permafrost temperatures are increasing, leading to thawing and degradation (Biskaborn et al., 2019; Nicolsky et al., 2009, 2017; Romanovsky et al., 2010; Shiklomanov et al., 2010). Understanding the ground's thermal state in permafrost regions is crucial to model and mitigate climate change impacts.

Permafrost structure is often complex due to fine-scale spatial heterogeneity of properties such as temperature and ice content. Temperature, water saturation, and ice content influence seismic wave velocities, including shear wave velocity (Vs) and compressional wave velocity (Vp) (Coduto, 1999; Hjort et al., 2022; Ji et al., 2024; Liew et al., 2022). Salinity is a key factor in coastal permafrost environments such as Utqiaġvik, Alaska. Studies by Brown (1969) and O'Sullivan et al. (1966) reveal how salinity affects permafrost's geochemistry and physical properties, such as its freezing point and stability. Dafflonet et al.'s research (2016, 2017) further demonstrates the impact of salinity on the distribution and characteristics of shallow permafrost, highlighting its connection with vegetation patterns and soil properties. Meyer et al. (2010) provide historical context, showing how historical salinity variations have influenced the permafrost landscape over time. Salinity plays a crucial role in key permafrost structures. Here we provide a brief overview of the active layer and some of the key permafrost structures investigated in this paper, including cryopegs, ice-rich zones, and thermokarst lakes. Jafarov et al. (2018) showed that the active layer thickness (ALT) of undisturbed tundra (without infrastructure development and low to medium water content) near Elson Lagoon in Utqiaġvik, Alaska, is approximately 0.2 to 0.6 m, measured in August 2013. A thermokarst is formed when the thermal equilibrium shifts, allowing the ground ice to thaw. Talik is a layer or body of year-round unfrozen ground (usually above 0 °C) occurring in a permafrost zone due to a local anomaly in thermal, hydrological, or hydrochemical conditions (e.g., underneath thermokarst lakes and rivers). Cryopegs can have temperatures below 0 °C, but freezing is prevented by freezing-point depression due to the dissolved-solids content of the pore water (van Everdingen et al., 1988). As the climate warms, the annual ground temperature increases, and annual thawing deepens until a certain threshold is met, after which a talik develops. Ice wedges form when water seeps into cracks in the ground during summer and then freezes during winter. The distribution of ice formations and ice content within the permafrost layer is highly variable (Liu et al., 2021). Previous studies confirm that the ice content in the permafrost around Barrow is very high in the upper part and decreases with depth (Brown et al., 1981). For the coastal plain along the Beaufort Sea from Point Barrow to the Canadian border, Kanevskiy et al. (2013) reported an average total ice content (i.e., ice wedge, segregated, and pore ice) of 83% and 82% for the primary surface and the drained-lakes basins, respectively. This results in a landscape vulnerable to widespread subsidence and thermokarst development, the magnitude of which may vary widely depending on surficial geology, ground ice volume, and the extent of past thermokarst activity (Farquharson et al., 2019). The warming and thawing of ice-rich permafrost pose changes in its interactions within the built environment (Hjort et al., 2022).

2.2.2 Seismic and Geoelectrical Methods in Permafrost Regions

Seismic imaging is a commonly used technique for characterizing the subsurface in permafrost regions (Justice & Zuba, 1986; Miller et al., 2000; Ramachandran et al., 2011) because seismic wave velocities, including shear wave velocity and compressional wave velocity, are sensitive to temperature, water saturation, and ice content (Coduto, 1999; Hjort et al., 2022; Ji et al., 2024; Liew et al., 2022; Liew et al., 2022). One of the main advantages of seismic imaging in permafrost regions is its ability to provide detailed information about the distribution and continuity of permafrost and the nature of the underlying soils, even 3D profiles with high resolution (e.g., Ramachandran et al., (2011) and Schwamborn et al., (2002)). This information is important for various applications, such as infrastructure planning and design, resource exploration, and environmental monitoring. Seismic refraction is a surface geophysics method that utilizes the refraction of body waves through layered media (Scott & Markiewicz, 1990). Seismic refraction has been used in several case studies of permafrost conditions and periglacial environments (Harris & Cook, 1986; Ikeda, 2006; Schrott & Hoffmann, 2008). Joint inversion of refraction seismic tomography (RST) and electrical resistivity tomography (ERT) has been used to characterize Alpine rock glaciers and permafrost (Wagner et al., 2019). Brothers et al. (2016) previously used seismic reflection data to delineate continuous subsea ice-bearing permafrost.

Surface wave methods are powerful tools for near-surface characterization of sites and mapping irregular Vs profiles in permafrost through acquisition, processing, and inversion of surface waves, typically Rayleigh waves (Alam & Jaiswal, 2017; Carr et al., 1998; Essien et al., 2014; Fortin et al., 2007; Letson et al., 2019; Socco & Strobbia, 2004; Taylor et al., 2022). Compared with seismic refraction and reflection, surface wave methods are advantageous for mapping permafrost structures with low-velocity layers embedded in high-velocity permafrost zones (Dou & Ajo-Franklin, 2014). Spectral Analysis of

Surface Waves (SASW) has been used to obtain S-wave velocity profiles of unfrozen and frozen soils in Fairbanks, Alaska (Cox et al., 2012; Hazirbaba et al., 2011). Multichannel Analysis of Surface Waves (MASW) has been applied in several glacial environments, including permafrost zones (Ajo-Franklin et al., 2017; Dou et al., 2012; Dou & Ajo-Franklin, 2014; Glazer et al., 2020; Majdański et al., 2022; Picotti et al., 2015; Rossi et al., 2018). Similar to surface wave methods, ERT technique excels in near-surface permafrost characterization by modeling subsurface resistivity to match observed apparent resistivity data, typically yielding a two-dimensional resistivity profile (Daily et al., 2000). ERT has been used in several permafrost studies to characterize permafrost thaw (Etzelmüller et al., 2020), distinguish ice content variations (Herring et al., 2023), and examine interactions between permafrost and infrastructure(You et al., 2017). MASW has often been combined with other technologies in permafrost research, such as seismic tomography and ERT (Dou & Ajo-Franklin, 2014; Glazer et al., 2020; Marciniak et al., 2018, 2019). In this study, we investigate the spatial variability of permafrost in Utqiaġvik, Alaska, using MASW and ERT techniques to characterize permafrost, identify cryostructure, and analyze the influence of temperature on tundra permafrost systems. The MASW results provide useful information to verify ERT results for subsurface features. We compare in-situ temperature profiles with seismic velocity profiles to better understand the ground condition of the permafrost. This study is carried out across sites in undisturbed tundra and near infrastructure. Our findings underscore the impact of civil infrastructure on permafrost degradation, particularly in designing and maintaining buildings in permafrost regions.

2.3 Study Area

Permafrost zones underlie 80% of Alaska, including 29% continuous permafrost (Jorgenson et al., 2008). The North Slope Borough is entirely within the continuous permafrost zone (Ferrians, 1965; Kerkering, 2008), shown in Figure 2.1a. The permafrost in Utqiaġvik, Alaska, is continuous and has a thickness of approximately 200–400 m (Jorgenson et al., 2008). Elson Lagoon forms the eastern land boundary of the study area, shown in Figure 2.1b. The ALT of undisturbed tundra near Elson Lagoon is approximately 0.2 to 0.6 m, and the soil volumetric water content varies from 17% to 88%, measured in August 2013 (Jafarov et al., 2018). The average ALT of the study area on the tundra in Utqiaġvik, Alaska, is also shallow (roughly less than 1.0 m), consisting of three distinct layers: the acrotelm (top), the catotelm (middle), and the mineral soil (bottom) (Chen et al., 2020). The ground conditions vary from dry to marshy, with surface vegetation. The seismic surveys (MASW) were performed on August 6 – 12, 2022. The plan view showing the layout of seismic survey lines and the temperature measurement locations is presented in Figure 2.1.

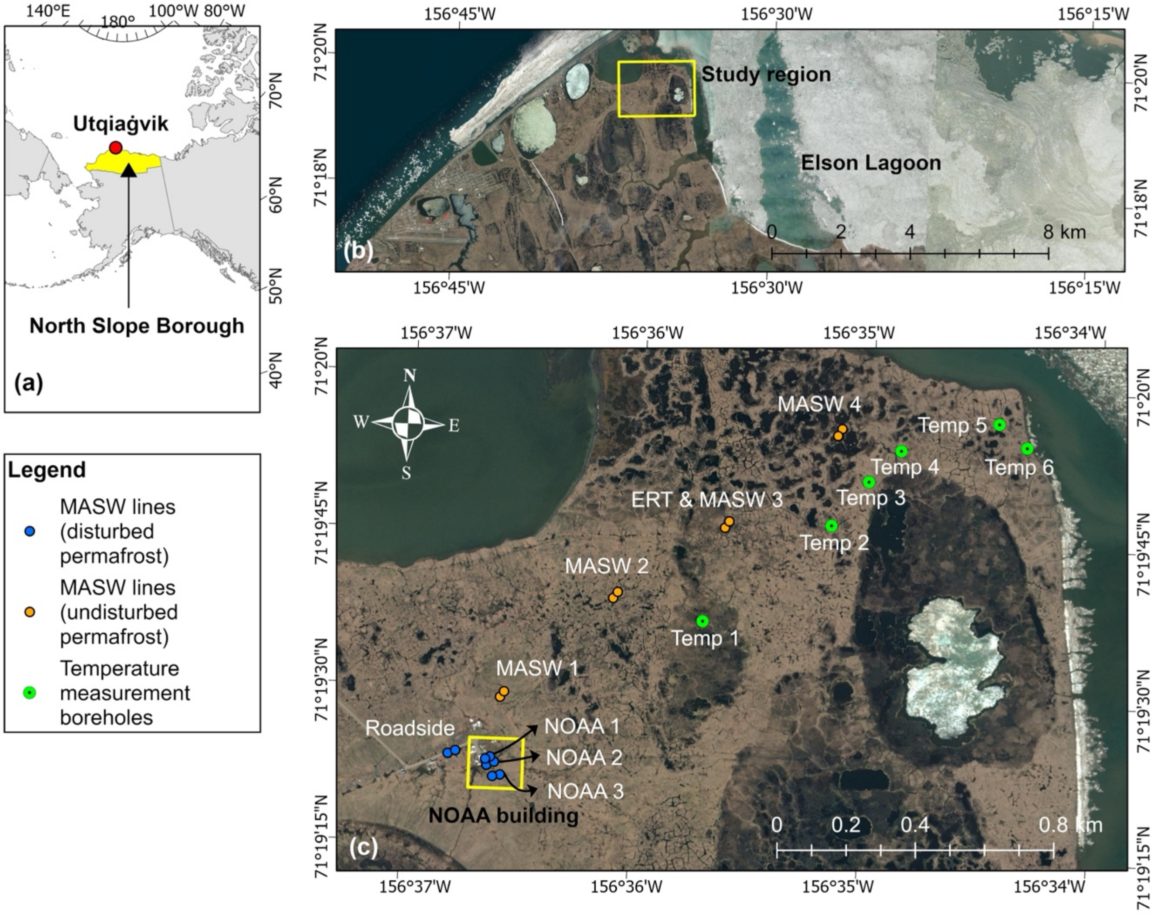

Figure 2.1 Geophysical survey and temperature measurement map: (a) Utqiaġvik, North Slope Borough, Alaska. (b) Study region. (c) Seismic survey, electrical resistivity survey, and temperature measurement locations.

2.4 Analytical Methods

2.4.1 The MASW Technique

Surface waves can be generated by an active source, such as a hammer, weight drop, vibroseis, or by a passively recorded source, such as anthropogenic, traffic, or several other environmental sources (e.g., ocean waves, wind), and these waves are recorded by an array of geophones. Because surface waves can provide information on the subsurface velocities over a wide range of frequencies and wavelengths, the MASW technique can generate high-quality velocity models. MASW is often used to produce 1D velocity profiles; it can also be used to assess the lateral variability of the subsurface shear wave velocities, which is essential for characterizing subsurface heterogeneity and identifying areas of potential geotechnical concern. The MASW method can be applied in a wide range of geological environments and has the advantages of being non-invasive, cost-effective, and capable of providing high-resolution Vs profiles to depths of up to several tens of meters.

In active-source surface seismic surveys, over two-thirds of the total seismic energy generated by compressional waves is transmitted to Rayleigh waves, sometimes referred to as "ground roll" (Park et al., 1999a). An example of surface waves in our collected data is shown in Figure 2.2a. Surface wave energy decays exponentially with depth beneath the surface. Longer wavelength (i.e., longer-period and lower-frequency) surface waves travel deeper, thus containing more information about deeper parts of the study area. Shorter wavelength (i.e., shorter-period and higher-frequency) surface waves travel shallower, thus containing more information about shallower parts of the study area. Surface waves are dispersive, meaning each wavelength propagates at a different phase velocity in a layered medium. Thus, we can analyze phase velocities of different frequency bands (corresponding to different wavelengths) and estimate the velocity profile of the subsurface.

Rayleigh wave dispersion curves describe the velocity at which each wavelength travels. To determine Rayleigh wave dispersion curves, we use the phase shift method, which provides accurate fundamental-mode phase velocities even when only four geophones are used (Dal Moro et al., 2003; Park et al., 1999b). Our detailed procedure is provided in Appendix A.

Figure 2.2 represents an example of the inversion procedure for estimating a 1D velocity profile. First, we applied a 7.50 - 327.68 Hz bandpass filter to all traces in a shot gather to remove high-frequency noise, and we muted noisy traces (Figure 2.2a). Then, we calculated dispersion images, determined phase velocities by picking the velocity with the maximum amplitude at each frequency (Figure 2.2b), and extracted the fundamental mode velocity profile of the Rayleigh surface wave from the dispersion image (Figure 2.2c). After wavelength-depth conversion, we generated an initial model based on the phase velocity picks. Finally, a non-linear least squares inversion method (Xia et al., 1999) was applied to the dispersion curve to reconstruct the Vs model (Figure 2.2d) using the SeisImagerSW software. The minimal depth at which shear wave velocity can be reliably inferred through inversion is contingent upon a confluence of site-specific variables. This interpretable depth is not a fixed measure but is instead modulated by an array of factors, including the fidelity of seismic data, particularly its high-frequency components, and the proximal spacing relative to the seismic source. Acceptable final 1D models should have a root mean square (RMS) error of the difference between the theoretical dispersion and measured dispersion curves (Figure 2.2c) below 5% (SeisImagerSW Manual v. 3.0, 2009). With this procedure, we obtain an average 1D Vs vertical profile along the seismic line.

For 2D Vs estimation, we carry out the same pre-processing, then we perform dispersion analysis using the common mid-point (CMP) cross-correlation gathers. The CMP cross-correlation method can increase the signal-to-noise ratio of the dispersion spectrum. A comprehensive explanation of this method is provided by Hayashi & Suzuki (2004). Here, we briefly discuss the following steps for CMP cross-correlation analysis: First, we calculate cross-correlations between every pair of traces in each shot gather. Second, we collect correlation traces with a common mid-point and stack those with the same spacing.

The resultant cross-correlation gathers resemble shot gathers and are known as CMP cross-correlation gathers. Third, we calculate the dispersion image of surface waves using the MASW technique (Park et al., 1999a) from the CMP cross-correlation gathers. Finally, for each CMP, we invert dispersion curves for Vs models. As a general guideline, acceptable 2D models should result in an RMS below 15% (SeisImagerSW Manual v. 3.0, 2009).

MASW is limited to shallow depth investigations, typically up to 30 m. Beyond this depth, the resolution and accuracy of the method decrease significantly. Moreover, MASW is more suitable for homogeneous soil conditions and struggles to characterize laterally varying structures or complex geological settings accurately (Boiero & Socco, 2011; Evangelista & Magistris, 2015). To overcome these limitations in the future, seismic refraction or reflection could be employed over a larger region as a complementary technique, although reliable picking of the unaliased arrivals in this complex near-surface zone will likely require more than 24 geophones and a high-frequency seismic source. The depth and compression velocity information of different subsurface layers can be determined by analyzing the travel time data. Seismic refraction has the advantage of investigating deeper depths, making it useful for studying subsurface structures beyond the reach of MASW. The material in section A.2 of the Appendix A can serve as a basis for a future permafrost study combining MASW and seismic refraction. Advances in data acquisition and processing should be taken into account to ensure the best possible outcomes in future investigations. By integrating the strengths of these two techniques, it may be possible to enhance the accuracy and depth range of permafrost characterization.

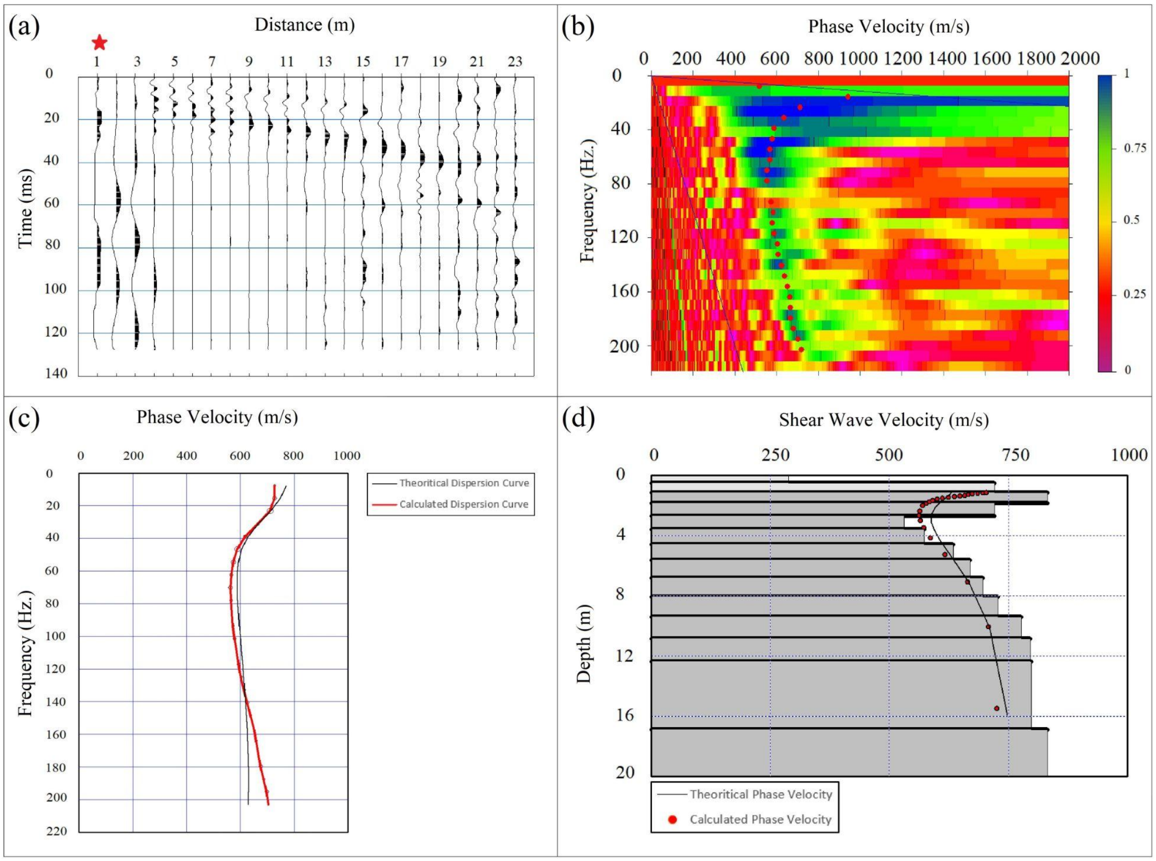

Figure 2.2 The procedure of building Vs models from extracted dispersion curve using MASW method: (a) The pre-processed shot-gather (Red star represents the shot location), (b) The calculated dispersion image representing Rayleigh wave phase velocity for each frequency (Red dots represent picks at high amplitudes), (c) The extracted dispersion curve from the dispersion image, and (d) Vs model inverted from the dispersion data.

2.4.2 Electrical Resistivity Tomography Method

Surface electrical resistivity surveying is based on the principle that the distribution of electrical potential in the ground around a current-carrying electrode depends on the electrical resistivities and distribution of the surrounding soils and rocks. The usual practice in the field is to apply an electrical direct current (DC) or alternating current (AC) of low frequency. The voltage between two potential electrodes and the current between two other electrodes are measured during the ERT survey. Measurements were provided using various pairs of electrodes along the transect. An increase in spacing between electrodes allows for deeper investigation depth. Therefore, apparent resistivity values can be obtained through the voltage, current, and geometry of array electrodes for each point laterally and with depth. The measured apparent resistivity values are used in the inversion to obtain resistivity models for subsurface material.

After data acquisition, the data was checked for large measurement errors (>2%) using Prosys II software (IRIS Instruments), which was provided with the Syscal equipment. During the data acquisition process, a roll-along technique was implemented, involving the relocation of the array's center to a distance of 18 m (approximately half of the initial length equal to 35.5 m). To assess the quality of the data, we computed the errors between measurements taken after this center movement. Approximately 20% of the total measurements were repeated, and the average error was found to be less than 1%. These metrics provide valuable insights into the overall data quality, indicating a relatively low average error and the redundancy of about 20% in the measurements. For the purpose of joint inversion, we combined Wenner-Schlumberger (WS) and Dipole-Dipole (DD) data into one dataset.

Res2Dinv software (Res2Dinv Manual, 2006) was used to generate a resistivity model from apparent resistivity values. The inversion software uses a smoothness-constrained least squares method with L2-norm (Loke & Barker, 1996). For the model mesh, we used half-electrode spacing (0.25 m) in the horizontal direction. In the vertical direction, the thickness for the first layer was set to 0.125 m with a 1.1 factor to increase the thickness with depth.

The inverted resistivity model can also be influenced by topographic changes along a transect, particularly in the top cells. Minor variations in topography may have negligible effects on the inversion process, but substantial changes can introduce distortions. Elevation changes along the transect are generally insignificant and less than 0.5 m on the edges of ice wedge polygons for our study site (at MASW 3 location). As a result, topography has not been integrated into the inversion process. In some cases, degraded polygons have large elevation changes, and it is crucial to carefully evaluate the significance of topographic changes for these areas when dealing with geophysical inversion models.

We used robust constraints and defined an initial half-space resistivity value of 10 Ωm to trace the spatial distribution of cryopeg layers based on low resistivities observed in previous studies (Hubbard et al., 2013; Overduin et al., 2012; Yoshikawa et al., 2004). A 2D ERT model was generated to invert WS and DD arrays jointly, and the result achieved an RMS error of 1.8%. Across different iterations, specifically the 3rd, 4th, and 5th, the percentage changes were 5.8%, 2.8%, and 1.86%, respectively. When comparing the results of inverted resistivity with varying RMS errors, notable variations were observed primarily in the lower cells of the model. The overall changes between the 4th and 5th iterations were evident in both resistivity and the bottom boundary for the deepest contrast layer. Nonetheless, these changes remained generally stable and did not substantially affect our interpretation results.

ERT and many other geophysical methods give us inherently non-unique solutions for mapped reconstructions of subsurface electrical properties. This non-uniqueness means that the measured data can be explained equally well by multiple models. To improve the reliability of subsurface interpretations, we use soil core sampling and comparison with other geophysical methods, such as the MASW technique.

2.4.3 Correlation of Soil Mechanical Properties with Shear Wave Velocity

Soil's mechanical properties can be determined using Vs, which is a commonly used geotechnical and geophysical parameter. There are empirical or analytical correlations between Vs and several other soil properties. For instance, there is a positive correlation between Vs and soil stiffness parameters such as shear modulus (G) and elastic modulus (Young's modulus, E). Stiffer soils generally exhibit higher shear wave velocities and are correlated with higher soil strength parameters such as undrained shear strength (Su) and peak shear strength. In addition, Vs is inversely correlated with soil porosity, where lower Vs values are often observed in soils with higher porosity. For a given soil type, with constant parameters like temperature and ice content, Vs is directly proportional to soil density, indicating that denser soils generally exhibit higher Vs values. Furthermore, soil classification, which determines the foundation design, directly correlates with VS30 and Su30, which are the averages of Vs and Su in the top 30 m (ASCE/SEI 7-16, 2017). Therefore, understanding the soil classification and Vs is crucial for assessing the seismic performance and stability of foundations and for designing appropriate foundation systems.

For soil that is elastic, isotropic, and homogeneous, the elastic theory can be used to establish the following relationship between elastic modulus and seismic wave velocity:

$$\mu = \frac{\left(\frac{V_p}{V_s}\right)^2 - 2}{2\left(\frac{V_p}{V_s}\right)^2 - 2} \tag{2.1}$$

$$G = \frac{\gamma V_s^2}{g} \tag{2.2}$$

$$E = 2G(1 + \mu) \tag{2.3}$$

where, μ is the Poisson's ratio, γ is the unit weight of the media, and g is the gravitational acceleration, which can affect the foundation design in various ways such as foundation type, foundation settlement, and allowable vertical and lateral loads (Coduto, 1999). The relationship between elastic modulus and bearing capacity of soils could depend on several factors such as soil classification, stress history, foundation type, etc. The elastic settlement beneath a flexible footing placed on the ground surface can be calculated as follows (Terzaghi et al., 1996):

$$S_e = \frac{qB(1 - \mu^2)\, I_f}{E} \tag{2.4}$$

where q is the surcharge load, B is the width of the footing, and I_f is the influence factor, which is a function of the ratio of length to width ($\frac{L}{B}$) and the thickness of the compressible layer. We will highlight the importance of Vs monitoring on the change in elastic modulus and elastic settlement in subsection 2.6.6.

2.5 Data Acquisition

There are eight seismic survey locations using MASW, six temperature measurement locations using thermistors, one ERT survey location (at MASW 3 location), and five core sampling locations (at Roadside and MASW 1-4 locations), as shown in Figure 2.1. The coordinates of these locations are provided in Table A.1 in Appendix A. The seismic surveys cover various soil conditions, including disturbed and undisturbed areas. Four seismic surveys (MASW 1-4) were performed on undisturbed tundra permafrost and four (Roadside and NOAA 1-3) on disturbed permafrost, shown in Figure 2.1c. The seismic surveys performed on disturbed permafrost include one survey along the gravel road near the National Oceanic and Atmospheric Administration (NOAA) facility (Roadside), one survey under the NOAA building (NOAA 1), one survey on the pre-existing building foundation next to the NOAA building (NOAA 2), and one survey on the tundra near the pile foundations (NOAA 3). At the NOAA 2 location, a building was demolished and removed one year prior to the seismic survey, but the pile foundations remain in the ground. The core sampling was performed at approximately 1 m from the seismic survey locations using a hand-held sampling drill (boring auger). The sampling depth is up to 103 cm.

2.5.1 Surface Wave Data Acquisition

Each seismic line consists of 24 vertical 4.5 Hz geophones (a 24-channel Geometrics Geode seismograph) positioned on the ground surface. Straight-line seismic profiles have a geophone spacing equal to 1 m, which gives us a 23 m spread in total. We generated seismic signals using a sledgehammer adjacent to the geophones as well as an extra shot at 5 m offset from the beginning of the lines. The seismic record length was 128 ms with a sample interval of 0.25 ms, and each recording was initiated by a trigger attached to the sledgehammer. No pre-acquisition filter was used on the seismic data. Note that with the vertical source and the vertical receivers, the type of surface waves we acquired are Rayleigh waves. An example of the collected seismic traces is shown in Figure 2.2a.

2.5.2 Temperature Data Acquisition

Small holes with 0.02 m diameter were punched in the ground to a depth of 1.5 m in August 2021. Four HOBO TMC6-HD temperature sensors were then lowered into the ground using wooden rods to the depths of 0.02, 0.2, 0.5, and 1.5 m below the surface. At each location, temperature sensors were connected to two 2-channel HOBO U23-003 loggers in September 2022 (Soil temperature measurement information is presented in Figure A.3 and Table A.2, Appendix A). The operating temperature range for loggers is -40 to 100 ℃ with an accuracy of 0.4 ℃ and 0.2 ℃ below and above 0 ℃, respectively. The resolution is 0.02 ℃. Data records were collected during the field trip in August 2022. Because most of the commonly used construction materials are prohibited in this study area, reducing the vulnerability of the sensor installation to damages by wildlife animals is a challenging task and several temperature sensor cables were severed by Arctic foxes. Nevertheless, temperature records were collected at the six following sites. Site conditions were described during installation as follows. The Temp 1 profiler was placed into a shallow pond with 10 cm of standing water; The Temp 2 profiler is located near a rim of the flat-center ice-wedge polygon; the site conditions could be described as moist. The Temp 3 station is placed at the center of a high-center polygon with a dry ground surface. The Temp 4 site is almost saturated, with a thin layer of standing water in the middle of the low-center polygon. The Temp 5 profiler is at the rim of the low-center polygon, with the dry ground around it. Finally, the Temp 6 profiler is approximately 9 m from shore, where the ground is rather moist.

2.5.3 Electrical Resistivity Tomography Data Acquisition

An Electrical Resistivity Tomography (ERT) survey was conducted to provide in-situ resistivity measurements (Ωm) along the MASW 3 transect from September 13, 2022. The ERT station Syscal-Pro 72 (IRIS instruments) and steel electrodes were used to acquire data. Electrodes were placed along the transect using measuring tape with a 0.5 m spacing. Inverse WS and DD arrays were applied for measurements. The minimum/maximum half electrode spacing was 0.75m/17.25m for WS and 0.5m/13.5 m for the DD array. A 50 V output voltage and 250 ms pulse duration were applied during the survey. Contact resistances for most of the electrodes were no more than 1 kΩ. Measurements with errors exceeding 2% were removed during processing.

2.5.4 Borehole Core Sample Acquisition

Permafrost core samples were collected using a hand-held boring auger at MASW1-4 and Roadside locations. The Auger boring technique is particularly effective in permafrost areas due to its ability to efficiently penetrate the frozen ground with limited disturbance to the surrounding soil. Core samples with diameters of 3.8 cm and depths of up to 103 cm were collected to determine active layer depth, identify soil type and density within the active layer and permafrost, evaluate salinity levels, and construct stratigraphy plots. Core samples were kept frozen during transportation to the University of Alaska Fairbanks for identification and density measurements. The thawed samples were then sent to the Pennsylvania State University for salinity measurements.

2.6 Results and Discussion

The following subsections provide an overview of the Vs, electrical resistivity, and temperature results. We highlight key findings related to permafrost, including site characterization (2.6.1), shear wave velocity interpretation (2.6.2-2.6.4), civil infrastructure's influence on permafrost (2.6.5), and applications to engineering properties and infrastructure design (2.6.6).

2.6.1 Site Characterization of Disturbed and Undisturbed Permafrost

We calculated 1D and 2D Vs models for 8 survey lines after performing inversion on the calculated dispersion curves using the MASW method (Park et al., 1999a, 1999b). This included both disturbed and undisturbed permafrost regions. Figure 2.3 shows the 1D Vs profiles for the survey locations on the tundra, which are categorized as undisturbed permafrost locations. Figure 2.3a shows the Vs profile for the first location of MASW survey in the tundra (MASW 1), approximately 500 m from the road and NOAA facility. A similar Vs profile is observed in Figures 2.3b-d (MASW 2-4), except that the relative high-velocity zone is located relatively at a higher depth than MASW 1. Also, MASW 1 has a more consistent velocity profile at deeper depths than MASW 2-4. These could be an effect of the different geology, vegetation, or the effect of anthropogenic activities over the years, as we observed many marked points for previous studies and tracks from vehicles in the field. Figure 2.3b represents the Vs for the second location in the tundra (MASW 2), approximately 1 km from the infrastructure. We observe a very high-velocity zone at a depth of 2-8 m below the surface, representing either a stiff lithology layer or an ice-rich zone. The highest Vs layers are located at a depth of 5 m and are as high as 1700 m/s. This location clearly shows the undisturbed permafrost area with higher Vs and higher ice content. Figure 2.3c illustrates the velocity model for the third location in the tundra (MASW 3), roughly 1.5 km from the road and NOAA building. While the low-high-low Vs pattern is obvious, the highest velocity is 1575 m/s, which is lower than that at the MASW 2 at 1 km. In the field, we observed that as we get further to the tundra, the ground gets wetter as indicated by many ponds in the area. This can also be seen on the satellite map in Figure 2.8c-d (presented later in this paper), where the last two lines (MASW 3 and 4) are located in darker areas that represent higher surface water content. Figure 2.3d illustrates the velocity model for the last location in the tundra (MASW 4) at roughly 2 km from the road and NOAA building. Like all other locations in the tundra, we observed the low-high-low velocity profile, but the highest velocity zone is located at deeper depths of 7 m. In addition, the highest Vs is 1150 m/s at MASW 4, which is lower than those at the two previous locations in undisturbed permafrost zones (MASW 2 and 3). These last two locations (MASW 3 and 4) represent the effect of vegetation and high surface water content. The previously observed low-high-low velocity profile below the surface by Dou & Ajo-Franklin (2014) is captured at all tundra locations (i.e., MASW 1-4 and NOAA 3).

Figures 2.3e-g show the 1D Vs profiles for the survey locations near the NOAA building, including the roadside, within 1.0 m of the NOAA building (NOAA 1), and ~80 m away from the NOAA building (NOAA 3), where we expect high disturbance in permafrost. These locations are categorized as disturbed permafrost locations. The Vs at disturbed permafrost locations is lower than that at undisturbed permafrost locations, as the vegetation and thus albedo are affected by human activities, and the ice content is lower than that in the undisturbed permafrost region. Figure 2.3e represents the Vs for the location within 1.0 m of the gravel road leading to the NOAA facility, where we expect high disturbance in permafrost. The 1D velocity profile represents a low-high-low velocity pattern with the highest Vs of 850 m/s. It is noted that the data at the pre-existing demolished building foundation next to the NOAA building (NOAA 2) are of low quality, which resulted in a higher RMS error than the acceptable error. As we performed sledgehammer shots on top of a pre-existing building foundation, the contrast in soil and pile material properties and the resulting scattered energy likely generated relatively larger errors than in other locations.

Figure 2.4 shows the 2D Vs models in the undisturbed (Figure 2.4a-d) and disturbed (Figure 2.4e-g) permafrost regions, similar to Figure 2.3. A low-high-low velocity pattern is evident in all models, indicating the active layer and transitional zone (with low velocity), ice-rich permafrost (with high velocity), and partially frozen permafrost with scattered ice (low velocity). Previous studies have shown a strong correlation between permafrost temperature and Vs (Ji et al., 2024; Kurfurst, 1976; Nakano et al., 1972). The low-high-low velocity pattern is consistent with the general trend of permafrost temperature variation with depth, as in a previous study (Smith et al., 2022). Although the velocity and depth vary spatially, the low-high-low pattern is consistent among all locations. The 2D models capture the spatial variability of permafrost, demonstrating the importance of multichannel seismic surveys and 2D modeling. We will discuss these models in detail in sections 2.6.2 and 2.6.3.

Meanwhile, we invert the electrical resistivity model (Figure 2.5a) from the ERT data, which can delineate several zones compared to the Vs model from the MASW 3 transect (Figure 2.5b). Each zone is characterized by different thicknesses, electrical resistivity, and velocity values. Zone A is characterized by relatively low resistivity up to 200-300 Ωm from the surface down to approximately 0.4 m. This layer represents the active layer and is characterized by low Vs of 240 m/s. Zone B is characterized by high resistivity values of 400-2000 Ωm. The thickness of this layer varies from 1 m at distances of 6-24 m to 4 m at distances 2-6 m. According to drilling data, the zone between 1.4 m and 1.7 m is a transition zone (black box marked in the borehole in Figure 2.5) between a frozen and unfrozen state and represents a boundary between zone B and C. Zone C is characterized by soils with low resistivity of 10-20 Ωm associated with cryopeg development in the study area. The thickness of the layer is about 2.5 m along the profile and decreases toward the beginning of the transect. At a depth of 0.5-0.6 m, the salinity measured approximately 0.84 ppt (parts per thousand, roughly equivalent to grams per liter). In contrast, at a deeper level, specifically 1.5-1.6 m, the salinity was significantly higher, measuring 8.03 ppt. Consequently, one can infer that salinity gradually increases from Zone B to Zone C, contributing to the low resistivity observed for cryopegs in Zone C. The characteristics of Zone C, exhibiting low resistivity and relatively high velocity, may be attributed to two potential factors. Firstly, it is plausible that this zone remains frozen, with its temperature lingering below the freezing point of cryopegs. Alternatively, the distinct lithology and soil mineral composition within this zone could be significantly influencing the resistivity and seismic velocity properties of unfrozen sediments in the near-surface, as highlighted in studies by

Rossi et al. (2022) and Accaino et al. (2023), respectively. These findings are aligned with previous studies demonstrating the complex and heterogeneous nature of permafrost in the study site (Brown, 1969; Dafflon et al., 2016). Zone D is characterized by relatively high resistivity values of 100–600 Ωm and a thickness of approximately 2 m and is located between two zones of low resistivity (both zones denoted as Zone C). The zone is also characterized by high Vs up to 1600 m/s, typical for frozen material and increased ice content. Due to the relatively high-velocity values, the high-resistivity layer D, and the presence of salt pockets even in ice-rich conditions in Utqiaġvik (Iwahana et al., 2021), we interpret this layer as an ice-rich layer. High-velocity values for zone D are also supported by the intra-ice brine pockets, where cryopeg brine is bounded by ice, and are generally in solidified form (Iwahana et al., 2021).

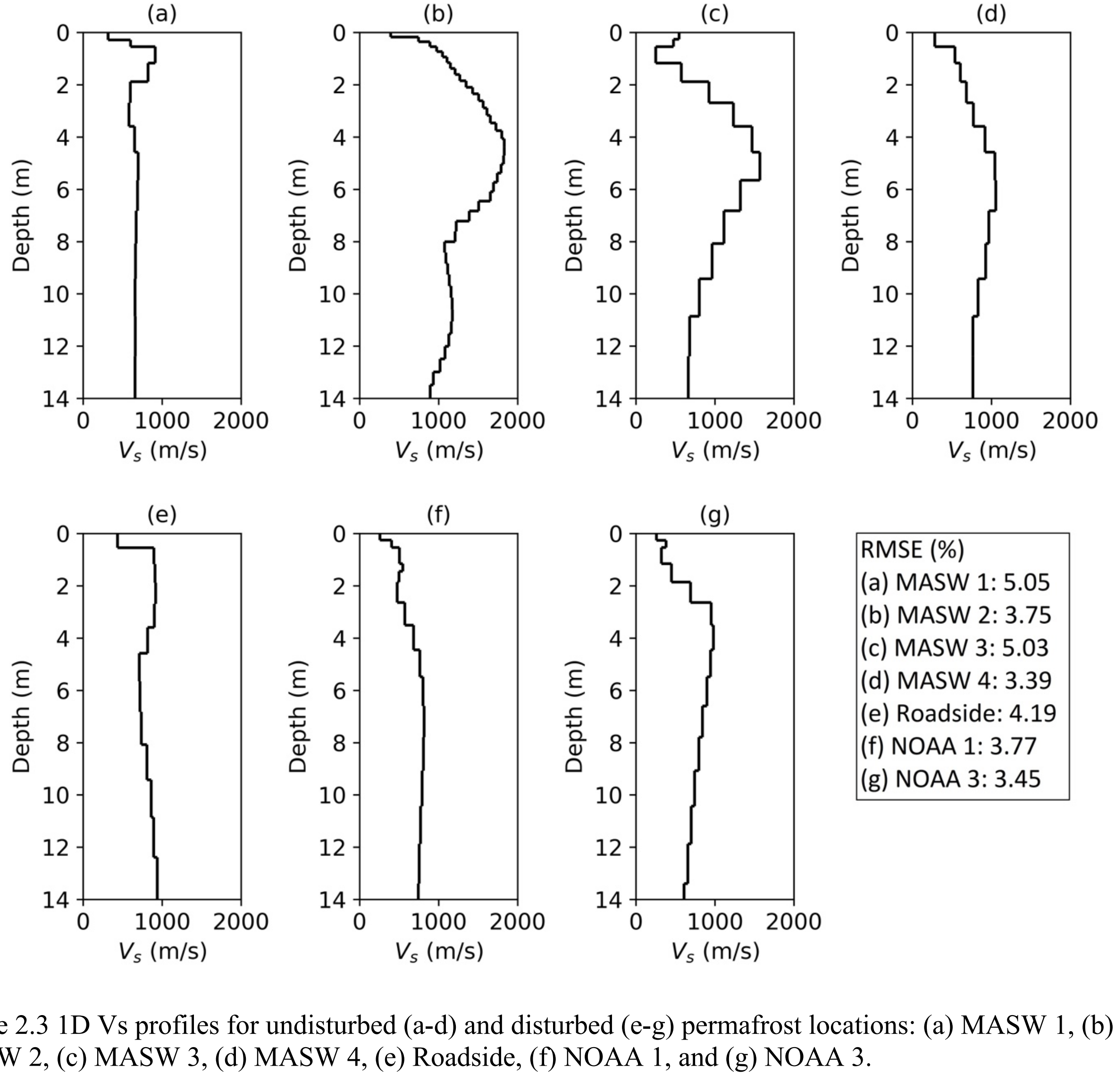

Figure 2.3 1D Vs profiles for undisturbed (a-d) and disturbed (e-g) permafrost locations: (a) MASW 1, (b) MASW 2, (c) MASW 3, (d) MASW 4, (e) Roadside, (f) NOAA 1, and (g) NOAA 3.

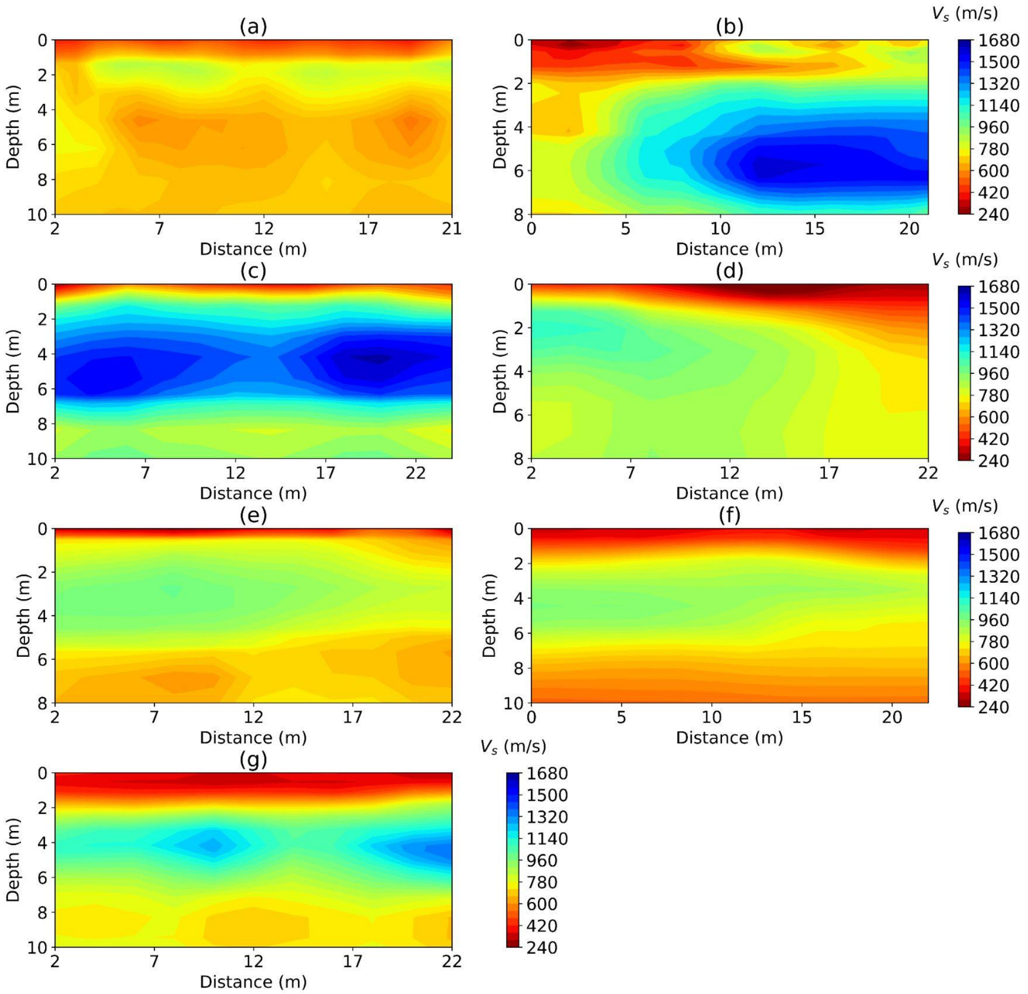

Figure 2.4 2D Vs profiles for undisturbed (a-d) and disturbed (e-g) permafrost locations: (a) MASW 1, (b) MASW 2, (c) MASW 3, (d) MASW 4, (e) Roadside, (f) NOAA 1, and (g) NOAA 3.

Due to the high contrast of the resistivity of different units, the ERT method helps to identify multiple layers in the upper part of the cross-section that cannot be clearly distinguished using the MASW method due to the lack of high-frequency signals. The MASW results provide useful information to verify ERT results at greater depths. The MASW method reveals a high degree of heterogeneity in the permafrost, possibly due to increased salinity at greater depths, resulting in unfrozen zones. Additionally, integrating ERT and MASW provides a more comprehensive assessment, offering insights into critical aspects, such as the salinity and ice content within the permafrost, which are crucial for understanding its physical properties and behavior. This methodological framework, effective in our specific study area, has potential applicability in diverse permafrost environments, indicating its potential for wider application and enhancing the knowledge of near-surface permafrost dynamics.

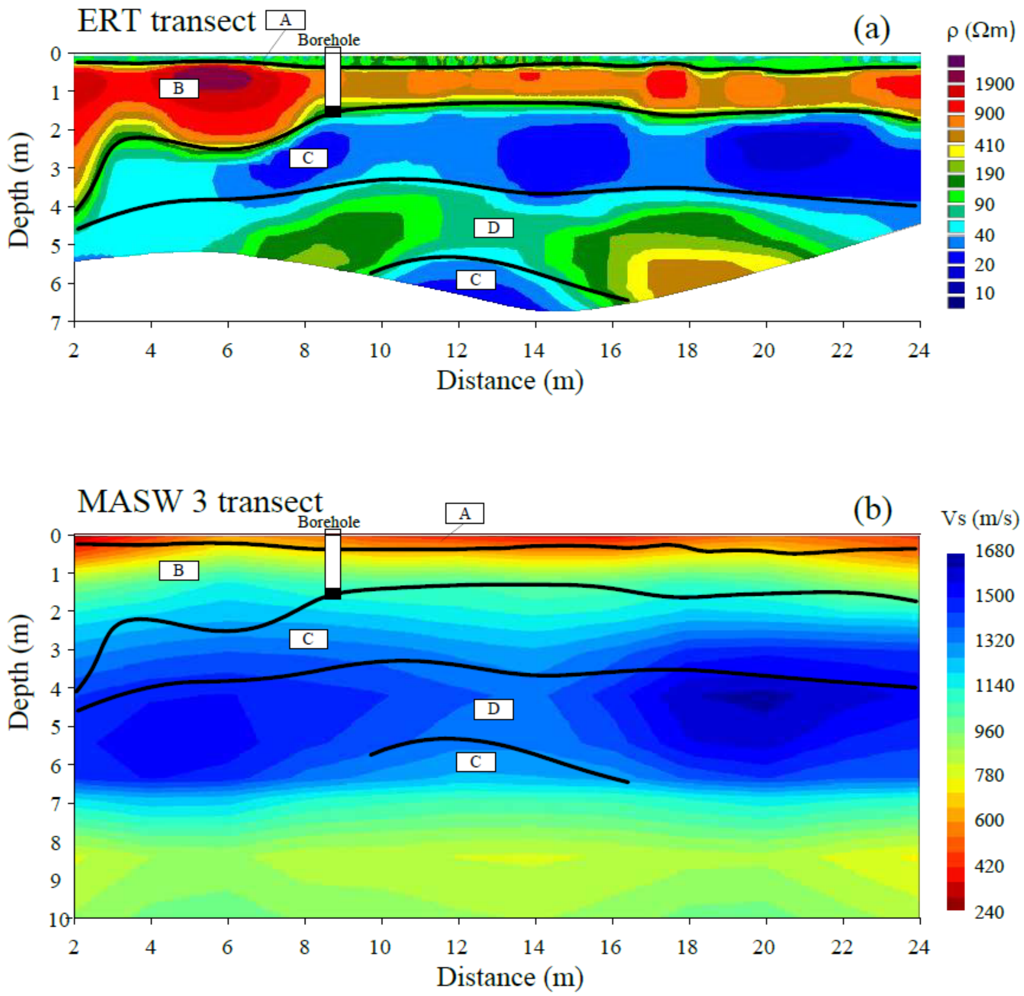

Figure 2.5 2-D ERT (a) and MASW (b) comparison results at the MASW 3 location. Black lines represent interpreted ERT boundaries based on resistivity values. Zones A to D specify different ranges of electrical resistivity and shear wave velocity values corresponding to various permafrost structures. The white box indicates the borehole sample, and the black box inside the white box shows the transition zone.

2.6.2 Identification of Active Layer Thickness

Significant variations in ALT exist between different landscape types, reflecting the influence of vegetation, substrate, microtopography, and especially soil moisture (Shiklomanov et al., 2010). From Vs profiles shown in Figure 2.4, we can identify the ALT range (roughly 0.3 m) and the shear wave velocities of the active layer (240 – 370 m/s) in most locations. However, in some undisturbed permafrost regions, ALT was found to be highly spatially heterogeneous due to differences in subsurface characteristics based on 2D Vs profiles shown in Figure 2.4. Therefore, ALT at some locations may be 0.5 – 0.6 m, which is consistent with the ALT range estimated from nearby temperature measurements (described in Section 2.5.2) and the earlier estimation by Jafarov et al. (2018). In contrast, ALT in disturbed permafrost regions presents higher values (0.5 – 1.0 m) and less spatial heterogeneity. The higher ALT indicates that the ground temperature is slightly higher for the permafrost with human activities than in the undisturbed permafrost. For NOAA 1 (Figure 2.3f), the high consistency in ALT is because the ground surface is under the NOAA facility, and the topsoil is gravel, which is different from all other locations. The coverage of the building, which produces continuous heat, and the high thermal conductivity of gravel compared to fine-grained soil like peat or silt are likely contributing factors to the temperature consistency of the tested line. The MASW results did not reveal the top shallow active layer of MASW 3 due to the small ALT (0.24 m based on soil sampling) and lack of high-frequency source signal required to image shallow depths. Figure 2.6 illustrates the stratigraphy of deposits up to 1.0 m at the five sampling locations. The permafrost mainly consists of silty soil with organics with an average unit weight of 19.62 kN/m^3. Ice layers are evident in the boreholes of MASW 1 and 2. Based on the boring samples collected at the same sites of the seismic surveys, ALT in the study regions were 0.14 – 0.28 m during sampling. The ALT range identified by MASW in most locations is within a reasonable range compared with the stratigraphy of deposits.

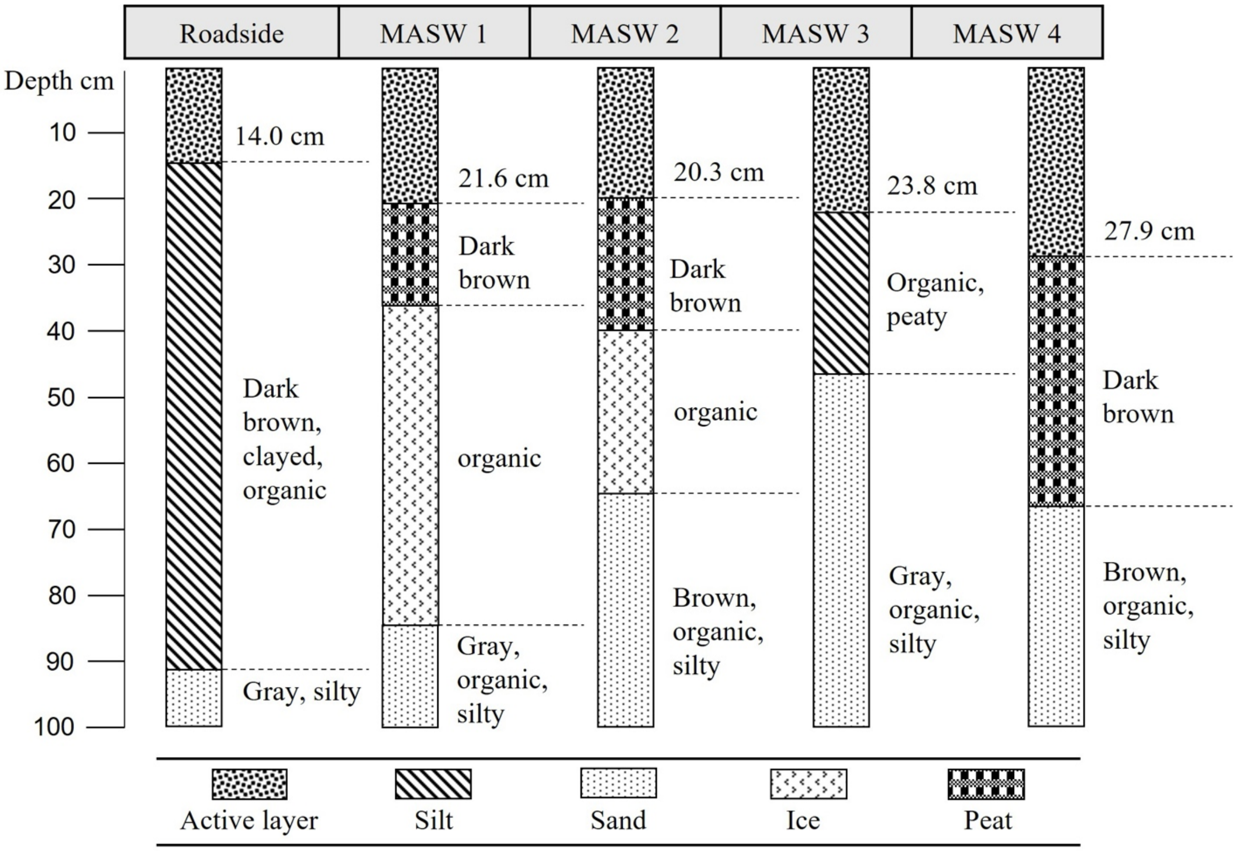

Figure 2.6 Stratigraphy of borehole core samples at five locations.

2.6.3 Identification of Spatial Heterogeneity of Permafrost

Spatial heterogeneity within the permafrost layer can be observed and quantified by analyzing Vs profiles, including ice-rich permafrost, low-velocity zones, and cryopeg. Shear wave velocities within the permafrost layer range from 450 to 1700 m/s. The shear wave velocities of ice-rich permafrost zones (MASW 2-4) are in the range of 700 – 1700 m/s, which is higher than the range of 500 – 900 m/s from other permafrost locations. Ice-rich permafrost can be identified in 2D Vs profiles, such as in Figure 2.4b (MASW 2), with a high-velocity zone (from 9 m to 22 m) with a Vs range of 1300 – 1700 m/s. The theoretical Vs of pure ice is approximately 1900 m/s at a temperature near -10 °C (Kohnen, 1974). Given that the effective Vs of a medium is a weighted average of the components of that material, the regions of the subsurface with velocities near 1700 m/s are expected to be ice-rich materials. This indicates that the center area of the ice-rich zone is likely composed primarily of ice layers. However, the gradual increase of the velocity near the ice-rich zone at MASW 2 indicates suspended soil around the ice layers.

Figure 2.1c shows that MASW 3 is located in a wetter area (darker image color is related to higher surface water content), which may lead to open talik regions around the large water body. A potential reason for the talik or cryopeg layer at MASW 3 is salinity, as higher salinity layers exist at MASW 3 due to proximity of the nearby saline thermokarst lake. This is consistent with our observation of core sample's salinity at MASW 3 (discussed in subsection 2.6.1).

2.6.4 Impacts of Ground Temperature and Ice Structure on Shear Wave Velocities

In subsections 2.6.4 and 2.6.5, we focus on the impacts of multiple factors on shear wave velocity in undisturbed permafrost to better understand permafrost behavior and stability. Figure 2.7 shows the composed profiles of Vs in undisturbed permafrost, temperature variation, and cryostratigraphy versus depth. Generally, the rate of temperature decrease lessens with increasing depth. The temperature measurements are derived from several locations in the North Slope Borough, Alaska, mainly near the study site. The detailed location and record date of the temperature measurement are presented in Figure A.2 and Table A.2 in Appendix A. The temperature reveals that the ALT is around 0.5 m, which agrees with the ALT determined from the MASW surveys.

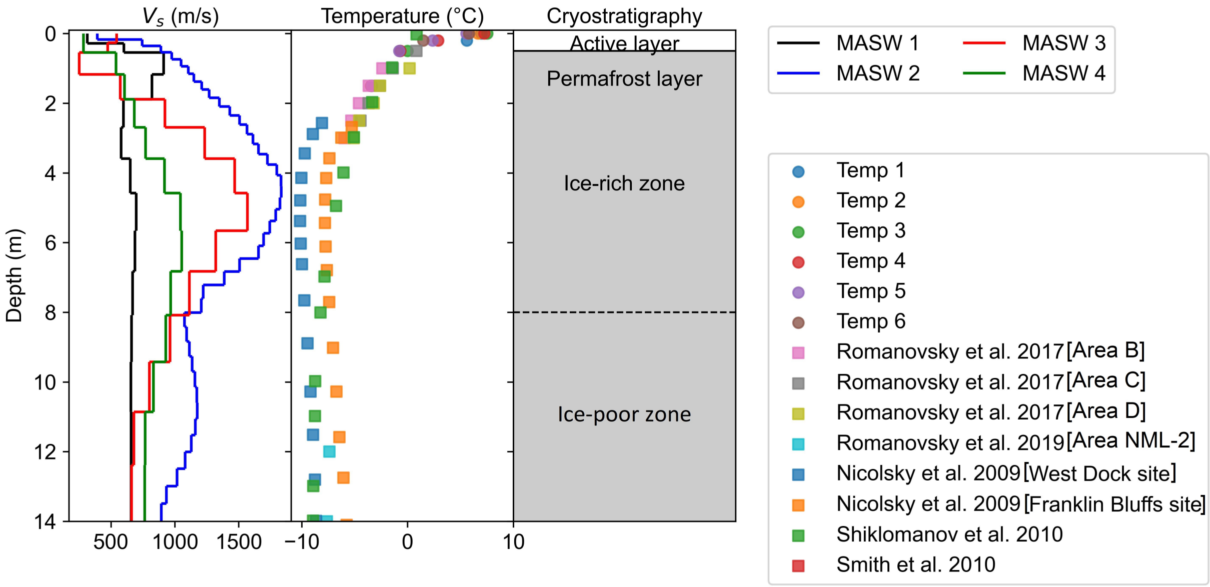

Figure 2.7 Composed velocity, temperature, and stratigraphy profiles in North Slope Borough, Alaska.

We observed that the depth variation of Vs (Figure 2.7) exhibits a consistent trend across different testing locations near Utqiaġvik. The Vs is low (~ 250 – 510 m/s) in the active layer and increases in the permafrost layer to around 1200 – 1700 m/s as depth increases to 5 – 8 m. Beyond this depth, the shear wave velocities decrease, forming a low-velocity permafrost zone (~500-700 m/s) beneath the high-velocity permafrost layer. Dou & Ajo-Franklin's (2014) study also reported the existence of a low-velocity permafrost zone at a location approximately 5 km south of the study area. This suggests that low-velocity permafrost zones may exist under the tundra near Elson Lagoon and east of Utqiaġvik. As shown in Figure 2.7, the Vs profiles are correlated with temperature profiles, with higher ground temperature corresponding to lower shear wave velocities of permafrost. We also observe that Vs below 8 m decreases, possibly due to discontinuous ice in deeper zones. Based on the 1D and 2D velocity profiles, we conclude that generally, the 2-8 m zone contains higher ice connectivity (and therefore less scattered or discontinuous ice), which causes high-velocity zones. This can clearly be seen in 2D plots where a high-velocity zone (and not a continuous layer) exists on two undisturbed permafrost velocity profiles (Figures 2.4b and 2.4c). Therefore, although the temperature can be consistent in higher depths (as shown in Figure 2.7 using the literature datasets collected near Utqiaġvik), the velocity could be different due to changes in ice content and the spatial distribution of ice. While the temperature profiles closely align with each other, there are clear disparities in the Vs profiles. Such differences might be indicative of pronounced lateral variations in ice content or could reflect changes in the lithology or texture of the underlying sediments.

Ice-wedge polygons occur on nearly all nearshore land surfaces (Kanevskiy et al., 2013) and can be outlined using 2D Vs profiles. The formation and degradation of these polygons are linked to climate change, resulting in severe landscape alteration. There are mainly three types of ice-wedge polygons in the tundra between Utqiaġvik and Elson Lagoon: high-centered polygons, flat-centered polygons (incipient polygons), and low-centered polygons. High-centered polygons are shown in Figure 2.8b, flat-centered polygons in Figure 2.8c, and low-centered polygons in Figure 2.8d, surrounded by thermokarst lakes. An early stage of high-centered polygon formation can be seen in Figure 2.8a. MASW 4 (Figure 8d) is surrounded by coalescent low-center polygons (Lara et al., 2015) and thermokarst lakes based on the satellite view nearby, presenting lower Vs compared with high-centered polygon regions (Figure 2.8b). The landscapes near MASW 4 develop and degrade from flat-centered and high-centered polygons (Nitzbon et al., 2019), showing severe landscape alteration due to climate change. This transformation is referred to as ice-wedge polygon degradation. A water body in the center of the low-centered polygons can change the hydrological regime of polygon nets and lead to the onset of thermokarst activity (Kartoziia, 2019). As shown in Figure 2.8b, some of the high-centered polygons are developing and connecting, presenting ice-rich permafrost zones with high Vs, which have the potential to form thermokarst lakes during permafrost degradation. MASW 2 and 3 cover the polygon centers and troughs of high-centered polygons, while MASW 4 is on the rim between thermokarst lakes. For locations with surface water, Vs presents lower values on the top of the permafrost layer than adjacent permafrost.

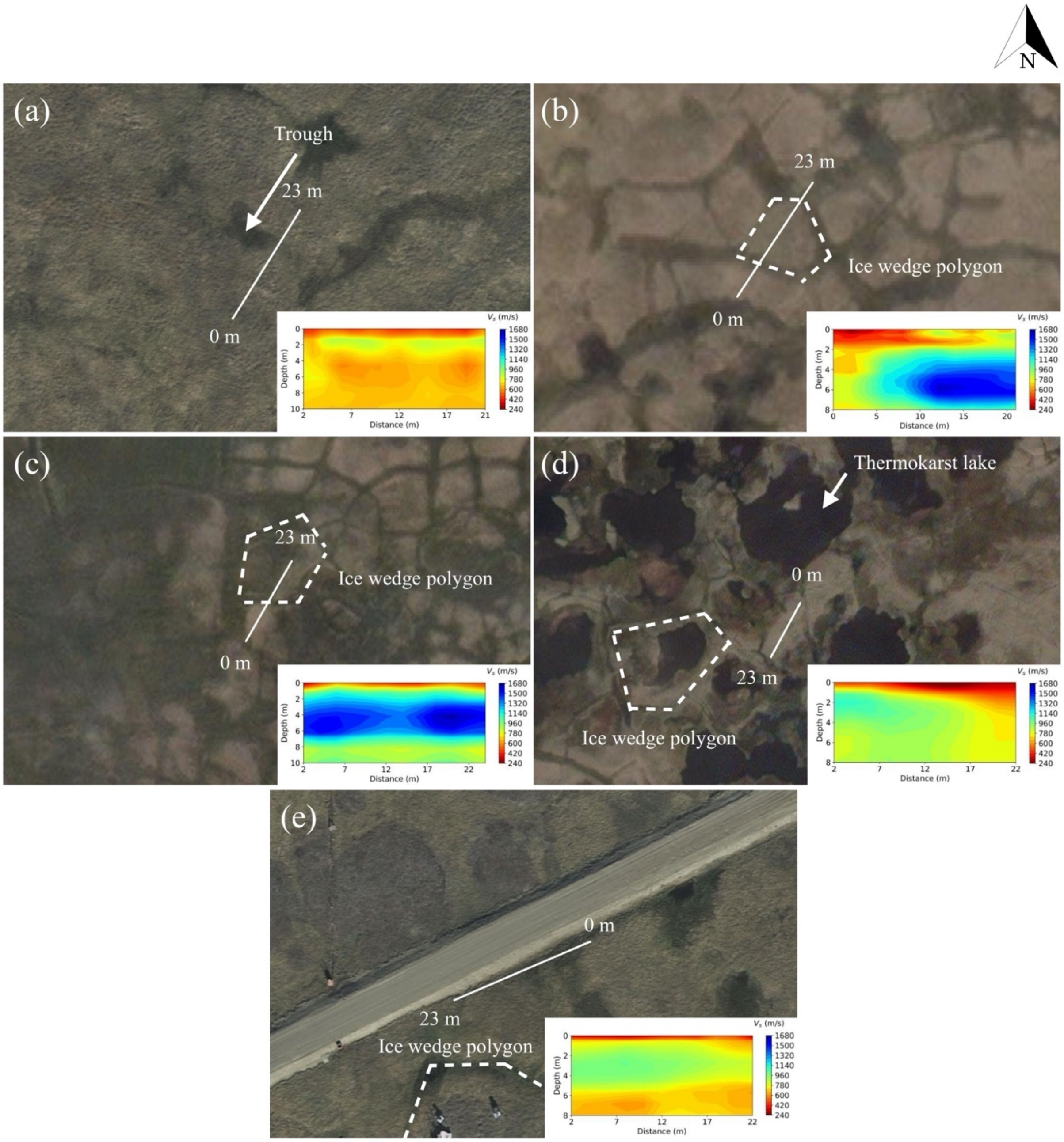

Figure 2.8 Satellite view of MASW testing locations in undisturbed permafrost tundra and disturbed permafrost roadside: (a) MASW 1 in the developing polygon trough area, (b) MASW 2 in the flat-centered polygon area, (c) MASW 3 in the low-centered polygon area, (d) MASW 4 surrounded by thermokarst lakes, and (e) Roadside.

2.6.5 Influence of Civil Infrastructure on Permafrost

In this section, we discuss the influence of civil infrastructures, including gravel roads and pile foundations, two of the most common civil infrastructures in Northern Alaska, based on seven MASW surveys. Comparison of Vs profiles of disturbed permafrost locations (Roadside and NOAA 1) and relatively undisturbed permafrost locations nearby (NOAA 3 and MASW 1) in Figure 2.4 demonstrates that the ALT is larger in disturbed permafrost due to higher surface temperature. For NOAA 3 and MASW 1, the maximum Vs is similar (~900 m/s), but the high-velocity zone is deeper (~4 m) in permafrost near civil infrastructure (NOAA 3) compared with MASW 1 (~1 m). This discrepancy may be due to the disturbed gravel topsoil and also higher air temperatures near civil infrastructure, causing diffusive heat transfer from a more absorptive material and resulting in temperature profiles that differ from undisturbed permafrost locations.

The MASW testing location beside a gravel road is shown in Figure 2.8e (Roadside). In cold regions, dry coarse-grained soil is often used to replace the foundation soil of roadbeds or airport runways to prevent frost heave (Vinson et al., 1996). The gravel fill reduces the road's frost heave and thaw settlement by providing better drainage capability but affects the moisture regime near the gravel road. As shown in Figure 2.8, high-centered polygons developed near the gravel road, with surface water accumulation next to the road embankment.

Ice-rich permafrost zones can be identified beneath the polygon landscape in the Vs profiles shown in Figures 2.4 and 2.8. The depth of the ice-rich permafrost zone along the roadside (Figure 2.4e) is shallower than the nearby tundra location at NOAA 3 (Figure 2.4g), suggesting the influence of the gravel road. Along the roadside, the ice-rich permafrost zone (~3 m thickness) is thicker than MASW 1. Different moisture migrations beside the gravel road may cause these differences. In addition to unfrozen water migration as the dominant mode of moisture movement, vapor flux also contributes to frost heaving (Currie, 1983; Farouki, 1981; Smith & Burn, 1987; Teng et al., 2020). Gaseous water (vapor) migrates from the warm and humid side of the soil layer to the cold and dry layer below the closed and impermeable ground surface in coarse-grained soil and then condenses into ice, causing frost heaving (Guthrie et al., 2006; Niu et al., 2017; Zhang et al., 2020). This phenomenon is known as the "pot effect" or "canopy effect". Generally, soil with an initial moisture content of less than 30% is more prone to showing the "pot effect" (Bai et al., 2018).

Pile foundations are the most common building foundation type in Arctic Alaska to overcome differential settlement. Figures 2.4f and 2.4g display the 2D Vs profiles for MASW surveys under the NOAA building (NOAA 1), and ~80 m from the building in the tundra (NOAA 3), respectively. As shown in Figure 2.3, NOAA 1 shows a similar low-high-low Vs trend to NOAA 3 (and also MASW 1-4). At depths of 0-2 m, shear wave velocities are slightly different for NOAA 1 and NOAA 3 due to the topsoil of NOAA 1 being gravel, while NOAA 3 is tundra permafrost. At 2-8 m depths, NOAA 3 presents an ice-rich permafrost zone, while NOAA 1 has much smaller Vs in this depth range, indicating softer soil. In addition, in NOAA 1, we observed a ~150 m/s decrease in Vs for the ice-rich zone compared to the ice-rich zone at NOAA 3 (farther into the tundra). This lower Vs in the ice-rich zone near the building suggests that the pile foundation impacts the soil properties in the surrounding area. Although there is lower Vs in the ice-rich zone near the building, the ice-rich zone near the building is more laterally uniform than the ice-rich zone further in the tundra. Because the building had been present in the area for many years, it could have contributed to the thawing and freezing of the surrounding ground, leading to a more uniform distribution of ice-rich soil after years of thermal diffusion of heat from the building. The substantial differences observed at these sites highlight the need to consider the long-term effects of anthropogenic activities on the geological and geotechnical properties of the ground.

2.6.6 Applications in Quantifying Engineering Properties and Infrastructure Design on Permafrost

Investigating the long-term effect of civil infrastructure on permafrost's stiffness could help improve the engineering design of structures' foundations on permafrost. Permafrost's parameters, such as V_{S30} and E, are affected by soil types (Coduto, 1999), soil temperature (Ji et al., 2024), and soil's ice content (Fisher et al., 2020). Changes in these soil properties show possible changes in soil types, thermal conditions, and cryostructure. For instance, the stability of the subgrade in permafrost regions, as noted by Anhua, (2014), is closely linked to the ice content in the permafrost beneath roadways. Here, we quantitatively analyze Vs profiles at NOAA 1 and NOAA 3 locations. Based on the MASW results, V_{S30} for locations NOAA 1 and NOAA 3 are equal to 744.2 m/s and 799.5 m/s, respectively. This reduction can affect the soil's ability to carry loads (as the soil at NOAA 1 is less stiff than the NOAA 3), leading to greater settlement or deformation under structural loads. Assuming a Vp/Vs = 1.6 for the site's permafrost layer based on (Ji et al., 2024), and γ and g equal to 19.62 kN/m^3 and 9.81 m/s^2, respectively, Equations 2.1-2.3 result in an elastic modulus of 261.07 MPa at NOAA 1 location and 301.31 MPa at NOAA 3 location. This indicates a 13.35% reduction in elastic modulus accompanied by an equivalent increase in settlement values, as delineated by Equation 2.4. While our findings offer useful insights for designing and maintaining infrastructure in polar regions, extending these findings to other permafrost settings should be approached with caution, considering local variations in soil composition, temperature trends, and permafrost degradation.

2.7 Conclusions

This study uses 1D and 2D Vs profiles from MASW along with temperature measurement, ERT, and permafrost sampling to reveal various permafrost features in Utqiaġvik, Alaska. Vs profiles, combined with electrical resistivity models and temperature measurements, can qualitatively characterize active layer, ice-rich permafrost, and cryopeg in the permafrost layer, but cannot identify small-scale cryostructures such as ice lenses. Vs in the active layer ranges from 240 to 370 m/s (silty peat to silt), while Vs in the permafrost layer ranged from 450 to 1700 m/s (silt to slightly sandy silt) in August 2022. Vs profiles demonstrate a consistent vertical low-high-low velocity trend in permafrost. Ice content, ice layers, and ice-wedge influence shear wave velocities, with higher Vs indicating higher ice content. Low Vs permafrost zones may exist across the tundra near Elson Lagoon and east of Utqiaġvik. The Vs variation in ice-rich permafrost correlates with ground temperature variation at 0-15 m depths at the study region. This correlation indicates that ice-rich permafrost with higher Vs values demonstrates lower temperatures than the active layer and ice-poor permafrost. By using ERT, multiple layers can be identified at shallow depths: active layer (200-300 Ωm), cryopeg (10-20 Ωm), and ice-rich permafrost (100-600 Ωm). The presence of ice becomes evident through the analysis of Vs and ERT profiles. To strengthen our conclusions, we validate geophysical results with stratigraphy and salinity analyses from permafrost cores. Integrating geophysical, temperature, and core sampling methods offers a reliable approach to evaluating and understanding permafrost spatial variability.

Civil infrastructure can impact permafrost, resulting in a higher active layer thickness and lower Vs. The influence of gravel road and pile foundation on permafrost degradation varies. Thicker ice-rich permafrost layers at shallower depths, surface water accumulation, and ice polygon development are identified near the gravel road on permafrost. At the sites with building and pile foundations, lower shear wave velocities are observed at depths shallower than 7 m when compared to nearby undisturbed tundra. The active layer and permafrost are more laterally homogeneous closer to the building compared to nearby undisturbed tundra, and a thinner high-velocity zone exists closer to the building. The resulting Vs profile indicates the presence of weaker ground near infrastructure, which should be accounted for in the design and construction of engineering structures by civil engineers.

2.8 Acknowledgements

We thank Roger Michaelides and two anonymous reviewers for their valuable comments and suggestions that have greatly enriched this research. This study is supported by the National Science Foundation under Grants CMMI-2034363, CMMI-2034366, CMMI-2034380, and ICER-1927718. We express our gratitude to Geometrics for providing us with the necessary equipment and software for our study. We also acknowledge the support and facilities provided by UIC Science, LLC, the National Oceanic and Atmospheric Administration (NOAA), and the Atmospheric Radiation Measurement Climate Research Facility of the Department of Energy (DOE ARM). Dmitry Nicolsky acknowledges support from the Tomsk State University Development Programme (Priority-2030). We thank Dr. Min Liew for her valuable professional knowledge and advice, and Dr. Chris McComb for his assistance with fieldwork. Our sincere thanks also go to Larry Irons, an IT support at Colorado School of Mines, and Brian Passerella, equipment pool at Colorado School of Mines, for their invaluable assistance throughout the study.

2.9 Open Research

The seismic and ERT data used for geophysical data processing are available through the Arctic Data Center (Tourei et al., 2023) at https://doi.org/10.18739/A2V40K14Q. The seismic data were processed using the SeisImagerSW software (GeometricsTM, Version 3.0.), with parameters described in Section 2.5.1. The ERT data were processed using Prosys II software (IRIS Instruments) and the Res2Dinv software (Geotomo SoftwareTM, Version 3.59.), with parameters described in Section 2.5.3. The temperature data are available through the Arctic Data Center Nicolsky and Wright (2023) at https://doi.org/10.18739/A2C53F305. The physical permafrost core samples in Figure 2.6 are registered and available through SESAR with the International Geo Sample Number (IGSN) of IENNA0001 (https://doi.org/10.58052/IENNA0001), IENNA0002, IENNA0003, IENNA0007, IENNA0008, IENNA0009, IENNA000A, IENNA000E, IENNA000F, IENNA000G, IENNA000K, IENNA000L, IENNA000M, and IENNA000N.

CHAPTER 3 ENHANCING DAS DATA MANAGEMENT WITH UNSUPERVISED ANOMALY DETECTION FOR SCALABLE MONITORING

An extended manuscript based on the conference paper that is included in Appendix B.

Ahmad Tourei[1], Alexander Ankamah[2], John Hole[3], Gabriel Rocha dos Santos[4],
Ming Xiao[5], Eileen Martin[1]

3.1 Abstract

Distributed acoustic sensing (DAS) often generates massive datasets due to its high spatial and temporal density, posing significant challenges for data management and interpretation. As DAS continues to be deployed in increasingly diverse environments–ranging from underground mines to permafrost regions and urban infrastructure–where traditional seismic arrays cannot easily be installed for long-term monitoring, it encounters complex signal types and noise conditions that have not been previously characterized. This diversity, coupled with the lack of labeled data, motivates the use of unsupervised methods for autonomous anomaly detection. To address this challenge, we present a convolutional autoencoder-based deep learning framework for unsupervised classification of DAS signals into noise and anomalous signals that deviate from typical environmental background noise. The autoencoder first compresses the spatial power spectral density (PSD) of DAS data into a low-dimensional latent space, where kernel density estimation is applied to compute density scores as a probabilistic metric for thresholding of anomaly detection. Reconstruction of the input data from the latent space provides a second metric, reconstruction error, enabling a dual-thresholding approach for robust anomaly detection. When applied to DAS data acquired in an underground mine, the proposed technique identifies (micro)seismic events. In comparison to a traditional seismometer network on the surface, underground DAS analyzed with the autoencoder enhances automated detection of induced seismic events, offering valuable insights for improving safety. A second application to passive permafrost monitoring demonstrates the model's generalizability, where a range of anomalies, including cryoseismic events, anthropogenic noise sources, and instrument noise, were detected. By filtering and retaining only anomalous segments, the framework significantly reduces data storage requirements and streamlines the development of labeled training data for supervised learning models focused on various types of events. These results highlight the framework's scalability and versatility, with applications extending from

---

[1] Hydrologic Science and Engineering Program, Colorado School of Mines, Golden, CO, USA
[2] Department of Geosciences, The Virginia Polytechnic Institute and State University, Blacksburg, VA, USA
[3] Department of Geosciences, The Virginia Polytechnic Institute and State University, Blacksburg, VA, USA
[4] Department of Geosciences, The Pennsylvania State University, State College, PA, USA
[5] Geophysical Institute, University of Alaska Fairbanks, Fairbanks, AK, USA

mining and permafrost monitoring to potential future applications in energy sectors and natural hazard assessment.

3.2 Introduction

DAS technology has enabled the acquisition of spatially and temporally dense seismic data, enhancing monitoring applications such as hydrofracturing (Binder & Chakraborty, 2019; Saw et al., 2025), offshore seismicity (Shi et al., 2025), permafrost dynamics (Cheng et al., 2022), and mining-induced seismicity (Chambers et al., 2025; Chambers & Shragge, 2023; Tourei et al., 2024), among others. Unlike traditional seismic networks, which rely on sparse arrays of seismic stations, DAS leverages photonics technology to transform fiber-optic cables into high-resolution seismic sensors (Lindsey & Martin, 2021). The spatially and temporally dense DAS data enable the detection of subtle seismic events that might otherwise go unnoticed with conventional monitoring systems (Agostinetti et al., 2022).

However, this data richness comes at a cost: kilometer-scale arrays can generate several terabytes of data per day, creating substantial challenges for storage, processing, and real-time analysis (Spica et al., 2023). These challenges are further compounded in passive monitoring studies, in which the lack of labeled training data limits the applicability of supervised machine learning approaches (Bergen et al., 2019). Moreover, DAS deployments often occur in environments where broadband seismic arrays were previously infeasible, and where the full spectrum of event types is not known a priori. In such cases, manual exploratory analysis of DAS data quickly becomes impractical, both in terms of time and computational resources. Therefore, the development of automated tools capable of detecting various anomalies such as seismic events, traffic noise, and instrument noise, is essential for the efficient storage, processing, and interpretation of DAS data.

3.2.1 Motivation in Passive Monitoring Contexts

We initially investigate this challenge in a mining-induced seismicity monitoring study in a longwall coal mine. Longwall mining is an efficient underground mining method for extracting a variety of stratified resources including coal, potash, and soda ash and represents a considerable advancement over conventional methods (Peng et al., 2020). A modern longwall consists of hydraulic shields that support the roof and floor, a cutting device (e.g., a shearer or plow) that travels along the face extracting slices of coal, and an armored conveyor belt, which transports the resource to a larger mine haulage system (Peng, 2019). Normally, longwall mining is safe and efficient, but a variety of ground control-related hazards are possible, especially in deep mines. One of the most significant of these hazards is a class of dynamic failures associated with induced seismicity, generally referred to as coal bursts or mine bumps. Much like tectonic earthquakes, mining-induced seismicity is difficult to predict and can have devastating consequences. Over the past several decades, coal bursts have killed hundreds of miners (Zhang et al., 2017). Although significant advancements have been made in the past 100 years of research, many aspects of coal bursts remain “enigmatic” (Mark, 2016). There are a variety of options to manage coal burst risks (Wei et al., 2018) but selecting and applying appropriate measures for dealing with coal bursts depends on an adequate understanding of the source, geology, and geomechanics associated with the bursts. Seismic monitoring is one of the tools often used to plan risk mitigation strategies. For underground coal mines, seismic monitoring is conducted using surface or in-mine sensors. Surface networks are usually less expensive and easier to maintain and install, but in-mine networks provide higher quality data in terms of event detection and location accuracy, especially event depth constraints (Swanson et al., 2016). However, in-mine seismometer networks are significantly more expensive than surface networks, and regulations aimed at reducing combustion risks in coal mines often prevent the use of many seismic sensors and digitizers in these environments. Deploying fire-safe DAS sensors underground can enable the characterization of various machinery-induced vibrations and also allow detection of smaller events since the sensors are closer to where these events occur (Tourei et al., 2024; Chambers et al., 2025).

3.2.2 Widely Used Event Detection Methods

One conventional approach for detecting seismic events is the short-term average/long-term average (STA/LTA) method, which calculates the energy ratio between a signal’s short-duration window and its preceding longer-duration window (Allen, 1978; Trnkoczy, 2012). However, the performance of STA/LTA is significantly influenced by variations in background noise, often resulting in false positives or missed detections, particularly for low-amplitude events with a small signal-to-noise (SNR) ratio (Zhu & Beroza, 2019). This limitation arises because thresholding is based on a single, simple ratio averaged over a fixed period, which is often insufficient in complex or variable noise environments. The method is robust for high-SNR events and sparse station networks but performs poorly in noisy underground settings like mines, where frequent non-seismic noise bursts lead to numerous false triggers and missed small events. Template matching has also proven highly effective in detecting small, repeating events by cross-correlating continuous waveforms with previously recorded templates (Gibbons & Ringdal, 2006; Li & Zhan, 2018). However, similar to supervised learning techniques, this method requires a set of known labeled events to construct templates and can only detect events that occur near the template locations with similar focal mechanisms, limiting its applicability in evolving settings such as longwall mines, where new or variable sources emerge.

3.2.3 AI-Based Anomaly Detection Methods

Anomaly detection techniques provide an alternative approach for event detection by identifying events that statistically deviate from the dominant background noise. In seismic analysis, this approach is particularly valuable as the occurrence of seismic events is relatively rare compared to continuous background signals. Leveraging this disparity, unsupervised deep learning methods have demonstrated superior performance in detecting seismic events compared to traditional signal processing techniques (Seo et al., 2024). A key advantage of these unsupervised methods is their ability to operate without labeled data, which are often unavailable for new scenarios or difficult to obtain in monitoring projects such as early warning systems and seismic hazard assessment studies (Jordan et al., 2011). Unlike conventional phase-picking techniques, AI-based methods operate much faster and can automatically extract relevant features, thereby improving data quality for subsequent analyses.

Principal component analysis (PCA) has also been used to reduce the dimensionality of multichannel data (Pedersen et al., 2025) and for leak detection applications (Gemeinhardt & Sharma, 2024), where events are identified as departures from the dominant low-rank subspace. While PCA provides a simple and computationally efficient approach, it assumes linear feature relationships and is sensitive to noise, making it less effective in the presence of complex or non-stationary seismic signals. Therefore, PCA-based methods may struggle to capture nonlinear features in high-dimensional DAS datasets, limiting their utility for generalizable event detection.

Unsupervised autoencoder (AE) techniques can play a crucial role in identifying anomalies in multichannel data. Convolutional AEs are a class of neural networks designed to learn common trends within the compressed representations of high-dimensional data, enabling them to detect unusual anomalies that differ from these trends. They have gained prominence in anomaly detection tasks due to their capability to effectively capture essential waveform characteristics (Mousavi et al., 2019; Neloy & Turgeon, 2024). AEs have demonstrated strong performance in denoising passive DAS data, enhancing the detection and characterization of seismic events (Shi et al., 2025). Chien et al. (2023) demonstrated the potential of autoencoder-based approaches for unsupervised classification of DAS seismic signals by combining a convolutional autoencoder with a Gaussian mixture model clustering to categorize injection-related seismicity in a geothermal setting. However, their framework was designed primarily for signal classification rather than anomaly detection, relied on an additional clustering step, and was tailored to a specific geothermal application. Xie et al. (2023) developed a shallow convolutional autoencoder with K-means clustering for label-free anomaly detection in a single application domain (railway intrusion monitoring). These prior studies highlight the growing use of autoencoder-based frameworks for DAS data interpretation but also underscore the need for a clustering-free approach capable of direct, quantitative anomaly detection. Thus, there remains a need for a technique that enables anomaly detection without clustering, and such a technique should be analyzed for generalizability across diverse DAS monitoring environments.

The present study addresses this gap by introducing a probabilistic–based thresholding method that enables unsupervised anomaly detection and evaluates its generalizability across diverse geophysical monitoring environments. It aims to develop a scalable and efficient anomaly detection algorithm for DAS data with applications to two monitoring projects. By integrating AE techniques with DAS data, our approach seeks to enhance DAS data management and improve seismic event detection. Identifying anomalous data as a preprocessing step can enhance data processing pipelines such as ambient wavefield interferometry, or in the identification of events to use for back-projection or imaging. It can effectively reduce computation and data management costs and speed up teams' understanding of their data in long-term monitoring projects.

3.3 Data Acquisition

To evaluate the feasibility of DAS for event detection in underground mines and automation of the process using machine learning techniques, we conducted a study in an approximately 550 m deep longwall coal mine in the USA, which has a history of seismicity concerns (Van Dyke et al., 2023). Following several relatively large magnitude seismic events, the mine installed a surface seismic monitoring network in January 2009, consisting of five stations. After conducting a pilot test on fiber-optic installation techniques around a single pillar, we deployed fiber-optic cables around an actively mined panel. The majority of fiber was pushed against the wall horizontally and covered with mud or rock dust (i.e., non-combustible dust that mines apply to suppress potential explosions), where possible, to increase the coupling to the ground. The optical interrogator, housed in a building on the surface near a ventilation shaft, was connected via a fiber patch panel to a cable in a borehole descending into the mine (Chambers et al., 2025; Tourei et al., 2024).

Data were collected using the Treble interrogator unit from Terra15 along 7.1 km during 47 days. With a channel spacing of 5.7 m, pulse length of 5.7 m, and sampling rate of 2,000 Hz, approximately 33 TB of DAS data were recorded. Based on the chosen pulse width, the shortest unaliased wavelength that can be sensed is 11.4 m.

3.4 Methodology and Workflow

The workflow of the label-free anomaly detection algorithm is presented in Figure 3.1. It begins with preparing training and validation datasets by reading the DAS data and applying preprocessing and transformation routines as described in subsection 3.1. Then, we train the autoencoder model on the data with no anomalies (the data with only typical background noise) in the frequency domain. By training, the model attempts to reconstruct the input based on its low-dimensional (latent space) representation by learning from common features of the data. During the training phase, the model assesses its performance using the validation dataset, which also does not include any anomalies. After training and validation, we evaluate the model's performance by setting up two simultaneous thresholds based on the evaluation dataset that includes example anomalies to define the boundary between noise and detectable anomalies. Finally, we apply the trained model with the defined thresholds to scan the DAS data and identify non-noise signals, i.e., anomalies, by comparing the input and output of the model using the mean squared error, MSE (first threshold), and the probability of a data feature in latent space, which is referred to as the density score (second threshold).

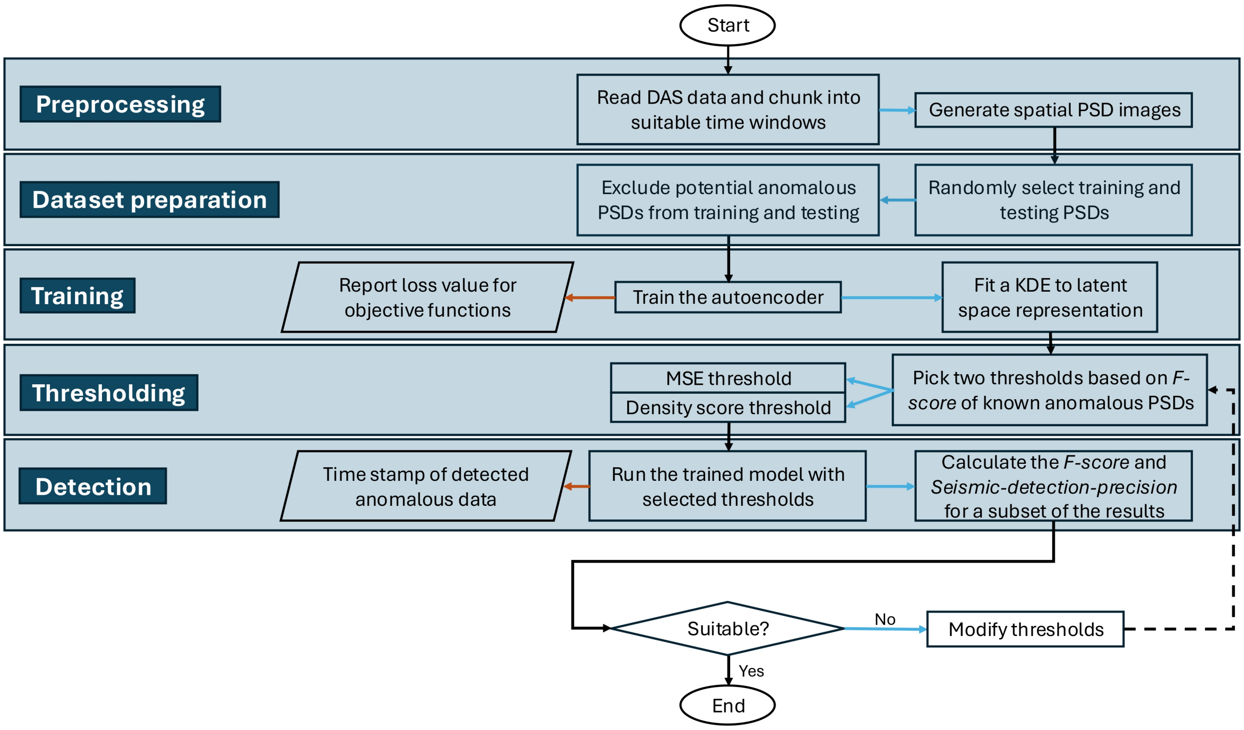

Figure 3.1 The general workflow for anomaly detection with the autoencoder model. Blue arrows indicate progression to the next sub-step within each major stage, while orange arrows denote intermediate reporting of statistics.

3.4.1 Data Preprocessing and Spectral Analysis

DAS data is often recorded by interrogator units as strain rate or its proportional optical phase rate. If the data is in other units such as (cumulative) velocity or optical interference phase, we first use a transform function so that it is proportional to strain rate (Chambers et al., 2025). After trimming the data into specific time and distance windows of interest with overlaps, we detrend the data by applying a linear detrend that removes the mean value of each channel from its time series and applying a cosine taper to smooth the edges of each data chunk. We then apply a short-time discrete Fourier transform to average the energy over the time window and create spatial power spectral density (PSD) plots. The primary motivation for this transformation is that the main anomaly of interest for this study is seismic events, which, if recorded using dense sensors, typically manifest more distinctly in the frequency domain than in the time domain. Figure 3.2 illustrates how an example seismic event appears in time and frequency domains. Comparing the event within a 2-second time window (Figure 3.2a) and a 10-second time window (Figure 3.2b) against a representative background noise segment (Figure 3.2c), we observe that increasing the time window reduces the visibility of the short-duration anomaly in the time domain, whereas the anomaly remains clearly distinguishable in the frequency domain (Figure 3.2b). These observations suggest that performing anomaly detection on PSD images is more effective, as larger time windows can be used. While a longer STFT is more expensive, we would be scanning fewer windows for anomaly detection with a longer window, which enables lower overall computational cost with a suitable window length. Furthermore, if the frequency characteristics of the primary anomaly of interest are known, applying a bandpass filter can optimize the algorithm by enhancing the visibility of the anomaly within the PSD, particularly in the lower-frequency range where such events are most pronounced. In this framework, the seismic data—representing strain rate as a function of frequency and channel number—are converted into pixel-based PSD images, where each pixel encodes amplitude through an RGB color scale; thus, the autoencoder operates on color intensity values rather than raw strain rate measurements.

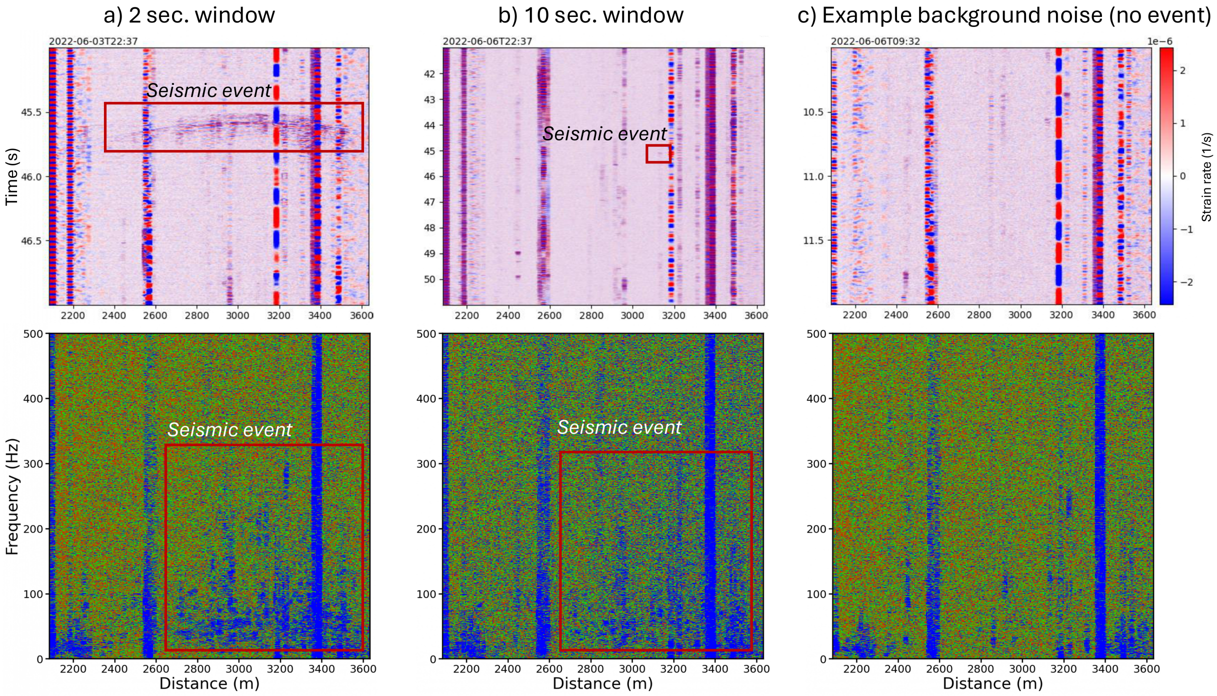

Figure 3.2 Comparison of event detection in the time domain (top figures) vs. the frequency domain (PSD plots, bottom figures in RGB); an example seismic event on a 2-second time window (a), the same seismic event on a 10-second time window (b), an example of background noise (with no expected anomaly) on a 2-second time window (c).

We selected a two-second sliding time window with a one-second overlap to capture anomalies. The overlap handles anomalies split between two windows and ensures that the anomaly is captured in at least one time window. A shorter time window enhances anomaly identification by averaging over a narrower temporal range around seismic events, improving the detection of transient signals. However, it also attenuates low-frequency components, amplifies the influence of changes in background noise variation, and increases computational costs, as a greater number of representations must be analyzed for anomaly detection. In contrast, longer time windows preserve low-frequency signals but may compromise the detection of impulsive seismic events. Thus, the choice of time window represents a trade-off between capturing high-frequency anomalies, maintaining sensitivity to low-frequency signals, and managing computational costs.

DAS averages the strain rate along the fiber over a distance, which is called the gauge length. Increasing the gauge length is required to effectively detect small anomalies such as weak seismic activities by increasing the SNR. However, this comes at the cost of reduced spatial resolution. Therefore, for the purpose of event detection, a larger gauge length needs to be used, and then a relatively smaller gauge length may be preferred for geophysical data processing, such as back-projection (Beskardes et al., 2018) or surface-wave dispersion calculation (Park et al., 1998), to preserve spatial resolution and prevent aliasing of longer wavelength signals. After preliminary data exploration and applying multiple gauge length values to a few seismic events from the surface network catalog, a gauge length of 22.9 m, which is four times the channel spacing, was chosen for the data preprocessing.

Before feeding the autoencoder, we apply a low-pass filter with a cutoff frequency of 500 Hz to capture high-frequency, nearby microseismic events while avoiding an excessively high frequency bound that could hinder the detection of distant events with dominant low-frequency and attenuated high-frequency signals. Conversely, maintaining the upper frequency bound sufficiently high prevents overemphasizing low-frequency anthropogenic (2–20 Hz) or instrument noise variations, thereby potentially enhancing the model's microseismic detection capability.

3.4.2 Convolutional Autoencoder Model

We use a simple encoder-decoder architecture with fully connected convolutional layers. The autoencoder model reconstructs the input data using the low-dimensional version of the high-dimensional input in the latent space, as described by:

$$\begin{gathered} LS = E(I) \\ O = D(LS) \end{gathered} \tag{3.1}$$

where I is input data, O is output data, E is encoder, D is decoder, and LS is the low-dimensional data in the latent space. When the model is trained on data with no anticipated anomalies, it learns to reconstruct the data with relatively lower error than anomalous data. Also, the low-dimensional representation of the anomaly-free data has common features that help identify data lacking the same feature patterns. The training procedure forces the model to find the most effective expression for the low-dimensional version of the high-dimensional data.

Figure 3.3 shows the generalized structure of the autoencoder model. The autoencoder consists of an encoder and a symmetric decoder. The encoder reduces the dimension of the input data (PSD image as described in Figure 3.2) into a lower-dimensional representation in the latent space, and the decoder reconstructs the original data using the latent space representation. The encoding and decoding branches are symmetric and both can be composed of several layers. Each encoding layer consists of a combination of filters for feature extraction, a ReLU activation to prevent linear collapse, and a 2×2 maxpool operation that reduces the height and width of the input image by half. Thus, n layers reduce the spatial dimensions to $1/2^n$ of the original resolution, while distilling the information into the latent space representation. This progressive reduction balances reconstruction fidelity against computational efficiency. Deeper encoders offer greater representational capacity but at the cost of heavier compression, which can hurt reconstruction fidelity if taken too far. The decoder reconstructs the image in reverse order. Each decoding layer is a combination of filters for feature refining, a ReLU activation, and a 2×2 upsampling layer that doubles the spatial dimensions. A final layer with three filters and a sigmoid activation maps the feature stack back to pixel space, producing values in [0, 1] that match the input normalization in RGB. The model is compiled with an Adam optimizer to update the network parameters. The two vertical bars in the input and output PSDs are due to vibrations of two buildings that touch the fiber.

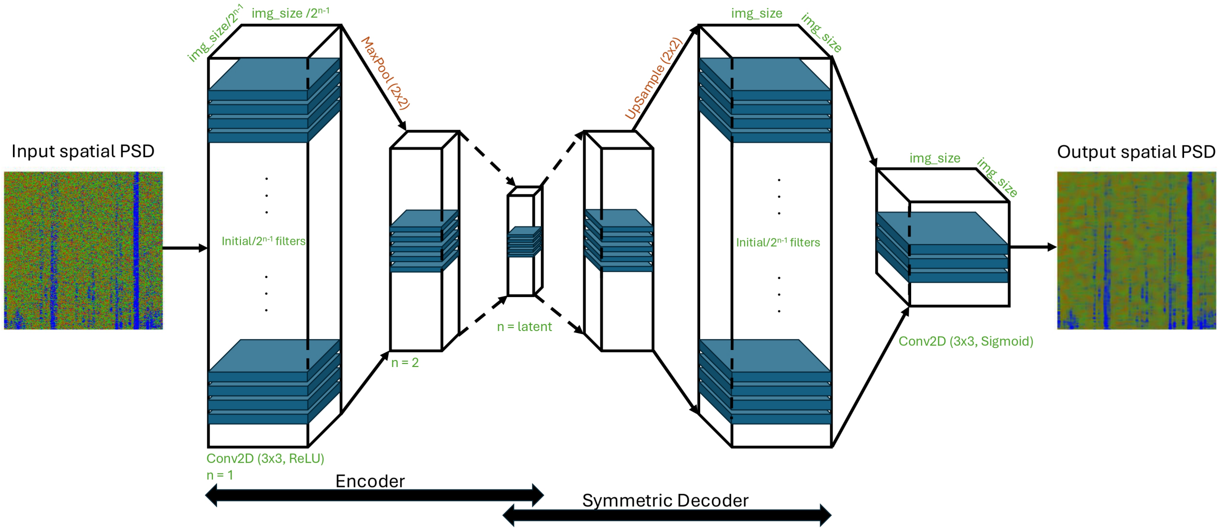

Figure 3.3 The architecture of the developed convolutional autoencoder with PSD input and outputs, with fiber distance on the X-axis and frequency on the Y-axis.

A straightforward metric for thresholding the anomaly detection task is the reconstruction MSE. However, relying solely on reconstruction error has inherent limitations: convolutional neural networks often over-generalize, leading to deceptively low reconstruction errors for some anomalous samples. To address this, we incorporated a probabilistic perspective by modeling the probability density function (PDF)—hereafter referred to as the density score—of PSD in the latent space using kernel density estimation (KDE). A KDE with a Gaussian kernel was first fitted to the encoded training dataset in the latent space. Then, using this KDE, the PDF value computed for each vectorized spatial PSD was used as its density score. This metric captures the local data density in latent space, with higher density values indicating sparser regions that are more likely to correspond to background noise (training dataset).

3.4.3 Hyperparameter Tuning and Training Strategy

The autoencoder model's key hyperparameters include the input image size, number of convolutional layers, number of filters, and the size of the training dataset. Input images were tested at square resolutions of 128, 256, 512, and 1,024 pixels. Increasing the input size generally improves the model's capacity to capture fine-scale features, but it also increases computational cost and memory requirements. The depth of the network, controlled by the number of convolutional layers, determines both the model's expressive power and the degree of spatial compression applied to the input. Configurations with 2, 3, and 4 layers were evaluated. The number of filters per layer was varied across 32, 64, 128, and 256. While larger filter banks allow the model to extract more complex features, they also result in slower training and higher resource demands. Finally, the effect of combined training and validation dataset size was investigated using subsets of 100, 400, 1,600, and 6,400 images. Although larger training and validation sets typically improve generalization, excessive data relative to model complexity can sometimes increase the risk of overfitting.

In total, 168 model configurations were evaluated. Configurations with an input size of 1024 combined with more than 128 or 256 filters were excluded, as their memory requirements exceeded the available GPU capacity. The first phase of tuning focused on minimizing the objective loss function while mitigating overfitting. The progressive decrease and convergence of the training and validation loss curves indicated that the model effectively learned the underlying patterns in the data. The consistent downward trend, without divergence between the two curves, further suggested successful convergence without signs of overfitting. From this stage, models achieving a loss value below 0.06 were selected for the second phase of hyperparameter tuning, which aimed to maximize the relative difference in reconstruction MSE and latent-space density scores between datasets with and without anomalies.

To maximize the relative difference in latent-space density scores between datasets with and without anomalies and choose the configuration that results in the most separation between two classes, we applied Fisher's discriminant criterion (Bishop, 2006), which maximizes the separation between class medians relative to within-class variance (Equation 3.2).

$$J = \frac{(median_{BN} - median_{ANM})^2}{{S_{BN}}^2 + {S_{ANM}}^2} \tag{3.2}$$

where S is the variance and BN and ANM subscript denote the background noise and anomaly classes, respectively. The final model, configured with an input size of 512, 256 3×3 filters, 4 convolutional layers, and a full (training and validation) dataset of 1,600 samples, achieved the highest discriminant score J of 26.57 with a loss function of 0.057 and therefore, was selected for thresholding and anomaly detection. The latent tensor is sufficiently compact—reduced to $1/16$ of the original spatial scale with a size of 32 and passed through a total of 480 filters—for efficient memory usage, while still retaining enough information for accurate reconstructions when the mirrored decoder restores the original resolution.

Figure 3.4 shows the histogram of normalized density scores for 20 previously identified seismic events (an example is illustrated in Figure 3.2a) and for the validation (testing) dataset, comprising 320 PSD images. The validation set represents a training-to-testing ratio of 4:1 and includes data that were unseen during training. As observed, although the selected configuration achieved the highest discriminant score J, some overlap between the two distributions remains. This can be attributed to two main factors: (i) certain anomalies were very weak and therefore difficult to distinguish from background activity, and (ii) the training and validation datasets were prepared manually, which may have introduced weak or ambiguous anomalies caused by changes in background noise (e.g., slight variations in machinery noise within the mining environment).

The model is trained on 1,280 randomly selected two-second spatial PSD images of 512^2 pixels and a training-to-validation ratio of 4. We first start with an exploratory data analysis, where we randomly select the training and validation datasets from the collected passive DAS data and ensure they do not include any seismic events or distinct noises such as those by interrogator units, by visually analyzing the data in time and frequency domains.

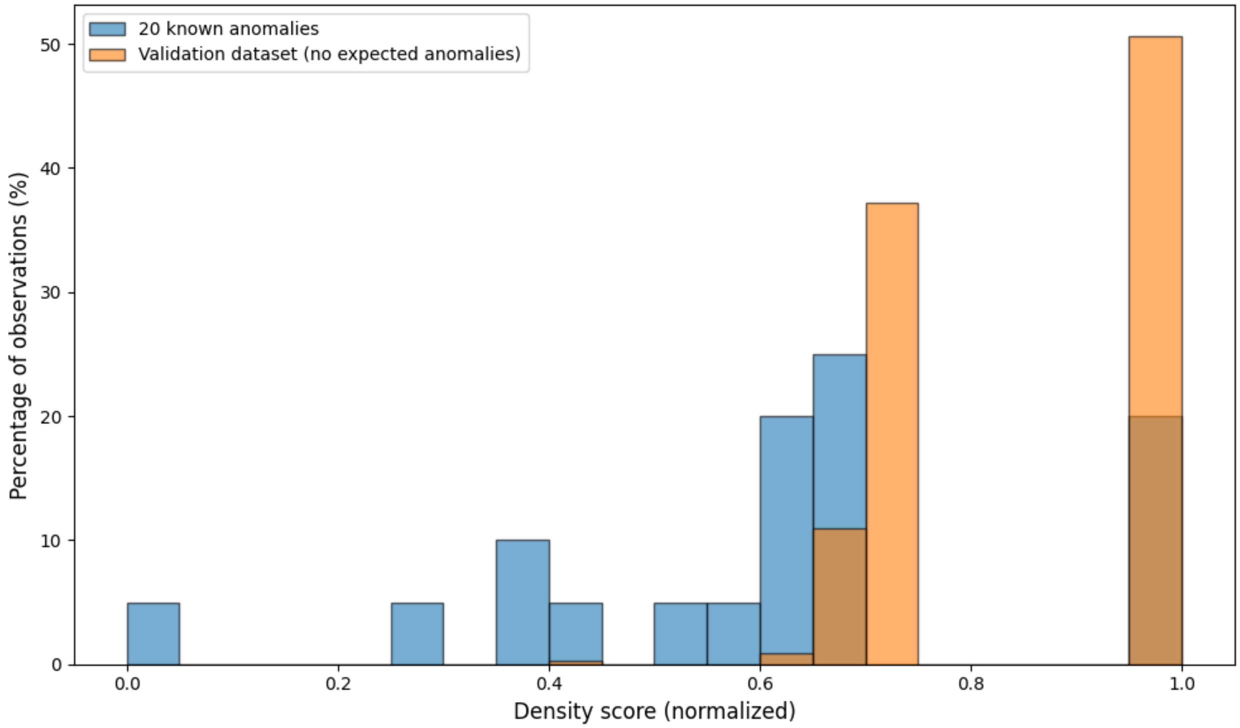

Figure 3.4 Histogram of the normalized density scores for a set of previously known anomalies and the validation dataset.

The objective function is the MSE, and it is defined as follows:

$$loss(I,O) = \frac{\sum_{0}^{n} \|I - O\|_2^2}{n} \tag{3.3}$$

where n is the batch size. The model was trained for 200 epochs on a single NVIDIA H200-141G GPU within a shared high-performance computing (HPC) environment, with the full training process completing in less than ten hours. Data preprocessing of two weeks of continuous DAS recordings, followed by anomaly detection, required less than sixty hours using an MPI-parallelized workflow across 24 cores of a Zen2 AMD EPYC 7702 CPU. Since training and detection were executed on shared HPC resources, the computational time reported here represents an upper bound; faster performance could be expected on dedicated devices without shared resource constraints (Bhatele et al., 2013).

3.4.4 Threshold Setting and Evaluation

After training the autoencoder, we established thresholds on both the reconstruction MSE and the density score to guide anomaly detection. A sample is flagged as anomalous only if it simultaneously exceeds the reconstruction MSE threshold and falls below the density score threshold. This joint criterion strengthens reliability by requiring anomalies to be consistently identified in both the reconstruction and latent-space domains

For reconstruction MSE, the threshold was defined as the MSE loss value observed during validation (i.e., 0.057) on the validation dataset. This non-conservative choice ensures that any sample with a reconstruction error greater than what was seen during validation is automatically classified as anomalous. In contrast, thresholding based on density scores is more nuanced and exerts a stronger influence on detection accuracy. Because density scores are derived from the PDF of the latent space, setting the threshold too strictly (i.e., too high) risks missing weak anomalies, whereas setting it too loosely may increase false positives. Practically, this means that if the density score for a given spatial PSD window deviates significantly from the average density score of the anomaly-free training dataset (as estimated by the fitted KDE) and exceeds the threshold, that window is classified as anomalous. This dual-threshold strategy provides a more comprehensive and reliable approach to anomaly detection.

We evaluate the model's performance using standard classification metrics, including precision, recall, and the F_β score:

$$Recall = \frac{TP}{TP + FN} \tag{3.4}$$

$$Precision = \frac{TP}{TP + FP} \tag{3.5}$$

$$F_\beta = \frac{(1 + \beta^2) \, * \, Precision \, * Recall}{(\beta^2 \, * \, Precision \, + \, Recall)} \tag{3.6}$$

where, TP denotes true positives (correctly detected anomalies), TN true negatives (correctly detected background noise), FP false positives (i.e., false alarms), and FN false negatives (i.e., missed anomalies). While recall measures the ability of the model to detect all anomalies, precision quantifies how many of the detected anomalies are correct. The F_β score provides a single metric representing the model's performance, and it balances these two quantities, where the parameter β allows weighting recall relative to precision.

Because the model is unsupervised, an evaluation dataset with known labels is required to compute F_β scores. To construct this set, we randomly selected 500 PSDs from the collected dataset and an additional 300 PSDs from time windows containing seismic events identified by a surface seismic network of seismometers (some of which were also detected by the fiber-optic array). The 800-evaluation dataset was then labeled as background noise or anomaly based on visual inspection of their time- and frequency-domain representations, and 93 seismic events were observed. The optimal density score threshold was determined through a sensitivity analysis of model performance on the evaluation dataset, with a focus on two primary applications: (i) anomaly detection for reducing storage requirements and (ii) seismic event detection, as discussed in detail in the Results section. For seismic event detection purposes, we use two metrics, defined as follows: seismic event precision is defined as the ratio of the number of detected seismic events to the number of triggers, and seismic event coverage is defined as the ratio of the number of detected seismic events to the number of total seismic events in the evaluation dataset.

3.5 Results and Discussion

Figure 3.5 illustrates the precision–recall trade-off resulting from density score thresholding on the evaluation labeled dataset. As the threshold becomes more permissive, recall increases because fewer weak anomalies are missed; however, this comes at the expense of reduced precision and a higher false alarm rate. Conversely, stricter thresholds maximize precision but exclude many weak events. This trade-off is inherent to the unsupervised nature of the model: without labeled training data, the autoencoder learns general data representations rather than explicit class boundaries, which limits its ability to perfectly separate anomalies from background noise. Therefore, thresholds must be selected with respect to the primary application of anomaly detection and whether minimizing false alarms or reducing missed anomalies is of greater importance.

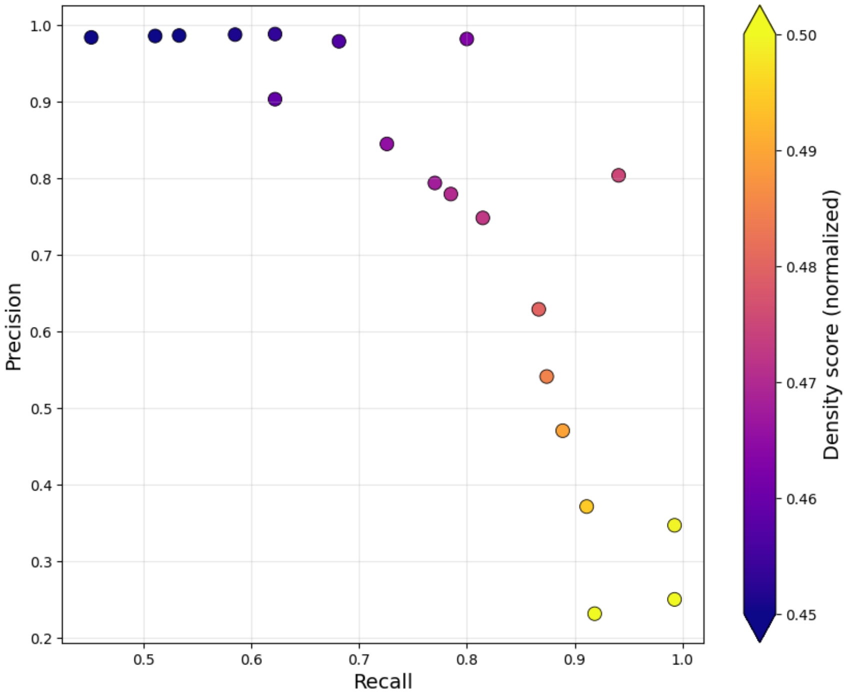

Figure 3.5 Precision–recall trade-off for density score thresholding, illustrating the balance between minimizing false alarms and capturing weak anomalies in the mine data.

The irregular and non-monotonic trend observed in the precision–recall curve (Figure 3.5) can be attributed to several factors. First, the evaluation dataset is imbalanced, containing only 139 anomalies among 800 samples, which causes discrete changes in precision and recall as the threshold varies. Second, the normalized density score thresholds were not uniformly sampled but selected through exploratory analysis around regions of high model sensitivity, leading to uneven spacing in performance metrics.

Finally, the autoencoder exhibits a highly nonlinear response to small changes in the density score, resulting in sharp local variations in detection behavior that manifest as the observed jagged pattern.

For anomaly detection tasks aimed at reducing storage requirements, recall is often prioritized, since missing an anomaly (false negative) can be more critical than raising a false alarm (false positive). To this end, an appropriate threshold can be selected by maximizing the F_2 score, which emphasizes recall, as defined in Equation 3.6. The estimated reduction factor is then calculated as the ratio of the number of triggered anomalies N_{trig} to the total volume of recorded raw data. Prioritizing F_2 ensures that fewer anomalies are missed, which is essential when the goal is storage reduction and the potential removal of raw data. Conversely, if storage reduction is less critical but minimizing false alarms is more important, one can instead select a threshold that maximizes the $F_{0.5}$ score, which emphasizes precision.

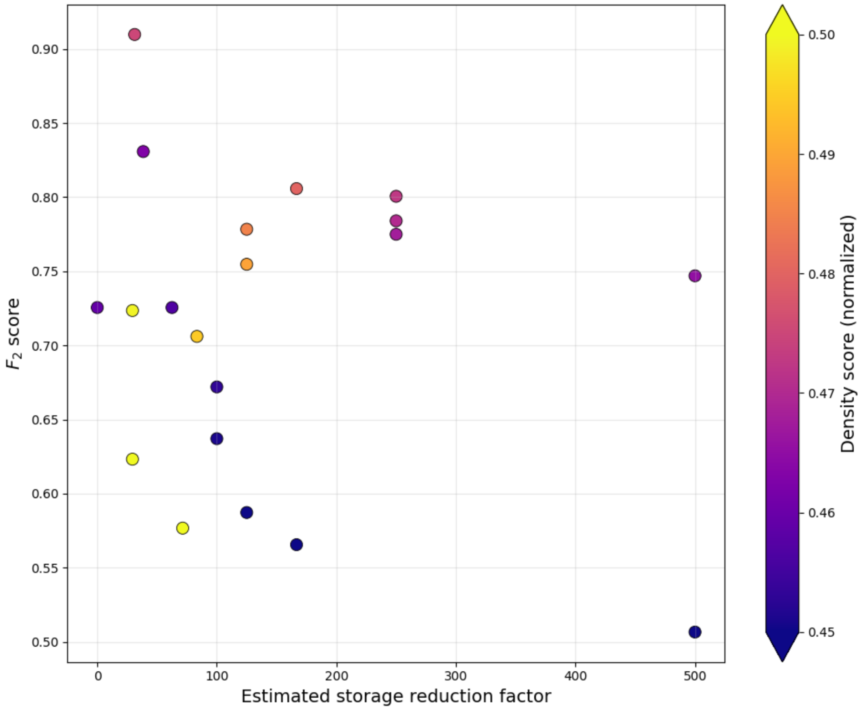

Figure 3.6 Relationship between F_2 score and estimated storage reduction factor across different density score thresholds.

Within two weeks of data, the system analyzed 1,209,600 two-second PSD plots (with one-second overlap). A normalized density score threshold of 0.475 maximized the F_2 score to 0.91 (Figure 3.6). Under this threshold, 24,092 anomalies were detected over a two-week continuous DAS recording period. In contrast to the model's rapid training and processing time, manually visualizing and classifying each PSD image—requiring roughly 10 seconds per image—would have required 84 work weeks at 40 hours of analysis per week, infeasible given the project's timeline and budget constraints. This result underscores the model's computational efficiency, enabling rapid, automated detection of anomalies while significantly reducing the workload associated with manual processing.

For seismic event detection, a clear trade-off arises between maximizing seismic event coverage, which prioritizes detecting weak events, and minimizing false triggers by prioritizing seismic event precision. Figure 3.7 shows this balance across varying density score thresholds. In the context of edge applications, particularly within mining environments, the cost of false alarms can be significant, as spurious triggers may undermine the reliability of real-time monitoring systems and complicate operational decision-making. Consequently, for this application, precision is prioritized over coverage when selecting an appropriate threshold. In contrast, if the purpose of event detection is subsequent analysis for characterizing microseismicity and assessing stress evolution due to mining, coverage may be prioritized to ensure that weak anomalies are not overlooked.

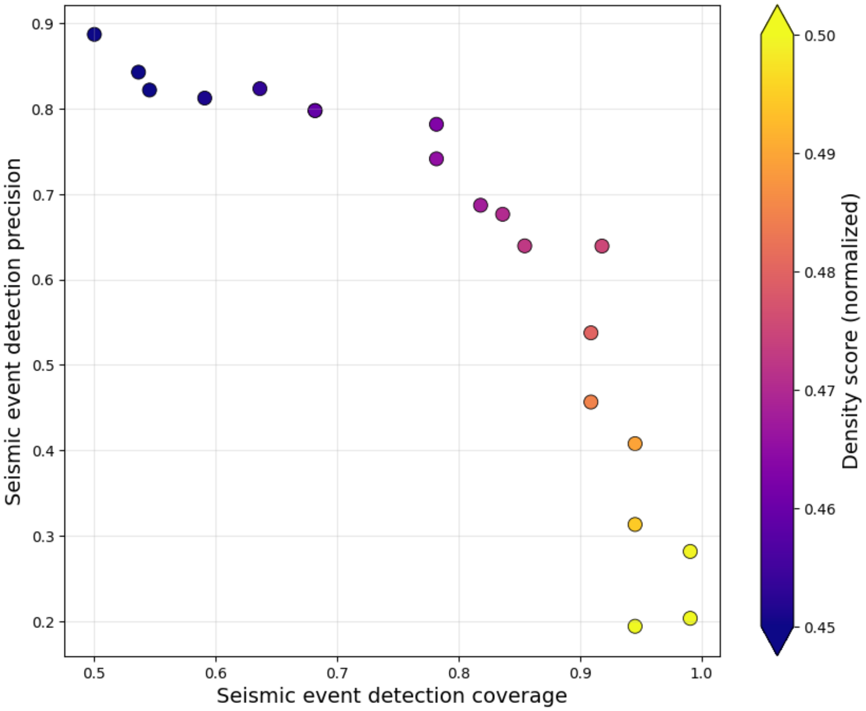

Figure 3.7 Precision–coverage trade-off for seismic event detection across different density score thresholds.

With precision prioritization, a normalized density score threshold of 0.459 was selected, which achieved an event precision of 0.8 and a coverage of 0.68, as shown in Figure 3.7. Using this threshold, 13,223 anomalies were detected, of which 10,586 can be considered potential seismic events based on the 0.8 event-precision ratio, while only 320 were already reported in the local seismic catalog. These results demonstrate that density score–based thresholding not only recovers cataloged seismic events but also identifies additional candidates that may enhance seismicity characterization. Overall, these findings underscore the practical feasibility of applying density score–based thresholding for seismic event detection in large-scale DAS deployments.

The density score–based thresholding approach successfully identified seismic events not previously cataloged by the surface seismic network, demonstrating the model's capability to detect new signals of interest. Figure 3.8 provides an example of such an event, where the raster plot (Figure 3.8a) shows coherent P- and S-wave arrivals propagating across the underground DAS with a zero-offset point around 3,050 m along the fiber, and the corresponding PSD plot (Figure 3.8b) highlights the characteristic frequency content of the signal. The high-frequency nature of this event and distance from the surface network likely contributed to its absence in the surface seismometer catalog, as geometric spreading and attenuation over distance reduce the detectability of higher frequencies. These newly detected events extend beyond the existing seismic catalog, thereby improving catalog completeness and offering valuable opportunities for advancing the characterization of subsurface processes. Although not pursued in this study, such events could be further analyzed using simple hyperbolic curve-fitting methods to estimate seismic velocity in the underground mine and to refine event location (Aki & Richards, 1980; Ankamah et al., 2024). However, it is important to note that because our DAS cable is predominantly straight, absolute event positioning in three dimensions is limited; only the distance along the fiber and the fiber location closest to the event can be constrained.

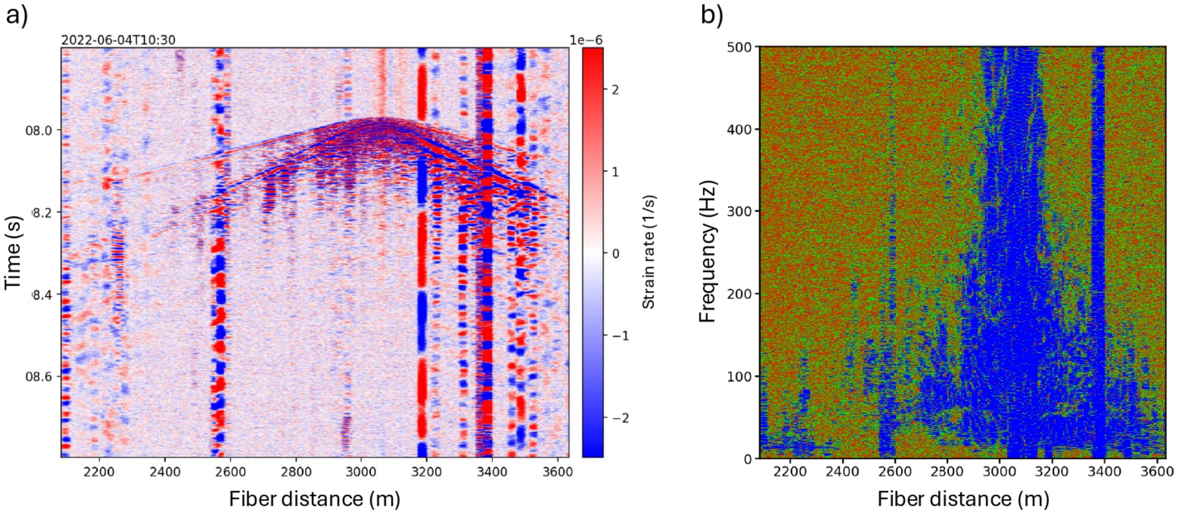

Figure 3.8 Raster plot in the time domain (a) and the spatial PSD in the frequency domain (b) of a new seismic event detected by the autoencoder.

3.5.1 Generalizability Study

To evaluate the generalizability of the model, the hyperparameter-tuned autoencoder originally developed for mining-induced seismicity was applied to a passive permafrost monitoring dataset. The objective was to assess how the previously established architecture performs when transferred to a different geophysical setting and to extend the scope of earlier active studies conducted near Utqiaġvik, Alaska (Tourei et al., 2024). The dataset was acquired from a 2 km DAS array deployed in August 2021 (Ji, 2025; Rocha dos Santos & Zhu, 2025). With a channel spacing of 2.45 m and a sampling rate of 500 Hz, the system produces roughly 150 GB of data per day. More details on the installation, fiber geometry, and DAS data acquisition are provided in Chapter 4.

Initial assessments indicated that longer gauge lengths improve the SNR for weak earthquakes and cryoseismic events, although this comes at the cost of reduced spatial resolution. Moreover, because a relatively short two-second time window was used to compute each PSD, some anthropogenic signals (e.g., vehicles passing slowly near the cable) are not fully captured. Increasing the gauge length helps to improve SNR and enhances the detection of such events as well. To balance these trade-offs, a gauge length of 49 m—equivalent to 20 times the native channel spacing—was selected.

In addition, a 50 Hz low-pass filter was applied, as the example of recorded earthquakes and cryoseismic events are dominated by low-frequency energy (typically 5-20 Hz) and the power spectra of their dominant wavefield rarely extend beyond 50 Hz. This filtering also ensures that the analyzed frequency band remains consistent with the typical 20–30 Hz maximum frequency range associated with traffic noise. Together, these preprocessing steps enhance the adaptability of the anomaly detection model and improve its capacity to distinguish between seismic and non-seismic signals in permafrost environments.

A similar procedure to that described in the thresholding section was applied here, but with an emphasis on anomaly detection where precision was prioritized over recall in order to minimize false alarms. A threshold of normalized density score equal to 0.97 was selected, yielding an $F_{0.5}$ score of 91.1% and a precision of 99.0% for the evaluation dataset containing known anomalous and normal data. This strategy reflects the study's focus on detecting high-amplitude anomalies, such as cryoseismic events, which can be leveraged for surface-wave analysis in near-surface imaging of permafrost, rather than capturing weaker, less relevant anomalies.

After training and thresholding, we applied it to the data to systematically isolate and analyze specific categories of anomalous data and filter out anomalies before further geophysical data processing. (e.g., ambient wavefield interferometry). The detected anomalies included natural events (e.g., earthquakes and cryoseismic events), anthropogenic noise (e.g., traffic-induced vibrations), instrument noise, and corrupted data arising from interrogator malfunctions.

Within one week of recorded DAS data (approximately 1 TB), the model flagged 9,008 anomalous time windows (equivalent to approximately 1.5 percent of the data), of which 1,204 were transient/impulsive events potentially associated with seismic activities such as cryoseismic events and traffic noise. The remaining 7,804 anomalies were characterized as persistent anomalies likely attributed to instrument noise, which, after collapsing consecutive detections, condensed into 1,434 unique persistent events. Figure 3.9 presents PSD examples of detected anomalies. The two vertical bars around 0 m and 250 m in each image are due to vibrations of two buildings where the fiber is exposed and installed on piles rather than buried. Figure 3.9a presents a PSD example of a regional M 2.8 earthquake that occurred 108 km NNW of Wainwright, Alaska, and was detected by the AE model. Given the source's proximity—with the epicenter located approximately 180 km from the cable—the high-frequency signals in the 5–15 Hz range are clearly observable. Figure 3.9b illustrates an impulsive cryoseismic event detected near the cable. The close arrival times of body and surface waves, along with high SNR in the time series analysis, confirm the event's impulsive nature. Figure 3.9c showcases an example of vehicle noise from a commuter traveling between two buildings. As previously discussed, the model struggles to detect some of the traffic activities due to the short two-second time window and their predominantly low-frequency signatures. To improve detection, a separate training model may be required with an extended time window and a lower cutoff in the low-pass filter to enhance sensitivity to these events. Figure 3.9d presents an instance of instrument noise, likely caused by phase unwrapping issues, which resulted in data corruption beyond the second building. For comparison, an example of a typical background noise PSD is also provided in Figure 3.9e.

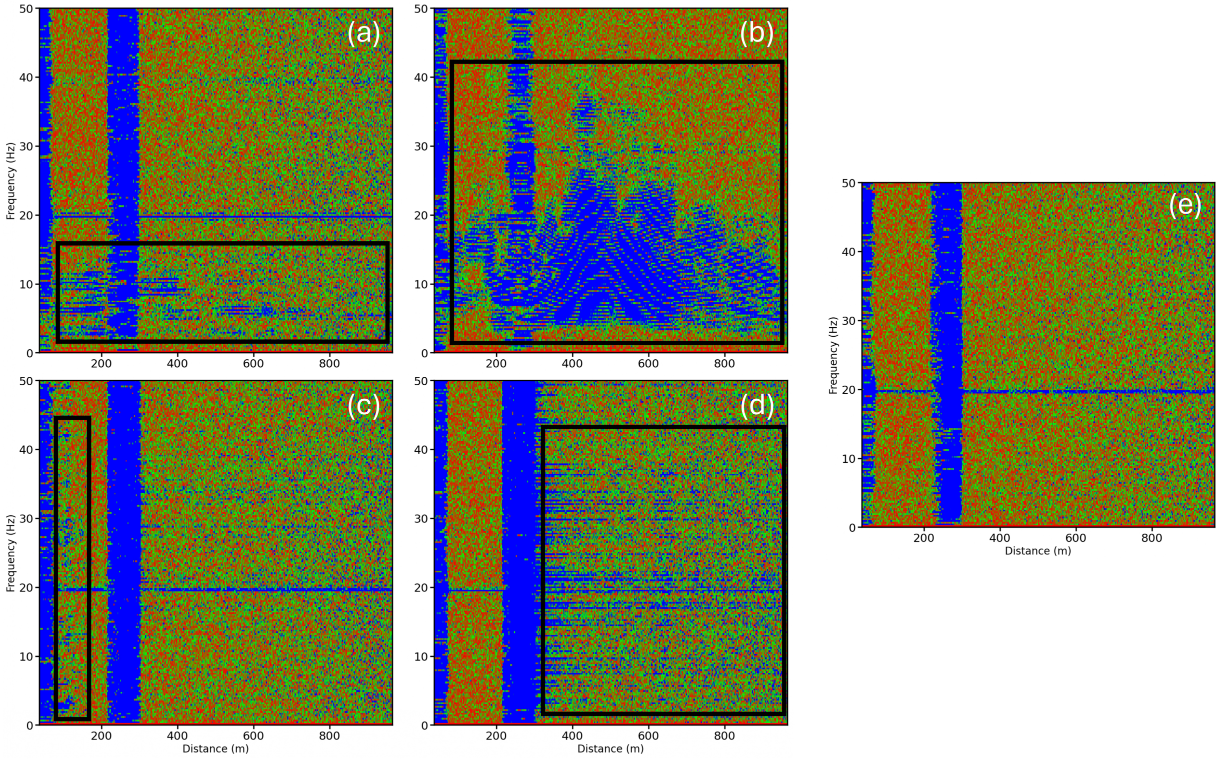

Figure 3.9 PSD images of example detected events in the AK dataset: earthquake (a), cryoseismic event (b), traffic noise that is annotated by an ellipse (c), and instrument noise beyond the second building (d), compared with an example PSD of a typical background noise with no events (e).

The impulsive cryoseismic events (an example shown in Figure 3.9b) detected near the cable are characterized by closely spaced body- and surface-wave arrivals and high SNR and are potentially associated with ice-wedge cracking and tensile failure within the permafrost. These events are of particular interest in passive permafrost monitoring because they generate strong surface-wave energy that can be exploited for dispersion analysis. Chapter 4 presents the data processing workflow for utilizing the energy of these events in MASW-based permafrost characterization. By systematically isolating high-SNR cryoseismic events, the proposed approach enables long-term monitoring of permafrost degradation and near-surface heterogeneity with improved temporal and spatial resolution.

Beyond direct event detection, the anomaly filtering framework has strong potential for improving seismic interferometry workflows. High-energy, non-seismic transients such as instrument noise and interrogator artifacts (e.g., Figure 3.9d) can dominate the wavefield and bias cross-correlation functions, leading to spurious arrivals and unstable Green's function estimates. Previous studies have emphasized the importance of excluding high-energy noise sources, or applying preprocessing steps such as temporal normalization techniques, to enhance the stability and accuracy of interferometric measurements (e.g., Bensen et al. (2007) and Xu et al. (2021)). By systematically identifying and removing these anomalous windows prior to interferometric processing, the proposed approach provides an automated means of data curation. This reduces computational costs by limiting correlation calculations to high-quality segments and improves the reliability of time-lapse monitoring applications, such as detecting subtle velocity changes in permafrost environments.

3.5.2 Limitations

Despite the demonstrated success of the proposed autoencoder framework for anomaly detection and seismic event characterization, several limitations must be acknowledged. First, the partial overlap between density score distributions for anomalies and background noise introduces uncertainty in threshold selection (Figure 3.4). This overlap is partly due to weak anomalies that share similar latent-space statistics with a slight change in background signals, highlighting the challenge of fully separating classes in an unsupervised setting.

Second, although the approach is unsupervised, some degree of labeled data remains necessary for training dataset preparation, evaluation, and thresholding. This labeling effort requires expert judgment and introduces subjectivity into the preparation of an event-free dataset for the training step and an anomalous dataset for the evaluation and thresholding steps.

Third, the model's performance is sensitive to the choice of time window size. As shown in the generalizability analysis, a two-second window is well-suited for high-frequency, impulsive events such as cryoseismic activity but is less effective for low-frequency, long-duration signals such as anthropogenic signals. In particular, traffic-induced anomalies often yield higher density scores because the short window fails to average energy across the fiber array (see Figure 3.9c). This suggests that multiple models with different temporal resolutions may be necessary–one optimized for high-frequency impulsive events and another for long-duration, low-frequency signals.

Fourth, the autoencoder must be retrained if the background noise environment changes significantly (e.g., due to changes in mining activity, changes in anthropogenic activity or construction, or instrument upgrades). This retraining requirement may limit the framework's long-term stability in continuously evolving noise conditions.

Finally, model performance has thus far been assessed only on two field datasets. While this provides valuable real-world validation, additional testing on synthetic datasets–with an oracle that has full knowledge of anomaly states (i.e., whether an anomaly is present and its relative significance)–would enable a more rigorous evaluation of threshold selection, as well as the model's precision and robustness under controlled conditions.

3.6 Conclusions

The developed model enhances DAS data management and seismic event detection by enabling efficient anomaly detection, thereby reducing computational effort and storage requirements across various applications. By leveraging reconstruction error and latent-space density scores as complementary thresholding metrics, the model provides a robust mechanism for distinguishing anomalous events from background noise across diverse monitoring environments. Such a tool can also enable experts to focus their attention on potential events more quickly than traditional manual review of continuous data.

Applied to mining-induced seismicity, the framework successfully identified both cataloged and previously uncatalogued seismic events, thereby enhancing event catalogs and supporting improved hazard characterization. Importantly, the framework also addresses the critical challenge of data volume: by retaining only anomalous segments, it achieves substantial reductions in storage requirements while maintaining events of interest. This capability makes the approach particularly valuable for large-scale DAS deployments, where data storage and processing constraints often limit analysis.

When applied to permafrost monitoring, the model detected a wide range of anomalies and further highlighted the potential for using cryoseismic events in surface-wave dispersion analysis for time-lapse imaging of permafrost structure. Beyond direct event detection, the anomaly filtering strategy also may improve the stability of seismic interferometry workflows by systematically removing high-energy transients that can bias cross-correlations, reducing computational costs and enhancing the reliability of long-term monitoring.

The proposed framework provides a scalable and generalizable solution for DAS-based anomaly detection, with demonstrated applications to induced seismicity, permafrost monitoring, and ambient noise interferometry. Although developed for DAS, the model architecture and training strategy may broadly be applicable to other linear array datasets, potentially including active seismic surveys. These advances highlight its potential to improve the efficiency, reliability, and interpretability of DAS data analysis across a broad range of geophysical monitoring and hazard assessment contexts.

3.7 Acknowledgements

This work was conducted in part within the Center to Advance the Science of Exploration to Reclamation in Mining, which is a joint industry-university collaborative research center between the Colorado School of Mines and Virginia Tech under National Science Foundation award numbers 2310920 and 2310948. We thank the National Science Foundation (grants CMMI-2034363, CMMI-2034366, and CMMI-2034380), the National Institute for Occupational Safety and Health, and the Center for Wave Phenomena for their support. We sincerely thank Derrick J.A. Chambers for valuable discussions. We thank Jake Beale of Pilot Geophysical for providing a catalog of seismic events from the surface seismic network. We appreciate Mines Research Computing for providing resources. DASCore Python library (Chambers et al., 2024) was used for DAS data processing. The code is available open-source on the das-anomaly GitHub repository (Tourei, 2025), and version 0.0.7 was used to produce the figures. Our development of this library compatible with DASCore was supported through National Science Foundation grant 2148614.

CHAPTER 4 PERMAFROST CHARACTERIZATION WITH PASSIVE CRYOSEISMIC DAS EVENTS

Ahmad Tourei[1], Nikhil Punithan[2], Gabriel Rocha dos Santos[3], Ming Xiao[4], Eileen Martin[1]

4.1 Abstract

Permafrost is often characterized by a complex and heterogeneous structure, and although it strongly influences Arctic hydrology, ecosystems, and infrastructure stability, its degradation processes under ongoing climate warming remain poorly understood. Distributed acoustic sensing (DAS) offers a practical, non-invasive method for high-resolution permafrost monitoring in remote regions without the need for active sources. We deployed an approximately 2 km fiber-optic DAS array across disturbed and undisturbed tundra near Utqiaġvik, Alaska, and used naturally occurring impulsive cryoseismic events generated by thermal contraction cracking to image permafrost. We examined the influence of gauge length and wave propagation directionality on the dispersion results and applied horizontal-to-vertical spectral ratio (HVSR) analysis from a nearby three-component seismometer to assess Rayleigh-wave mode content. Surface-wave dispersion was extracted using the phase-shift method and inverted for shear-wave velocity (Vs) using both nonlinear least-squares (NLLS) and Monte Carlo (MC) algorithms to evaluate inversion stability and uncertainty. The inverted Vs models for two cryoseismic events recorded on separate segments of the fiber reveal high-velocity (2-3 km/s) deep ice-rich layers, interpreted as massive, segregated ground ice formed under high overburden stress and low temperatures. These findings demonstrate the feasibility of using passive DAS for time-lapse, high-resolution permafrost imaging and emphasize its potential for long-term monitoring of thaw dynamics in Arctic environments.

4.2 Introduction

Permafrost is a key component of the cryosphere, playing a crucial role in maintaining the stability of Arctic and sub-Arctic ecosystems and ensuring the integrity of infrastructure (Hjort et al., 2022). Permafrost composition might be highly heterogeneous due to variations in ice content, grain size, salinity, and moisture distribution, all of which exert strong controls on its thermal and mechanical behavior (Tourei et al., 2024; Wu et al., 2017). With ongoing climate warming, thawing permafrost leads to rapid changes in subsurface structure, including ice thaw, pore pressure buildup, and subsidence. Shear-wave velocity (Vs) profiling is a key component of near-surface characterization, providing critical

---

[1] Hydrologic Science and Engineering Program, Colorado School of Mines, Golden, CO, USA
[2] Department of Geophysics, Colorado School of Mines, Golden, CO, USA
[3] Department of Geosciences, The Pennsylvania State University, State College, PA, USA
[4] Department of Civil and Environmental Engineering, The Pennsylvania State University, State College, PA, USA

insights into the mechanical properties and stability of subsurface materials (Socco & Strobbia, 2004). High-resolution imaging and time-lapse monitoring are crucial to capture the spatial and temporal evolution of these changes, thereby enabling the quantification of degradation rates and enhancing predictive models of permafrost stability under future warming scenarios. However, the logistics and cost of conducting repeated active-source surveys in remote Arctic regions limit repeat studies, whereas passive seismic monitoring often lacks sufficient high-frequency energy to resolve shallow permafrost layers.

Distributed Acoustic Sensing (DAS) offers a transformative approach for large-scale and continuous permafrost monitoring, enabling dense spatial sampling over kilometers of fiber-optic cable (Cheng et al., 2022; Wagner et al., 2018). Furthermore, DAS can be coupled with ambient noise interferometry techniques to image the subsurface and its changes over time (Dou et al., 2017; Rodríguez Tribaldos & Ajo-Franklin, 2021). Despite its potential, ambient noise levels during winter in remote locations may be insufficient to produce stable Green's functions through ambient noise interferometry, limiting time-lapse imaging sensitivity. Passive DAS applications in the Arctic environments face significant challenges due to low ambient seismic energy and highly anisotropic noise fields (Cheng et al., 2022; Sun et al., 2025). Additionally, the coupling between the fiber and frozen ground and signal attenuation through ice-rich sediments may complicate waveform coherence and amplitude interpretation (Castongia et al., 2017; Harmon et al., 2022).

DAS strain-rate measurements are inherently directional, being most sensitive to axial strain induced by particle motion along the fiber axis. As shown by Martin et al. (2021), this makes DAS particularly responsive to Rayleigh waves propagating longitudinally along the cable, but it also introduces mode-dependent biases when compared to traditional vertical-component geophones (Luo et al., 2021; Yuan & Martin, 2025). Moreover, higher-order Rayleigh modes may exhibit stronger horizontal particle motion compared to the fundamental mode, which can enhance their visibility in DAS recordings (Gribler et al., 2016; Shapiro et al., 2001; Viens et al., 2022). Fiber orientation and wave propagation characteristics, therefore, play a crucial role in interpreting DAS surface-wavefields.

Cryoseisms, or frost quakes, can occur when rapid surface cooling causes frozen, water-saturated ground to contract and crack, releasing accumulated stress explosively (Barosh, 2000). These shallow events generate strong surface waves and may be accompanied by audible cracking or booming sounds, but their seismic energy decays quickly with distance (Leung et al., 2017; Nikonov, 2010). A recent study in Svalbard has demonstrated the potential of cryoseismic and surface-wave analyses to characterize near-surface permafrost structure and dynamics. Passive seismic recordings of cryoseisms in Adventdalen reveal that frost-quake events generate strong surface-wave energy, enabling multichannel analysis of surface waves (MASW), a non-invasive monitoring technique, to delineate ice-rich layers within the active layer and upper permafrost (Romeyn et al., 2021). Similarly, long-term cryoseismic catalogs derived from their small-aperture Spitsbergen seismic array highlight the sensitivity of ground thermal stress and frost cracking to environmental forcing (Romeyn et al., 2022).

Since ice content strongly influences the mechanical strength of permafrost, seismic velocity measurements provide a highly sensitive means for investigating the subsurface distribution of ground ice (Akhtarshenas et al., 2024; Wu et al., 2017). However, the inversion of surface-wave dispersion data from permafrost terrains remains challenging. Strong velocity contrasts between layers and lateral heterogeneity associated with ice wedges may yield non-unique or unstable solutions. Inverting surface-wave dispersion curves to derive subsurface elastic properties is a classic nonlinear problem in near-surface seismic characterization. Linearized approaches are widely used due to their computational efficiency and rapid convergence; however, their solutions are often sensitive to the initial model (Wang et al., 2022). However, non-linear inversion methods are better suited for capturing the strong parameter trade-offs and complex velocity gradients typically present in permafrost, as they do not rely on model linearization and can handle broader ranges of parameter variability. Yet, these methods may still converge toward local minima and provide limited uncertainty quantification, making it difficult to assess the reliability of the retrieved models (Xia et al., 1999). To address these limitations, stochastic global search algorithms, such as grid search (Macquet et al., 2014), Monte Carlo (Maraschini & Foti, 2010; Socco & Boiero, 2008), genetic algorithms (Lomax & Snieder, 1994), and neighborhood algorithms (Mordret et al., 2014), are commonly employed, as they explore broader model spaces and can estimate model uncertainty (Lehujeur et al., 2021).

In this study, we use the energy from impulsive cryoseismic events recorded with DAS to image permafrost heterogeneity. We extract surface-wave dispersion curves from these passive events and apply a suite of MASW techniques with two inversion strategies to build Vs profiles. Furthermore, we analyze the effects of gauge length and wave propagation directionality on the resulting dispersion characteristics. By integrating field DAS cryoseismic observations, inversion analyses, and insights from elastic-wave forward modeling, we aim to evaluate the feasibility, sensitivity, and limitations of this approach for time-lapse permafrost characterization and to propose recommendations for optimal data acquisition and processing strategies.

4.3 Study Site and Data Acquisition

The DAS dataset was collected from a continuous passive field experiment conducted near Utqiaġvik, Alaska, on the Arctic Coastal Plain, approximately 2 km inland from the coastline (Figure 4.1). The region is underlain by continuous permafrost extending 200–400 m deep (Jorgenson et al., 2008), with an active layer ranging from 0.2 m to 0.3 m (Tourei et al., 2024). A 2 km-long DAS array was installed in August 2021, originating at the Department of Energy (DOE) Atmospheric Radiation Measurement (ARM) facility, running alongside a gravel road near the National Oceanic and Atmospheric

Administration (NOAA) facility, and extending northeast toward Elson Lagoon. The route crossed both undisturbed tundra and disturbed permafrost zones associated with roads and infrastructure. The fiber was installed manually using shallow trenches to minimize surface disturbance with air temperatures ranging from −1 °C to 10 °C during the cable installation. The DAS data are collocated with a collection of borehole core samples, an electrical resistivity tomography (ERT) survey, and five active-source MASW surveys acquired by geophones in August 2022 (Tourei et al., 2024).

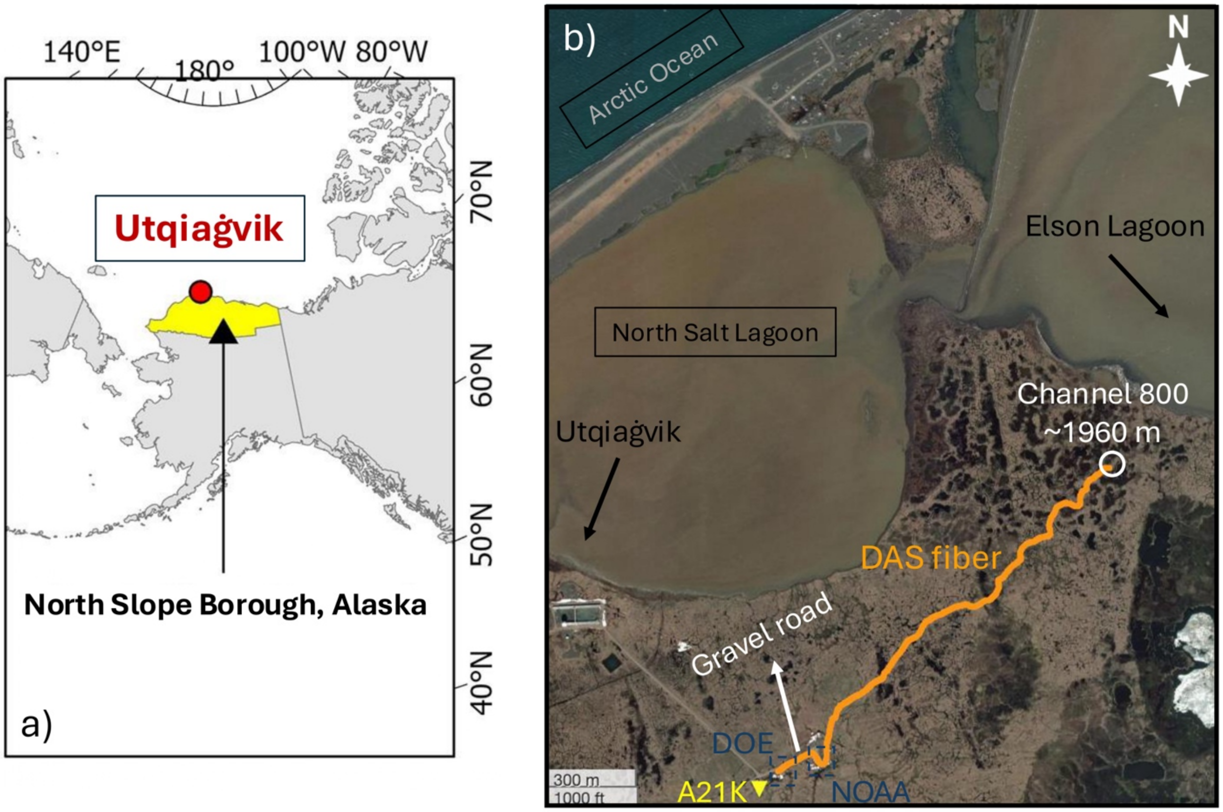

Figure 4.1 Map of the North Slope Borough, Alaska (a) and the study site on the northeast side of Utqiaġvik (b), showing fiber-optic cable route (in orange) and the A21K seismometer (yellow triangle).

The system employed a Treble interrogator unit from Terra15 interrogator housed at the DOE facility, operating at a 500 Hz sampling rate and 2.45 m spatial channel spacing. The fiber-optic cable acts as a distributed vibration sensor, capturing axial strain variations from the ambient wavefield, including traffic signal (mainly from the road between the DOE and NOAA buildings as shown in Figure 4.1), earthquakes, seismic tremors from sea ice (Rocha dos Santos & Zhu, 2025), and cryoseismic events potentially due to ice-wedge cracking. This dataset forms the basis for passive permafrost imaging using surface-wave dispersion analysis and inversion techniques, as discussed in subsequent sections.

4.4 Data Processing Scheme

The first step of data processing is to transform the recorded data from cumulative velocity into the strain rate. Assuming a homogeneous isotropic medium and seismic wavelengths at least twice the interrogator gauge length (l), the DAS-measured strain rate ($\dot{\varepsilon}$) can be expressed as the finite difference of fiber-aligned particle velocities ($\dot{u}$) recorded by two hypothetical horizontal geophones separated by l. Equation 4.1 was applied to convert the signals into strain rate, allowing for flexibility in selecting the effective gauge length for data processing.

$$\dot{\varepsilon}(x,t) = \frac{\dot{u}(x + l/2\,, t) - \dot{u}(x - l/2\,, t)}{l} \tag{4.1}$$

Surface-wave energy attenuates exponentially with depth, and its penetration is frequency dependent: longer wavelengths (lower frequencies) sample deeper layers. Shorter wavelengths (higher frequencies) are sensitive to near-surface structures, leading to frequency-dependent phase velocities in layered media (Park et al., 1998). By analyzing this frequency–velocity relationship, the MASW method enables estimation of the Vs structure of the subsurface.

The initial processing step involved applying seismic ambient noise interferometry to the passive data to generate virtual shot gathers for dispersion analysis (Wapenaar et al., 2010). However, the tundra environment near Utqiaġvik lacks continuous anthropogenic or natural noise sources, resulting in insufficient ambient energy for stable cross-correlation. Even after stacking three weeks of continuous recordings, no coherent surface-wave arrivals were observed. This limitation motivated the use of alternative energy sources for imaging. To discover new sources, we employed an autoencoder-based anomaly detection model (Tourei et al., 2024) to automatically identify anomalies, which were then investigated to find impulsive cryoseismic events that exhibit strong surface-wave energy.

To extract Rayleigh-wave dispersion curves, we applied the phase-shift method, which provides robust estimates of phase velocity as a function of frequency. As discussed earlier, increasing the gauge length improves the signal-to-noise ratio (SNR) of DAS measurements but reduces spatial resolution. While applying a longer gauge length enhances the detectability of cryoseismic events by increasing the SNR, it limits the shortest measurable wavelength (highest resolvable frequency) for a given wave speed. Figure 4.2 illustrates the effect of gauge length selection on surface-wave characterization, showing that increasing the gauge length influences the fidelity of the retrieved dispersion curves at higher frequencies and increases the uncertainty in phase velocities. This occurs because a longer gauge length averages strain rate over a greater fiber distance, effectively smoothing out high-frequency, short-wavelength signals. The dashed lines on the dispersion images indicate the minimum and maximum wavelengths that can be reliably sampled based on the gauge length and total array aperture.

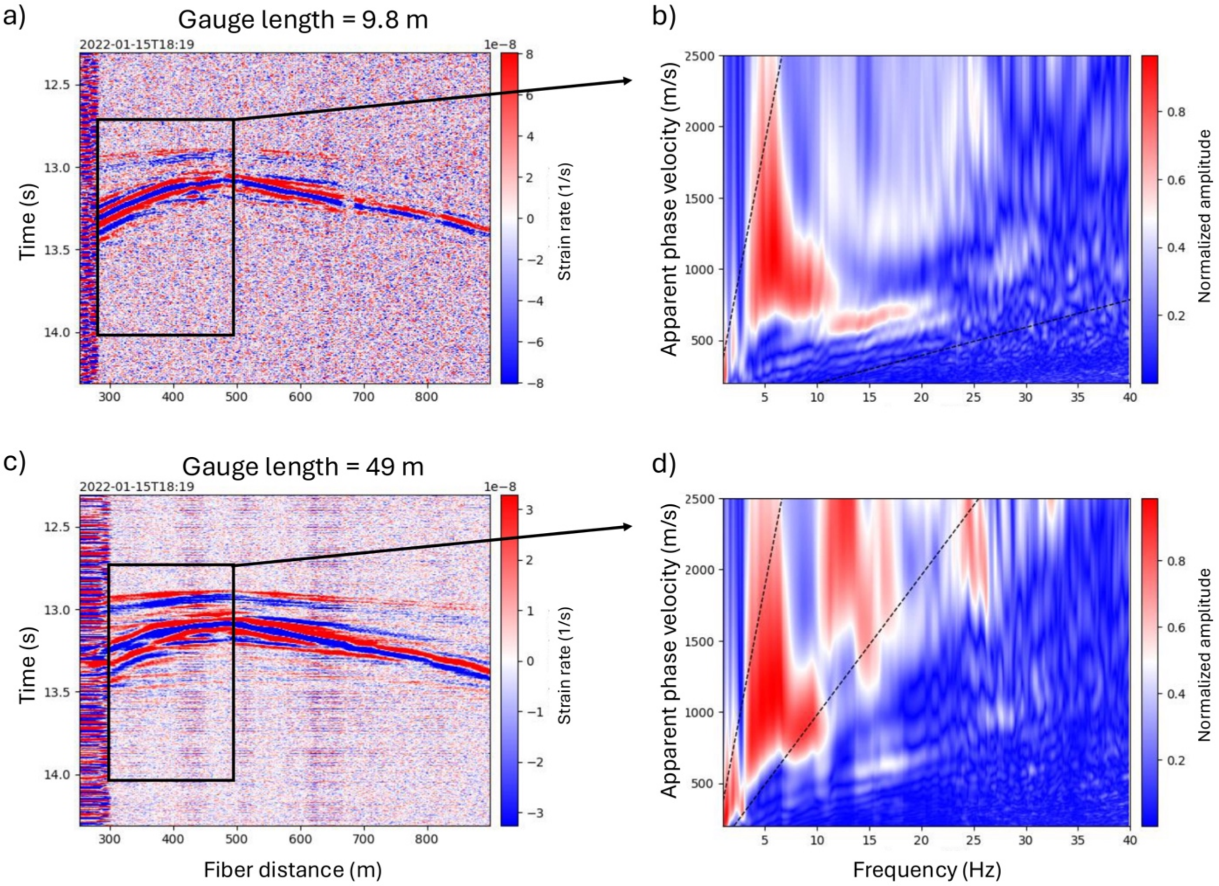

Figure 4.2 The time-domain raster plots (a and c) and the gauge length’s effect on the dispersion results (b and d) for Cryoseismic Event 1.

Prior to inversion analysis, we examined the recorded wavefield to determine the dominant surface-wave mode. Cryoseismic events are primarily tensile cracking phenomena, involving volumetric expansion and opening of frozen ground rather than shear displacement, generating strong P- and SV-wave energy but minimal SH-wave radiation slip (Afonin et al., 2024; Okkonen et al., 2020). Consequently, Love waves’ transverse shear motion is expected to be weak or absent. Similar vertical S-wave polarization has been reported in Finnish frost-quake studies (Afonin et al., 2024). To confirm the dominant surface wavefield in our dataset, we analyzed waveforms from the regional AK-A21K broadband station near Utqiaġvik (shown as a yellow triangle in Figure 4.1). We investigate two cryoseismic events in detail, which we refer to as Events 1 and 2. For Cryoseismic Event 1 (Figure 4.2a), the root-mean-square (RMS) ratios between the horizontal and vertical components of surface-wave arrivals were 0.32 for N/Z and 0.27 for E/Z components, respectively. These low horizontal-to-vertical amplitude ratios indicate that the recorded energy is primarily associated with Rayleigh-type motion, consistent with the SV-polarized wavefields generated by tensile cracking sources. The subsequent dispersion analysis and inversion were therefore performed under the assumption of Rayleigh-wave–dominated energy, using dispersion images extracted from the DAS recordings.

Horizontal DAS arrays are inherently more sensitive to Rayleigh wave components with strong horizontal motion (i.e., high ellipticity), which can enhance the detection of higher-order modes that exhibit greater ellipticity than the fundamental mode (Fang et al., 2023; Shapiro et al., 2001; Viens et al., 2022). For a few cryoseismic events, the presence of higher-order modes was evident. For example, Figure 4.3 illustrates an example cryoseismic event, where both the fundamental and first higher-order Rayleigh modes are clearly identified. In contrast, higher-order modes were not initially observed for Cryoseismic Event 1 (Figure 4.2a-b) or Event 2 (Figure 4.5).

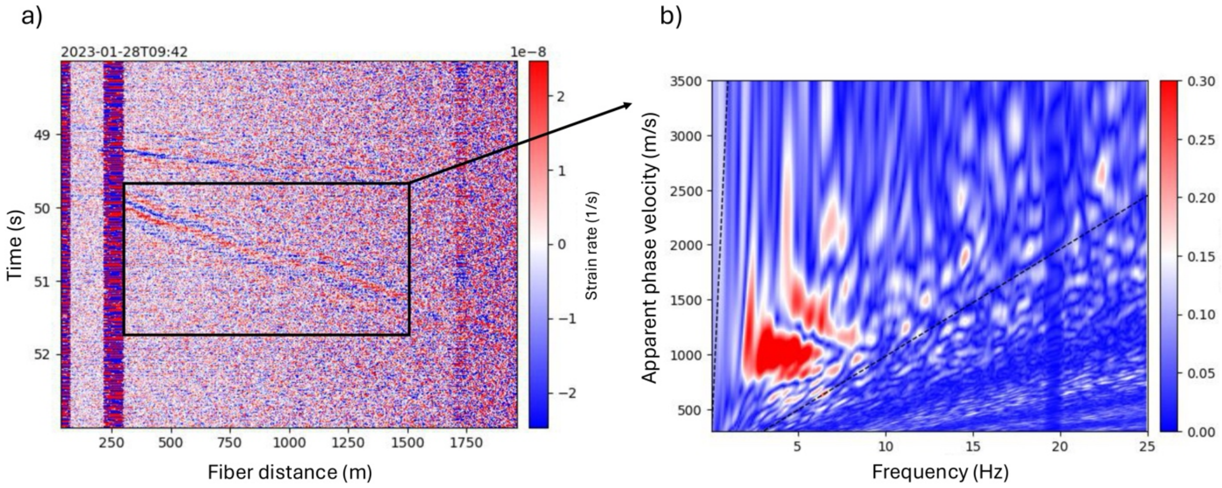

Figure 4.3 The time-domain raster plot (a) and the dispersion image with fundamental and first-order mode Rayleigh wave (b) for an example cryoseismic event.

As a complementary assessment of Rayleigh-wave modal content for Event 1, we performed horizontal-to-vertical spectral ratio (HVSR) analysis on the 3C seismometer data using a statistical approach to account for azimuthal variability (Cheng et al., 2020; Vantassel, 2025). As illustrated in Figure 4.4, results showed HVSR values exceeding unity above 11 Hz (observed as a separate moveout in Figure 4.2b), suggesting increased ellipticity at higher frequencies. Consequently, frequencies above 11 Hz were excluded from the inversion to ensure that only fundamental-mode Rayleigh-wave energy was considered. The absence of a prominent HVSR peak below 10 Hz suggests that the ellipticity for this event is relatively small, and thereby, the fundamental-mode Rayleigh response should be considered for DAS-based analysis and inversion. The HVSR results for Event 2 were noisier and exhibited greater fluctuation but remained mostly below 1, also supporting a fundamental-mode Rayleigh-wave interpretation. Additionally, the preliminary numerical modeling results provided in Appendix C suggest that the discontinuity of dispersion around 10 Hz (Figure 4.2b) is potentially due to strong scattering and mode conversion caused by the ice-wedge or ice-rich layer heterogeneity, where impedance contrasts between frozen and unfrozen layers disrupt the continuity of the Rayleigh-wave fundamental mode and lead to partial energy redistribution into higher modes.

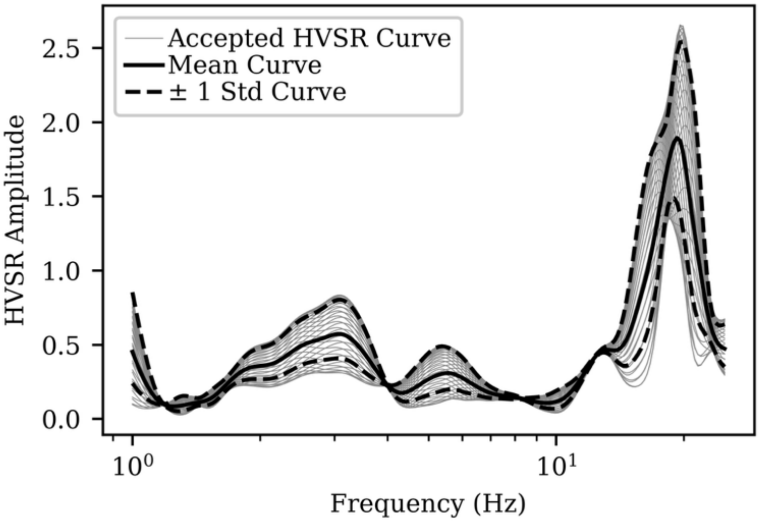

Figure 4.4 The HVSR curves from the 3-C seismometer for Cryoseismic Event 1.

Inversion of Rayleigh-wave dispersion curves to estimate Vs profiles is inherently non-unique, as several subsurface models can reproduce the same dispersion curve within the data uncertainty. To better understand the reliability of the inverted Vs profiles, we applied two complementary inversion approaches: a deterministic non-linear least-squares (NLLS) method and a stochastic Monte Carlo (MC) global search. The NLLS inversion iteratively adjusts model parameters to minimize the difference between the measured and calculated dispersion curves using the Levenberg–Marquardt algorithm (Xia et al., 1999). The MC inversion, on the other hand, randomly samples possible combinations of layer thicknesses and velocities within predefined bounds, producing a range of models that fit the observed data and help quantify uncertainty and trade-offs, such as the correlation between Vs and layer thickness (Olafsdottir et al., 2020; Shapiro & Ritzwoller, 2002). Combining the NLLS results with the MC ensemble enables a more comprehensive assessment of the uncertainty and non-uniqueness inherent in the derived Vs structures.

4.5 Results and Discussion

The dispersion results for Cryoseismic Event 2 (Figure 4.5c), whose source was located at approximately the same distance along the fiber as Event 1 (Figure 4.2a), show that phase velocity increases with frequency, indicating inverse dispersion behavior common in permafrost. In typical subsurface conditions, where soil stiffness increases with depth as a result of higher effective stress, the phase velocity generally decreases with frequency (normal dispersion). A similar behavior was observed in Figure 4.2b, where phase velocity increased between 3-6 Hz, decreased near 10 Hz, and then increased again up to 18 Hz. These alternating dispersion trends likely reflect layered permafrost structure, in which contrasting ice content and stiffness produce alternating low–high–low Vs patterns observed in the previous permafrost studies in Utqiaġvik (e.g., Dou & Ajo-Franklin (2014); Tourei et al. (2024)). This complex velocity distribution suggests that ice-rich layers or frozen interbeds may be embedded within softer frozen soils, producing localized impedance contrasts that influence surface-wave propagation.

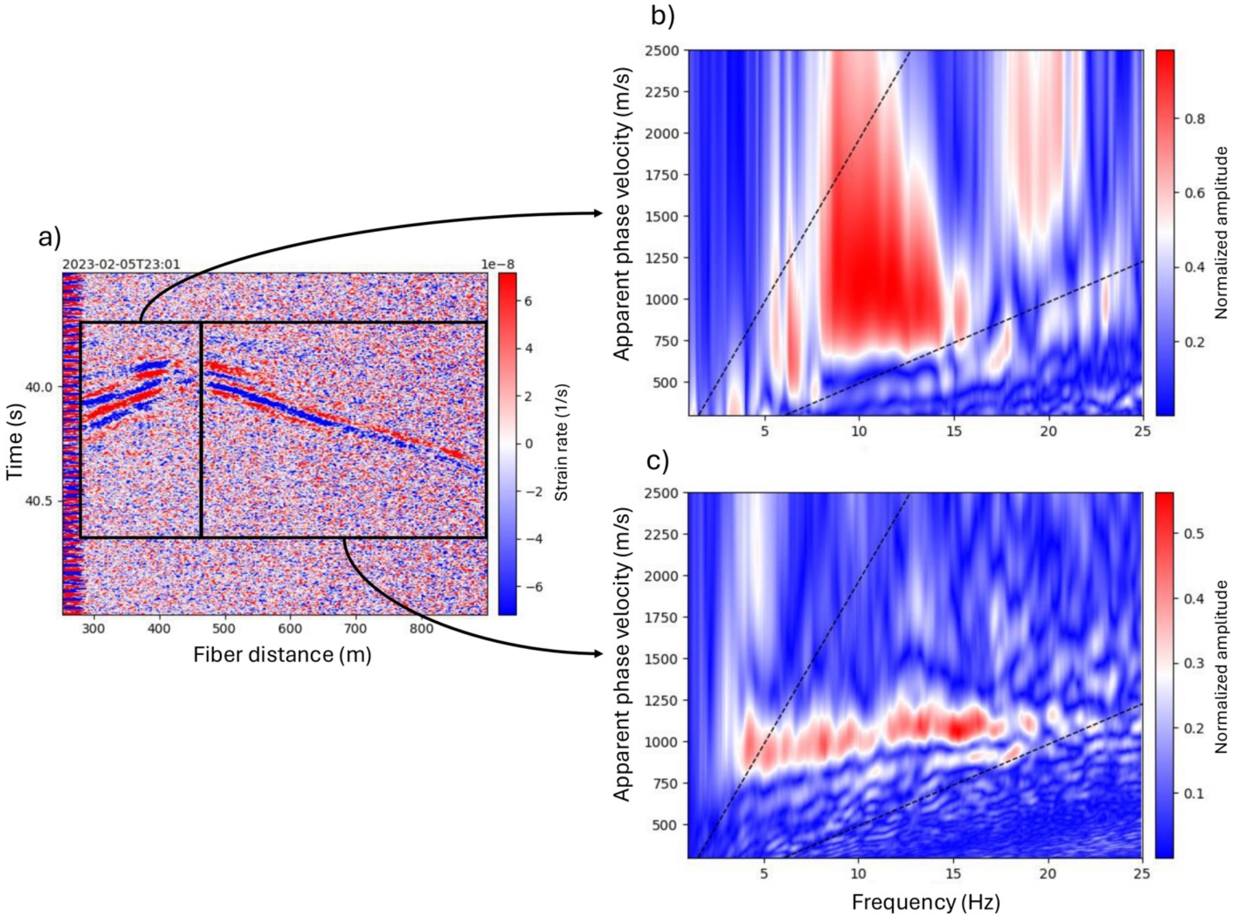

Figure 4.5 The time-domain raster plot (a) for Cryoseismic Event 2 and the wave propagation effect on the dispersion results for the southwest (b) and northeast (c) segments of the fiber.

By inverting the dispersion curves derived from the phase-velocity–frequency images, we generated 1D Vs profiles from individual cryoseismic events. Figure 4.6b presents two representative Vs profiles inverted from Cryoseismic Events 1 and 2 on two different array segments (Figure 4.6a), using the NLLS method with an L2-norm misfit between the theoretical and observed dispersion curves of 69 m/s and 61 m/s, respectively. We observe the low-high-low velocity structure in both Vs profiles. Thanks to the large spatial coverage provided by the DAS array and the low-frequency content of the recorded surface waves from these naturally occurring cryoseismic events, resulting in relatively longer wavelengths that penetrate deeper, it was possible to invert for Vs down to depths of approximately 110 m and 82 m for Events 1 and 2, respectively. Such depth penetration would not be achievable using a conventional 24 m active-source survey line as discussed by Tourei et al. (2024). This extended depth sensitivity provides valuable subsurface information for geotechnical engineering applications, such as pile foundation design for high-rise infrastructure that requires characterization of deeper, load-bearing strata. It should be noted that although the array length for Event 2 (420 m) is greater than that of Event 1 (190 m), the maximum investigation depth for Event 1 is deeper. This is because the dispersion picks for Event 1 include lower-frequency components (starting around 3 Hz, as shown in Figure 4.2b) associated with higher phase velocities, which correspond to longer wavelengths and, consequently, greater penetration depth.

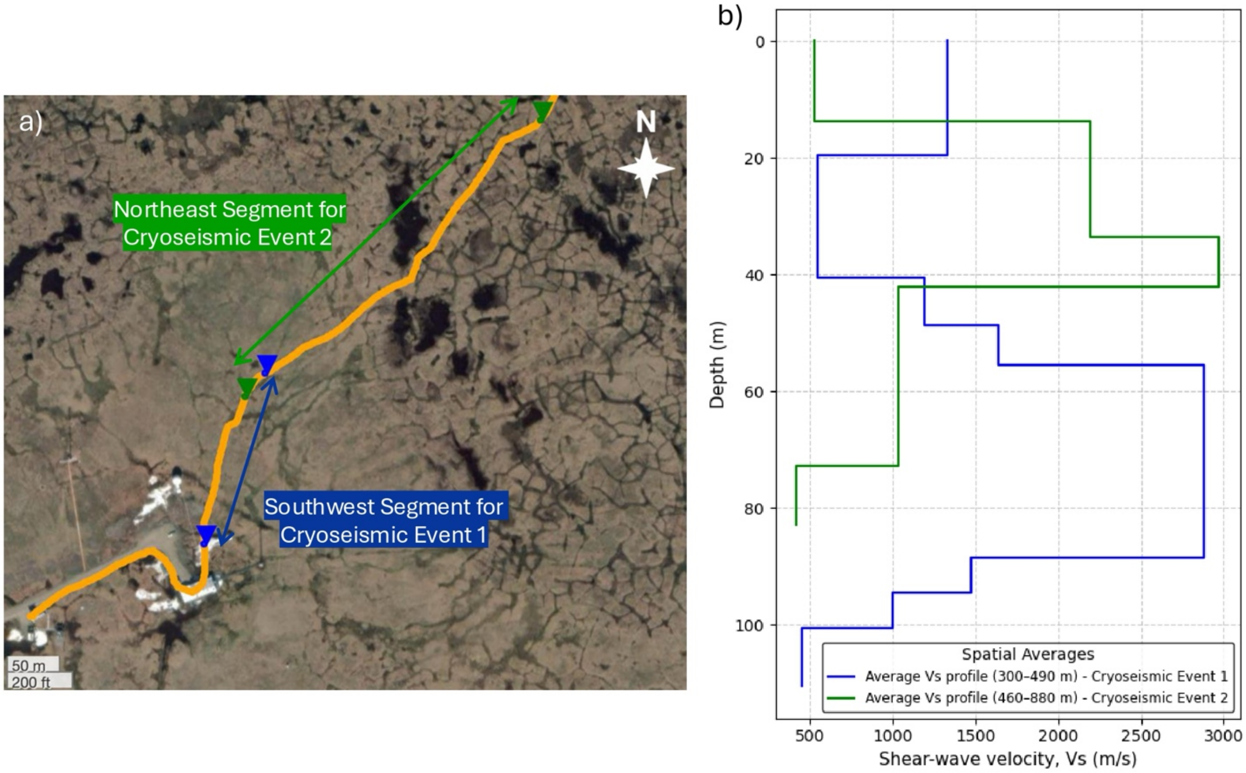

Figure 4.6 Enlarged view of the fiber segments used for MASW analysis (a) and the corresponding inverted Vs profiles (b).

As shown in Figure 4.6a, the dispersion analyses were performed on array segments of approximately 320 m for Event 1 (Figure 4.3a) and 420 m for Event 2 (Figure 4.5a), both during winter 2023. Consequently, the resulting Vs models represent spatially averaged properties over those intervals. Despite this spatial averaging, the results reveal pronounced vertical and lateral heterogeneity and distinct high-velocity zones within the upper permafrost. As shown in Figure 4.6, elevated Vs values occur between 47-88 m depth for Event 1 on the southwest segment of the fiber (noted in Figure 4.6a and blue Vs profile in Figure 4.6b), while for Event 2 on the northeast segment of the fiber (green Vs profile in

Figure 4.6b), a similar high-velocity interval is observed between 13-42 m. These high-velocity layers likely correspond to ice-rich zones, where increased ice bonding substantially enhances the stiffness and shear rigidity of the frozen soil matrix. The presence of a stiff layer is consistent with the occurrence of ice-cemented permafrost, overlying softer, partially frozen sediments (Lachenbruch, 1962; Loktev et al., 2012; Munroe et al., 2007; Tourei et al., 2024). In contrast, low-velocity zones are observed below 13 m and between 42–82 m on the northeast segment, and between 20-40 m on the southwest segment. These zones potentially reflect discontinuous ice or saline layers, such as cryopeg, that inhibit complete freezing. Similar low-velocity anomalies attributed to saline cryopeg layers have been reported previously in Utqiaġvik (Brown, 1969; Meyer et al., 2010a; O'Sullivan et al., 1966; Overduin et al., 2012; Tourei et al., 2024).

Furthermore, the observation that the high-Vs layer on the southwest segment appears deeper than that on the northeast segment suggests a dipping geometry of the ice-rich permafrost horizon, possibly due to variability of surface water drainage direction towards the coastline and localized ground-ice accumulation or differential freezing along the cable path. These findings demonstrate the capability of fiber-based, multichannel near-surface techniques to capture distributed variations in permafrost structure over large spatial regions. Unlike conventional borehole or point-based geotechnical observations, DAS enables continuous, distributed measurements, offering a powerful framework for improving the resolution and spatial coverage of in-situ permafrost characterization.

It should also be noted that the obtained phase velocities represent apparent velocities, as the exact source-to-array orientation is approximate; therefore, deviations from an ideal in-line configuration can lead to a slight overestimation of phase velocity (Foti et al., 2018; Park et al., 1999a). In this study, sources were selected with features suggesting an approximately in-line source orientation, supported by the close temporal alignment of body- and surface-wave arrivals (Figure 4.2a). Nonetheless, although the depth-wise trend of the Vs profile is expected to remain consistent, potential azimuthal variations or lateral source offsets may have slightly increased the inverted Vs values, introducing uncertainties into the Vs profiles and highlighting the importance of precise event localization and azimuthal corrections in future analyses.

Figure 4.7 presents the ensemble of accepted Vs models from the MC inversion with misfit below 5%, colored by misfit percentile (10th–90th; darkest near the median) to convey posterior dispersion, together with the MC median profile and the NLLS solution for Cryoseismic Event 1. The concentration of the model's percentile delineates depth intervals that are well constrained by the data (narrow, dark bands) versus poorly resolved sections (broad, pale spreads), reflecting the principal trade-offs between Vs and layer thickness in Rayleigh-wave inversion. The light green bar marks the depth range corresponding to approximately half a wavelength of the analyzed dispersion picks, whereas the light-red sections represent the fitted Vs profiles derived from the inversion, signifying regions of lower confidence and interpretational uncertainty. The NLLS model closely tracks the MC median, particularly at depths greater than 50 m, indicating that the deterministic optimum lies near the center of the posterior. Departures occur where the percentile spread widens, with the NLLS solution preferentially selecting one end of the admissible Vs-thickness manifold. These differences underscore the non-uniqueness of the inverse problem: the NLLS profile provides a single best-fit realization, whereas the MC percentile analysis quantifies the range of models that fit the data within tolerance, thereby offering a more complete characterization of parameter uncertainty and resolution.

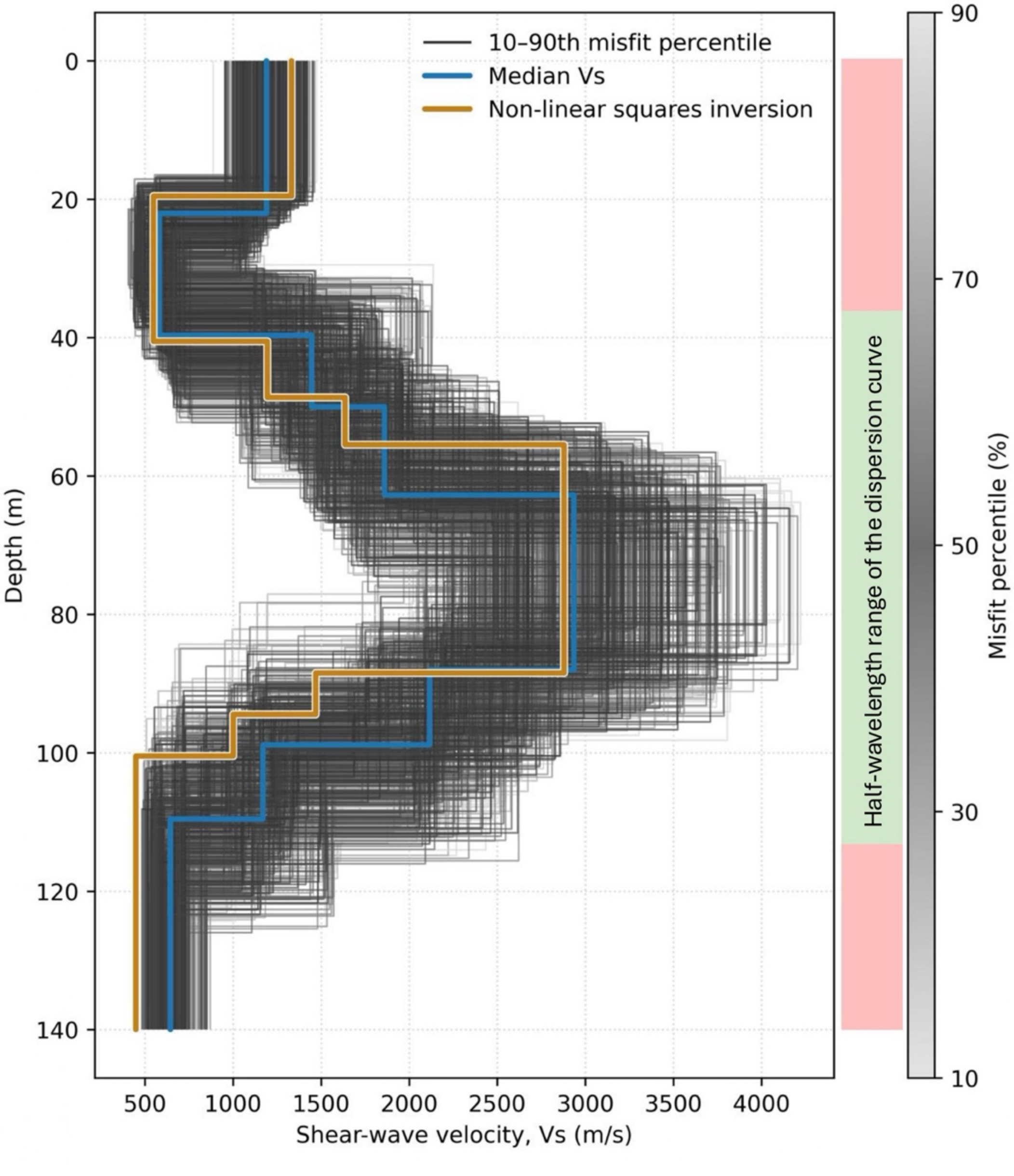

Figure 4.7 Ensemble of accepted MC Vs models for Cryoseismic Event 1, shaded by misfit percentile (10–90; darkest at the median), overlaid with the median Vs (blue) and the NLLS solution (orange).

Comparing the characterized high-Vs zone with the active-source MASW study in Utqiaġvik (Tourei et al., 2024), the high-Vs zone in the present study appears at greater depths, primarily due to the lower source depth of the cryoseismic events and the use of longer array apertures. Furthermore, the limited high-frequency content in this dataset reduces our ability to resolve the upper 20–40 m with confidence. In contrast, the active-source survey achieved higher resolution in the shallow subsurface down to approximately 10 m, benefiting from a shorter array geometry and a richer high-frequency wavefield. Joint interpretation of both surveys enables multiscale characterization of permafrost structure. The shallow ice-rich zones are associated with ice-wedge polygons and near-surface ice variability patterns, while the deeper high-velocity zones may reflect long-term climatic influences that facilitated the formation of persistent ice-rich layers, potentially accounting for the elevated Vs at depth.

Laboratory and field studies have reported Vs values up to about 3,000 m/s in ice-cemented or ice-rich sandy permafrost (Ji et al., 2024; Young et al., 2022). Additionally, Shaw (1986) demonstrated that the elastic properties of ice vary substantially among crystalline phases depending on their formation temperature and pressure. These findings support our interpretation that the deeper, high-velocity layers identified in the inversions likely represent dense, ice-rich permafrost formed under low-temperature and high-confining-pressure conditions. Such conditions are consistent with long-term cold climate regimes and prolonged freezing periods, which may promote the accumulation and preservation of massive ground ice at depth. Figure 4.5 also compares dispersion images computed for the propagating wavefields recorded during Cryoseismic Event 2 on two segments of the fiber: 290 to 460 m (southwest), and 460 to 880 m (northeast). The dispersion image for the southwest part of the fiber shows no coherent surface-wave energy (Figure 4.5b), whereas the recorded wavefield on the northeast part of the fiber exhibits clear and continuous energy between 5 Hz and 20 Hz (Figure 4.5c), which was used for Vs inversion. A similar wave directionality effect was observed for Event 1 (Figure 4.2), but in the opposite sense: the propagating wave recorded on the southwest portion of the fiber (blue double-headed arrow in Figure 4.6a) displays clear moveout, whereas the northeast portion does not. These observations suggest that asymmetry in the source radiation pattern for these two events may have influenced the coherence of the wavefield on each side of the recorded hyperbola (Roy & Jakka, 2017; Taipodia et al., 2019). In addition, these variations may result from anisotropic ice distribution or localized scattering effects near the source region (Steinel et al., 2014). Simple 2D elastic modeling of a source originating at the boundary of an ice wedge embedded in a layered permafrost medium suggests that we should expect to see some differences on either side of the data array, as shown in Appendix C. Future 3D elastic-wave forward modeling and cryoseismic simulations, accounting for source mechanism and wave-azimuthal dependence, will help to better quantify these propagation effects and to constrain the true source geometry and wavefield characteristics within the permafrost environment.

4.6 Conclusions

Because passive DAS monitoring is non-destructive to permafrost and provides large spatial coverage with fine spatial resolution, it improves understanding of permafrost structure over km-scale arrays and the degradation over time. Naturally occurring cryoseismic events supply the seismic energy needed for near-surface imaging, enabling time-lapse monitoring in remote areas where the lack of ambient energy makes ambient noise interferometry impractical. By detecting these events and analyzing their surface-wave dispersion response and accounting for the effects of DAS-specific parameters such as gauge length, inversion of Vs profiles becomes possible. Depending on the frequency content and corresponding wavelength, characterization to depths of up to ~140 m can be achieved. Comparison between NLLS and MC inversions further demonstrates that integrating deterministic and stochastic approaches improves the robustness and uncertainty assessment of the derived Vs models. However, ground-truth validation through borehole or direct sampling is essential to improve confidence in the results.

These findings highlight the importance of developing non-destructive, long-term monitoring techniques that avoid further disturbance to sensitive permafrost environments. Relying on passive seismic sources eliminates the need for frequent field mobilization and active energy generation, making this approach particularly suitable for remote Arctic regions. Such methods can provide valuable input for geotechnical engineers and infrastructure designers developing foundations and support systems on thaw-affected permafrost, helping ensure safety and resilience under ongoing climate change.

4.7 Acknowledgments

This study was supported by the National Science Foundation under Grants CMMI-2034363, CMMI-2034366, and CMMI-2034380. We gratefully acknowledge the support and facilities provided by UIC Science, LLC, the National Oceanic and Atmospheric Administration (NOAA), and the Atmospheric Radiation Measurement (ARM) Climate Research Facility of the U.S. Department of Energy (DOE). We would like to thank John Hole, Xiohang Ji, and Tieyuan Zhu for the thoughtful discussions. We also sincerely thank Xiaohang Ji, Min Liew, Tieyuan Zhu, Nolan Roth, Anne Jensen, Dmitry Nicolsky, and Chris McComb for their invaluable field and project support. We thank Terra15 for their support on the DAS interrogator. The das-anomaly (Tourei, 2025) Python package was used for detecting cryoseismic events. DASCore (Chambers et al., 2024) was used for reading, processing, and DAS dispersion analysis, along with hvsrpy (Vantassel, 2025) and SWinvert (Vantassel & Cox, 2021) packages for post-processing of the dispersion images. MasavesPy Python library (Olafsdottir et al., 2024) was used for MC inversion, and Intelligent-MASW (Liu et al., 2020) was used for NLLS inversion of the dispersion curves.

CHAPTER 5 CONCLUSIONS

The primary objectives of this research are: (1) to integrate multiple geophysical techniques to improve the characterization of permafrost and understanding its heterogeneity and degradation; (2) to apply AI–based methods to effectively enhance large-scale DAS data management through unsupervised anomaly detection; and (3) to detect and utilize naturally occurring cryoseismic events and develop non-destructive seismic monitoring techniques for scalable permafrost characterization using fiber-optic sensing technology. This final chapter summarizes the progress achieved toward these objectives, elaborates on the potential of scalable passive monitoring approaches, discusses the implications for large-scale DAS data management, and outlines future research directions.

5.1 Summary and Key Findings

The overarching objective of this research was to enhance the interpretation of permafrost heterogeneity by integrating multiple monitoring techniques and to establish a scalable framework for DAS-based permafrost characterization and data management. This work developed and demonstrated integrated, high-resolution, and scalable active and passive site characterization techniques for permafrost monitoring, combining seismic and electrical methods with temperature sensing and borehole core sampling observations.

Field investigations in Utqiaġvik, Alaska, integrated active MASW, ERT, borehole temperature logging, and permafrost core sampling to characterize the thermo-mechanical and cryogenic variability of tundra permafrost. The MASW data revealed systematic low–high–low Vs trends with depth, reflecting the active layer, ice-rich permafrost, and underlying low-velocity zones. Combined MASW–ERT inversions resolved distinct cryostructures, including cryopeg layers, and showed strong correspondence with borehole stratigraphy and salinity profiles. The analyses also demonstrate that engineered structures, such as gravel roads and pile foundations, alter the subsurface thermal regime, causing active-layer thickening and stiffness reduction, with implications for long-term infrastructure stability. Additionally, the active-source MASW results revealed meter-scale horizontal variability in permafrost stiffness, emphasizing the need for high-resolution techniques in site characterization.

Beyond field characterization, the study developed a computationally efficient deep-learning framework for anomaly detection in large-scale DAS datasets. The convolutional autoencoder architecture enabled unsupervised classification of background noise and anomalous events by leveraging a latent-space representation of power spectral density features in addition to reconstruction error thresholding. This dual-metric approach, using reconstruction error and density-based thresholds, effectively isolated anomalous signals such as microseismic, cryoseismic, instrument noise, and anthropogenic events while discarding non-informative background data. The workflow achieved significant data reduction with limited loss of important anomalous data in two distinct DAS monitoring projects, demonstrating its generalizability for continuous monitoring and its adaptability to different geologic and operational settings.

Furthermore, the research demonstrated that naturally occurring cryoseismic events can be detected with autoencoders, and they serve as passive seismic sources for permafrost characterization and degradation monitoring. Analysis of these events using DAS provided surface-wave dispersion data suitable for Vs inversion, yielding Vs structures that delineate frozen and thawed zones and identify massive ice-rich layers with velocities exceeding 2 km/s. Sensitivity tests highlighted the effects of gauge length, event directionality, and mode content on dispersion stability, indicating the effectiveness of passive DAS for non-invasive and time-lapse permafrost monitoring in remote regions with limited passive noise sources. This work provides a foundation for continuous Arctic subsurface monitoring and offers transferable methodologies for other geotechnical and environmental sensing domains.

5.2 Implications for Permafrost Characterization with Integrated Active Techniques

The combined use of MASW and ERT provides complementary sensitivity to the thermo-mechanical and hydrogeophysical properties of frozen ground: Vs profiling constrains stiffness and ice bonding, whereas resistivity reflects temperature, salinity, and unfrozen layers. Joint interpretation of these parameters substantially reduces the non-uniqueness of individual inversions and yields a more complete picture of permafrost heterogeneity that cannot be resolved from isolated geotechnical boreholes or temperature profiles. Field results from Utqiaġvik revealed low–high–low Vs patterns corresponding to the active layer, frozen permafrost, and underlying thawed zones, as well as distinct ice-rich and cryopeg features corroborated by borehole stratigraphy and salinity data. These results show that combining seismic and electrical imaging reduces inversion non-uniqueness and yields more physically consistent models. Borehole core data and temperature logs remain essential for validating geophysical interpretations and constraining inversion uncertainties.

The broader landscape of permafrost monitoring is evolving toward high-resolution, continuous observation enabled by in-situ technologies such as seismic node arrays (Colombero et al., 2025; Liu et al., 2021a), fiber-optic DAS and DTS systems (Cheng et al., 2022; Fichtner et al., 2025; Quinn et al., 2024), autonomous long-term ERT (Farzamian et al., 2024), 3D GPR (Koyan et al., 2025), and unmanned electromagnetic systems (Hallissey, 2025). These approaches address critical limitations of remote sensing tools like InSAR, which despite their utility for regional-scale deformation mapping, struggle to resolve subsurface heterogeneity or ice content directly. The shift toward autonomous, long-duration geophysical deployments reflects growing recognition that permafrost change is often spatially localized and temporally episodic. The implications of this shift are twofold: first, that scalable field-based techniques are essential for bridging surface observations with subsurface processes; and second, that integrated geophysical monitoring can serve as a foundation for coupled environmental–infrastructure models. This study contributes to that foundation by validating a reproducible, field-deployable active and passive monitoring framework for permafrost characterization with multiple techniques. It supports future efforts to better understand Arctic ground stability and the long-term impacts of civil infrastructure on permafrost under accelerating climate change.

5.3 Practical Insights on Non-destructive and Scalable Passive Permafrost Monitoring

Building on the integrated active methods discussed previously, this study also highlights the potential of passive, non-destructive seismic monitoring for long-term permafrost characterization. DAS, when paired with naturally occurring seismic sources such as cryoseisms and the ambient wavefield generated by human activity, offers a viable pathway toward scalable time-lapse subsurface imaging without the need for active sources or invasive deployments that may accelerate permafrost degradation. In remote Arctic settings, where logistical and environmental constraints limit repeated active surveys, the ability to continuously exploit ambient seismic energy along buried fiber-optic cables provides a low-maintenance, high-resolution alternative. This passive approach enables repeated shear-wave velocity imaging to track changes in ground stiffness, ice content, and thaw progression over time.

Although DAS provides high-resolution measurements over long distances, it mainly records a single component of ground motion, which must be considered during installation design. However, given the availability of seismometers at many Arctic locations, integrated processing of seismometer and DAS data can be leveraged to improve cryoseismic event detection and to estimate source azimuth prior to MASW analysis. Additionally, incorporating orthogonal DAS installations–at least along a small portion of the fiber–would enable two-component measurements, offering enhanced constraints on wavefield directionality and source characterization. When deployed in permafrost environments, such systems may reveal spatial patterns of degradation influenced by surface infrastructure. The findings of this work demonstrate that cryoseismic events can produce sufficient surface-wave energy to resolve Vs structure at a tens-of-meters scale, allowing meaningful interpretation of frozen and thawed zones. By enabling continuous, non-invasive monitoring of evolving subsurface conditions, passive DAS offers a practical tool for quantifying the long-term impacts of permafrost warming on Arctic ground stability and the coupled response of built environments.

5.4 Broader Impacts on Large-Scale DAS Data Management

DAS is revolutionizing subsurface monitoring by transforming standard fiber-optic cables into dense seismic arrays capable of capturing high-resolution seismic data over tens of kilometers. Its broad applicability across geotechnical, environmental, and energy sectors has made DAS a suitable tool for long-term, scalable monitoring of dynamic ground processes and geohazard characterization. However, one of the primary challenges in operationalizing DAS for large-scale deployment lies in the overwhelming data volume it produces–often terabytes per day for a single km-scale arrays–making real-time processing, storage, and interpretation increasingly difficult. Furthermore, extracting actionable information from such data typically requires specialized expertise in signal processing and geophysical analysis, limiting the accessibility and utility of DAS outside research contexts. This study addresses that barrier by demonstrating an unsupervised deep learning framework based on convolutional autoencoders to automate anomaly detection and isolate segments of interest from continuous DAS records. By compressing and filtering the data stream to highlight informative events such as seismic and traffic signals, this approach enables efficient data reduction while preserving critical subsurface signals. The insights gained from two passive seismic monitoring studies in Utqiaġvik, AK (permafrost characterization application), and in a longwall coal mine (seismicity monitoring applications) underscore the need for intelligent, unsupervised workflows to fully leverage DAS as a continuous, high-density monitoring platform in Arctic and other data-intensive environments. The developed anomaly detection framework may be broadly applicable to other monitoring scenarios–such as energy infrastructure surveillance, security applications, and the detection of cable-proximal hazards–where rapid identification of abnormal signals is critical for mitigating risk and ensuring system integrity.

5.5 Future Research Directions

Conducting active-source seismic and electrical surveys across different seasons to assess temporal variations in near-surface velocity and resistivity, and to correlate them with DTS and borehole temperature data, can provide direct constraints on thermal and mechanical changes in permafrost. Additionally, performing active-source hammer shots adjacent to the DAS array and collecting both DAS and vertical and horizontal geophone data would help better characterize the DAS response and its sensitivity to surface-wave modal variability compared to traditional geophone measurements.

In remote coastal environments where high-frequency anthropogenic sources are scarce and the ambient field is dominated by low-frequency oceanic noise, using DAS interrogator units with a low noise floor optimized for low-frequency response can more effectively harness the available environmental energy, thereby improving near-surface characterization. Such systems may also facilitate monitoring of low-frequency strain variations along the fiber, providing insights into permafrost subsidence and long-term ground deformation. Furthermore, given that DAS is inherently a single-component sensing technique, future deployments should incorporate orthogonal or multi-directional fiber layouts to capture multi-azimuthal wavefields and enhance the ability to capture between different body wave and surface wavefields.

The autoencoder-based detection framework developed in this study will be compared with physics-based back-projection methods to evaluate relative performance for earthquake and cryoseismic event detection in terms of accuracy, sensitivity, and computational efficiency. The open-source das-anomaly software introduced in Chapter 3 requires a diverse user community to thrive. To that end, future efforts will emphasize DAS research community engagement, including the development of tutorials and detailed application examples. A major feature the software currently lacks is automated density-score threshold selection based on example anomalous datasets, although preliminary implementations exist.

Developing multimodal inversion schemes that incorporate higher-order Rayleigh modes from cryoseismic events recorded on horizontal DAS arrays can improve shear-wave velocity imaging in heterogeneous permafrost environments. Complementary three-dimensional numerical modeling can be used to investigate how array geometry, source location, and source azimuth influence MASW dispersion and Vs inversion results in complex media. Such modeling efforts will also enhance understanding of how wavefield characteristics and source directionality affect surface-wave propagation and dispersion across different segments of the fiber. In addition, a quantitative assessment of the vertical and lateral resolution limits of MASW and DAS-based methods will help guide future survey design and the interpretation of both cryoseismic and active-source data. Reducing inversion uncertainty and mitigating non-uniqueness remain essential for improving the robustness of shear-wave velocity estimates, thereby enabling more reliable interpretation of two-dimensional MASW results in spatially variable permafrost settings.

REFERENCES

Abadi, M., Barham, P., Chen, J., Chen, Z., Davis, A., Dean, J., Devin, M., Ghemawat, S., Irving, G., Isard, M., Kudlur, M., Levenberg, J., Monga, R., Moore, S., Murray, D. G., Steiner, B., Tucker, P., Vasudevan, V., Warden, P., … Zheng, X. (2016). TensorFlow: A system for large-scale machine learning. *Proceedings of the 12th USENIX Symposium on Operating Systems Design and Implementation, OSDI 2016*, 265–283.

Degnan, J. R., Pelham, K., Terry, N., Welch, S., & Johnson, C. D. (2023). Advancing subsurface investigations beyond the borehole with passive seismic horizontal-to-vertical spectral ratio and electromagnetic geophysical methods at transportation infrastructure sites in New Hampshire | *U.S. Geological Survey*. (2023). Retrieved October 2, 2025, from https://www.usgs.gov/publications/advancing-subsurface-investigations-beyond-borehole-passive-seismic-horizontal

Afonin, N., Kozlovskaya, E., Moisio, K., Kokko, E. R., & Okkonen, J. (2024). Frost quakes in wetlands in northern Finland during extreme winter weather conditions and related hazard to urban infrastructure. *Cryosphere*, *18*(5), 2223–2238. https://doi.org/10.5194/TC-18-2223-2024

Ajo-Franklin, J., Dou, S., Lindsey, N., Daley, T. M., Freifeld, B., Martin, E. R., Robertson, M., Ulrich, C., Wood, T., Eckblaw, I., & Wagner, A. (2017). Timelapse Surface Wave Monitoring of Permafrost Thaw Using Distributed Acoustic Sensing and a Permanent Automated Seismic Source. *SEG Technical Program Expanded Abstracts*, *c*, 5223–5227. https://doi.org/10.1190/segam2017-17774027.1

Akhtarshenas, S., & Abdelaziz, S. L. (2024). Dynamic Properties of Frozen Soils: A Literature Review and Future Research Needs. *ASCE,* 421–431. https://doi.org/10.1061/9780784485408.042

Aki, K., & Richards, P. G. (1980). Principles of Seismometry. *Quantitative Seismology, Theory and Methods, Volume 1*.

Alam, M. I., & Jaiswal, P. (2017). Near Surface Characterization Using VP/VS and Poisson's Ratio from Seismic Refractions. *Journal of Environmental and Engineering Geophysics*, *22*(2), 101–109. https://doi.org/10.2113/JEEG22.2.101

Allen, R. V. (1978). Automatic earthquake recognition and timing from single traces. *Bulletin of the Seismological Society of America*, *68*(5), 1521–1532. https://doi.org/10.1785/BSSA0680051521

AMAP, A. C. C. U. (2021). *Key Trends and Impacts. Summary for Policy-Makers, Arctic Monitoring and Assessment Programme (AMAP)* (Vol. 16).

Anhua, X. U. (2014). Analysis of the sensitivity of highway diseases in permafrost regions to ground temperatures and ice contents. *Journal of Glaciology & Geocryology*, *36*(3), 622–625.

Ankamah, A., Hole, J. A., Tourei, A., Chambers, D. J., Martin, E., Beale, J., Ankamah, A., Hole, J. A., Tourei, A., Chambers, D. J., Martin, E., & Beale, J. (2024). Improved Monitoring of Mining-Induced Seismicity in a Longwall Coal Mine Using an Underground Distributed Acoustic Sensing Array. *AGUFM*, *2024*(327), S51D-327. https://ui.adsabs.harvard.edu/abs/2024AGUFMS51D..327A/abstract

Ankamah, A., Hole, J. A., Tourei, A., Martin, E. R., Chambers, D., Beale, J., & Garner, J. (2023). Monitoring Mining-Induced Seismicity and Mine Operations Using an Underground Distributed Acoustic Sensing Array. *AGU*.

ASCE/SEI 7-16: Minimum Design Loads and Associated Criteria for Buildings and Other Structures. (2017). American Society of Civil Engineers. https://doi.org/10.1061/9780784414248

Bai, R., Lai, Y., Zhang, M., & Gao, J. (2018). Water-vapor-heat behavior in a freezing unsaturated coarse-grained soil with a closed top. *Cold Regions Science and Technology*, *155*, 120–126.

Barosh, P. J. (2000). Frostquakes in New England. *Engineering Geology*, *56*(3–4), 389–394. https://doi.org/10.1016/S0013-7952(99)00092-7

Bensen, G. D., Ritzwoller, M. H., Barmin, M. P., Levshin, A. L., Lin, F., Moschetti, M. P., Shapiro, N. M., & Yang, Y. (2007). Processing seismic ambient noise data to obtain reliable broad-band surface wave dispersion measurements. *Geophysical Journal International*, *169*(3), 1239–1260. https://doi.org/10.1111/j.1365-246X.2007.03374.x

Bergen, K. J., Johnson, P. A., De Hoop, M. V., & Beroza, G. C. (2019). Machine learning for data-driven discovery in solid Earth geoscience. *Science*, *363*(6433). https://doi.org/10.1126/SCIENCE.AAU0323

Bery, A. A., & Bery, A. A. (2013). High Resolution in Seismic Refraction Tomography for Environmental Study. *International Journal of Geosciences*, *4*(4), 792–796. https://doi.org/10.4236/IJG.2013.44073

Beskardes, G. D., Hole, J. A., Wang, K., Michaelides, M., Wu, Q., Chapman, M. C., Davenport, K. K., Brown, L. D., & Quiros, D. A. (2018). A comparison of earthquake backprojection imaging methods for dense local arrays. *Geophysical Journal International*, *212*(3), 1986–2002. https://doi.org/10.1093/GJI/GGX520

Bhatele, A., Mohror, K., Langer, S. H., & Isaacs, K. E. (2013). There goes the neighborhood: Performance degradation due to nearby jobs. *International Conference for High Performance Computing, Networking, Storage and Analysis, SC*. https://doi.org/10.1145/2503210.2503247;ISSUE:ISSUE:DOI

Bhattiprolu, S. (2023). Python for Microscopists. In *GitHub Repository*. https://github.com/bnsreenu/python_for_microscopists/blob/master/260_image_anomaly_detection_using_autoencoders/260_image_anomaly_detection_using_autoencoders.py.

Binder, G., & Chakraborty, D. (2019). Detecting microseismic events in downhole distributed acoustic sensing data using convolutional neural networks. *SEG Technical Program Expanded Abstracts*, 4864–4868. https://doi.org/10.1190/SEGAM2019-3214863.1

Birnie, C., & Hansteen, F. (2022). Bidirectional recurrent neural networks for seismic event detection. *Geophysics*, *87*(3). https://doi.org/10.1190/geo2020-0806.1

Bishop, C. M. (2006). Pattern Recognition and Machine Learning. In *Pattern Recognition and Machine Learning*. Springer New York. https://doi.org/10.1007/978-0-387-45528-0

Biskaborn, B. K., Smith, S. L., Noetzli, J., Matthes, H., Vieira, G., Streletskiy, D. A., Schoeneich, P., Romanovsky, V. E., Lewkowicz, A. G., Abramov, A., Allard, M., Boike, J., Cable, W. L., Christiansen, H. H., Delaloye, R., Diekmann, B., Drozdov, D., Etzelmüller, B., Grosse, G., … Lantuit, H. (2019). Permafrost is warming at a global scale. *Nature Communications*, *10*(1), 1–11. https://doi.org/10.1038/S41467-018-08240-4;TECHMETA

Bohlen, T. (2002). Parallel 3-D Viscoelastic Finite-Difference Seismic Modelling. *Computers & Geosciences*, *28*(8), 887–899.

Boiero, D., & Socco, L. V. (2011). The meaning of surface wave dispersion curves in weakly laterally varying structures. *Near Surface Geophysics*, *9*, 561–570. https://doi.org/10.3997/1873-0604.2011042

Braga, M. A., & Gama, M. F. (2024). Advancements in geophysical monitoring of tailings dams: Integrating geophysical methods with geotechnical instrumentation for improved safety and environmental management. *Global Meeting Abstracts*, 7–10. https://doi.org/10.1190/GEM2024-003.1

Brothers, L. L., Herman, B. M., Hart, P. E., & Ruppel, C. D. (2016). Subsea ice-bearing permafrost on the US Beaufort Margin: 1. Minimum seaward extent defined from multichannel seismic reflection data. *Geochemistry, Geophysics, Geosystems*, *17*(11), 4354–4365.

Brown, J. (1969). *Ionic Concentration Gradients in Permafrost Barrow, Alaska, Cold Regions Research and Engineering Laboratory, Corps of Engineers*. US Army.

Brown, J., Miller, P. C., Tiezen, L. L., & Bunnell, F. L. (1981). *An Arctic ecosystem: The Coastal Tundra at Barrow, Alaska*. Van Nostrand Reinhold Co. Inc., New York, NY.

Bryant, M. B., Borsa, A. A., Anderson, E. J., Masteller, C. C., Michaelides, R. J., Siegfried, M. R., & Young, A. P. (2025). Multiple modes of shoreline change along the Alaskan Beaufort Sea observed using ICESat-2 altimetry and satellite imagery. *Cryosphere*, *19*(5), 1825–1847. https://doi.org/10.5194/TC-19-1825-2025

Carr, B. J., Hajnal, Z., & Prugger, A. (1998). Shear-wave studies in glacial till. 1273–1284. *GEOPHYSICS*, *63*(4), 1273–1284. https://doi.org/10.1190/1.1444429

Castongia, E., Wang, H. F., Lord, N., Fratta, D., Mondanos, M., & Chalari, A. (2017). An Experimental Investigation of Distributed Acoustic Sensing (DAS) on Lake Ice. *Journal of Environmental and Engineering Geophysics*, *22*(2), 167–176. https://doi.org/10.2113/JEEG22.2.167

Chambers, D., Ankamah, A., Tourei, A., Martin, E. R., Dean, T., Shragge, J., Hole, J. A., Czarny, R., Goldswain, G., du Toit, J., Boltz, M. S., & McGuiness, J. (2025). Distributed acoustic sensing (DAS) for longwall coal mines. *International Journal of Rock Mechanics and Mining Sciences*, *189*, 106090. https://doi.org/10.1016/J.IJRMMS.2025.106090

Chambers, D., Jin, G., Tourei, A., Issah, A. H. S., Lellouch, A., Martin, E. R., Zhu, D., Girard, A. J., Yuan, S., Cullison, T., Snyder, T., Kim, S., Danes, N., Punithan, N., Boltz, M. S., & Mendoza, M. M. (2024). DASCore: a Python Library for Distributed Fiber Optic Sensing. *Seismica*, *3*(2), 10.26443/seismica.v3i2.1184. https://doi.org/10.26443/SEISMICA.V3I2.1184

Chambers, D., & Shragge, J. (2023). Seismoacoustic Monitoring of a Longwall Face Using Distributed Acoustic Sensing. *Bulletin of the Seismological Society of America*, *113*(4), 1652–1663. https://doi.org/10.1785/0120220219

Chen, J., Vissinga, M., Shen, Y., Hu, S., Beal, E., & Newlin, J. (2021). Machine Learning–Based Digital Integration of Geotechnical and Ultrahigh–Frequency Geophysical Data for Offshore Site Characterizations. *Journal of Geotechnical and Geoenvironmental Engineering*, *147*(12), 04021160. https://doi.org/10.1061/(ASCE)GT.1943-5606.0002702

Chen, J., Wu, Y., O'Connor, M., Cardenas, M. B., Schaefer, K., Michaelides, R., & Kling, G. (2020). Active layer freeze-thaw and water storage dynamics in permafrost environments inferred from InSAR. *Remote Sensing of Environment*, *248*, 112007. https://doi.org/10.1016/J.RSE.2020.112007

Chen, S. X. (2000). Probability density function estimation using gamma kernels. *Annals of the Institute of Statistical Mathematics*, *52*(3). https://doi.org/10.1023/A:1004165218295

Chen, Y. C. (2017). A tutorial on kernel density estimation and recent advances. *Biostatistics and Epidemiology*, *1*(1). https://doi.org/10.1080/24709360.2017.1396742

Cheng, F., Lindsey, N. J., Sobolevskaia, V., Dou, S., Freifeld, B., Wood, T., James, S. R., Wagner, A. M., & Ajo-Franklin, J. B. (2022). Watching the Cryosphere Thaw: Seismic Monitoring of Permafrost Degradation Using Distributed Acoustic Sensing During a Controlled Heating Experiment. *Geophysical Research Letters*, *49*(10), e2021GL097195. https://doi.org/10.1029/2021GL097195

Cheng, T., Cox, B. R., Vantassel, J. P., & Manuel, L. (2020). A statistical approach to account for azimuthal variability in single-station HVSR measurements. *Geophysical Journal International*, *223*(2), 1040–1053. https://doi.org/10.1093/GJI/GGAA342

Chien, C. C., Jenkins, W. F., Gerstoft, P., Zumberge, M., & Mellors, R. (2023). Automatic classification with an autoencoder of seismic signals on a distributed acoustic sensing cable. *Computers and Geotechnics*, *155*, 105223. https://doi.org/10.1016/J.COMPGEO.2022.105223

Colombero, C., Di Toro, L., Khosro Anjom, F., Godio, A., & Morra Di Cella, U. (2025). Ambient Seismic Noise and Microseismicity Monitoring of Periglacial Bodies: A Case Study on the Gran Sometta Rock Glacier (NW Italian Alps). *Permafrost and Periglacial Processes*, *36*(3), 580–595. https://doi.org/10.1002/PPP.2286;SUBPAGE:STRING:FULL

Cox, B. R., Wood, C. M., & Hazirbaba, K. (2012). Frozen and unfrozen shear wave velocity seismic site classification of Fairbanks, Alaska. *Journal of Cold Regions Engineering*, *26*(3), 118–145.

Currie, J. A. (1983). Gas diffusion through soil crumbs: the effects of wetting and swelling. *Journal of Soil Science*, *34*(2), 217–232.

Dafflon, B., Hubbard, S., Ulrich, C., Peterson, J., Wu, Y., Wainwright, H., & Kneafsey, T. J. (2016). Geophysical estimation of shallow permafrost distribution and properties in an ice-wedge polygon-dominated Arctic tundra region. *Geophysics*, *81*(1), 247 – 263.

Dafflon, B., Oktem, R., Peterson, J., Ulrich, C., Tran, A. P., Romanovsky, V., & Hubbard, S. S. (2017). Coincident aboveground and belowground autonomous monitoring to quantify covariability in permafrost, soil, and vegetation properties in Arctic tundra. *Journal of Geophysical Research: Biogeosciences*, *122*(6), 1321–1342.

Daily, W., Ramirez, A., Binley, A., & Labrecque, D. (2000). Electrical resistance tomography—theory and practice. In *Near-surface Geophysics* (pp. 525–550). Society of Exploration Geophysicists. https://doi.org/10.1190/1.9781560801719.ch17

Daily, W., Ramirez, A., Binley, A., & LaBrecque, D. (2005). 17. Electrical Resistance Tomography—Theory and Practice. *Investigations in Geophysics Series*, 525–550. https://doi.org/10.1190/1.9781560801719.CH17

Dal Moro, G., Pipan, M., Forte, E., & Finetti, I. (2003). Determination of rayleigh wave dispersion curves for near surface applications in unconsolidated sediments. *SEG Technical Program Expanded Abstracts*, *22*(1), 1247–1250. https://doi.org/10.1190/1.1817508

Donald P. Coduto. (1999). Geotechnical Engineering Principles and practices. In *Prentice-Hall,Inc*.

Dou, S. (2015). *Field and Laboratory Investigations on Seismic Properties of Unconsolidated Saline Permafrost*. University of California, Berkeley.

Dou, S., Ajo Franklin, J. B., & Dreger, D. S. (2012). Mapping Deep Low Velocity Zones in Alaskan Arctic Coastal Permafrost using Seismic Surface Waves. *AGU Fall Meeting Abstracts*, *2012*, 22 – 07.

Dou, S., & Ajo-Franklin, J. B. (2014). Full-wavefield inversion of surface waves for mapping embedded low-velocity zones in permafrost. *Geophysics*, *79*(6), EN107–EN124. https://doi.org/10.1190/geo2013-0427.1

Dou, S., Lindsey, N., Wagner, A. M., Daley, T. M., Freifeld, B., Robertson, M., Peterson, J., Ulrich, C., Martin, E. R., & Ajo-Franklin, J. B. (2017). Distributed Acoustic Sensing for Seismic Monitoring of the Near Surface: A Traffic-Noise Interferometry Case Study. *Scientific Reports*, *7*(1), 1–12. https://doi.org/10.1038/s41598-017-11986-4

Ekimova, V., Nelson, M. A., Sullivan, T., Douglas, T. A., Epstein, H. E., & Jull, M. G. (2025). *Characterizing Near-Surface Permafrost in Utqiaġvik, Alaska, using Electrical Resistivity Tomography and Ground Penetrating Radar*. https://doi.org/10.5194/EGUSPHERE-2025-4702

Elkateb, T., Chalaturnyk, R., & Robertson, P. K. (2011). An overview of soil heterogeneity: quantification and implications on geotechnical field problems. *Https://Doi.Org/10.1139/T02-090*, *40*(1), 1–15. https://doi.org/10.1139/T02-090

Essien, U. E., Akankpo, A. O., & Igboekwe, M. U. (2014). Poisson's Ratio of Surface Soils and Shallow Sediments Determined from Seismic Compressional and Shear Wave Velocities. *International Journal of Geosciences*, *5*(12), 1540–1546. https://doi.org/10.4236/IJG.2014.512125

Etzelmüller, B., Guglielmin, M., Hauck, C., Hilbich, C., Hoelzle, M., Isaksen, K., & Ramos, M. (2020). Twenty years of European mountain permafrost dynamics—the PACE legacy. *Environmental Research Letters*, *15*(10), 104070.

Evangelista, L., & Magistris, F. (2015). Some Limits in the Use of the MASW Technique in Soils with Inclined Layers. *Geotech Geol Eng*, *33*, 701–711. https://doi.org/10.1007/s10706-015-9852-1

Evangelista, L., & Santucci de Magistris, F. (2015). Some Limits in the Use of the MASW Technique in Soils with Inclined Layers. *Geotechnical and Geological Engineering*, *33*(3), 701–711. https://doi.org/10.1007/S10706-015-9852-1/FIGURES/11

Fang, J., Yang, Y., Shen, Z., Biondi, E., Wang, X., Williams, E. F., Becker, M. W., Eslamian, D., Zhan, Z., Yang, Y., Shen, Z., Biondi, E., Wang, X., Williams, E. F., Becker, M. W., Eslamian, D., & Zhan, Z. (2023). Directional Sensitivity of DAS and Its Effect on Rayleigh-Wave Tomography: A Case Study in Oxnard, California. *Seismological Research Letters*, *94*(2A), 887–897. https://doi.org/10.1785/0220220235

Farouki, O. T. (1981). The thermal properties of soils in cold regions. *Cold Regions Science and Technology*, *5*(1), 67–75.

Farquharson, L. M., Romanovsky, V. E., Cable, W. L., Walker, D. A., Kokelj, S. V, & Nicolsky, D. (2019). Climate change drives widespread and rapid thermokarst development in very cold permafrost in the Canadian High Arctic. *Geophysical Research Letters*, *46*(12), 6681–6689.

Farzamian, M., Blanchy, G., McLachlan, P., Vieira, G., Esteves, M., de Pablo, M. A., Triantifilis, J., Lippmann, E., & Hauck, C. (2024). Advancing Permafrost Monitoring With Autonomous Electrical Resistivity Tomography (A-ERT): Low-Cost Instrumentation and Open-Source Data Processing Tool. *Geophysical Research Letters*, *51*(6), e2023GL105770. https://doi.org/10.1029/2023GL105770;CTYPE:STRING:JOURNAL

Ferdinand, P. (2014). *The Evolution of Optical Fiber Sensors Technologies During the 35 Last Years and Their Applications in Structure Health Monitoring*. 914–929. https://doi.org/10.34894/VQ1DJA

Ferrians Jr., O. J. (1965). *Permafrost map of Alaska* (Issue 445)).

Fichtner, A., Walter, F., Brisbourne, A., Booth, A., Kendall, J.-M., Hudson, T., Paitz, P., & Lipovsky, B. (2025). Fibre-optic exploration of the cryosphere. *EarthArXiv Prepreint*. https://doi.org/10.31223/X5T73D

Fisher, D. A., Lacelle, D., & Pollard, W. (2020). A model of unfrozen water content and its transport in icy permafrost soils: Effects on ground ice content and permafrost stability. *Permafrost and Periglacial Processes*, *31*(1), 184–199.

Fortin, J., Guéguen, Y., & Schubnel, A. (2007). Effects of pore collapse and grain crushing on ultrasonic velocities and Vp/Vs. *Journal of Geophysical Research: Solid Earth*, *112*(B8), 8207. https://doi.org/10.1029/2005JB004005

Foti, S., Comina, C., Boiero, D., & Socco, L. V. (2009). Non-uniqueness in surface-wave inversion and consequences on seismic site response analyses. *Soil Dynamics and Earthquake Engineering*, *29*(6), 982–993. https://doi.org/10.1016/J.SOILDYN.2008.11.004

Foti, S., Hollender, F., Garofalo, F., Albarello, D., Asten, M., Bard, P. Y., Comina, C., Cornou, C., Cox, B., Di Giulio, G., Forbriger, T., Hayashi, K., Lunedei, E., Martin, A., Mercerat, D., Ohrnberger, M., Poggi, V., Renalier, F., Sicilia, D., & Socco, V. (2018). Guidelines for the good practice of surface wave analysis: a product of the InterPACIFIC project. *Bulletin of Earthquake Engineering*, *16*(6), 2367–2420. https://doi.org/10.1007/S10518-017-0206-7/FIGURES/34

Gemeinhardt, H., & Sharma, J. (2024). Machine-Learning-Assisted Leak Detection Using Distributed Temperature and Acoustic Sensors. *IEEE Sensors Journal*, *24*(2), 1520–1531. https://doi.org/10.1109/JSEN.2023.3337284

Gibbons, S. J., & Ringdal, F. (2006). The detection of low magnitude seismic events using array-based waveform correlation. *Geophysical Journal International*, *165*(1), 149–166. https://doi.org/10.1111/J.1365-246X.2006.02865.X

Glazer, M., Dobiński, W., Marciniak, A., Majdański, M., & Błaszczyk, M. (2020). Spatial distribution and controls of permafrost development in non-glacial Arctic catchment over the Holocene, Fuglebekken, SW Spitsbergen. *Geomorphology*, *358*, 107128.

Gribler, G., Liberty, L. M., Mikesell, T. D., & Michaels, P. (2016). Isolating retrograde and prograde Rayleigh-wave modes using a polarity mute. *Https://Doi.Org/10.1190/Geo2015-0683.1*, *81*(5), V379–V385. https://doi.org/10.1190/GEO2015-0683.1

Grussing, M. N. (2013). Life Cycle Asset Management Methodologies for Buildings. *Journal of Infrastructure Systems*, *20*(1), 04013007. https://doi.org/10.1061/(ASCE)IS.1943-555X.0000157

Guthrie, W. S., Hermansson, Å., & Woffinden, K. H. (2006). Saturation of granular base material due to water vapor flow during freezing: laboratory experimentation and numerical modeling. In *Current Practices in Cold Regions Engineering(pp* (pp. 1–12).

Hallissey, M. (2025). *Development of Electromagnetic Geophysical Surveys for Permafrost using Unmanned Aerial System*. The Pennsylvania State University.

Harmon, N., Rychert, C. A., Davis, J., Brambilla, G., Buffet, W., Chichester, B., Dai, Y., Bogiatzis, P., Snook, J., van Putten, L., & Masoudi, A. (2022). Surface deployment of DAS systems: Coupling strategies and comparisons to geophone data. *Near Surface Geophysics*, *20*(5), 465–477. https://doi.org/10.1002/NSG.12232

Harris, C., & Cook, J. D. (1986). The detection of high altitude permafrost in Jotunheimen, Norway using seismic refraction techniques: an assessment. *Arctic and Alpine Research*, *18*(1), 19–26.

Hartog, A. H. (2017). An introduction to distributed optical fibre sensors. *An Introduction to Distributed Optical Fibre Sensors*, 1–440. https://doi.org/10.1201/9781315119014/INTRODUCTION-DISTRIBUTED-OPTICAL-FIBRE-SENSORS-ARTHUR-HARTOG/RIGHTS-AND-PERMISSIONS

Hayashi, K., & Suzuki, H. (2004). CMP cross-correlation analysis of multichannel surface-wave data. *Exploration Geophysics*, *35*.

Hazirbaba, K., Zhang, Y., & Hulsey, J. L. (2011). Evaluation of temperature and freeze–thaw effects on excess pore pressure generation of fine-grained soils. *Soil Dynamics and Earthquake Engineering*, *31*(3), 372–384.

Herring, T., Lewkowicz, A. G., Hauck, C., Hilbich, C., Mollaret, C., Oldenborger, G. A., Uhlemann, S., Farzamian, M., Calmels, F., & Scandroglio, R. (2023). Best practices for using electrical resistivity tomography to investigate permafrost. *Permafrost and Periglacial Processes*, *34*(4), 494–512. https://doi.org/10.1002/PPP.2207

Hjort, J., Streletskiy, D., Doré, G., Wu, Q., Bjella, K., & Luoto, M. (2022). Impacts of permafrost degradation on infrastructure. *Nature Reviews Earth & Environment*, *3*(1), 24–38.

Huang, L., Li, J., Hao, H., & Li, X. (2018). Micro-seismic event detection and location in underground mines by using Convolutional Neural Networks (CNN) and deep learning. *Tunnelling and Underground Space Technology*, *81*. https://doi.org/10.1016/j.tust.2018.07.006

Hubbard, S. S., Gangodagamage, C., Dafflon, B., Wainwright, H., Peterson, J., Gusmeroli, A., & Ulrich, C. (2013). Quantifying and relating land-surface and subsurface variability in permafrost environments using LiDAR and surface geophysical datasets. *Hydrogeology Journal*, *21*, 149–169. https://doi.org/10.1007/s10040-012-0939-y

Ikeda, A. (2006). Combination of conventional geophysical methods for sounding the composition of rock glaciers in the Swiss Alps. *Permafrost and Periglacial Processes*, *17*(1), 35–48.

I.P.C.C. (2021). *Climate Change 2021: The Physical Science Basis, Contribution of Working Group I to the Sixth Assessment Report of the Intergovernmental Panel on Climate Change*. Cambridge University Press.

Jafarov, E., Parsekian, A., Schaefer, K., Liu, L., Chen, A., Panda, S. K., & Zhang, T. (2018). *Pre-ABoVE: Active Layer Thickness and Soil Water Content*. ORNL DAAC.

Ji, X. (2025). *Understanding Seasonal Variations of In-Situ Thermal and Seismic Characteristics of Degrading Permafrost in The Arctic Based on Distributed Fiber Optic Sensing*. The Pennsylvania State University.

Ji, X., Xiao, M., Martin, E. R., & Zhu, T. (2024). Statistical Evaluation of Seismic Velocity Models of Permafrost. *Journal of Cold Regions Engineering*, *38*(3), 04024021. https://doi.org/10.1061/JCRGEI.CRENG-760

Jiang, J., Ren, H., & Zhang, M. (2022). A Convolutional Autoencoder Method for Simultaneous Seismic Data Reconstruction and Denoising. *IEEE Geoscience and Remote Sensing Letters*, *19*. https://doi.org/10.1109/LGRS.2021.3073560

Jordan, T. H., Chen, Y. T., Gasparini, P., Madariaga, R., Main, I., Marzocchi, W., Papadopoulos, G., Sobolev, G., Yamaoka, K., & Zschau, J. (2011). OPERATIONAL EARTHQUAKE FORECASTING. State of Knowledge and Guidelines for Utilization. *Annals of Geophysics*, *54*(4), 319–391. https://doi.org/10.4401/ag-5350

Jorgenson, M. T., Yoshikawa, K., Kanevskiy, M., Shur, Y., Romanovsky, V., Marchenko, S., & Jones, B. (2008). Permafrost characteristics of Alaska. *Proceedings of the ninth international conference on permafrost*, *3*, 121–122.

Justice, J. H., & Zuba, C. (1986). Transition zone reflections and permafrost analysis. *Geophysics*, *51*(5), 1075–1086.

Kanevskiy, M., Shur, Y., Jorgenson, M. T., Ping, C. L., Michaelson, G. J., Fortier, D., & Tumskoy, V. (2013). Ground ice in the upper permafrost of the Beaufort Sea coast of Alaska. *Cold Regions Science and Technology*, *85*, 56–70.

Kartoziia, A. (2019). Assessment of the ice wedge polygon current state by means of UAV imagery analysis (Samoylov Island, the Lena Delta. *Remote Sensing*, *11*(13), 1627. https://doi.org/10.3390/rs11131627

Kerkering, J. (2008). *Mapping past and future permafrost extent on the North Slope Borough*.

Kneisel, C., Hauck, C., Fortier, R., & Moorman, B. (2008). Advances in geophysical methods for permafrost investigations. *Permafrost and Periglacial Processes*, *19*(2), 157–178. https://doi.org/10.1002/PPP.616

Kohnen, H. (1974). The temperature dependence of seismic waves in ice. *Journal of Glaciology*, *13*(67), 144–147.

Koven, C. D., Ringeval, B., Friedlingstein, P., Ciais, P., Cadule, P., Khvorostyanov, D., Krinner, G., & Tarnocai, C. (2011). Permafrost carbon-climate feedbacks accelerate global warming. *Proceedings of the National Academy of Sciences*, *108*(36), 14769–14774. https://doi.org/10.1073/PNAS.1103910108

Koyan, P., Tronicke, J., Guillemoteau, J., & Overduin, P. P. (2025). The Potential of 3D GPR for Imaging and Characterizing Permafrost Regions. *13th International Workshop on Advanced Ground Penetrating Radar, IWAGPR 2025 - Proceedings*. https://doi.org/10.1109/IWAGPR65621.2025.11109025

Kurfurst, P. J. (1976). Ultrasonic wave measurements on frozen soils at permafrost temperatures. *Canadian Journal of Earth Sciences*, *13*(11), 1571–1576. https://doi.org/10.1139/e76-163

Lachenbruch, A. H. (1962). *Mechanics of thermal contraction cracks and ice-wedge polygons in permafrost*. 69.

Larivière, V., Pontille, D., & Sugimoto, C.R. (2021). Investigating the division of scientific labor using the contributor roles taxonomy (CRediT). *Quant. Sci. Stud.*, 2(1):111-128. https://credit.niso.org/

Langer, M., Deimling, T. S., Westermann, S., Rolph, R., Rutte, R., Antonova, S., & Grosse, G. (2023). Thawing permafrost poses environmental threat to thousands of sites with legacy industrial contamination. *Nature Communications*, *14*(1), 1721. https://doi.org/10.1038/s41467-023-37276-4

Lantuit, H., Overduin, P. P., Couture, N., Wetterich, S., Aré, F., Atkinson, D., Brown, J., Cherkashov, G., Drozdov, D., Donald Forbes, L., Graves-Gaylord, A., Grigoriev, M., Hubberten, H. W., Jordan, J., Jorgenson, T., Ødegård, R. S., Ogorodov, S., Pollard, W. H., Rachold, V., … Vasiliev, A. (2012). The Arctic Coastal Dynamics Database: A New Classification Scheme and Statistics on Arctic

Permafrost Coastlines. *Estuaries and Coasts*, *35*(2), 383–400. https://doi.org/10.1007/S12237-010-9362-6

Lara, M. J., McGuire, A. D., Euskirchen, E. S., Tweedie, C. E., Hinkel, K. M., Skurikhin, A. N., & Genet, H. (2015). Polygonal tundra geomorphological change in response to warming alters future CO 2 and CH 4 flux on the Barrow Peninsula. *Global Change Biology*, *21*(4), 1634–1651.

Lehujeur, M., Chevrot, S., Villaseñor, A., Masini, E., Saspiturry, N., Lescoutre, R., & Sylvander, M. (2021). Three-dimensional shear velocity structure of the Mauléon and Arzacq Basins (Western Pyrenees). *Bulletin de La Société Géologique de France*, *192*(1), 47. https://doi.org/10.1051/BSGF/2021039

Letson, F., Barthelmie, R. J., Hu, W., Brown, L. D., & Pryor, S. C. (2019). Wind gust quantification using seismic measurements. *Natural Hazards*, *99*(1), 355–377. https://doi.org/10.1007/S11069-019-03744-8/FIGURES/11

Li, Z., & Zhan, Z. (2018). Pushing the limit of earthquake detection with distributed acoustic sensing and template matching: a case study at the Brady geothermal field. *Geophysical Journal International*, *215*(3), 1583–1593. https://doi.org/10.1093/GJI/GGY359

Liew, M., Ji, X., Xiao, M., Farquharson, L., Nicolsky, D., Romanovsky, V., & McComb, C. (2022). Synthesis of physical processes of permafrost degradation and geophysical and geomechanical properties of permafrost. *Cold Regions Science and Technology*, *198*, 103522.

Liew, M., Xiao, M., Farquharson, L., Nicolsky, D., Jensen, A., Romanovsky, V., Peirce, J., Alessa, L., McComb, C., Zhang, X., & Jones, B. (2022). Understanding Effects of Permafrost Degradation and Coastal Erosion on Civil Infrastructure in Arctic Coastal Villages: A Community Survey and Knowledge Co-Production. *Journal of Marine Science and Engineering*, *10*(3), 422. https://doi.org/10.3390/JMSE10030422/S1

Lindsey, E., Lindsey, N. J., & Martin, E. R. (2021). *Fiber-Optic Seismology*. 309–336.

Liu, H., Maghoul, P., & Shalaby, A. (2020). Intelligent MASW. *Zenodo.* https://doi.org/10.5281/ZENODO.3776875

Liu, H., Maghoul, P., & Shalaby, A. (2021a). *Seismic physics-based characterization of permafrost sites using surface waves*. *August*, 1–38.

Liu, H., Maghoul, P., & Shalaby, A. (2021b). *Seismic physics-based characterization of permafrost sites using surface waves. Cryosphere Discussions*.

Liu, L., Zhang, T., & Wahr, J. (2010). InSAR measurements of surface deformation over permafrost on the North Slope of Alaska. *Journal of Geophysical Research: Earth Surface*, *115*(F3), 3023. https://doi.org/10.1029/2009JF001547

Loke, M. H., & Barker, R. D. (1996). Rapid least-squares inversion of apparent resistivity pseudosections by a quasi-Newton method. *Geophysical Prospect*, *44*, 131–152.

Loktev, A., Bondarev, V., Kulikov, S., & Rokos, S. (2012). Russian arctic offshore permafrost. *SUT Offshore Site Investigation and Geotechnics.*

Lomax, A., & Snieder, R. (1994). Finding sets of acceptable solutions with a genetic algorithm with application to surface wave group dispersion in Europe. *Geophysical Research Letters*, *21*(24), 2617–2620. https://doi.org/10.1029/94GL02635

Luo, B., Jin, G., & Stanek, F. (2021). Near-field strain in distributed acoustic sensing-based microseismic observation. *Https://Doi.Org/10.1190/Geo2021-0031.1*, *86*(5), P49–P60. https://doi.org/10.1190/GEO2021-0031.1

Luo, X., & Duan, Y. (2021). Microseismic monitoring of longwall caving process using distributed optic fiber sensing. *55th U.S. Rock Mechanics / Geomechanics Symposium 2021*, *2*.

Macquet, M., Paul, A., Pedersen, H. A., Villaseñor, A., Chevrot, S., Sylvander, M., & Wolyniec, D. (2014). Ambient noise tomography of the Pyrenees and the surrounding regions: inversion for a 3-D Vs model in the presence of a very heterogeneous crust. *Geophysical Journal International*, *199*(1), 402–415. https://doi.org/10.1093/GJI/GGU270

Mahmoudian, A., Tajik, N., Taleshi, M. M., Shakiba, M., & Yekrangnia, M. (2023). Ensemble machine learning-based approach with genetic algorithm optimization for predicting bond strength and failure mode in concrete-GFRP mat anchorage interface. *Structures*, *57*. https://doi.org/10.1016/j.istruc.2023.105173

Majdański, M., Dobiński, W., Marciniak, A., Owoc, B., Glazer, M., Osuch, M., & Wawrzyniak, T. (2022). Variations of permafrost under freezing and thawing conditions in the coastal catchment Fuglebekken (Hornsund, Spitsbergen, Svalbard). *Permafrost and Periglacial Processes*, *33*(3), 264–276. https://doi.org/10.1002/ppp.2147

Maraschini, M., & Foti, S. (2010). A Monte Carlo multimodal inversion of surface waves. *Geophysical Journal International*, *182*(3), 1557–1566. https://doi.org/10.1111/J.1365-246X.2010.04703.X

Marciniak, A., Owoc, B., Grzyb, J., Glazer, M., Dobiński, W., & Majdański, M. (2018). Seismic Tomography and MASW analysis of the results of Spitsbergen seismic experiment-case study. *EGU General Assembly Conference Abstracts*, 280.

Marciniak, A., Owoc, B., Wawrzyniak, T., Nawrot, A., Glazer, M., Osuch, M., & Majdański, M. (2019). Near-Surface Geophysical Imaging of the Permafrost—Initial Result of Two High Arctic Expeditions to Spitsbergen. *25th European Meeting of Environmental and Engineering Geophysics (Vol*, *1*, 1–5.

Mark, C. (2016). Coal bursts in the deep longwall mines of the United States. *International Journal of Coal Science and Technology*, *3*(1). https://doi.org/10.1007/s40789-016-0102-9

Mark, C. (2018). Coal bursts that occur during development: A rock mechanics enigma. *International Journal of Mining Science and Technology*, *28*(1). https://doi.org/10.1016/j.ijmst.2017.11.014

Martin, E. R., Lindsey, N. J., Ajo-Franklin, J. B., & Biondi, B. L. (2021). *Introduction to Interferometry of Fiber-Optic Strain Measurements*. 111–129. https://doi.org/10.1002/9781119521808.CH9

Melvin, A. M., Larsen, P., Boehlert, B., Neumann, J. E., Chinowsky, P., Espinet, X., & Marchenko, S. S. (2017). Climate change damages to Alaska public infrastructure and the economics of proactive adaptation. *Proceedings of the National Academy of Sciences*, *114*(2), 122– 131.

Meyer, H., Schirrmeister, L., Andreev, A., Wagner, D., Hubberten, H. W., Yoshikawa, K., Bobrov, A., Wetterich, S., Opel, T., Kandiano, E., & Brown, J. (2010a). Lateglacial and Holocene isotopic and environmental history of northern coastal Alaska – Results from a buried ice-wedge system at Barrow. *Quaternary Science Reviews*, *29*(27–28), 3720–3735. https://doi.org/10.1016/J.QUASCIREV.2010.08.005

Meyer, H., Schirrmeister, L., Andreev, A., Wagner, D., Hubberten, H.-W., Yoshikawa, K., Bobrov, A., Wetterich, S., Opel, T., Kandiano, E., & Brown, J. (2010b). Lateglacial and Holocene isotopic and environmental history of northern coastal Alaska - Results from a buried ice-wedge system at Barrow. *Quaternary Science Reviews*, *29*(27–28), 3720–3735.

Michaelides, R. J., Bryant, M. B., Siegfried, M. R., & Borsa, A. A. (2021). Quantifying Surface-Height Change Over a Periglacial Environment with ICESat-2 Laser Altimetry. *Earth and Space Science*, *8*(8), e2020EA001538. https://doi.org/10.1029/2020EA001538;JOURNAL:JOURNAL:23335084;WGROUP:STRING:PUBLICATION

Miller, R. D., Laflen, D. R., Hunter, J. A., Burns, R. A., Good, R. L., Douma, M., & Carr, B. J. (2000). Imaging permafrost with shallow P-and S-wave reflection. *SEG International Exposition and Annual Meeting*, 2000.

Mordret, A., Landés, M., Shapiro, N. M., Singh, S. C., & Roux, P. (2014). Ambient noise surface wave tomography to determine the shallow shear velocity structure at Valhall: depth inversion with a Neighbourhood Algorithm. *Geophysical Journal International*, *198*(3), 1514–1525. https://doi.org/10.1093/GJI/GGU217

Mousavi, S. M., Zhu, W., Ellsworth, W., & Beroza, G. (2019). Unsupervised Clustering of Seismic Signals Using Deep Convolutional Autoencoders. *IEEE Geoscience and Remote Sensing Letters*, *16*(11). https://doi.org/10.1109/LGRS.2019.2909218

Mousavi, S. M., Zhu, W., Sheng, Y., & Beroza, G. C. (2019). CRED: A Deep Residual Network of Convolutional and Recurrent Units for Earthquake Signal Detection. *Scientific Reports*, *9*(1). https://doi.org/10.1038/s41598-019-45748-1

Munroe, J. S., Doolittle, J. A., Kanevskiy, M. Z., Hinkel, K. M., Nelson, F. E., Jones, B. M., Shur, Y., & Kimble, J. M. (2007). Application of ground-penetrating radar imagery for three-dimensional visualisation of near-surface structures in ice-rich permafrost, Barrow, Alaska. *Permafrost and Periglacial Processes*, *18*(4), 309–321. https://doi.org/10.1002/PPP.594

Nakano, Y., Martin, R. J., & Smith, M. (1972). Ultrasonic velocities of the dilatational and shear waves in frozen soils. *Water Resources Research*, *8*(4), 1024–1030. https://doi.org/10.1029/WR008I004P01024

Neloy, A. A., & Turgeon, M. (2024). A comprehensive study of auto-encoders for anomaly detection: Efficiency and trade-offs. *Machine Learning with Applications*, *17*, 100572. https://doi.org/10.1016/J.MLWA.2024.100572

Nicolsky, D. J., Romanovsky, V. E., Panda, S. K., Marchenko, S. S., & Muskett, R. R. (2017). Applicability of the ecosystem type approach to model permafrost dynamics across the Alaska North Slope. *Journal of Geophysical Research: Earth Surface*, *122*(1), 50–75.

Nicolsky, D. J., Romanovsky, V. E., & Panteleev, G. G. (2009). Estimation of soil thermal properties using in-situ temperature measurements in the active layer and permafrost. *Cold Regions Science and Technology*, *55*(1), 120–129.

Nicolsky, D. J., & Wright, T. (2023). *Understand and forecast long-term variations of in-situ geophysical and geomechanical characteristics of degrading permafrost in the Arctic - continuously observed ground temperatures, 2021-2022. [Dataset]*. Arctic Data Center. https://doi.org/10.18739/A2C53F305

Nitzbon, J., Langer, M., Westermann, S., Martin, L., Aas, K. S., & Boike, J. (2019). Pathways of ice-wedge degradation in polygonal tundra under different hydrological conditions. *The Cryosphere*, *13*(4), 1089–1123.

Niu, F., Li, A., Luo, J., Lin, Z., Yin, G., Liu, M., & Liu, H. (2017). Soil moisture, ground temperatures, and deformation of a high-speed railway embankment in Northeast China. *Cold Regions Science and Technology*, *133*, 7–14.

Okkonen, J., Neupauer, R. M., Kozlovskaya, E., Afonin, N., Moisio, K., Taewook, K., & Muurinen, E. (2020). Frost Quakes: Crack Formation by Thermal Stress. *Journal of Geophysical Research: Earth Surface*, *125*(9), e2020JF005616. https://doi.org/10.1029/2020JF005616

Olafsdottir, E. A., Bessason, B., Erlingsson, S., Kaynia, A. M., Olafsdottir, E. A., Bessason, B., Erlingsson, S., & Kaynia, A. M. (2024). A Tool for Processing and Inversion of MASW Data and a Study of Inter-session Variability of MASW. *Geotechnical Testing Journal*, *47*(5), 1006–1025. https://doi.org/10.1520/GTJ20230380

Olafsdottir, E. A., Erlingsson, S., & Bessason, B. (2020). Open-Source MASW Inversion Tool Aimed at Shear Wave Velocity Profiling for Soil Site Explorations. *Geosciences 2020, Vol. 10, Page 322*, *10*(8), 322. https://doi.org/10.3390/GEOSCIENCES10080322

Olayanju, G. M., Mogaji, K. A., Lim, H. S., & Ojo, T. S. (2017). Foundation integrity assessment using integrated geophysical and geotechnical techniques: case study in crystalline basement complex, southwestern Nigeria. *Journal of Geophysics and Engineering*, *14*(3), 675–690. https://doi.org/10.1088/1742-2140/AA64F7

Oldenborger, G. A., & LeBlanc, A. M. (2018). Monitoring changes in unfrozen water content with electrical resistivity surveys in cold continuous permafrost. *Geophysical Journal International*, *215*(2), 965–977. https://doi.org/10.1093/GJI/GGY321

O'Sullivan, J. B. (1966). Geochemistry of permafrost, Barrow, Alaska. *Permafrost International Conference*, *117*, 30–37.

Osterkamp, T. E. (2003). A thermal history of permafrost in Alaska. *Proceedings of the 8th International Conference on Permafrost.* Retrieved October 5, 2025, from https://www.researchgate.net/profile/Tom-Osterkamp/publication/312600841_A_thermal_history_of_permafrost_in_Alaska/links/64b36e60b9ed6874a521b7d5/A-thermal-history-of-permafrost-in-Alaska

Overduin, P. P., Westermann, S., Yoshikawa, K., Haberlau, T., Romanovsky, V., & Wetterich, S. (2012). Geoelectric observations of the degradation of nearshore submarine permafrost at Barrow (Alaskan Beaufort Sea). *Journal of Geophysical Research: Earth Surface*, *117*(F2), 2004. https://doi.org/10.1029/2011JF002088

Park, C. B. (2011). Imaging dispersion of MASW data - Full vs. Selective offset scheme. *Journal of Environmental and Engineering Geophysics*, *16*(1). https://doi.org/10.2113/JEEG16.1.13

Park, C. B., Miller, R. D., & Xia, J. (1998). Imaging dispersion curves of surface waves on multi-channel record. *SEG Technical Program Expanded Abstracts*. https://doi.org/10.1190/1.1820161

Park, C. B., Miller, R. D., & Xia, J. (1999a). Multichannel analysis of surface waves. *Geophysics*, *64*(3), 800–808. https://doi.org/10.1190/1.1444590

Park, C. B., Miller, R. D., & Xia, J. (1999b). Multimodal Analysis of High Frequency Surface Waves. In *Symposium on the Application of Geophysics to Engineering and Environmental Problems 1999* (pp.

115–121). Environment and Engineering Geophysical Society. https://doi.org/doi:10.4133/1.2922596

Pedersen, H. B., Heiselberg, P., Heiselberg, H., Simonsen, A., & Sørensen, K. A. (2025). A Feasibility Study of Automated Detection and Classification of Signals in Distributed Acoustic Sensing. *Sensors (Basel, Switzerland)*, *25*(17), 5445. https://doi.org/10.3390/S25175445

Peng, P., He, Z., Wang, L., & Jiang, Y. (2020). Automatic classification of microseismic records in underground mining: A deep learning approach. *IEEE Access*, *8*. https://doi.org/10.1109/ACCESS.2020.2967121

Peng, S. S. (2019). Longwall Mining, 3rd Edition. In *Longwall Mining*. CRC Press. https://doi.org/10.1201/9780429260049

Pfaffhuber, A. A., Bazin, S., & Frauenfelder, R. (2020). Near-surface methods in the geotechnical industry: Challenges, opportunities and limitations. *Global Meeting Abstracts*, 20–23. https://doi.org/10.1190/ICEG2019-005.1

Agostinetti, N. P., Villa, A., & Saccorotti, G. (2022). Distributed acoustic sensing as a tool for subsurface mapping and seismic event monitoring: A proof of concept. *Solid Earth*, *13*(2), 449–468. https://doi.org/10.5194/SE-13-449-2022

Picotti, S., Vuan, A., Carcione, J. M., Horgan, H. J., & Anandakrishnan, S. (2015). Anisotropy and crystalline fabric of Whillans Ice Stream (West Antarctica) inferred from multicomponent seismic data. *Journal of Geophysical Research: Solid Earth*, *120*(6), 4237–4262.

Piolat, L., Geraud, Y., Revil, A., Diraison, M., Favier, A., & Cosme, P. (2024). *Quantifying Geophysical Electrical Signatures in Hydrothermal Reservoirs*. *2024*(1), 1–5. https://doi.org/10.3997/2214-4609.202421134

Quinn, M. C. L., Wagner, A. M., Engel, C. S., Winters, K. E., Coclin, C. G., & Picucci, J. R. (2024). *Distributed Fiber Optic Sensing in Cold Regions*. 536–544. https://doi.org/10.1061/9780784485330.054

Ramachandran, K., Bellefleur, G., Brent, T., Riedel, M., & Dallimore, S. (2011). Imaging permafrost velocity structure using high resolution 3D seismic tomography. *Geophysics*, *76*(5), 187 – 198.

Rantanen, M., Karpechko, A. Y., Lipponen, A., Nordling, K., Hyvärinen, O., Ruosteenoja, K., Vihma, T., & Laaksonen, A. (2022). The Arctic has warmed nearly four times faster than the globe since 1979. *Communications Earth & Environment*, *3*(1), 1–10.

Res2Dinv Manual. (2006). *Geoelectrical Imaging 2D and 3D*. [Software]. Geotomo SoftwareTM.

Rocha dos Santos, G., & Zhu, T. (2025). Seismic Tremors From Sea-Landfast Ice Interactions Near Utqiaġvik, Alaska. *Geophysical Research Letters*, *52*(15), e2025GL117458. https://doi.org/10.1029/2025GL117458

Rodríguez Tribaldos, V., & Ajo-Franklin, J. B. (2021). Aquifer Monitoring Using Ambient Seismic Noise Recorded With Distributed Acoustic Sensing (DAS) Deployed on Dark Fiber. *Journal of Geophysical Research: Solid Earth*, *126*(4). https://doi.org/10.1029/2020JB021004

Romanovsky, V. E., Drozdov, D. S., Oberman, N. G., Malkova, G. V, Kholodov, A. L., Marchenko, S. S., & Vasiliev, A. A. (2010). Thermal state of permafrost in Russia. *Permafrost and Periglacial Processes*, *21*(2), 136–155.

Romanovsky, V. E., Kholodov, A., Wright, T., & Hasson, N. (2019). *Thermal State of Permafrost in North America - annually observed ground temperatures*. https://doi.org/10.18739/A20R9M42C.

Romanovsky, V., Kholodov, A., Nicolsky, D., Hasson, N., & Wright, T. (2020). *Thermal state of permafrost in North America - annually observed ground temperatures, 2019*. https://doi.org/10.18739/A20R9M47S

Romeyn, R., Hanssen, A., & Kohler, A. (2022). Long-term analysis of cryoseismic events and associated ground thermal stress in Adventdalen, Svalbard. *Cryosphere*, *16*(5), 2025–2050. https://doi.org/10.5194/TC-16-2025-2022

Romeyn, R., Hanssen, A., Ole Ruud, B., Meling Stemland, H., & Arne Johansen, T. (2021). Passive seismic recording of cryoseisms in Adventdalen, Svalbard. *Cryosphere*, *15*(1), 283–302. https://doi.org/10.5194/TC-15-283-2021

Rossi, G., Accaino, F., Boaga, J., Petronio, L., Romeo, R., & Wheeler, W. (2018). Seismic survey on an open pingo system in Adventdalen Valley, Spitsbergen, Svalbard. *Near Surface Geophysics*, *16*(1), 89–103.

Roy, N., & Jakka, R. S. (2017). Near-field effects on site characterization using MASW technique. *Soil Dynamics and Earthquake Engineering*, *97*, 289–303. https://doi.org/10.1016/J.SOILDYN.2017.02.011

Ryden, N., Park, C. B., Ulriksen, P., & Miller, R. D. (2004). Multimodal Approach to Seismic Pavement Testing. *Journal of Geotechnical and Geoenvironmental Engineering*, *130*(6), 636–645. https://doi.org/10.1061/(ASCE)1090-0241(2004)130:6(636)

Saw, J., Zhu, X., Luo, L., Correa, J., Soga, K., & Ajo-Franklin, J. (2025). Distributed Fiber Optic Sensing for in-well hydraulic fracture monitoring. *Geoenergy Science and Engineering*, *250*, 213792. https://doi.org/10.1016/J.GEOEN.2025.213792

Schneider Von Deimling, T., Lee, H., Ingeman-Nielsen, T., Westermann, S., Romanovsky, V., Lamoureux, S., Walker, D. A., Chadburn, S., Trochim, E., Cai, L., Nitzbon, J., Jacobi, S., & Langer, M. (2021). Consequences of permafrost degradation for Arctic infrastructure - Bridging the model gap between regional and engineering scales. *Cryosphere*, *15*(5), 2451–2471. https://doi.org/10.5194/TC-15-2451-2021

Schrott, L., & Hoffmann, T. (2008). Refraction seismics. In *Applied Geophysics in periglacial environments* (pp. 57–79).

Schwamborn, G. J., Dix, J. K., Bull, J. M., & Rachold, V. (2002). High-resolution seismic and ground penetrating radar–geophysical profiling of a thermokarst lake in the western Lena Delta, Northern Siberia. *Permafrost and Periglacial Processes*, *13*(4), 259–269.

Scott, J. H., & Markiewicz, R. D. (1990). Dips and Chips—PC Programs for Analyzing Seismic Refraction Data. *Symposium on the Application of Geophysics to Engineering and Environmental Problems 1990*, 175–200.

SeisImagerSW Manual v. 3.0. (2009). [Software]. Geometrics.

Seo, J., Kim, Y., Ha, J., Kwak, D., Ko, M., & Yoo, M. (2024). Unsupervised anomaly detection for earthquake detection on Korea high-speed trains using autoencoder-based deep learning models. *Scientific Reports*, *14*(1), 639. https://doi.org/10.1038/s41598-024-51354-7

Shaheen, A., Waheed, U. Bin, Fehler, M., Sokol, L., & Hanafy, S. (2021). Groningennet: Deep learning for low-magnitude earthquake detection on a multi-level sensor network. *Sensors*, *21*(23). https://doi.org/10.3390/s21238080

Shapiro, N. M., & Ritzwoller, M. H. (2002). Monte-Carlo inversion for a global shear-velocity model of the crust and upper mantle. *Geophysical Journal International*, *151*(1), 88–105. https://doi.org/10.1046/J.1365-246X.2002.01742.X

Shapiro, N. M., Singh, S. K., Almora, D., & Ayala, M. (2001). Evidence of the dominance of higher-mode surface waves in the lake-bed zone of the Valley of Mexico. *Geophysical Journal International*, *147*(3), 517–527. https://doi.org/10.1046/J.0956-540X.2001.01508.X

Shaw, G. H. (1986). Elastic properties and equation of state of high pressure ice. *The Journal of Chemical Physics*, *84*(10), 5862–5868. https://doi.org/10.1063/1.449897

Shi, Q., Denolle, M. A., Ni, Y., Williams, E. F., & You, N. (2025). Denoising Offshore Distributed Acoustic Sensing Using Masked Auto-Encoders to Enhance Earthquake Detection. *Journal of Geophysical Research: Solid Earth*, *130*(2), e2024JB029728. https://doi.org/10.1029/2024JB029728

Shiklomanov, N. I., Streletskiy, D. A., Nelson, F. E., Hollister, R. D., Romanovsky, V. E., Tweedie, C. E., & Brown, J. (2010). Decadal variations of active-layer thickness in moisture-controlled landscapes, Barrow, Alaska. *Journal of Geophysical Research: Biogeosciences*, *115*(G4).

Smith, M. W., & Burn, C. R. (1987). Outward flux of vapour from frozen soils at Mayo, Yukon, Canada: results and interpretation. *Cold Regions Science and Technology*, *13*(2), 143–152.

Smith, S. L., O'Neill, H. B., Isaksen, K., Noetzli, J., & Romanovsky, V. E. (2022). The changing thermal state of permafrost. *Nature Reviews Earth & Environment*, *3*(1), 10–23. https://doi.org/10.1038/s43017-021-00240-1

Smith, S. L., Romanovsky, V. E., Lewkowicz, A. G., Burn, C. R., Allard, M., Clow, G. D., Yoshikawa, K., & Throop, J. (2010). Thermal state of permafrost in North America: a contribution to the international polar year. *Permafrost and Periglacial Processes*, *21*(2), 117–135.

Socco, L. V., & Boiero, D. (2008). Improved Monte Carlo inversion of surface wave data. *Geophysical Prospecting*, *56*(3), 357–371. https://doi.org/10.1111/J.1365-2478.2007.00678.X

Socco, L. V., & Strobbia, C. (2004). Surface-wave method for near-surface characterization: a tutorial. *Near Surface Geophysics*, *2*(4), 165–185. https://doi.org/10.3997/1873-0604.2004015

Spica, Z. J., Ajo-Franklin, J., Beroza, G. C., Biondi, B., Cheng, F., Gaite, B., Luo, B., Martin, E., Shen, J., Thurber, C., Viens, L., Wang, H., Wuestefeld, A., Xiao, H., & Zhu, T. (2023). PubDAS: A PUBlic Distributed Acoustic Sensing Datasets Repository for Geosciences. *Seismological Research Letters*, *94*(2A), 983–998. https://doi.org/10.1785/0220220279

Steinel, H., Hausmann, J., Werban, U., & Dietrich, P. (2014). Reliability of MASW profiling in near-surface applications. *Near Surface Geophysics*, *12*(6), 731–737. https://doi.org/10.3997/1873-0604.2014029

Streletskiy, D. A., Anisimov, O., & Vasiliev, A. (2015). Permafrost degradation. In *Snow and ice-related hazards, risks, and disasters* (pp. 303–344). Academic Press.

Streletskiy, D. A., Shiklomanov, N. I., & Nelson, F. E. (2012). Permafrost, infrastructure, and climate change: a GIS-based landscape approach to geotechnical modeling. *Arctic, Antarctic, and Alpine Research*, *44*(3), 368–380.

Sun, H., Cheng, F., Xia, J., Guan, J., Li, Z., & Ajo-Franklin, J. B. (2025). Unveiling Cryosphere Dynamics by Distributed Acoustic Sensing and Data-Driven Hydro-Thermo Coupled Simulation. *Geophysical Research Letters*, *52*(2), e2024GL111188. https://doi.org/10.1029/2024GL111188

Swanson, P., Boltz, M. S., & Chambers, D. (2016). Seismic Monitoring Strategies for Deep Longwall Coal Mines. In *Centers for Disease Control and Prevention, National Institute for Occupational Safety and Health*. https://stacks.cdc.gov/view/cdc/43944

Taipodia, J., Baglari, D., & Dey, A. (2019). Effect of Source Characteristics on the Resolution of Dispersion Image from Active MASW Survey. *Indian Geotechnical Journal*, *49*(3), 314–327. https://doi.org/10.1007/S40098-018-0335-1/METRICS

Taylor, O. D. S., Abdollahi, M., & Vahedifard, F. (2022). Statistical distributions of wave velocities and elastic moduli in near-surface unsaturated soils. *Soil Dynamics and Earthquake Engineering*, *157*, 107247. https://doi.org/10.1016/J.SOILDYN.2022.107247

Teng, J., Liu, J., Zhang, S., & Sheng, D. (2020). Modelling frost heave in unsaturated coarse-grained soils. *Acta Geotechnica*, *15*, 3307–3320.

Terzaghi, K., Peck, R. B., & Mesri, G. (1996). *Soil mechanics in engineering practice*. John Wiley & Sons.

Thoman, R., & Walsh, J. E. (2019). *Alaska's changing environment: Documenting Alaska's physical and biological changes through observations*. International Arctic Research Center, University of Alaska Fairbanks.

Tourei, A. (2025). das-anomaly. *Zenodo,* ahmadtourei/das-anomaly: v0.0.7. https://doi.org/10.5281/ZENODO.17122769

Tourei, A., Ji, X., Rocha dos Santos, G., Czarny, R., Rybakov, S., Wang, Z., Hallissey, M., Martin, E. R., Xiao, M., Zhu, T., Nicolsky, D., & Jensen, A. (2024). Mapping Permafrost Variability and Degradation Using Seismic Surface Waves, Electrical Resistivity, and Temperature Sensing: A Case Study in Arctic Alaska. *Journal of Geophysical Research: Earth Surface*, *129*(3), e2023JF007352. https://doi.org/10.1029/2023JF007352

Tourei, A., Ji, X., Santos, G. R. dos, Czarny, R., Rybakov, S., Wang, Z., Hallissey, M., Martin, E., Xiao, M., Zhu, T., Nicolsky, D., Jensen, A., & McComb, C. (2023). *Seismic and Electrical Resistivity Datasets for Characterizing Permafrost in Alaska (August 2023)*. https://doi.org/10.18739/A2V40K14Q

Tourei, A., Martin, E. R., Ankamah, A. T., Hole, J. A., & Chambers, D. J. A. (2024). An Autoencoder-Based Deep Learning Model for Enhancing Noise Characterization and Microseismic Event Detection in Underground Longwall Coal Mines Using Distributed Acoustic Sensing Monitoring. *58th US Rock Mechanics / Geomechanics Symposium 2024, ARMA 2024*. https://doi.org/10.56952/ARMA-2024-0207

Trnkoczy, A. (2012). Understanding and parameter setting of STA/LTA trigger algorithm. In *New Manual of Seismological Observatory Practice 2 (NMSOP-2)*. https://doi.org/10.2312/GFZ.NMSOP-2_IS_8.1

Van Dyke, M., Klemetti, T., Khademian, Z., Wickline, J., & Beale, J. (2023). Evaluation of Seismic Potential in a Longwall Mine with Massive Sandstone Roof Under Deep Overburden: an Update. *Mining, Metallurgy and Exploration*, *40*(5). https://doi.org/10.1007/s42461-023-00818-x van Everdingen, R. O., Harris, S. A. , French, H. M. , Heginbottom, J. A. , Johnston, G. H. , Ladanyi, B. , & Sego, D. ,. (1988). *Glossary of permafrost and related ground-ice terms. Associate Committee on Geotechnical Research*. 1–156. https://nrc-publications.canada.ca/eng/view/ft/?id=69fb8993-1baa-4225-b33a-6a02341d383d

Vantassel, J. P. (2025). hvsrpy: An Open-Source Python Package for Microtremor and Earthquake Horizontal-to-Vertical Spectral Ratio Processing. *Seismological Research Letters*, *96*(4), 2671–2682. https://doi.org/10.1785/0220240395

Vantassel, J. P., & Cox, B. R. (2021). SWinvert: a workflow for performing rigorous 1-D surface wave inversions. *Geophysical Journal International*, *224*(2), 1141–1156. https://doi.org/10.1093/GJI/GGAA426

Viens, L., Perton, M., Spica, Z. J., Nishida, K., Yamada, T., & Shinohara, M. (2022). Understanding surface wave modal content for high-resolution imaging of submarine sediments with distributed acoustic sensing. *Geophysical Journal International*, *232*(3), 1668–1683. https://doi.org/10.1093/GJI/GGAC420

Vinson, T. S. ., Rooney, J. W. ., & Haas, W. H. . (1996). *Roads and airfields in cold regions : a state of the practice report*. 321.

Wagner, A. M., Lindsey, N. J., Dou, S., Gelvin, A., Saari, S., Williams, C., Ekblaw, I., Ulrich, C., Borglin, S., Morales, A., & Ajo-Franklin, J. (2018). Permafrost Degradation and Subsidence Observations during a Controlled Warming Experiment. *Scientific Reports*, *8*(1), 1–9. https://doi.org/10.1038/s41598-018-29292-y

Wagner, F. M., Mollaret, C., Günther, T., Kemna, A., & Hauck, C. (2019). Quantitative imaging of water, ice and air in permafrost systems through petrophysical joint inversion of seismic refraction and electrical resistivity data. *Geophysical Journal International*, *219*(3), 1866–1875.

Walker, D. A., Raynolds, M. K., Kanevskiy, M. Z., Shur, Y. S., Romanovsky, V. E., Jones, B. M., & Peirce, J. L. (2022). Cumulative impacts of a gravel road and climate change in an ice-wedge-polygon landscape, Prudhoe Bay, Alaska. *Arctic Science*, *8*(4), 1040–1066.

Wang, H., Fratta, D., Lord, N., Zeng, X., & Coleman, T. (2018). Distributed Acoustic Sensing (DAS) Field Trials for Near-Surface Geotechnical Properties, Earthquake Seismology, and Mine Monitoring. *SEG Technical Program Expanded Abstracts*. https://doi.org/10.1190/segam2018-2997833.1

Wang, Z., Sun, C., & Wu, D. (2022). Multiscale linearized inversion of surface-wave dispersion curves. *Geophysical Prospecting*, *70*(1), 19–34. https://doi.org/10.1111/1365-2478.13149/CITE/REFWORKS

Wapenaar, K., Draganov, D., Snieder, R., Campman, X., & Verdel, A. (2010). Tutorial on seismic interferometry: Part 1 - Basic principles and applications. *Geophysics*, *75*(5). https://doi.org/10.1190/1.3457445

Wei, C., Zhang, C., Canbulat, I., Cao, A., & Dou, L. (2018). Evaluation of current coal burst control techniques and development of a coal burst management framework. *Tunnelling and Underground Space Technology*, *81*, 129–143. https://doi.org/10.1016/J.TUST.2018.07.008

Wu, Y., Nakagawa, S., Kneafsey, T. J., Dafflon, B., & Hubbard, S. (2017). Electrical and seismic response of saline permafrost soil during freeze - Thaw transition. *Journal of Applied Geophysics*, *146*, 16–26. https://doi.org/10.1016/J.JAPPGEO.2017.08.008

Xia, J., Miller, R. D., & Park, C. B. (1999). Configuration of Near-Surface Shear-Wave Velocity by Inverting Surface Wave. In *Symposium on the Application of Geophysics to Engineering and Environmental Problems 1999* (pp. 95–104). Environment and Engineering Geophysical Society. https://doi.org/doi:10.4133/1.2922698

Xie, Y., Wang, M., Zhong, Y., Deng, L., & Zhang, J. (2023). Label-Free Anomaly Detection Using Distributed Optical Fiber Acoustic Sensing. *Sensors 2023, Vol. 23, Page 4094*, *23*(8), 4094. https://doi.org/10.3390/S23084094

Xu, Y., Lebedev, S., Meier, T., Bonadio, R., & Bean, C. J. (2021). Optimized workflows for high-frequency seismic interferometry using dense arrays. *Geophysical Journal International*, *227*(2), 875–897. https://doi.org/10.1093/GJI/GGAB260

Yang, Z., Li, Z., Zhu, J., Wang, Y., & Wu, L. (2020). Use of SAR/InSAR in Mining Deformation Monitoring, Parameter Inversion, and Forward Predictions: A Review. *IEEE Geoscience and Remote Sensing Magazine*, *8*(1), 71–90. https://doi.org/10.1109/MGRS.2019.2954824

Yao, H., Zhang, Y., Xu, J., Covey, K. R., Larson, K. A., Herczeg, G. J., Previdi, M., Smith, K. L., & Polvani, L. M. (2021). Arctic amplification of climate change: a review of underlying mechanisms. *Environmental Research Letters*, *16*(9), 093003. https://doi.org/10.1088/1748-9326/AC1C29

Yilmaz, O. (1987). Seismic data processing. *Investigation in Geophysics,* 2, 526.

Yoshikawa, K., Romanovsky, V., Duxbury, N., Brown, J., & Tsapin, A. (2004). The use of geophysical methods to discriminate between brine layers and freshwater taliks in permafrost regions. *J. Glaciol. Geocryology*, *26*, 301–309.

You, Y., Wang, J., Wu, Q., Yu, Q., Pan, X., Wang, X., & Guo, L. (2017). Causes of pile foundation failure in permafrost regions: The case study of a dry bridge of the Qinghai-Tibet Railway. *Engineering Geology*, *230*, 95–103.

Young, C., Shragge, J., Schultz, W., Haines, S., Oren, C., Simmons, J., & Collett, T. S. (2022). Advanced Distributed Acoustic Sensing Vertical Seismic Profile Imaging of an Alaska North Slope Gas Hydrate Field. *Energy & Fuels*, *36*(7), 3481–3495. https://doi.org/10.1021/ACS.ENERGYFUELS.1C04102

Yuan, S., & Martin, E. (2025). Potential higher-mode bias in DAS-based MASW for near-surface characterization. *Center for Wave Phenomena, Colorado School of Mines.*

Zakharova, E. A., Kouraev, A. V., Rémy, F., Zemtsov, V. A., & Kirpotin, S. N. (2014). Seasonal variability of the Western Siberia wetlands from satellite radar altimetry. *Journal of Hydrology*, *512*, 366–378. https://doi.org/10.1016/J.JHYDROL.2014.03.002

Zhang, C., Canbulat, I., Hebblewhite, B., & Ward, C. R. (2017). Assessing coal burst phenomena in mining and insights into directions for future research. *International Journal of Coal Geology* (Vol. 179). https://doi.org/10.1016/j.coal.2017.05.011

Zhang, Y., Wen, A., Zhao, W., Liang, X., Li, P., & Černý, R. (2020). Influence of Compaction Level on the Water-Heat-Vapor Characteristics of Unsaturated Coarse-Grained Fillings Exposed to Freezing and Thawing. *Advances in Civil Engineering*, 1–10.

Zhang, Z., Lin, H., Wang, M., Liu, X., Chen, Q., Wang, C., & Zhang, H. (2022). A Review of Satellite Synthetic Aperture Radar Interferometry Applications in Permafrost Regions: Current status, challenges, and trends. *IEEE Geoscience and Remote Sensing Magazine*, *10*(3), 93–114. https://doi.org/10.1109/MGRS.2022.3170350

Zhu, W., & Beroza, G. C. (2019). PhaseNet: A deep-neural-network-based seismic arrival-time picking method. *Geophysical Journal International*, *216*(1). https://doi.org/10.1093/gji/ggy423

Zipfel, J., Verworner, F., Fischer, M., Wieland, U., Kraus, M., & Zschech, P. (2023). Anomaly detection for industrial quality assurance: A comparative evaluation of unsupervised deep learning models. *Computers and Industrial Engineering*, *177*. https://doi.org/10.1016/j.cie.2023.109045

Zwieback, S., Liu, L., Rouyet, L., Short, N., & Strozzi, T. (2024). Advances in InSAR Analysis of Permafrost Terrain. *Permafrost and Periglacial Processes*, *35*(4), 544–556. https://doi.org/10.1002/PPP.2248

APPENDIX A SUPPORTING INFORMATION FOR CHAPTER 2

The supporting information includes five main parts:

- Surface wave dispersion/inversion analysis procedure (A.1)
- Discussion on the adopted bandpass filter (A.2)
- Compressional wave velocities using seismic refraction (Text 3 and Figure A.2)
- Surface wave survey information (Table A.1)
- Soil temperature measurement information (Figure A.3 and Table A.2)

A.1 Surface wave dispersion/inversion analysis procedure

The first step in the MASW process is to select an appropriate impulse source and geophone array configuration based on the size and complexity of the study area. Surface wave records are described in the form of $u(x_j, t)$, where $x_j = x_1 + (j-1)dx$ is the distance from the impact load point to the j th receiver ($j = 1, \ldots, N$) and t is time. After applying a Fourier transform to each trace of the multichannel record, its frequency-domain representation $\tilde{u}(x_j, \omega)$ will be provided (Park, 2011; Park et al., 1998):

$$\tilde{u}(x_j, \omega) = FFT\left[u(x_j, t)\right] \tag{A.1}$$

where $\omega = 2\pi f$ is the angular frequency. It is possible to express the transformed record as an amplitude $A_j(\omega)$ and phase $\Phi_j(\omega)$ function. The phase term is determined by the characteristic phase velocity of each frequency component $c(\omega)$ and the offset x_j. Additionally, the amplitude term provides information about the attenuation and geometric spread of the signal (Park, 2011; Park et al., 1998):

$$\tilde{u}(x_j, \omega) = A_j(\omega) e^{-i\Phi_j(\omega)} \tag{A.2}$$

$$\Phi_j(\omega) = \frac{\omega x_j}{c(\omega)} = \frac{\omega[x_1 + (j-1)dx]}{c(\omega)} \tag{A.3}$$

and $i^2 = -1$.

In order to remove the effects of geometrical spreading and attenuation, the amplitude of the transformed record is normalized in both the offset and frequency dimensions (Park, 2011; Park et al., 1998). Hence, the analysis is focused on the dispersive properties of the signal.

$$\tilde{u}_{norm}(x_j, \omega) = \frac{\tilde{u}(x_j, \omega)}{\left|\tilde{u}(x_j, \omega)\right|} = e^{-i\Phi_j(\omega)} \tag{A.4}$$

The time domain representation of each frequency component of $\tilde{u}_{norm}(x_j, \omega)$ is an array of normalized sinusoidal curves that have the same phase along the slope determined by their actual phase velocity $c(\omega)$. The phase of the curves varies along slopes corresponding to other phase velocities. In a perfectly constructive superposition, the normalized sinusoidal curves that have been added up along the slope corresponding to $c(\omega)$ will produce another sinusoidal curve with amplitude N. However, if the normalized curves are added up along any other slope, the amplitude of the resulting summed curve will be less than N due to destructive superposition (Park, 2011; Ryden et al., 2004). This process is known as slant-stacking, and it involves summarizing amplitudes along slanted paths (Yilmaz, 1987).

For a given testing phase velocity, c_T, and a given frequency, ω, the amount of phase shifts required to counterbalance the time delay corresponding to specific offsets x_j are determined. To obtain the slant-stacked amplitude $A_s(\omega, c_T)$ corresponding to each pair of ω and c_T, the phase shifts are applied to distinct traces of the normalized, transformed record $u\tilde{}_{norm}\left(x_j, \omega\right)$ that are thereafter added (Park, 2011; Park et al., 1998). Normalizing slant-stacked amplitudes ensures that the peak value will not be dependent on the number of receivers:

$$A_s(\omega, c_T) = \frac{1}{N}\sum_{j=1}^{N} e^{-i\Phi_T,u} u\tilde{}_{norm}\left(x_j, \omega\right) \tag{A.5}$$

where

$$\Phi_{T,j} = \frac{\omega x_j}{c_T} \tag{A.6}$$

The summation operation defined by Equations A6 and A7 is repeated for all the different frequency components of the transformed record in a scanning manner, changing the testing phase velocity in small increments within a previously specified testing range $\left(c_{T,min} \le c_T \le c_{T,max}\right)$. The dispersion image is thereafter obtained by plotting the slant-stacked amplitude in the frequency-phase velocity domain, in either two or three dimensions. To construct the fundamental-mode and higher-mode dispersion curves for the site, high-amplitude bands show the dispersion properties of all types of waves in the recorded data (Park, 2011; Park et al., 1998). Upper and lower boundaries for the modal dispersion curves $((p_A/100)A_{s,max}A_s \le A_{s,max})$ can be obtained by identifying the testing phase velocity values that provide p_A% of the corresponding spectral peak value $\left(A_{s,max}\right)$ at each frequency.

The $\left(c_{e,q}, \lambda_{e,q}\right)(q = 1, \dots, Q)$ equation represents the experimental fundamental-mode dispersion curve. In this equation, Q is the number of data points, $c_{e,q}$ is the Rayleigh wave phase velocity of the q^{th} data point, and $\lambda_{e,q}$ is the corresponding wavelength.

After extracting dispersion curves from shot gathers, we generate an initial model by a simple wavelength-depth conversion. Then, we use an adaptive non-linear least squares method proposed by Xia et al. (1999) to invert dispersion curves and reconstruct the shear wave velocity models. The method involves minimizing the difference between the measured and calculated dispersion curves using an iterative process that updates the shear wave velocity profile until a good match is achieved. The method is based on a layered model with variable shear wave velocities and thicknesses, and the calculation of the dispersion curve is performed using a numerical solution of the wave equation. The inversion process involves iteratively updating the model parameters until a good match between the measured and calculated dispersion curves is achieved.

The forward problem is based on the solution of the wave equation for a layered medium with N layers, where the shear wave velocity and thickness of the i^{th} layer are denoted by v_i and h_i, respectively. The wave number k is defined as $k = \left(\frac{\omega}{v}\right)$, where ω is the angular frequency and v is the phase velocity. The dispersion curve of the i^{th} layer can be calculated using the following equation:

$$k_i^2 = \left(\frac{\omega^2}{v_i^2}\right) - \left(\frac{n\pi}{h_i}\right)^2 \tag{A.7}$$

where n is an integer that represents the mode number. The total dispersion curve for the N-layer model is obtained by combining the individual dispersion curves for each layer. The i^{th} point on the total dispersion curve is given by:

$$D_i(\omega) = \left(\frac{\omega}{k}\right) \tag{A.8}$$

where k is the solution of the wave equation for the current model parameters.

$$\emptyset(m) = \frac{\left\| D_{obs} - D(m)^{th} \right\|^2}{2} \tag{A.9}$$

where D_{obs} is the observed dispersion curve, $D(m)^{th}$ is the theoretical dispersion curve calculated for the current model m, and $\|\quad\|^2$ denotes the Euclidean norm. The inversion algorithm updates the model parameters by solving the following linear system at each iteration:

$$(JTJ + \lambda I)\Delta m = JT\Delta D \tag{A.10}$$

where Δm is the update to the model parameters, J is the Jacobian matrix, λ is a regularization parameter, I is the identity matrix, and ΔD is the difference between the observed and theoretical dispersion curves. The regularization parameter is introduced to stabilize the inversion and prevent overfitting. The updated model parameters are obtained by $m = m + \Delta m$.

A.2 Discussion on the adopted bandpass filter

Using 4.5 Hz geophones, energy below 4.5 Hz may have been recorded, though dampened according to the sensitivity of the geophone. Please note that SeisImager allows low-pass and high-pass filtering using a 0.8 and a 1.5 multiplier, respectively. Therefore, for low-pass filters, the corner frequency of [1000 Hz, 800 Hz, 640 Hz, 512 Hz, 409.6 Hz, 415 Hz, 327.68 Hz, 272.144 Hz, and so on] is allowed. For high-pass filters, a corner frequency of [5 Hz, 7.5 Hz, 11.25 Hz, 16.875 Hz, and so on] is allowed. We select 7.5 Hz as the lower band limit because 7.5 Hz is the first allowed corner frequency greater than 5 Hz in the software. Based on the amplitude spectrum for Figure A.1a shot-gather (below), we tried to keep the limit as wide as possible to allow the processing of any high-frequency signals that were recorded and can help with characterizing very shallow depths (in our case, the active layer). For the upper limit, we could use the 272.144 Hz limit, but it cuts high-frequency signals recorded by channels 4-8, 11, 15, and 18 below 327.68 Hz (indicated by the purple box). Therefore, we select the 327.68 Hz upper band limit to reduce very high-frequency noise effects, smoothen the signal, and keep the high-frequency signal recorded at some channels.

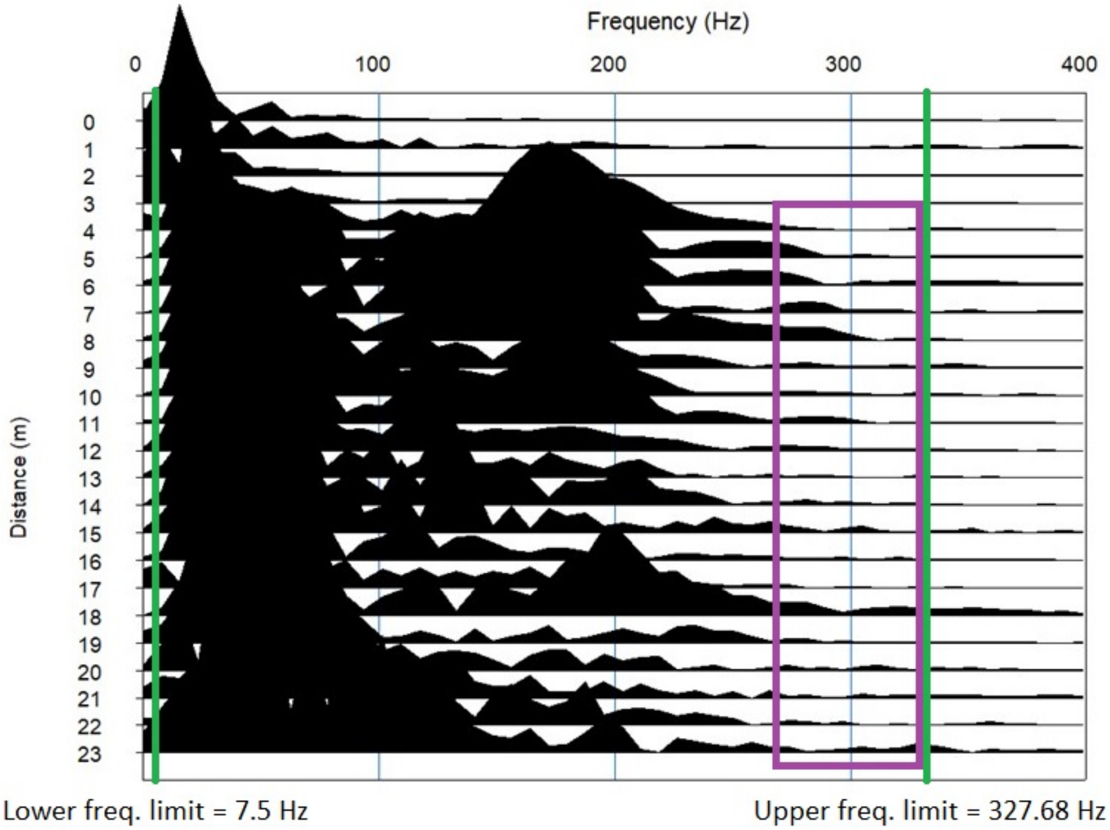

Figure A.1 Amplitude spectrum plot illustrating the frequency band (green lines) and high-frequency recordings by some channels (purple box).

A.3 Compressional wave velocities using seismic refraction

Seismic refraction tomography is a geophysical method used to measure the compressional wave velocity of layered subsurface materials. Seismic refraction involves the geophysical principle governed by Snell's Law, which describes the relationship between the angle of incidence and refraction of the wave that passes through two layers (Bery & Bery, 2013). The refracted wave travels along the interface of the upper and lower media and is recorded by the receivers as head waves when it is critically refracted (Kneisel et al., 2008). In this study, critical refraction occurs because the high seismic velocity permafrost layer is underlying the low seismic velocity active layer.

Due to velocity inversion below the permafrost layer in the research area, refracted seismic waves for short geophone spread (24 m) can only be observed between the active layer and permafrost. However, the seismic source should contain a relatively high frequency to track P-wave velocity using refraction tomography for the first 50 cm of the subsurface. Soft and wet soil ground surface limit seismic waves frequency band up to 150 Hz with a dominant frequency of around 50 Hz (Figure A.2a). Based on our numerical simulation of wave propagation (Bohlen, 2002) for the velocity model obtained from MASW and prior seismic velocity results by Dou and Ajo-Franklin (2014), the refracted seismic wave for the top permafrost boundary would be visible for a seismic source around 300 Hz (Figure A.2d). Therefore, refraction tomography is neglected in this study due to low seismic source resolution. However, this provides a useful guideline for future survey design.

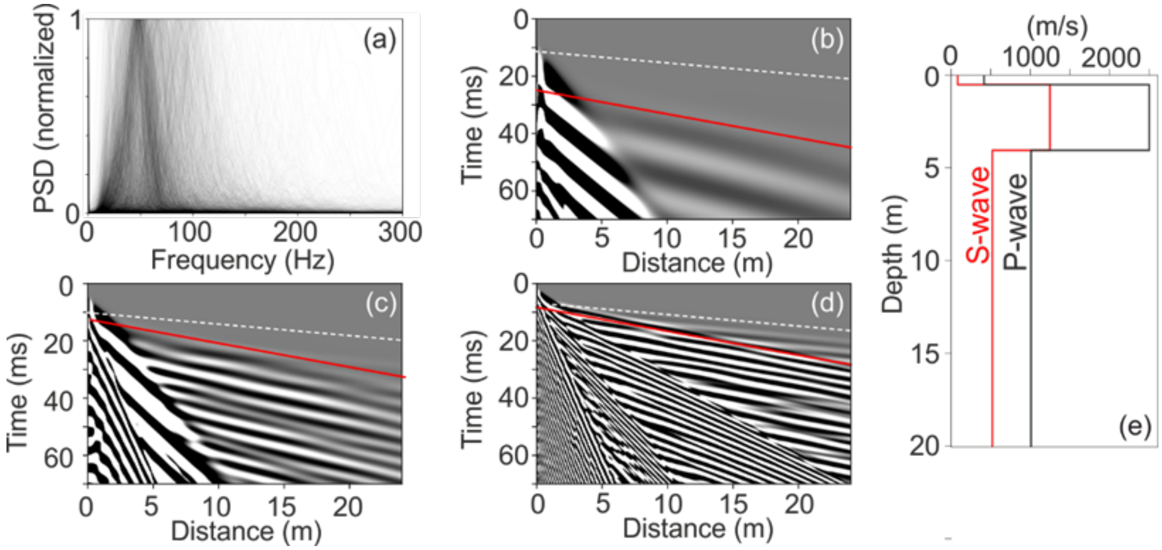

Figure A.2 (a) Normalized power spectrum density for all 8 lines (24x8 seismic traces). (b-d) Synthetic waveforms of vertical particle motions for the Ricker wavelet 50 Hz, 100 Hz, and 300 Hz, respectively. The dashed white line indicates the P-wave velocity of the permafrost layer (2500 m/s). The solid red line is the velocity 1200 m/s that corresponds with the Rayleigh surface wave. (e) Velocity models for numerical simulation.

Figure A.3 Soil temperature measurement locations (Temp 1-6 are measurements reported by this study.)

Table A.1 Location coordinates and recorded date for the collected surface-wave data.

MASW Location	Coordinates	Recording dates
Roadside	Start: 156.613894°W, 71.323272°N End: 156.614492°W, 71.323190°N	August 8, 2022
NOAA 1	Start: 156.611517°W, 71.323077°N End: 156.611130°W, 71.323138°N	August 11, 2022
NOAA 2	Start: 156.611393°W, 71.322915°N End: 156.610812°W, 71.323008°N	August 11, 2022
NOAA 3	Start: 156.610911°W, 71.322625°N End: 156.610319°W, 71.322671°N	August 10, 2022
MASW 1	Start: 156.610527°W, 71.324739°N End: 156.610231°W, 71.324891°N	August 9, 2022
MASW 2	Start: 156.601901°W, 71.327483°N End: 156.601572°W, 71.327644°N	August 12, 2022
MASW 3	Start: 156.593297°W, 71.329459°N End: 156.592982°W, 71.329636°N	August 12, 2021
MASW 4	Start: 156.584669°W, 71.332016°N End: 156.584355°W, 71.332203°N	August 12, 2022

Table A.2 Soil temperature measurement locations (Temp 1-6 are measurements reported by this study.)

Temperature Location	Coordinates	Recording dates
Temp 1	156.59478946°W, 71.32695537°N	August 8, 2022
Temp 2	156.584913°W, 71.32962323°N	August 8, 2022
Temp 3	156.58209051°W, 71.33082065°N	August 8, 2022
Temp 4	156.57963073°W, 71.33167261°N	August 8, 2022
Temp 5	156.57196933°W, 71.33247695°N	August 8, 2022
Temp 6	156.56971257°W, 71.33186914°N	August 6, 2022
Romanovsky et al. (2019) NML-2	156.661517°W, 71.309033°N	August 5, 2021
Romanovsky et al. (2019) B	156.603472°W, 71.279765°N	August 9, 2022
Romanovsky et al. (2019) C	156.60123°W, 71.279737°N	August 8, 2021
Romanovsky et al. (2019) D	156.600651°W, 71.28205°N	August 8, 2022
Shiklomanov et al. (2010)	156.6°W, 71.29°N	October 9, 2006
Nicolsky et al. (2009) West Doc site	148.55°W, 70.366667°N	June 18, 2001
Nicolsky et al. (2009) Franklin Bluffs site	148.716667°W, 69.65°N	June 18, 2001
Smith et al. (2010)	156.7°W, 71.3°N	Mean annual ground temperature in 2008

APPENDIX B AN AUTOENCODER-BASED DEEP LEARNING MODEL FOR ENHANCING NOISE CHARACTERIZATION AND MICROSEISMIC EVENT DETECTION IN UNDERGROUND LONGWALL COAL MINES USING DAS MONITORING

Reproduced from a conference paper published in the American Rock Mechanics Association proceedings[1].

Ahmad Tourei[2], Eileen Martin[2], Alexander Ankamah[3], John Hole[3], Derrick Chambers[4]

B.1 Abstract

The longwall mining method is designed to optimize coal extraction through controlled roof caving, which inevitably induces seismicity. This research employs a Distributed Acoustic Sensing (DAS) system incorporating a fire-safe fiber-optic cable strategically installed underground within an operational longwall coal mine. Despite lower sensitivity than traditional seismometers, DAS sensing technology benefits from dense sensor spacing and close proximity to the active face, where many microseismic events occur. To automatically detect and cluster seismic events within the voluminous DAS data records, we employ convolutional autoencoder deep learning models that can be used for anomaly (potential seismic event) detection in DAS spectral density images. The Kernel Density Estimation (KDE) technique is used to calculate the Probability Density Function (PDF) for the density scores of the latent space (representation of compressed data) in our model. We then use this calculated parameter as a threshold to distinguish between the Power Spectral Density (PSD) associated with background noise and with potential seismic events. The DAS monitoring system in conjunction with the developed deep learning model could enhance longwall coal mining safety and efficiency by offering valuable data from its densely deployed multichannel sensors near mining operations.

B.2 Introduction

Longwall mining is an efficient underground mining method for extracting a variety of stratified resources including coal, potash, and soda ash and represents a considerable advancement over conventional methods (Peng, 2019). A modern longwall primarily consists of hydraulic shields that

---

[1] Reproduced with the permission from the American Rock Mechanics Association. Tourei, A., Martin, E.R., Ankamah, A.T., Hole, J.A., & Chambers, D.J.A. (2024, June). An autoencoder-based deep learning model for enhancing noise characterization and microseismic event detection in underground longwall coal mines using distributed acoustic sensing monitoring. In *ARMA US Rock Mechanics/Geomechanics Symposium* (p. D041S052R005). ARMA.

[2] Hydrologic Science and Engineering Program, Colorado School of Mines, Golden, CO, USA

[3] Department of Geosciences, The Virginia Polytechnic Institute and State University, Blacksburg, VA, USA

[4] Department of Geophysics, Colorado School of Mines, Golden, CO, USA

support the roof and floor, a cutting device (e.g., a shearer or plow) that travels along the face extracting slices of coal, and an armored conveyor belt, which transports the resource to a larger mine haulage system. Normally longwall mining is safe and efficient, but a variety of ground control-related hazards are possible, especially in deep mines. One of the most significant of these hazards is a class of dynamic failures associated with induced seismicity and damage to mine workings, generally referred to as coal bursts or mine bumps. Much like tectonic earthquakes, mining-induced seismicity is difficult to predict and can have devastating consequences. For example, over the past several decades, coal bursts have killed hundreds of miners (Zhang et al., 2017).

The mechanisms and severity of coal bursts and mine bumps can vary widely, including localized failures occurring in the coal or near-seam strata, failure of competent strata in the overburden, and catastrophic chain failure of pillars, which can span large areas (Mark, 2016). Although significant advancements have been made in the past 100 years of research, many aspects of coal bursts remain “enigmatic” (Mark, 2018). There are a variety of options for managing coal bursts risk (Wei et al., 2018), but selecting and applying appropriate measures for dealing with coal bursts depends on an adequate understanding of the source, geology, and geomechanics associated with the bursts. For this, a variety of information sources are useful, including seismic monitoring. Apart from helping to address coal bursts, seismic monitoring can be useful for a variety of other safety applications in underground coal mining.

For underground coal mines, seismic monitoring is conducted using surface or in-mine sensors. Surface networks are usually less expensive and easier to maintain and install, but in-mine networks provide higher quality data in terms of event detection and location accuracy, especially event depth constraints (Swanson et al., 2016). In addition to much greater costs, regulations designed to help avoid fires and explosions in coal mines restrict the use and placement of electronics, including many seismic sensors and most digitizers. Deploying seismic sensors underground enables the characterization of various noises and also allows detection of smaller events since the sensors are closer to where these events occur (i.e., where the signal is strongest). The characterization of machinery noise is important for both operational efficiency and worker safety (P. Peng et al., 2020). Machinery noise cannot only be a significant occupational hazard but also a critical indicator of equipment condition and operational anomalies. Accurate noise characterization helps identify impending machinery failures, enabling preventative maintenance and a reduction in downtime. Furthermore, it is crucial to differentiate between mechanical noise and seismic events to get a proper understanding of the rockmass response to mining.

One promising technology to improve in-mine seismic monitoring of underground coal mines is distributed acoustic sensing (DAS) (Ankamah et al., 2023; Chambers & Shragge, 2023; H. Wang et al., 2018; C. Zhang et al., 2017). A DAS system is composed of an interrogator unit with optical and electronic components plugged into a fiber-optic cable. The interrogator probes the cable with light to measure a vibration time series at each position along the cable. Unlike most traditional seismic systems, MSHA-approved optical fibers pose no risk of causing a fire and so can be placed anywhere in coal mines. Another challenge encountered by underground networks of traditional seismic sensors or nodes is the need to maintain precise time synchronization underground, but the channels (i.e. sensing locations) along a DAS fiber are all automatically synchronized throughout data collection. As mining progresses, old cables can be cut and new cables surrounding the current region of interest can be connected to the system, which can measure tens of kilometers of fiber.

The spatially and temporally dense DAS data enables the detection of subtle seismic events that might otherwise go unnoticed with conventional monitoring systems. This enhanced detection capability is particularly advantageous in the context of underground coal mines, where early identification of minor seismic activities can be useful for delineating weak zones and identifying progressive failures quickly. DAS cables installed in boreholes have been previously tested for detecting microseismicity (X. Luo & Duan, 2021), as well as deployed on a longwall for monitoring face bursts (Chambers & Shragge, 2023). This study differs by focusing on deploying fiber throughout the more easily accessible entries of the mine, which could yield a more cost-effective strategy that is less intrusive to operations.

One conventional approach to seismic event detection involves using the short-term average/long-term average (STA/LTA) technique, which calculates the ratio of energy in a signal’s short and preceding longer time windows (Trnkoczy, 2012). However, this method often leads to false or missed seismic event identification due to its dependency on background noise levels. Hence, there has been growing interest in using deep learning techniques for seismic event detection, which have proven effective even for small-magnitude events (Huang et al., 2018; Shaheen et al., 2021; Zhu & Beroza, 2019). The two primary methods used for implementing deep learning in this context are supervised (Birnie & Hansteen, 2022; Mahmoudian et al., 2023) and unsupervised learning (Zipfel et al., 2023). In supervised learning, data are labeled as either seismic event or background noise (Mousavi, Zhu, Sheng, et al., 2019), whereas in unsupervised learning, such labels are not required for training (Seo et al., 2024). Each of these approaches has its advantages, but supervised approaches require numerous labeled seismic events, which can be difficult to acquire. Despite the potential of unsupervised learning, there are limited examples of its application in distinguishing seismic events. Leveraging artificial intelligence to improve seismic event detection, this study employs an unsupervised approach to train a deep learning model for identifying seismic activities over continuous DAS recordings.

Anomaly detection is one of the leading applications in unsupervised learning (Seo et al., 2024). Anomaly detection aims to identify statistical outliers and is useful in seismic analysis because data containing seismic events are much rarer than data containing only background noise. Unsupervised learning-based anomaly detection methods leverage this fact to train deep neural network models, often leading to superior performance compared to traditional methods in event detection. In this study, we aimed to develop a seismic event detection system that uses DAS multichannel measurements and improves existing seismic catalogs generated from surface seismic data. DAS can easily generate terabytes of data per day, and therefore, the use of an automated tool for anomaly (i.e., seismic event) detection is necessary. Hence, this research provides an unsupervised deep learning model that helps with the detection of seismic events on multichannel DAS recordings. After verifying the trained deep learning model on a sample of event-free background noise and achieving a satisfactory performance using seismic events from the surface seismometer network, we ran the model on DAS recordings to find seismic events that were not previously recorded. This anomaly-detection algorithm for seismic event detection could function as a warning system, potentially enhancing safety in coal mines by providing advanced notices of seismic activity.

B.3 Field Study Design and DAS Data Acquisition

To determine if DAS could be a practical tool to improve event detection in underground coal mines, we carried out a study in a longwall mine in Virginia, USA, which has a history of seismicity concerns (Van Dyke et al., 2023). Based on our experience in a small pilot test around one pillar, we decided to focus on surrounding the active panel with fiber optic cables. The optical interrogator unit was stored in a building on the surface with power and climate control adjacent to an elevator and ventilation shaft. The interrogator unit was connected to a fiber optic patch panel, which led to a fiber cable in a borehole that descended into the mine. At the bottom of the shaft, a new fiber was spliced to a cable deployed in the mains leading to the active panel (~1490 m of fiber from the shaft). From the mains on the west side of the panel, the fiber was spliced to another cable that extended ~1790 m along the headgate (Figure B.1). That headgate fiber was spliced to another fiber in the same cable at the east end of the segment to double the density, and then that fiber's west end was connected near the mains to another fiber that extended to the east along the tailgate ~1580 m. Unfortunately, the splice to the tailgate did not receive enough backscattered light, either due to a splice stored with too tight a bend in its protective case, or simply too poor quality of a splice. Alternatively, the signal in the tailgate was reduced too much by traveling through multiple splices. Therefore, only the mains and headgate (forward and reverse) sections of the fiber were used for data processing, as shown using a blue line in Figure B.1.

The fiber in the headgate and tailgate was installed in entries that were least likely to collapse early, and which had less machinery activity to reduce the likelihood of fiber breaks. In the headgate and tailgate, the majority of fiber was pushed against the rib (wall) and covered with mud or rock dust (non-combustible dust that mines apply to suppress potential explosions) where possible to increase the coupling to the ground. In the mains, most fiber was strung up on hooks along with other cables, and along the entry to the headgate and tailgate it was connected to rib and roof bolts using zip ties. The cable was not coupled well to the rock in these regions because mine traffic would likely break cable on the floor. The data were acquired for 46 days from May 11 – June 27, 2022, during which time the orange region in Figure B.1 was mined. The data were acquired at a channel spacing of 5.7 m (i.e., distance between new measurements), a gauge length of 11.4 m (i.e., distance over which average strain rate is measured), and a sampling rate of 2000 Hz, resulting in 33 T.B. of data.

Figure B.2a illustrates the full fiber route (i.e., main, headgate, and tailgate) and a couple of the seismic events detected by both surface seismometers (noted as yellow triangles in Figure B.1) and DAS cable. The DAS recording of the 1.2 magnitude event shown in Figure B.2a is presented in Figure B.2b. Clear P- and S-wave arrivals appear in the headgate forward and reverse DAS channels.

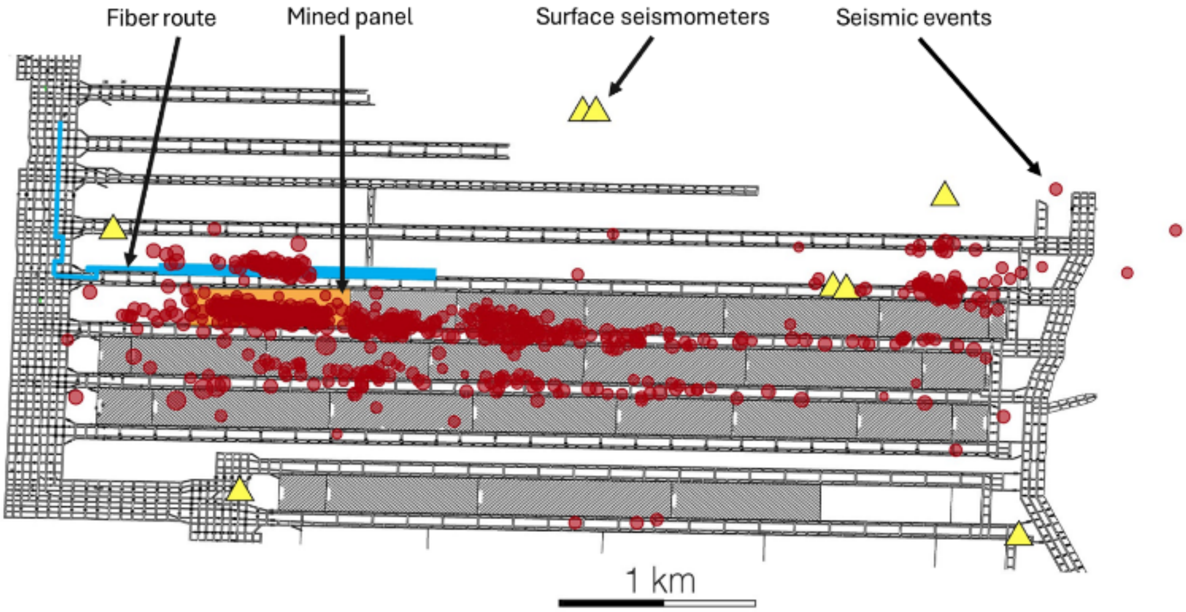

Figure B.1 Mine map showing the locations of seismic events (red dots) detected by surface network and mined panel (orange rectangle) during the experiment, surface seismic stations (yellow triangles), and DAS fiber in headgate (blue line).

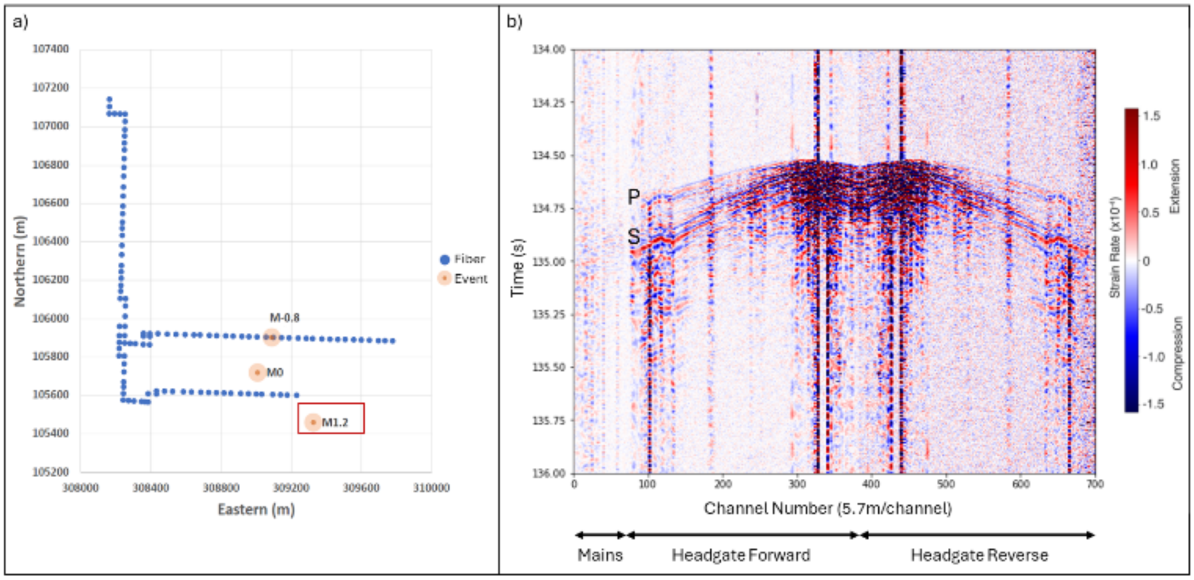

Figure B.2 DAS array channel locations with three seismic events (a) and the 1.2 magnitude event's P- and S-wave arrivals detected by DAS (b).

B.4 Methodology and DAS Data Analysis Workflow

The DAS technique enables us to record seismicity with a dense channel spacing, yielding higher resolution measurements compared to traditional seismic arrays. Although the signal-to-noise ratio of DAS measurements is lower than traditional seismometers, the spatially dense sampling and continuous recording enables characterization of various machinery noises and detection of subtle seismic events that might otherwise go unnoticed with conventional seismic monitoring systems. We use spectral methods to detect and classify both machinery noise and seismicity, which offer significant advantages over the time-domain alternative for several reasons. Primarily, the spectral approach allows for improved identification and analysis of different frequency components which often shed light on the nature of the sources. The frequency content of seismic signals can help differentiate between various types of seismic events, such as those caused by natural tectonic processes versus those induced by machinery or human activities. Furthermore, spectral analysis enhances the detection of low-amplitude signals that may be obscured by noise in the time domain, potentially improving the sensitivity and reliability of seismic monitoring systems. This capability is particularly beneficial in environments such as coal mines where the background noise level is high.

To monitor seismic activities using spectral analysis, we apply the Fast Fourier Transform to each trace recorded by a DAS channel, but a selection of a time window length to compute the power spectral density (PSD) is crucial. A long time window may not clearly represent the seismic event, especially for small-magnitude events far from the cable. On the other hand, if a time window is too short, the low-frequency content of the event signal may not be captured. A time window that includes the P- and S-wave arrivals, but not much more, is ideal. Figure B.3 demonstrates the capability of spectral analysis in identifying a seismic event that was not previously detected by the surface network. Figure B.3a shows the seismic event recorded by DAS in the time domain along with the PSD results in the frequency domain over different time windows in Figure B.3b-d.

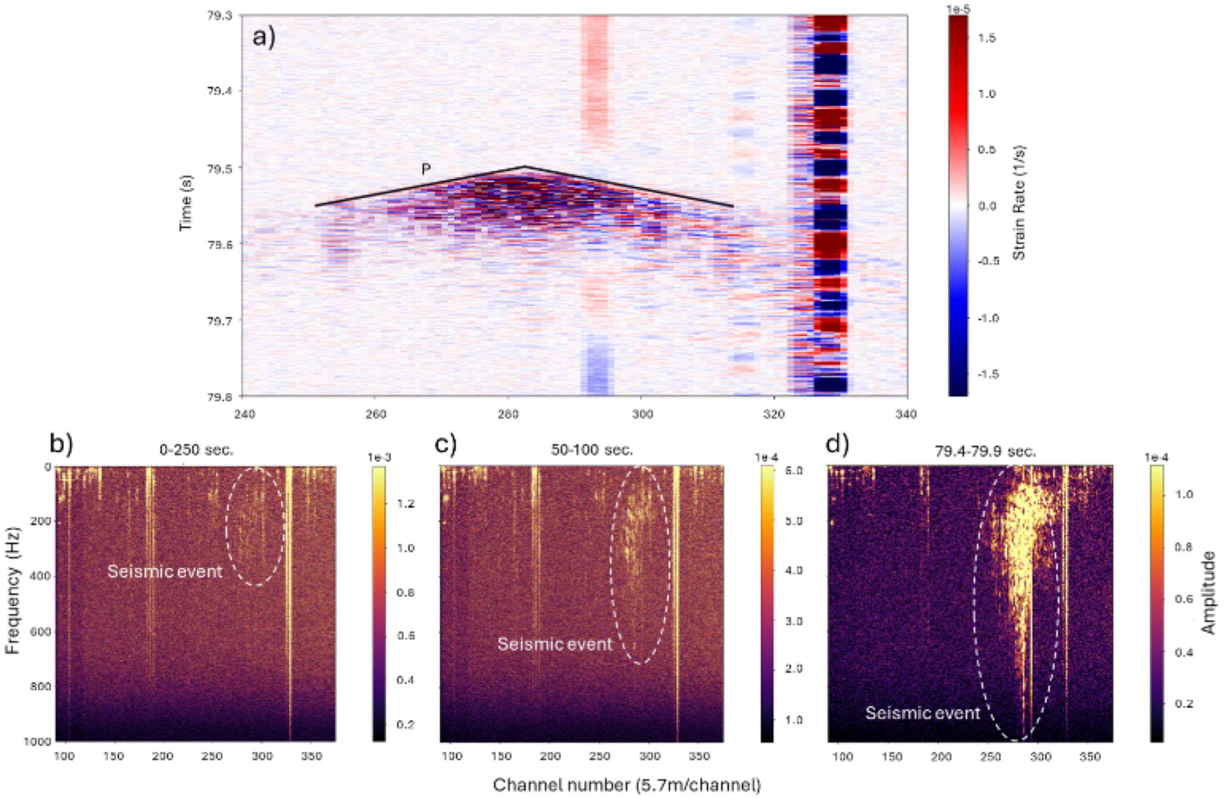

Figure B.3 A detected seismic event's P-wave arrival using DAS (a) and its power spectrum density (PSD) plots across 275 channels during (b) 250, (c) 50, and (d) 0.5 seconds.

Autoencoders are a type of convolutional neural network that are often used for unsupervised learning and are particularly useful for anomaly detection (Jiang et al., 2022; Mousavi et al., 2019). An anomaly is any portion of a dataset that has attributes that are different from the rest of the dataset. An autoencoder is designed to compress (encode) the input data into a lower-dimensional representation (latent space) and then reconstruct (decode) the compressed data back to its original form using only the reduced representation. In the context of anomaly detection in images, such as those of Figure B.3b-d, the autoencoder is trained exclusively on data representing the "normal", anomaly-free state of the data. During this training phase, we train the autoencoder to capture the essential characteristics of the normal images in the compressed representation. When the trained autoencoder is exposed to new images, it attempts to reconstruct them based on the model weights that best fit the training data. Images similar to the training data are reconstructed with relatively minor errors. Anomalous images, which contain patterns or features, such as seismic events that are not present in the training data, result in significantly higher reconstruction errors. By quantifying this error, anomalies can be detected.

Quantifying reconstruction error solely with simple metrics like root mean squared error often works well; however, it does come with certain limitations. One primary challenge is the autoencoder's potential to over-generalize from the training data, which can lead to lower-than-expected reconstruction errors for anomalous images. An alternative approach is to use kernel density estimation (KDE) as a non-parametric estimator to model the probability density function (PDF) of the encoded latent space's density score (Chen, 2000; Chen, 2017). A density score, attributed to a specific point within the data space, is the computed value of the estimated PDF at that point. This quantification can serve as a direct measure of the local density or crowding of the data space in the vicinity of the point in question. Elevated density scores are indicative of the point's location within a region characterized by a significant concentration of data points, denoting a high probability density region. In contrast, reduced density scores signal the point's placement in a region of a sparse data point distribution, suggesting its association with low probability density or outlier regions. Such a distinction offers a granular perspective on the spatial distribution of data points, enabling the identification of anomalies based on deviations from established density norms within the multidimensional data space.

Figure B.4 presents a schematic illustration of the autoencoder model. The autoencoder comprises an input layer designed to accommodate batches of 64 images of size 512x512 pixels. The encoder segment of the model consists of a series of convolutional layers with 64, 32, and 16 filters, respectively, to progressively reduce the spatial dimensions while retaining essential information about the original images. These layers utilize the ReLU activation function for non-linearity (Agarap, 2018) and are arranged to ensure minimal information loss up to the bottleneck layer, which serves as the latent space representation of the input data. The decoder mirrors this with upsampling and convolutional layers, culminating in an output that is a reconstructed version of the input. An Adam optimizer and mean squared error loss were used during training to ensure the model emphasizes the precision of reconstruction discrepancy for anomaly identification.

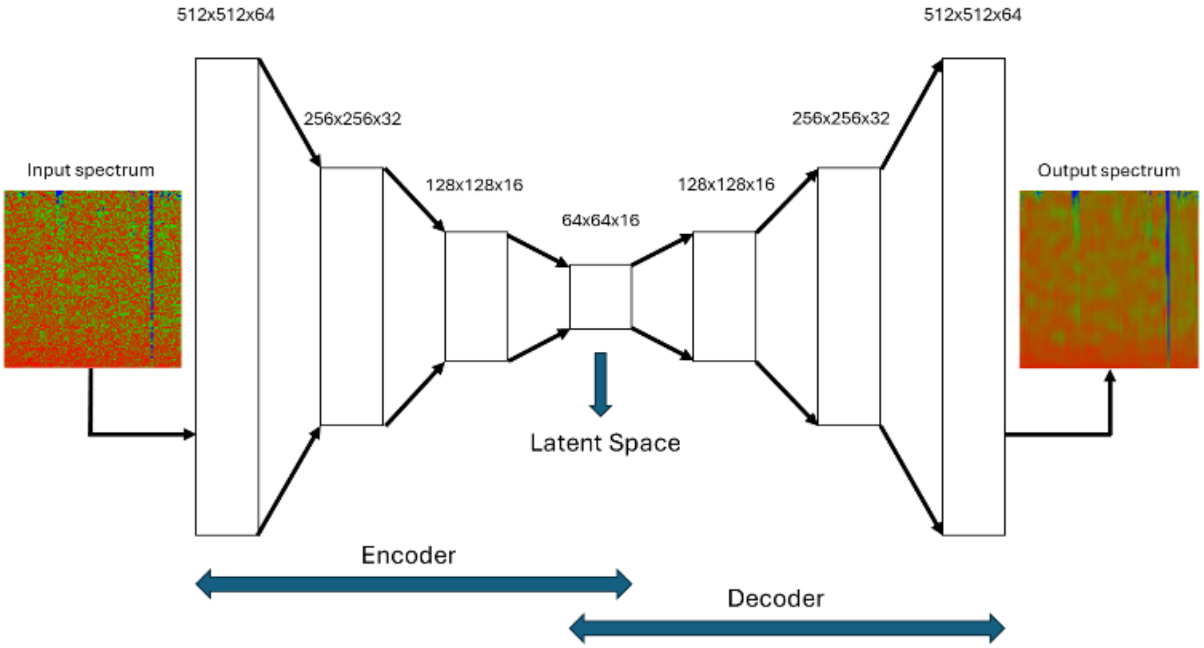

Figure B.4 Schematic representation of the autoencoder model, highlighting its multilayer architecture that consists of fully connected layers.

To train the unsupervised deep learning model, we randomly selected 1000 two-second time windows of the multichannel DAS recordings which do not contain any events according to the surface seismic catalog. Then, we plotted their normalized PSD in RGB format and visually excluded any spectrum plot with anomaly. Finally, we trained the model on 960 spectrum plots of background DAS noise (normal data), using 768 (80%) for training and 192 (20%) for testing, over 250 training cycles (epochs). Figure B.5 shows the deep learning model performance on training and testing datasets based on the loss value, calculated as the mean squared error of the difference between the predicted output and the actual output across both training and testing datasets. As the epochs progress, the convergence of loss values suggests that the model is effectively capturing the underlying patterns within the training data.

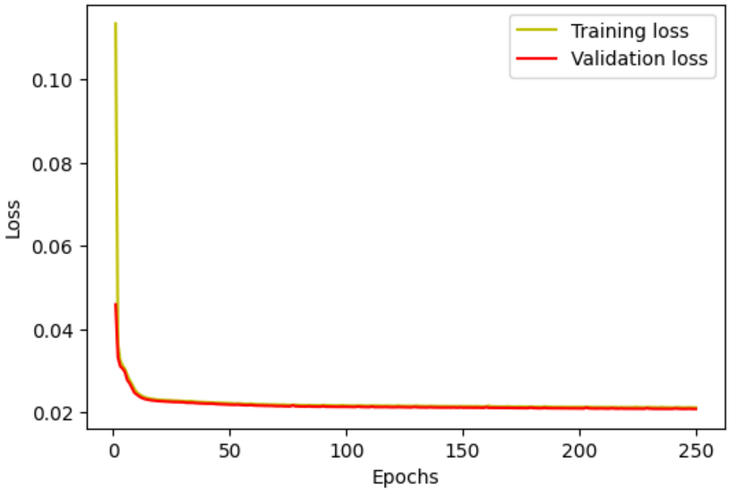

Figure B.5 Training and validation loss over 250 epochs. The training and validation loss strictly decreasing suggests convergence without overfitting.

After analyzing records with known seismic events and noting that the duration of all seismic events is between 0.5 and 1 second, we selected two-second time windows (chunks) with a one-second overlap between chunks. The overlap ensures every event is fully captured by at least one window. We implemented the proposed workflow on 26 hours of continuous DAS recording, generating 2,140,710 two-second chunks with 1 second of overlap and calculating their PSD plots. Subsequently, we employed the trained autoencoder on the PSD plots to detect seismic events.

B.5 Results and Discussion

Noise characterization of mining operations offers the potential for insights into equipment conditions and operations monitoring. Figure B.6 showcases the PSD of different noises averaged across a group of 10 adjacent DAS channels. Figure B.6a highlights a discernible daily variation in operational noise levels, with a pronounced increase during day shifts—a time of heightened activity—compared to the quieter night shifts. Figure B.6b reveals distinct on-and-off noise patterns associated with machinery over a 9-hour timeframe. The longwall shearer is a probable noise source based on the power distribution of the channels near the longwall. The noise is broadband and the oscillation at the high frequency is apparent. Monitoring this noise could inform predictive equipment maintenance, potentially reducing downtime and resulting in cost savings on equipment maintenance.

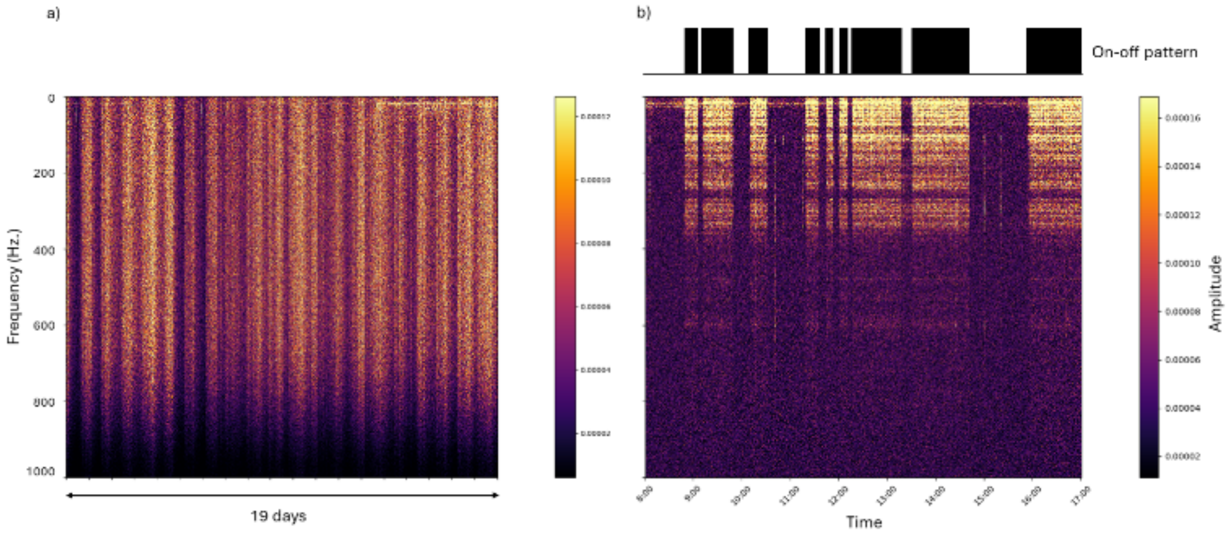

Figure B.6 PSD of DAS recording showing mine’s working shifts daily pattern (a) and machinery on-off pattern 245 m from the active face (b).

We employed the trained autoencoder on the training dataset containing PSD images that only include background noise and on the PSD images from known seismic events. This approach enabled us to analyze the distribution of the KDE for the latent space’s density score. A higher density score indicates a higher likelihood that the PSD data corresponds to the normal dataset, facilitating the detection of seismic activity. This unsupervised strategy, augmented with the incorporation of some labeled anomalous data, enhances the model's reliability, particularly in reducing false detections.

During the autoencoder model's development, a parametric study revealed the significant influence of input image size on the model's performance. The size parameter mandates resizing all input images to square dimensions defined by this parameter before either training or processing. This uniformity in image size is a restriction of the model's architecture. The selected image size directly affects the model’s computational demands, its precision in capturing details, and its overall efficacy in differentiating between normal and anomalous seismic activities based on visual data. Although enlarging the size parameter enhances the model’s anomaly detection capabilities, it substantially escalates computation time and memory usage. Figure B.7 illustrates the density score for both normal (PSD data containing background noise) and anomalous (PSD data containing seismic events) datasets across varying image input sizes. The histograms, based on different size parameters, represent the distribution of the density scores for anomalous PSD data (left Y-axis). In contrast, the lines indicate the mean density score of the normal PSDs. The results highlight that increasing the size spreads out the density scores for PSDs with anomalies and also amplifies the disparity between the density scores for anomalous and normal PSD data. This amplification boosts the model's discriminative capability. For a size parameter of 512, the density score for the normal PSD is shown as a solid line at ~45,000, which contrasts distinctly with the distribution and histogram for the anomalous PSD data. Therefore, a size parameter of 512 was selected for the autoencoder model. Leveraging the outcomes from this primarily unsupervised approach, we set the 95th percentile of the anomalous PSDs' density scores at ~16,000 as the threshold for event detection. Thus, any PSD data with a density score below this threshold is classified as an anomaly, indicating a seismic event. However, although adopting the 95th percentile rather than the maximum density score from known events may overlook a couple of very weak events with high density scores (around 40,000 and potentially events that are far from the DAS cable), it effectively reduces false positives. This methodology may ensure that the model is appropriately calibrated to avoid excessive sensitivity to minor anomalies in the PSD data, such as those caused by nearby vehicles.

Figure B.8 illustrates the application of the developed autoencoder model for the detection and labeling of seismic events. In this figure, two PSD images are fed into the model as inputs: one representing background noise (Figure B.8a) and the other depicting a seismic event (Figure B.8b). The model processes these inputs to generate outputs that are reconstructions of their encoded latent space representations. The noise image produced a density score of 45,246, which is not anomalous. The reconstructed image of the noise image is a faithful but smoothed reproduction of the actual image. In contrast, the seismic event is identified as anomalous based on its density score of –12,373. The reconstructed image of the seismic event exhibits noticeable discrepancies from the original PSD image, as highlighted by the ovals in Figure B.8b.

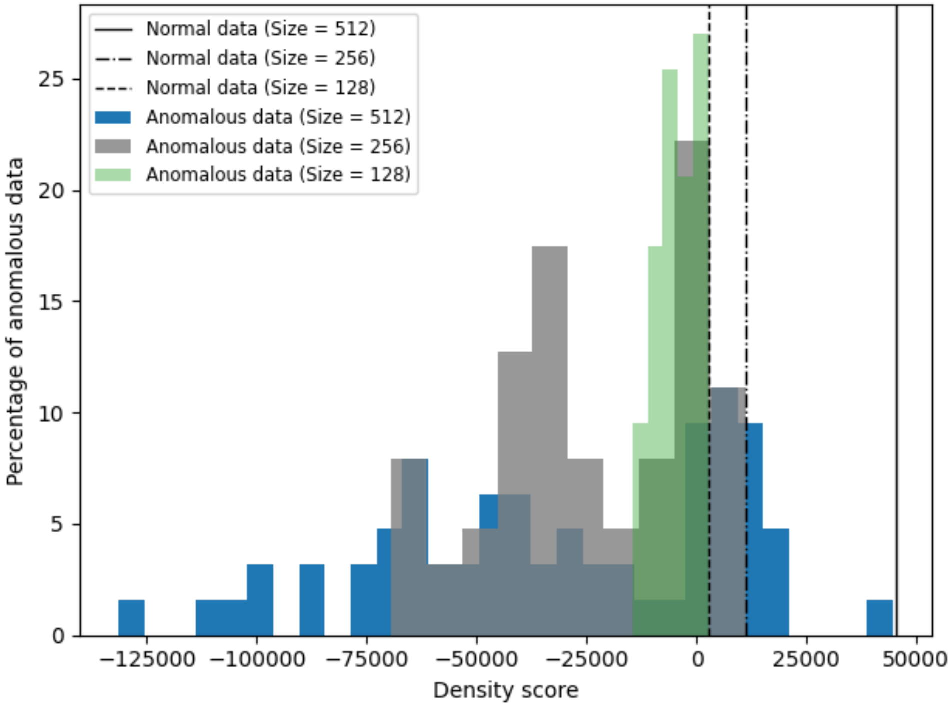

Figure B.7 Histogram of density score for normal (containing only background noise) and anomalous (containing a seismic event) data based on different input image sizes along with the mean density score of the normal PSDs.

a) High Density Score → Not an Anomaly → Background Noise

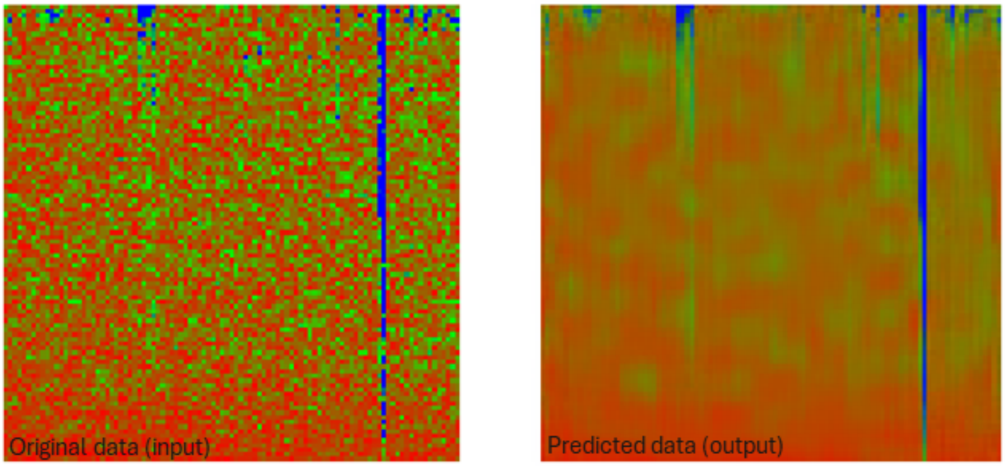

b) Low Density Score → An Anomaly → Detected Seismic Event

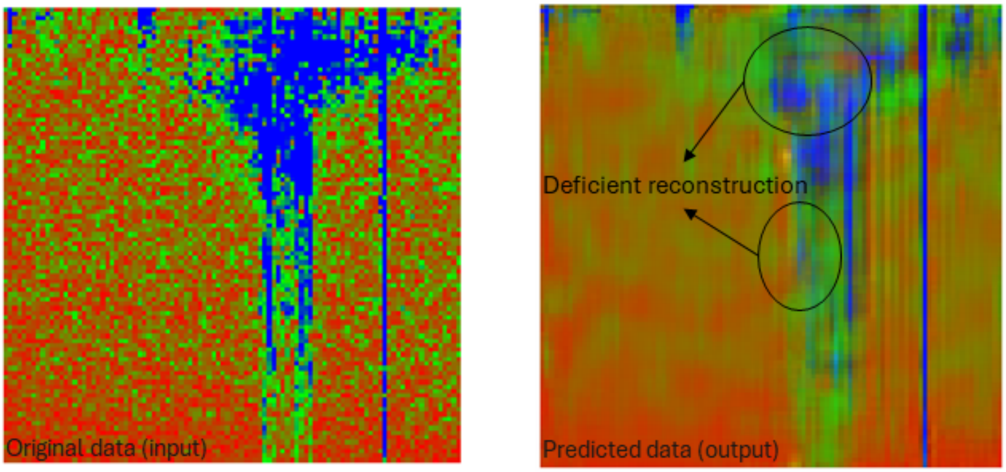

Figure B.8 Comparison of a background noise (a) and a seismic event (b) using the developed autoencoder deep learning method (X-axis: Sensors [275 channels (headgate forward) = 1570 m]; Y-axis: Frequency [0-1000 Hz. (Gradually increasing from top to bottom)]; Color: PSD amplitude in RGB).

We ran the developed model on 15.6 TB of DAS data collected over 26 days, utilizing 275 channels (spanning 1570 m) of the headgate forward cable for the purpose of event detection. After processing all the two-second PSD images with a one-second overlap, the model identified 56,558 anomalies as potential seismic events, compared to the sparse surface network's seismic catalog of 528 events during the same time period. Note that the surface array covers a much larger area than the DAS array, but is located farther from the active longwall face, complicating the comparison. We reviewed time series and PSD plots of 500 instances randomly selected from data labeled as background noise and 500 selected from data labeled as anomalies, comparing them with seismic events recorded by the surface seismic network. 496 of the 500 (99.2%) visually inspected data detected as background noise did not include seismic events. Of the data labeled as anomalies, at least 85 of the 500 (17.0%) are potentially seismic events. None of the 85 events existed in the surface network catalog. The absence of the surface network catalog events in the reviewed time series and PSDs is attributed to the mere small random sampling of anomalous data, 500 out of 56,558 (0.9%). These newly detected events are likely of small magnitude and close to the DAS cable. The relatively low prediction accuracy is due to the high threshold for the density score, which led to many false positives. Based on analyzing known seismic events detected by both the surface seismic network and DAS, we have observed that for events occurring relatively far from the cable, especially those of smaller magnitude, the anomalies are not clearly apparent in the DAS data. Therefore, by lowering the threshold of the density score, we can more effectively detect apparent anomalies, potentially those of higher magnitude or occurring closer to the fiber. However, this approach introduces a trade-off in that while we can achieve a more robust outcome for seismic event detection, we may overlook labeling other weak potential seismic activities. For future studies, a more robust outcome may be achieved by employing additional metrics, such as the reconstruction root mean squared error, alongside the density score to detect seismic events more effectively.

Results show that the model successfully identified new seismic events that are likely small but close to the DAS cable and had not been previously recorded by the surface seismic network. This showcases the enhanced sensitivity and effectiveness provided by DAS technology deployed underground in detecting seismic events that are otherwise elusive to traditional surface monitoring systems. The integration of underground DAS and surface seismometers represents a useful advance in applied seismology, suggesting the potential for improved predictive models and safety measures in mines with seismic events.

B.6 Conclusions

This research provides an unsupervised deep learning model that helps with the detection of anomalies on multichannel DAS recordings. We applied the Kernel Density Estimation (KDE) method to estimate the Probability Density Function (PDF) of the density scores of the model's latent space. This parameter was then utilized as a threshold to differentiate between the Power Spectral Density (PSD) of background noise and that of seismic events. We selected this threshold based on the density score’s distribution across various input image sizes. After verification of the trained deep learning model on the normal data (background noise) and achieving satisfactory performance on known seismic events recorded by the surface seismometer network, we ran the model on 15.6 T.B. of DAS recordings collected over 26 days while the longwall mining was occurring in the adjacent panel. 56,558 potential seismic events were detected, compared to the surface network’s seismic catalog of 528 events, more than a 100x increase. We analyzed time series and PSD plots of 1,000 instances—500 labeled as background noise and 500 as anomalies—against seismic events recorded by the surface network. The findings indicate a

99.2% accuracy in identifying non-seismic background noise, thanks to model training on such data. Additionally, preliminary analysis suggests that at least 17.0% of the anomalies could be seismic events, none of which were detected by the surface network. The modest success in detecting anomalies stems from a high density score threshold, which limits clear anomaly detection in DAS data, particularly for distant or low-magnitude events. The developed anomaly detection algorithm for seismic event identification could serve as a warning system, potentially enhancing safety in coal mines by offering advanced notice of seismic activities. Furthermore, this algorithm could reduce data storage requirements by a factor of 50 by recording data when the algorithm detects an anomaly, thereby facilitating a mine's ability to manage voluminous DAS data more effectively.

B.7 Acknowledgements

This research was funded by the NSF IUCRC Center to Advance the Science of Exploration to Reclamation in Mining (CASERM), including through additional support from the National Institute for Occupational Safety and Health (NIOSH). We would like to thank Virginia Tech Department of Geosciences IT, Virginia Tech ARC and Colorado School of Mines CIARC for computing resources and data management support. We appreciate the collaboration, guidance, and site access of the team at the Buchanan Mine Complex of Coronado Global Resources. We thank James Garner of Oak Ridge National Laboratory for his collaboration on the data acquisition. We thank experts from NIOSH and Compass Minerals for their advice. We thank Jake Beale of Pilot Geophysical for his collaboration related to the surface seismic network.

DASCore Python library (Chambers et al., 2024) was used for DAS PSD analysis along with TensorFlow Python library (Abadi et al., 2016) and Bhattiprolu’s GitHub repository (2023) for developing the autoencoder algorithm.

The findings and conclusions in this report are those of the author(s) and do not necessarily represent the official position of the National Institute for Occupational Safety and Health, Centers for Disease Control and Prevention. Mention of any company or product does not constitute endorsement by NIOSH, CDC.

APPENDIX C NUMERICAL MODELING AND DISPERSION ANALYSIS

C.1 Numerical Array Geometry and Elastic Model

A 2-D PSV elastic plane-strain domain with Lx=Lz=500 m and Δx=Δz=1 m (501×501 nodes) was modeled. The PSV supports P- (compressional) and SV-waves (vertically polarized shear waves), but not SH-waves (horizontally polarized shear waves). The Devito finite-difference framework was employed and customized for elastic wave modeling.

Stratigraphy of 5 layers as shown in Figure C.1 (Vp in km/s; Vs is assumed to be Vp/1.6):

- 0–2 m: 0.5
- 2–22 m: 1.5
- 22–142 m: 4.5
- 142–192 m: 2.5
-192-500 m: 1.5

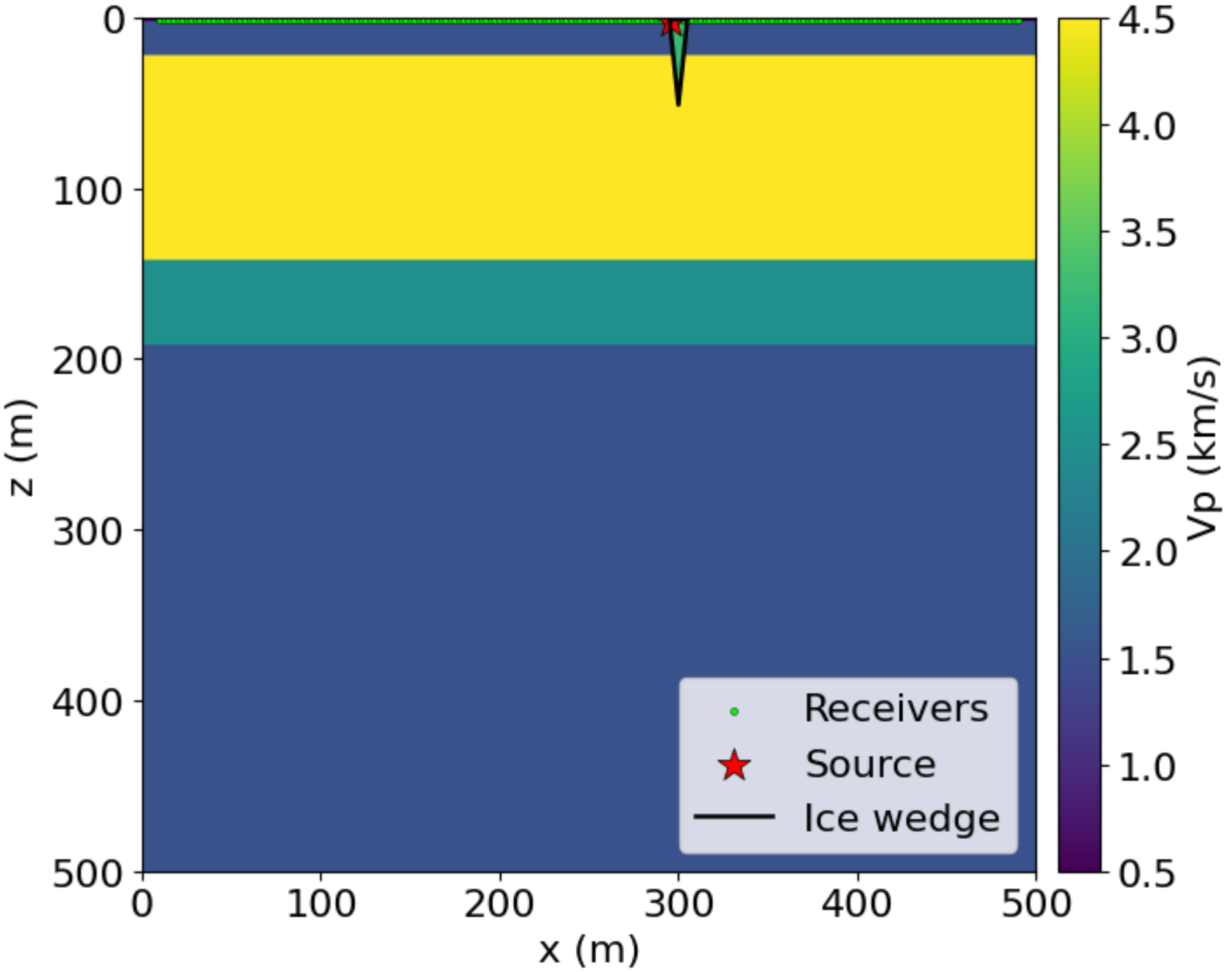

Figure C.1 Geometry of the elastic model.

The model parameters and boundary conditions are as follows:

- Mass density: 2,000 kg/m³ everywhere except for the top 2 m with 1500 kg/m³
- Ice wedge: A triangular inclusion centered at x=300 m, top at z=1 m, 10 m base width and 50 m height; ice properties assigned inside the triangle.
- Source: Ricker wavelet, f0=10 Hz, implemented as an explosive (isotropic) stress source by injecting into τxx and τzz. The source is placed just beneath the free surface at xs=296 m, zs=2 m (at the left side of the ice-wedge)
- Receivers: A horizontal line at z=1 m with 2.5 m spacing. With the sponge margin, the active aperture is ~10–490 m. We record the horizontal particle velocity vx(t,x).
- Boundary conditions: Traction-free at the top; quadratic sponge on the left, right, and bottom boundaries (thickness nbl=10 grid points, strength factor α=3) added to both velocity and stress updates to suppress side/bottom reflections.
- Time stepping: CFL-limited Δt (0.45 Courant factor for 2-D), total record length up to 2 s

C.2 Strain-Rate Preprocessing

Figure C.2 shows the shot gather horizontal particle velocity response in the time domain.

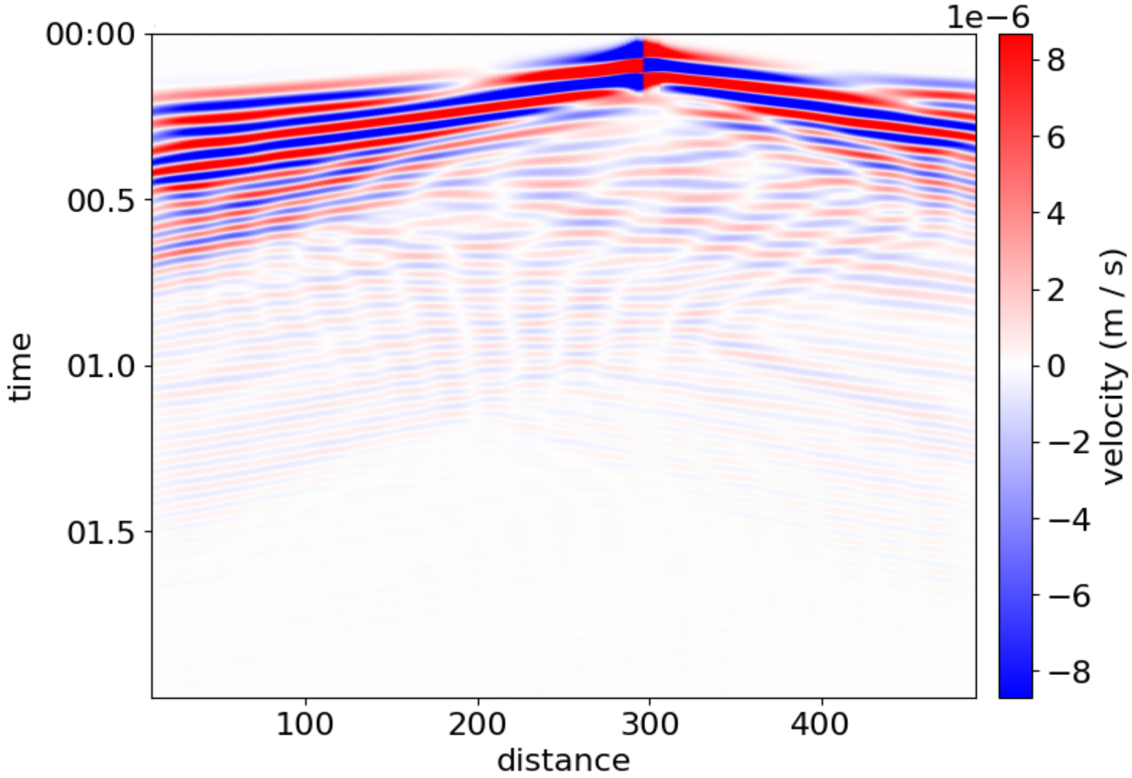

Figure C.2 Raster plot of the horizontal particle velocity response of the array.

To emphasize the DAS response for a horizontal array, we use Equation 4.1 to convert particle velocity to strain rate by a finite difference along the array with a gauge length of 5 m. That is a central difference over the gauge length using every other receiver (receiver spacing = 2.5 m, therefore step of two channels). Edges are discarded after differencing.

As illustrated in Figure C.3, the strain-rate raster plot in the time domain shows a strong Rayleigh wavefield propagating away from the source on both sides (dominant energy just beneath the surface); later arrivals with higher apparent velocities correspond to deeper reverberations and converted modes. A local amplitude notch near x=300 m corresponds to scattering and mode conversion at the ice wedge.

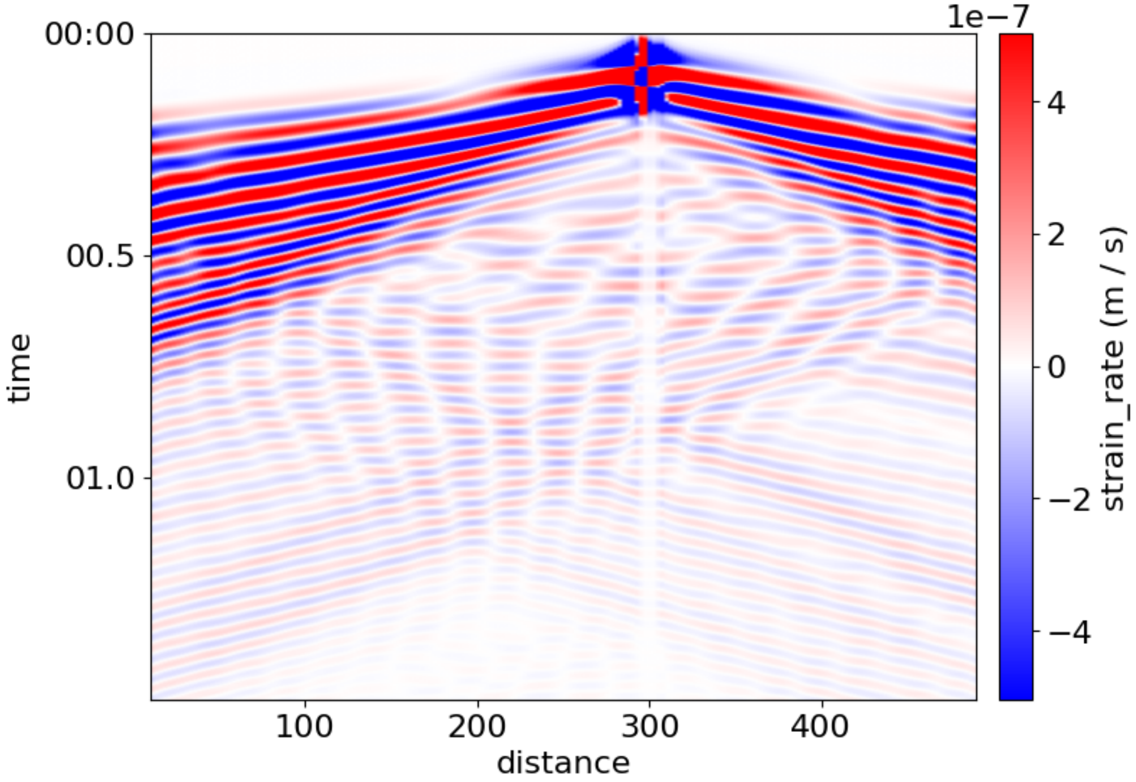

Figure C.3 Raster plot of the horizontal strain rate response of the array.

Because the explosive source is symmetric, any left–right differences in the recorded strain-rate field arise primarily from geometric asymmetry and lateral velocity contrasts introduced by the ice wedge. The wedge, centered 50 m right of the array mid-point, acts as a localized scatterer and impedance contrast, generating secondary reflected and mode-converted waves. These scattered wavefronts propagate laterally and upward, producing enhanced amplitudes and interference patterns. Consequently, the left sub-array (0-250 m) exhibits slightly delayed but higher-amplitude scattered coda following the main Rayleigh train, while the right array (250-500 m, directly above the wedge) shows more complex near-field interactions and partial shadowing immediately beneath the source. This asymmetric energy distribution emphasizes the strong sensitivity of near-surface wavefields to even modest lateral heterogeneity in permafrost or frozen-soil conditions.

C.3 MASW Dispersion Images on Sub-Arrays

To probe directionality and lateral heterogeneity, we compute frequency-apparent velocity dispersion images separately over two sub-apertures:

- Left sub-array (Figure C.4): 0–250 m (operationally 10–250 m due to the applied boundary condition)
- Right sub-array (Figure C.5): 250–500 m (operationally 250–490 m due to the applied boundary condition)

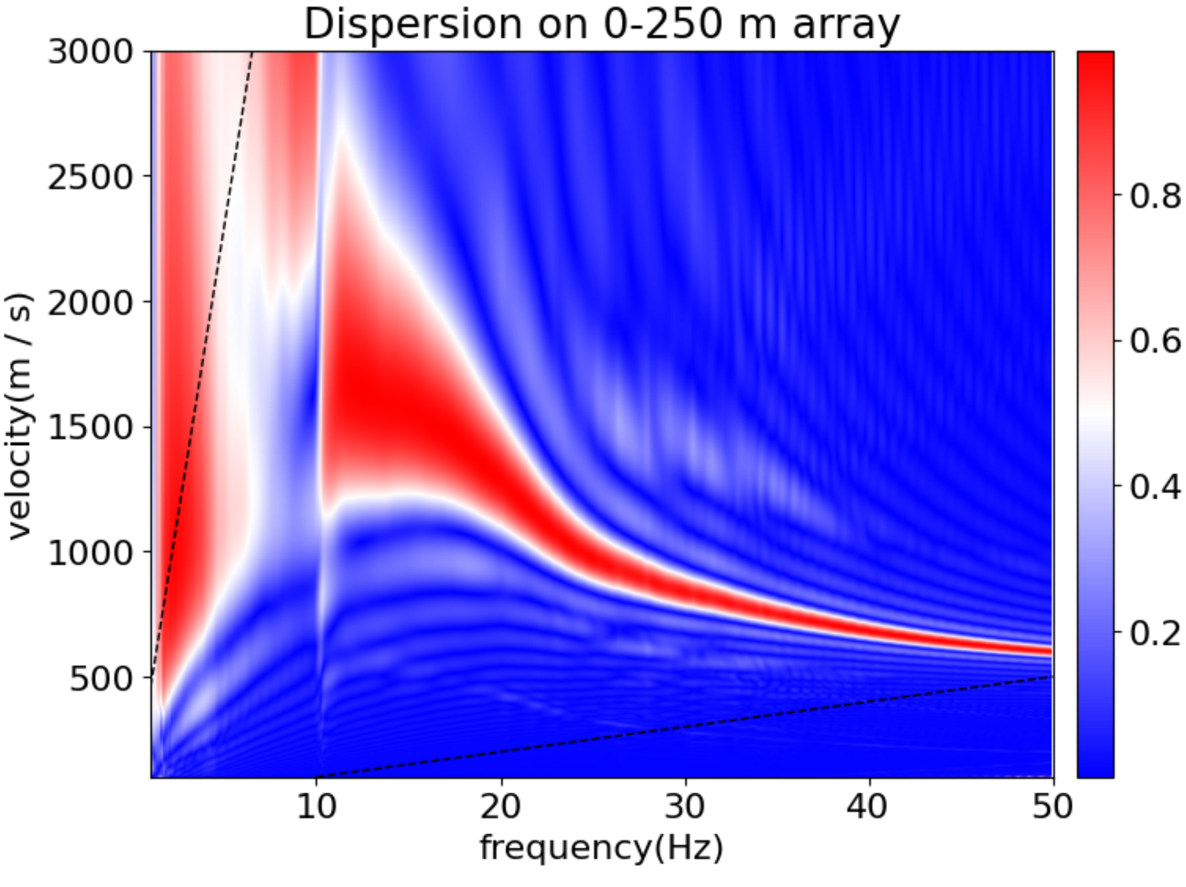

Figure C.4 Dispersion image of the left sub-array. The colorbar indicates the normalized amplitude of energy stacked at each frequency–velocity pair.

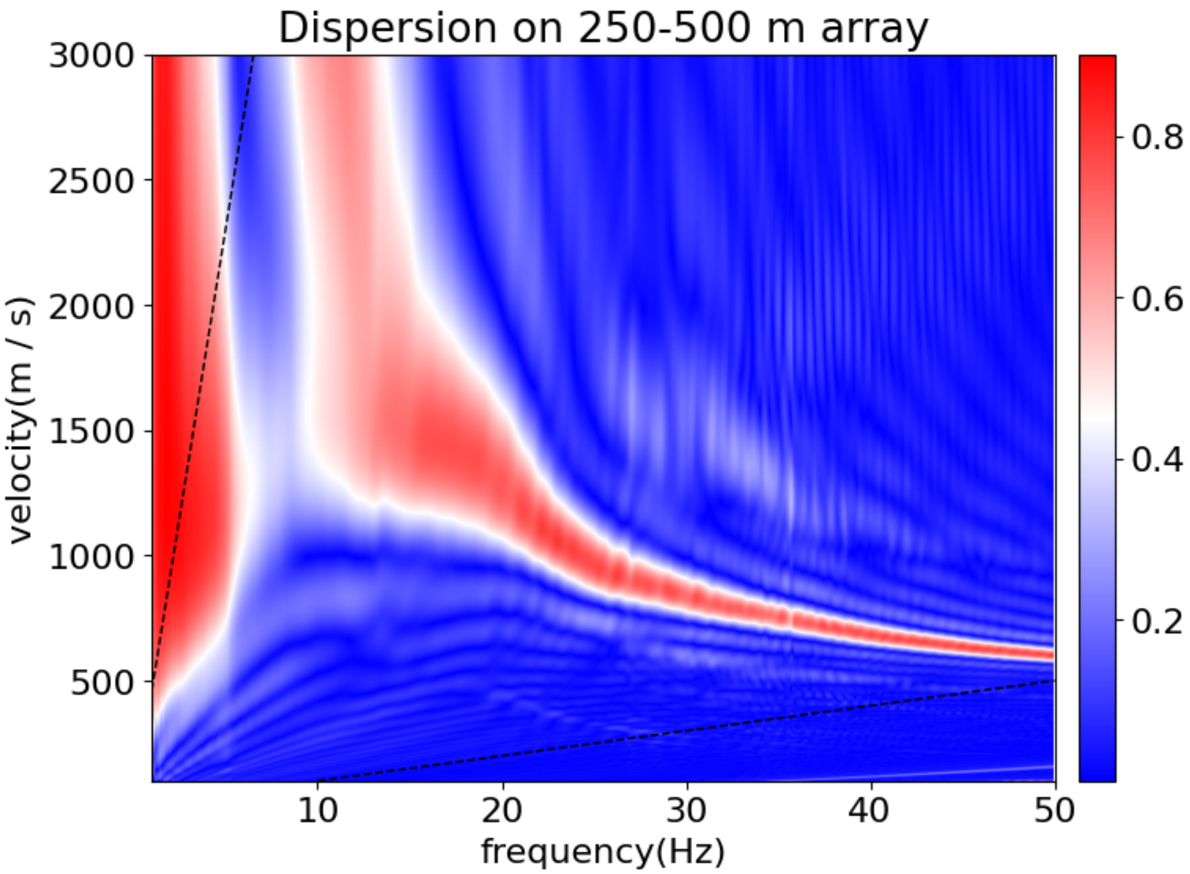

Figure C.5 Dispersion image of the right sub-array. The colorbar indicates the normalized amplitude of energy stacked at each frequency–velocity pair.

Even considering one relatively small ice wedge, both halves show a clear, continuous fundamental Rayleigh mode, but the right sub-array (with ice wedge) exhibits broader energy lobes and slightly higher low-frequency phase velocity. The left sub-array represents a narrower and cleaner dispersion moveout. However, the right sub-array shows enhanced higher-mode energy (10–30 Hz), indicative of local impedance contrast and surface-wave multipathing.

The right sub-array exhibits concentration of the lowest frequencies at slightly higher apparent velocities than the left side, indicating local stiffening of the near-surface materials. The overall bandwidth remains comparable between the two sides, although coherence is marginally reduced on the right. In contrast, the left sub-array shows mild distortion in the lower-frequency range around 10 Hz, likely caused by scattering of long-wavelength energy from the ice wedge as it propagates toward the more distant receivers. These observations demonstrate that lateral heterogeneity can induce measurable left–right asymmetry in dispersion characteristics, expressed through phase-velocity bias, increased modal complexity, and dispersion branch broadening.

Furthermore, to accentuate the scattering effects of the ice wedge, the wedge base was increased to 100 m, and the source was relocated inside the wedge at 300 m along the x axis and a depth of 5 m. Under these conditions, the resulting dispersion image (Figure C.6) exhibits a discontinuous moveout around 25 Hz and a complete loss of coherence above 30 Hz. This disruption of modal continuity reflects the strong scattering and mode conversion induced by the highly heterogeneous velocity field within and beneath the ice wedge. The internal impedance contrasts between frozen and unfrozen zones promote energy partitioning into scattered body waves and guided modes, reducing the coherence of the Rayleigh-wave fundamental branch. Additionally, frequency-dependent attenuation and phase interference from multiply reflected and mode-converted SV and P components further degrade the dispersion energy concentration at higher frequencies. The influence of higher-order Rayleigh modes also becomes more pronounced in this case, consistent with enhanced ellipticity and strong vertical gradients near the ice–soil interface. These results underscore that large-scale frozen inclusions can substantially distort the surface-wave field, producing apparent dispersion discontinuities and frequency-dependent mode scattering that may mimic strong lateral heterogeneity in permafrost terrains.

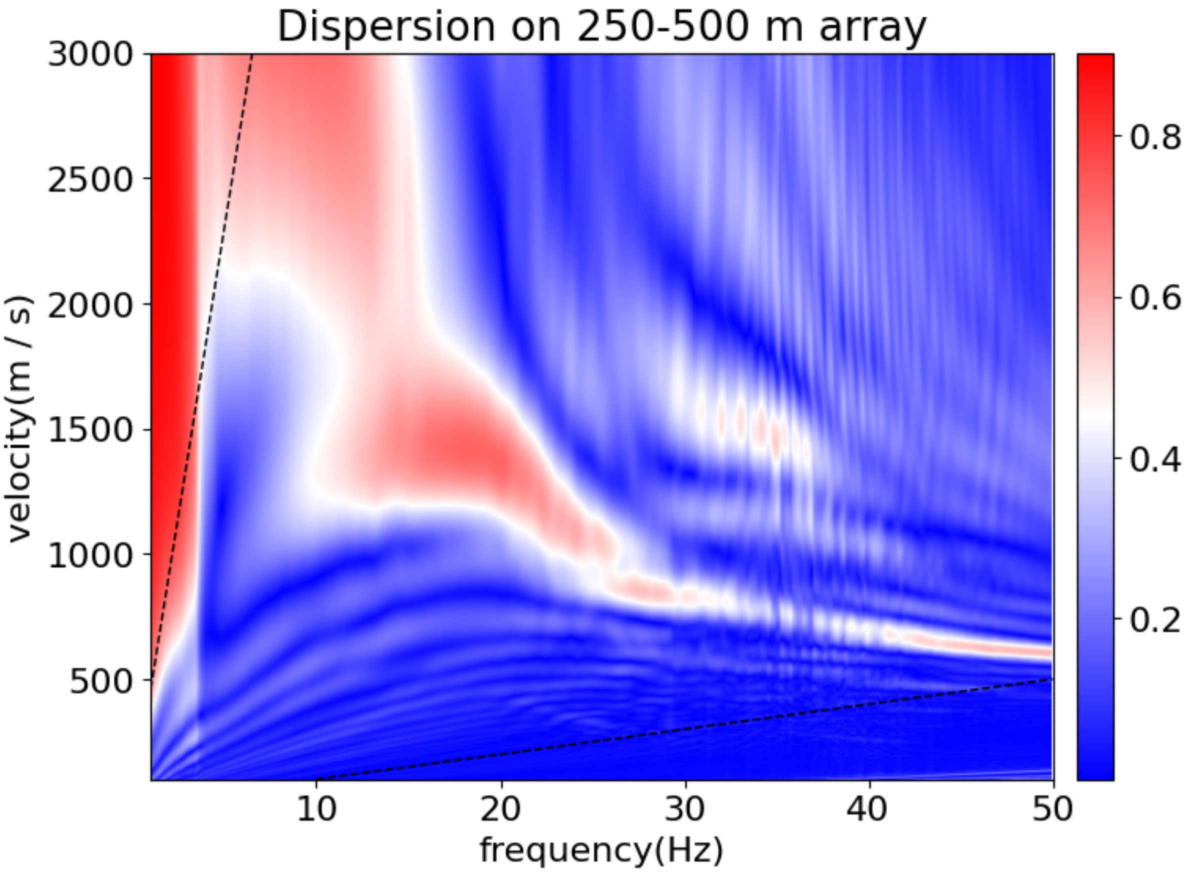

Figure C.6 The extreme effect of the ice-wedge on the dispersion image. The colorbar indicates the normalized amplitude of energy stacked at each frequency–velocity pair.

APPENDIX D ATTRIBUTIONS AND COPYRIGHT PERMISSIONS

This appendix provides publication details of the contents of each chapter as well as defined author roles according to the Contributor Roles Taxonomy– CRediT, available at credit.niso.org and in the References section. The standard defines the following roles, and for brevity, only their numbers will be listed:

1. Conceptualization – Ideas; formulation or evolution of overarching research goals and aims.
2. Data curation – Management activities to annotate (produce metadata), scrub data and maintain research data (including software code, where it is necessary for interpreting the data itself) for initial use and later re-use.
3. Formal analysis – Application of statistical, mathematical, computational, or other formal techniques to analyze or synthesize study data.
4. Funding acquisition - Acquisition of the financial support for the project leading to this publication.
5. Investigation – Conducting a research and investigation process, specifically performing the experiments, or data/evidence collection.
6. Methodology – Development or design of methodology; creation of models.
7. Project administration – Management and coordination responsibility for the research activity planning and execution.
8. Resources – Provision of study materials, reagents, materials, patients, laboratory samples, animals, instrumentation, computing resources, or other analysis tools.
9. Software – Programming, software development; designing computer programs; implementation of the computer code and supporting algorithms; testing of existing code components.
10. Supervision – Oversight and leadership responsibility for the research activity planning and execution, including mentorship external to the core team.
11. Validation – Verification, whether as a part of the activity or separate, of the overall replication/reproducibility of results/experiments and other research outputs.
12. Visualization – Preparation, creation and/or presentation of the published work, specifically visualization/data presentation.
13. Writing – original draft – Preparation, creation and/or presentation of the published work, specifically writing the initial draft (including substantive translation).
14. Writing – review and editing – Preparation, creation and/or presentation of the published work by those from the original research group, specifically critical review, commentary or revision – including pre- or post-publication stages.

Each chapter in this work is based on the referenced published or submitted work, with minor editing and the consolidation of introductory material into Chapter 1.

Chapter 1

This chapter includes original, unpublished material, along with background and introductory content adapted from papers discussed in other chapters and a research proposal defense in the Hydrologic Science and Engineering program at Colorado School of Mines.

Contributions:

- Ahmad Tourei: Write the text, created the figures, and participated in the editing (1, 12, 13, 14)
- Eileen Martin: Reviewed the contents and helped with the editing (14)

Chapter 2

The contents of this chapter were published by the Journal of Geophysical Research – Earth Surface in March 2024 (Tourei et al., 2024). Figure D.1 shows the copyright information, and Figure D.2 shows the email thread of co-authors consenting to the paper being included in this dissertation.

Contributions:

- Ahmad Tourei: Conceptualized the study, curated and validated data, performed formal analysis (MASW) and investigation, developed methodology, managed the project, provided resources, developed software, supervised research activities, prepared visualizations, wrote the original draft, and revised the manuscript (1, 2, 3, 5, 6, 7, 8, 9, 10, 11, 12, 13, 14).
- Xiaohang Ji: Contributed to conceptualization, data curation, investigation, validation, visualization, and original draft preparation, and participated in manuscript review and editing (1, 2, 5, 11, 12, 13, 14).
- Gabriel Rocha dos Santos: Contributed to conceptualization, data curation, formal analysis, investigation, software development, validation, visualization, and manuscript review and editing (1, 2, 3, 5, 9, 11, 12, 14).
- Rafal Czarny: Contributed to conceptualization, formal analysis (seismic refraction), methodology development, validation, visualization, original draft writing, and manuscript review and editing (1, 3, 6, 11, 12, 13, 14).
- Sergei Rybakov: Contributed to conceptualization, formal analysis (ERT), methodology development, investigation, validation, visualization, original draft writing, and manuscript review and editing (1, 3, 6, 5, 11, 12, 13, 14).
- Ziyi Wang: Contributed to data curation, investigation, validation, visualization, original draft writing, and manuscript review and editing (2, 4, 5, 11, 12, 13, 14).
- Matthew Hallissey: Participated in investigation and fieldwork (5, 8).
- Eileen Martin: Contributed to conceptualization, data curation, investigation, methodology development, project administration, resource provision, funding acquisition, supervision, and manuscript review and editing (1, 2, 4, 5, 6, 7, 8, 10, 14).

- Ming Xiao: Contributed to conceptualization, data curation, investigation, methodology development, project administration, resource provision, funding acquisition, supervision, and manuscript review and editing (1, 2, 4, 5, 6, 7, 8, 10, 14).
- Tieyuan Zhu: Contributed to conceptualization, data curation, investigation, methodology development, project administration, resource provision, funding acquisition, supervision, and manuscript review and editing (1, 2, 4, 5, 6, 7, 8, 10, 14).
- Dmitry Nicolsky: Contributed to conceptualization, data curation, investigation, methodology development, resource provision, funding acquisition, supervision, and manuscript review and editing (1, 2, 4, 5, 6, 8, 10, 14).
- Anne Jensen: Contributed to conceptualization, data curation, investigation, resource provision, funding acquisition, supervision, and manuscript review and editing (1, 2, 4, 5, 8, 10, 14)

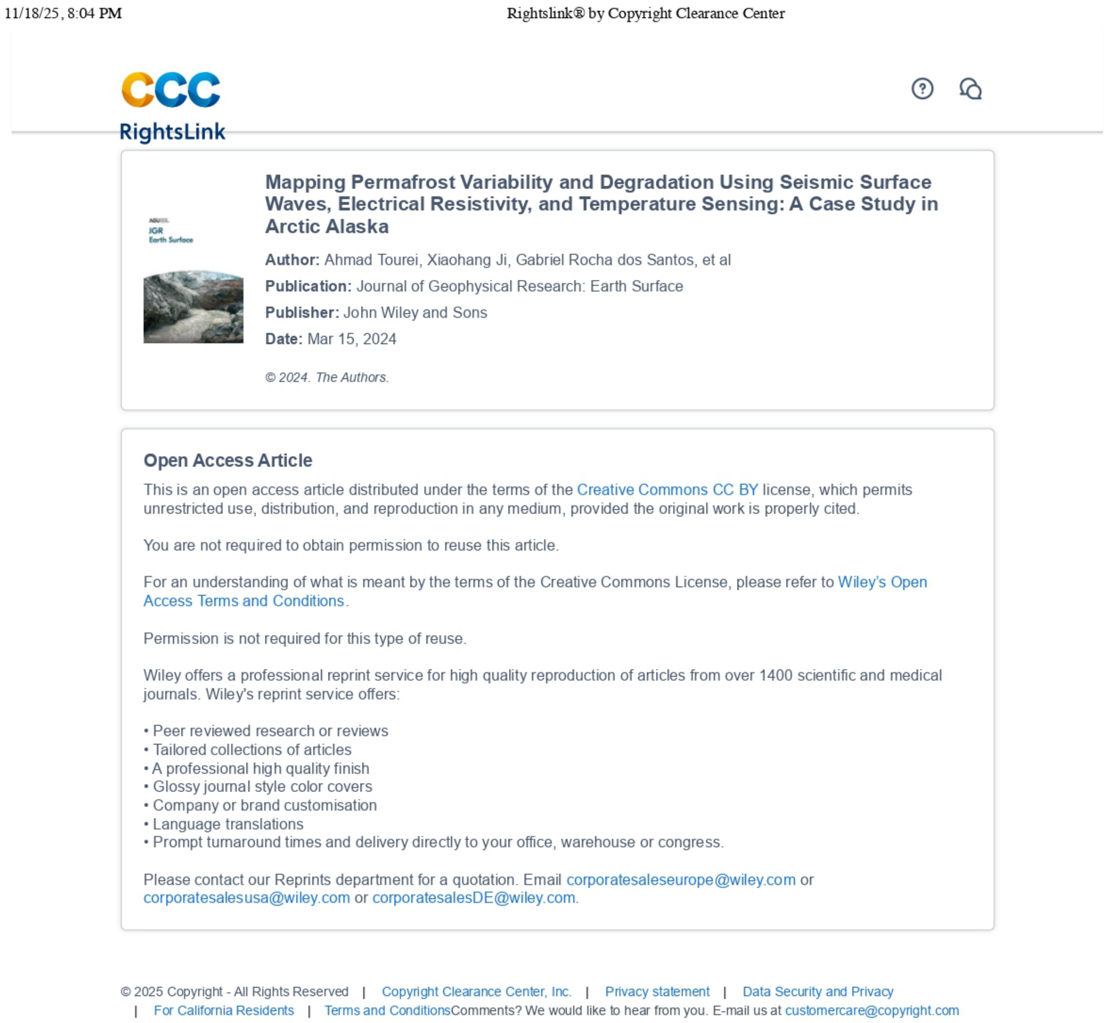

11/18/25, 8:04 PM Rightslink® by Copyright Clearance Center

Mapping Permafrost Variability and Degradation Using Seismic Surface Waves, Electrical Resistivity, and Temperature Sensing: A Case Study in Arctic Alaska

Author: Ahmad Tourei, Xiaohang Ji, Gabriel Rocha dos Santos, et al
Publication: Journal of Geophysical Research: Earth Surface
Publisher: John Wiley and Sons
Date: Mar 15, 2024

© 2024. The Authors.

Open Access Article

This is an open access article distributed under the terms of the Creative Commons CC BY license, which permits unrestricted use, distribution, and reproduction in any medium, provided the original work is properly cited.

You are not required to obtain permission to reuse this article.

For an understanding of what is meant by the terms of the Creative Commons License, please refer to Wiley's Open Access Terms and Conditions.

Permission is not required for this type of reuse.

Wiley offers a professional reprint service for high quality reproduction of articles from over 1400 scientific and medical journals. Wiley's reprint service offers:

- Peer reviewed research or reviews
- Tailored collections of articles
- A professional high quality finish
- Glossy journal style color covers
- Company or brand customisation
- Language translations
- Prompt turnaround times and delivery directly to your office, warehouse or congress.

Please contact our Reprints department for a quotation. Email corporatesaleseurope@wiley.com or corporatesalesusa@wiley.com or corporatesalesDE@wiley.com.

© 2025 Copyright - All Rights Reserved | Copyright Clearance Center, Inc. | Privacy statement | Data Security and Privacy | For California Residents | Terms and ConditionsComments? We would like to hear from you. E-mail us at customercare@copyright.com

Figure D.1 Copyright approval for Chapter 2.

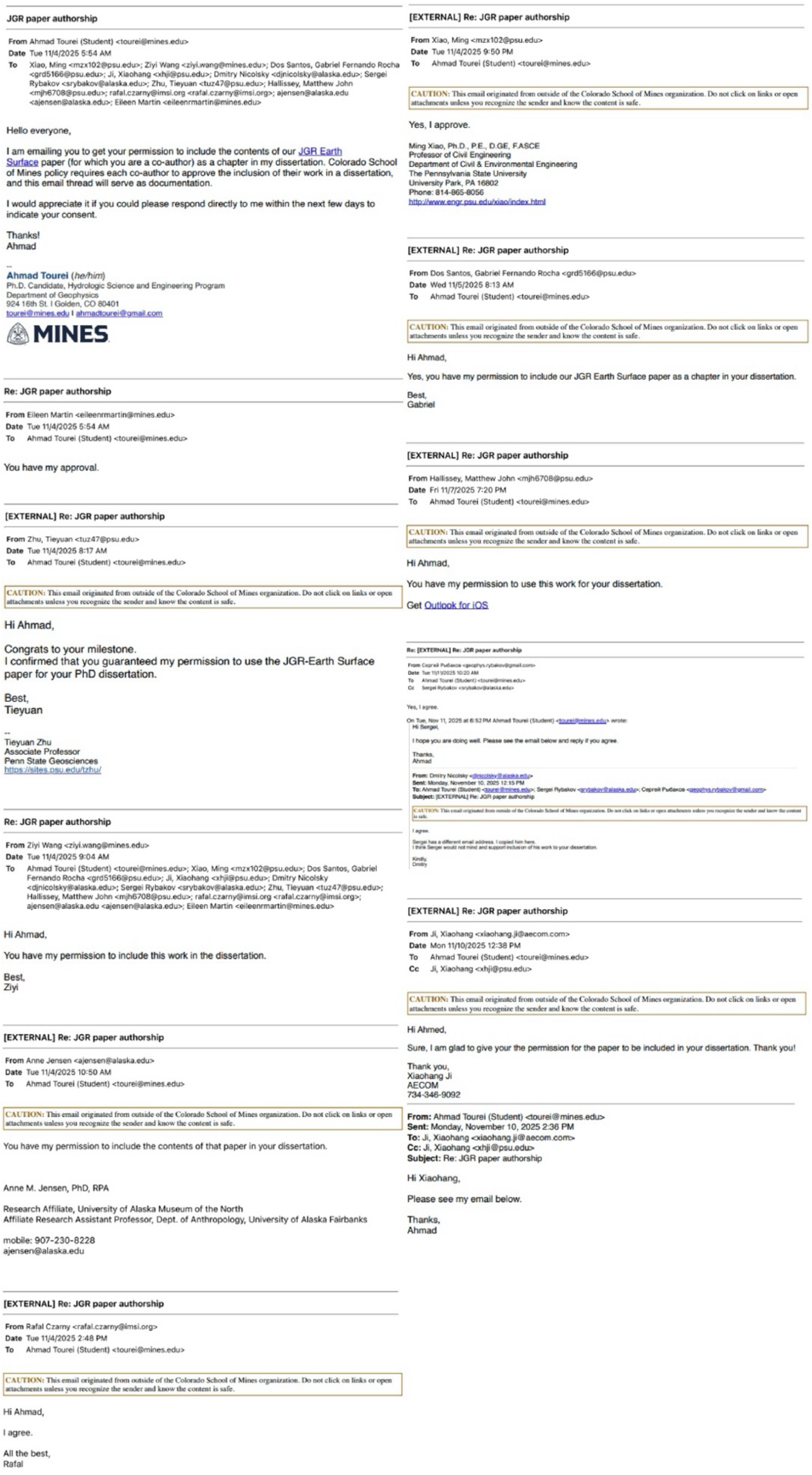

JGR paper authorship

From Ahmad Tourei (Student) <tourei@mines.edu>
Date Tue 11/4/2025 5:54 AM
To Xiao, Ming <mzx102@psu.edu>; Ziyi Wang <ziyi.wang@mines.edu>; Dos Santos, Gabriel Fernando Rocha <grd5166@psu.edu>; Ji, Xiaohang <xhji@psu.edu>; Dmitry Nicolsky <djnicolsky@alaska.edu>; Sergei Rybakov <srybakov@alaska.edu>; Zhu, Tieyuan <tuz47@psu.edu>; Hallissey, Matthew John <mjh6708@psu.edu>; rafal.czarny@imsi.org <rafal.czarny@imsi.org>; ajensen@alaska.edu <ajensen@alaska.edu>; Eileen Martin <eileenrmartin@mines.edu>

Hello everyone,

I am emailing you to get your permission to include the contents of our JGR Earth Surface paper (for which you are a co-author) as a chapter in my dissertation. Colorado School of Mines policy requires each co-author to approve the inclusion of their work in a dissertation, and this email thread will serve as documentation.

I would appreciate it if you could please respond directly to me within the next few days to indicate your consent.

Thanks!
Ahmad

--
Ahmad Tourei (*he/him*)
Ph.D. Candidate, Hydrologic Science and Engineering Program
Department of Geophysics
924 16th St. I Golden, CO 80401
tourei@mines.edu I ahmadtourei@gmail.com

Re: JGR paper authorship

From Eileen Martin <eileenrmartin@mines.edu>
Date Tue 11/4/2025 5:54 AM
To Ahmad Tourei (Student) <tourei@mines.edu>

You have my approval.

[EXTERNAL] Re: JGR paper authorship

From Zhu, Tieyuan <tuz47@psu.edu>
Date Tue 11/4/2025 8:17 AM
To Ahmad Tourei (Student) <tourei@mines.edu>

CAUTION: This email originated from outside of the Colorado School of Mines organization. Do not click on links or open attachments unless you recognize the sender and know the content is safe.

Hi Ahmad,

Congrats to your milestone.
I confirmed that you guaranteed my permission to use the JGR-Earth Surface paper for your PhD dissertation.

Best,
Tieyuan

--
Tieyuan Zhu
Associate Professor
Penn State Geosciences
https://sites.psu.edu/tzhu/

Re: JGR paper authorship

From Ziyi Wang <ziyi.wang@mines.edu>
Date Tue 11/4/2025 9:04 AM
To Ahmad Tourei (Student) <tourei@mines.edu>; Xiao, Ming <mzx102@psu.edu>; Dos Santos, Gabriel Fernando Rocha <grd5166@psu.edu>; Ji, Xiaohang <xhji@psu.edu>; Dmitry Nicolsky <djnicolsky@alaska.edu>; Sergei Rybakov <srybakov@alaska.edu>; Zhu, Tieyuan <tuz47@psu.edu>; Hallissey, Matthew John <mjh6708@psu.edu>; rafal.czarny@imsi.org <rafal.czarny@imsi.org>; ajensen@alaska.edu <ajensen@alaska.edu>; Eileen Martin <eileenrmartin@mines.edu>

Hi Ahmad,

You have my permission to include this work in the dissertation.

Best,
Ziyi

[EXTERNAL] Re: JGR paper authorship

From Anne Jensen <ajensen@alaska.edu>
Date Tue 11/4/2025 10:50 AM
To Ahmad Tourei (Student) <tourei@mines.edu>

CAUTION: This email originated from outside of the Colorado School of Mines organization. Do not click on links or open attachments unless you recognize the sender and know the content is safe.

You have my permission to include the contents of that paper in your dissertation.

Anne M. Jensen, PhD, RPA

Research Affiliate, University of Alaska Museum of the North
Affiliate Research Assistant Professor, Dept. of Anthropology, University of Alaska Fairbanks

mobile: 907-230-8228
ajensen@alaska.edu

[EXTERNAL] Re: JGR paper authorship

From Rafal Czarny <rafal.czarny@imsi.org>
Date Tue 11/4/2025 2:48 PM
To Ahmad Tourei (Student) <tourei@mines.edu>

CAUTION: This email originated from outside of the Colorado School of Mines organization. Do not click on links or open attachments unless you recognize the sender and know the content is safe.

Hi Ahmad,

I agree.

All the best,
Rafal

[EXTERNAL] Re: JGR paper authorship

From Xiao, Ming <mzx102@psu.edu>
Date Tue 11/4/2025 9:50 PM
To Ahmad Tourei (Student) <tourei@mines.edu>

CAUTION: This email originated from outside of the Colorado School of Mines organization. Do not click on links or open attachments unless you recognize the sender and know the content is safe.

Yes, I approve.

Ming Xiao, Ph.D., P.E., D.GE, F.ASCE
Professor of Civil Engineering
Department of Civil & Environmental Engineering
The Pennsylvania State University
University Park, PA 16802
Phone: 814-865-8056
http://www.engr.psu.edu/xiao/index.html

[EXTERNAL] Re: JGR paper authorship

From Dos Santos, Gabriel Fernando Rocha <grd5166@psu.edu>
Date Wed 11/5/2025 8:13 AM
To Ahmad Tourei (Student) <tourei@mines.edu>

CAUTION: This email originated from outside of the Colorado School of Mines organization. Do not click on links or open attachments unless you recognize the sender and know the content is safe.

Hi Ahmad,

Yes, you have my permission to include our JGR Earth Surface paper as a chapter in your dissertation.

Best,
Gabriel

[EXTERNAL] Re: JGR paper authorship

From Hallissey, Matthew John <mjh6708@psu.edu>
Date Fri 11/7/2025 7:20 PM
To Ahmad Tourei (Student) <tourei@mines.edu>

CAUTION: This email originated from outside of the Colorado School of Mines organization. Do not click on links or open attachments unless you recognize the sender and know the content is safe.

Hi Ahmad,

You have my permission to use this work for your dissertation.

Get Outlook for iOS

Re: [EXTERNAL] Re: JGR paper authorship

From Сергей Рыбаков <geophys.rybakov@gmail.com>
Date Tue 11/11/2025 10:20 AM
To Ahmad Tourei (Student) <tourei@mines.edu>
Cc Sergei Rybakov <srybakov@alaska.edu>

Yes, I agree.

On Tue, Nov 11, 2025 at 6:52 PM Ahmad Tourei (Student) <tourei@mines.edu> wrote:

> Hi Sergei,
>
> I hope you are doing well. Please see the email below and reply if you agree.
>
> Thanks,
> Ahmad
>
> **From:** Dmitry Nicolsky <djnicolsky@alaska.edu>
> **Sent:** Monday, November 10, 2025 12:15 PM
> **To:** Ahmad Tourei (Student) <tourei@mines.edu>; Sergei Rybakov <srybakov@alaska.edu>; Сергей Рыбаков <geophys.rybakov@gmail.com>
> **Subject:** [EXTERNAL] Re: JGR paper authorship
>
> CAUTION: This email originated from outside of the Colorado School of Mines organization. Do not click on links or open attachments unless you recognize the sender and know the content is safe.
>
> I agree.
>
> Sergei has a different email address. I copied him here.
> I think Sergei would not mind and support inclusion of his work to your dissertation.
>
> Kindly,
> Dmitry

[EXTERNAL] Re: JGR paper authorship

From Ji, Xiaohang <xiaohang.ji@aecom.com>
Date Mon 11/10/2025 12:38 PM
To Ahmad Tourei (Student) <tourei@mines.edu>
Cc Ji, Xiaohang <xhji@psu.edu>

CAUTION: This email originated from outside of the Colorado School of Mines organization. Do not click on links or open attachments unless you recognize the sender and know the content is safe.

Hi Ahmed,

Sure, I am glad to give your the permission for the paper to be included in your dissertation. Thank you!

Thank you,
Xiaohang Ji
AECOM
734-346-9092

From: Ahmad Tourei (Student) <tourei@mines.edu>
Sent: Monday, November 10, 2025 2:36 PM
To: Ji, Xiaohang <xiaohang.ji@aecom.com>
Cc: Ji, Xiaohang <xhji@psu.edu>
Subject: Re: JGR paper authorship

Hi Xiaohang,

Please see my email below.

Thanks,
Ahmad

Figure D.2 Author approval for Chapter 2.

Chapter 3

The contents of this chapter have not yet been submitted to a peer-reviewed venue.

Contributions:

- Ahmad Tourei: Led conceptualization and methodology development, curated data, performed formal analysis and investigation, managed project administration, developed software, supervised research activities, validated results, prepared visualizations, wrote the original draft, and contributed to manuscript revision (1, 2, 3, 5, 6, 7, 9, 10, 11, 12, 13, 14).
- Alexander Ankamah: Contributed to data curation, formal analysis, investigation, and manuscript review and editing (2, 3, 5, 14).
- John Hole: Contributed to funding acquisition, methodology development, project administration, resources, supervision, validation, and manuscript review and editing (4, 6, 7, 8, 10, 11, 14).
- Gabriel Rocha dos Santos: Contributed to data curation, resource provision, and manuscript review and editing (2, 8, 14).
- Ming Xiao: Contributed to data curation, funding acquisition, project administration, resource provision, and manuscript review and editing (2, 4, 7, 8, 14).
- Eileen Martin: Contributed to conceptualization, data curation, funding acquisition, project administration, resource provision, software support, supervision, and manuscript review and editing (1, 2, 4, 7, 8, 9, 10, 14).

Chapter 4

The contents of this chapter have not yet been submitted to a peer-reviewed venue.

Contributions:

- Ahmad Tourei: Led conceptualization and methodology development, curated data, performed formal analysis and investigation, managed the project, developed software, supervised research activities, validated results, prepared visualizations, wrote the original draft, and revised the manuscript (1, 2, 3, 5, 6, 7, 9, 10, 11, 12, 13, 14).
- Nikhil Punithan: Contributed to methodology development, investigation, and manuscript review and editing (5, 6, 14).
- Gabriel Rocha dos Santos: Contributed to methodology development, and investigation (5, 6).
- Ming Xiao: Contributed to funding acquisition, project administration, resource provision, and manuscript review and editing (4, 7, 8, 14).
- Eileen Martin: Contributed to conceptualization, data curation, funding acquisition, project administration, resource provision, and manuscript review and editing (1, 2, 4, 7, 8, 14).

Chapter 5

This chapter includes original, unpublished material, along with discussions, conclusions, and contents adapted from papers discussed in other chapters

Contributions:

- Ahmad Tourei: Write the text and participated in the editing (1, 13, 14)
- Eileen Martin: Reviewed the contents and helped with the editing (14)

Appendix A

This appendix provides additional material related to Chapter 2. The contents of this appendix provide supporting information for the paper published by the Journal of Geophysical Research – Earth Surface in March 2024 (Tourei et al., 2024). The authors' contributions are the same as those listed for Chapter 2.

Appendix B

The contents of this chapter were presented at the 58th U.S. Rock Mechanics/Geomechanics Symposium held in Golden, Colorado, USA in June 2024 (Tourei et al., 2024). Figure D.3 shows the copyright information, and Figure D.4 shows the email thread of co-authors consenting to the paper being included in this dissertation.

Contributions:

- Ahmad Tourei: Led conceptualization and methodology development, curated data, performed analysis and investigation, managed project tasks, developed software, supervised research activities, validated results, prepared visualizations, drafted the manuscript, and contributed to revision (1, 2, 3, 5, 6, 7, 9, 10, 11, 12, 13, 14).
- Eileen Martin: Contributed to conceptualization and data curation, secured funding, coordinated project administration, provided resources and software support, supervised research activities, and reviewed and edited the manuscript (1, 2, 4, 7, 8, 9, 10, 14).
- Alexander Ankamah: Contributed to data curation, formal analysis, investigation, and manuscript review and editing (2, 3, 5, 14).
- John Hole: Contributed to funding acquisition, methodology development, project administration, resource provision, supervision, validation, and manuscript review and editing (4, 6, 7, 8, 10, 11, 14).
- Derrick Chambers: Contributed to data curation, investigation, software support, and manuscript review and editing (2, 5, 9, 14).

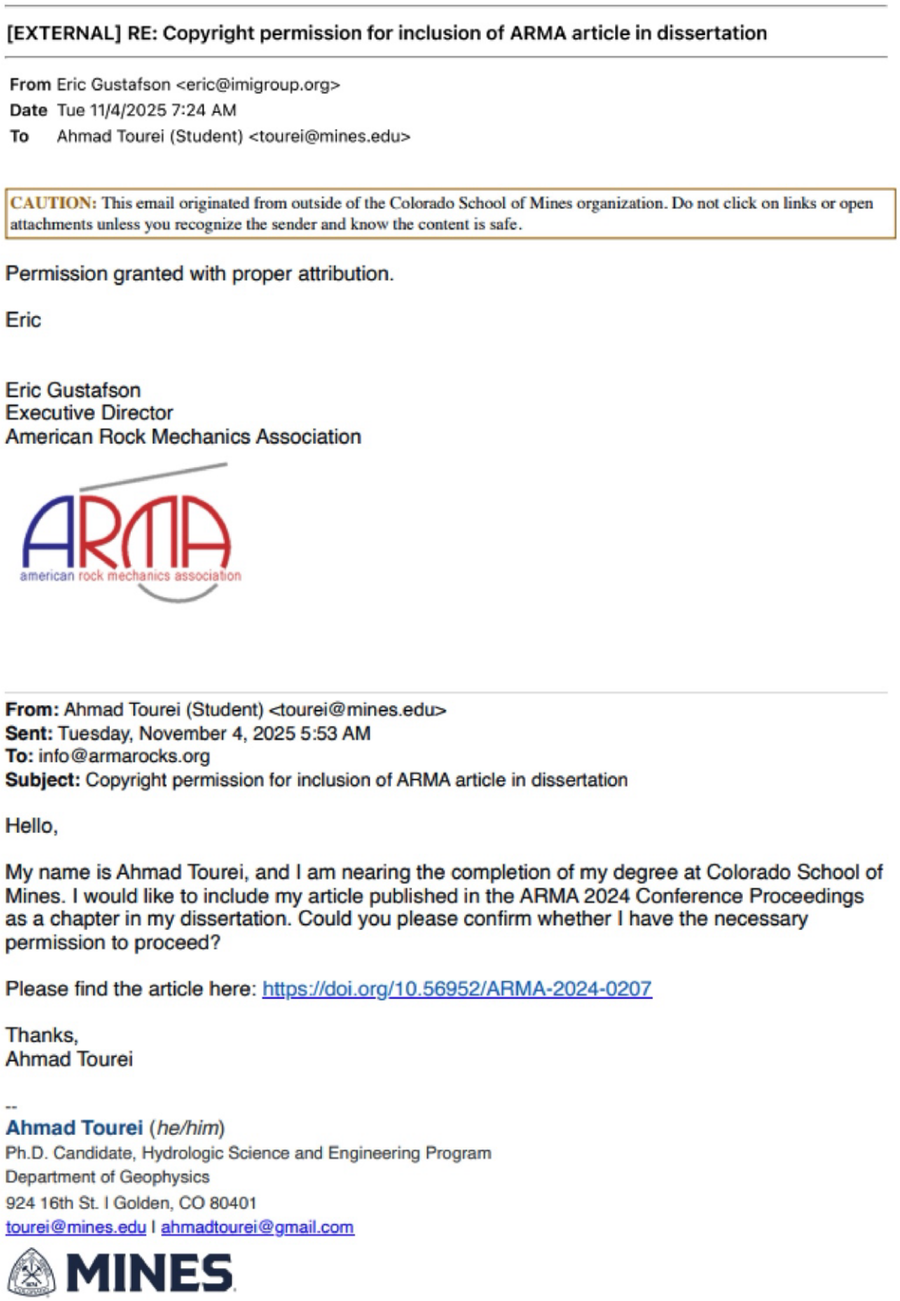

[EXTERNAL] RE: Copyright permission for inclusion of ARMA article in dissertation

From Eric Gustafson <eric@imigroup.org>
Date Tue 11/4/2025 7:24 AM
To Ahmad Tourei (Student) <tourei@mines.edu>

CAUTION: This email originated from outside of the Colorado School of Mines organization. Do not click on links or open attachments unless you recognize the sender and know the content is safe.

Permission granted with proper attribution.

Eric

Eric Gustafson
Executive Director
American Rock Mechanics Association

From: Ahmad Tourei (Student) <tourei@mines.edu>
Sent: Tuesday, November 4, 2025 5:53 AM
To: info@armarocks.org
Subject: Copyright permission for inclusion of ARMA article in dissertation

Hello,

My name is Ahmad Tourei, and I am nearing the completion of my degree at Colorado School of Mines. I would like to include my article published in the ARMA 2024 Conference Proceedings as a chapter in my dissertation. Could you please confirm whether I have the necessary permission to proceed?

Please find the article here: https://doi.org/10.56952/ARMA-2024-0207

Thanks,
Ahmad Tourei

--
Ahmad Tourei (*he/him*)
Ph.D. Candidate, Hydrologic Science and Engineering Program
Department of Geophysics
924 16th St. I Golden, CO 80401
tourei@mines.edu I ahmadtourei@gmail.com

Figure D.3 Copyright approval for Appendix B.

ARMA paper authorship

From Ahmad Tourei (Student) <tourei@mines.edu>
Date Tue 11/4/2025 5:53 AM
To Hole, John <hole@vt.edu>; Eileen Martin <eileenrmartin@mines.edu>; Derrick Chambers (Student) <derrickchambers@mines.edu>; Ankamah, Alexander <alexanderta@vt.edu>

Hello everyone,

I am emailing you to get your permission to include the contents of our ARMA paper on mining-induced seismicity monitoring (for which you are a co-author) as an appendix in my dissertation. Colorado School of Mines policy requires each co-author to approve the inclusion of their work in a dissertation, and this email thread will serve as documentation.

I would appreciate it if you could please respond directly to me within the next few days to indicate your consent.

Thanks!
Ahmad

--
Ahmad Tourei (*he/him*)
Ph.D. Candidate, Hydrologic Science and Engineering Program
Department of Geophysics
924 16th St. I Golden, CO 80401
tourei@mines.edu I ahmadtourei@gmail.com

Re: ARMA paper authorship

From Eileen Martin <eileenrmartin@mines.edu>
Date Tue 11/4/2025 5:55 AM
To Ahmad Tourei (Student) <tourei@mines.edu>

You have my approval.

[EXTERNAL] Re: ARMA paper authorship

From Ankamah, Alexander <alexanderta@vt.edu>
Date Tue 11/4/2025 6:51 AM
To Ahmad Tourei (Student) <tourei@mines.edu>

CAUTION: This email originated from outside of the Colorado School of Mines organization. Do not click on links or open attachments unless you recognize the sender and know the content is safe.

Hi Ahmad,
You have my permission to include the contents of the ARMA paper in your dissertation.

Alex

[EXTERNAL] Re: ARMA paper authorship

From Hole, John <hole@vt.edu>
Date Tue 11/4/2025 6:45 AM
To Ahmad Tourei (Student) <tourei@mines.edu>
Cc Hole, John <hole@vt.edu>; Eileen Martin <eileenrmartin@mines.edu>; Derrick Chambers (Student) <derrickchambers@mines.edu>; Ankamah, Alexander <alexanderta@vt.edu>

CAUTION: This email originated from outside of the Colorado School of Mines organization. Do not click on links or open attachments unless you recognize the sender and know the content is safe.

You have my permission for this.
John

Re: [EXTERNAL] Re: ARMA paper authorship

From Derrick Chambers (Student) <derrickchambers@mines.edu>
Date Fri 11/7/2025 5:12 PM
To Hole, John <hole@vt.edu>; Ahmad Tourei (Student) <tourei@mines.edu>
Cc Eileen Martin <eileenrmartin@mines.edu>; Ankamah, Alexander <alexanderta@vt.edu>

I also grant my permission.

Derrick

Figure D.4 Author approval for Appendix B.

Appendix C

This appendix provides additional material for Chapter 4. Its contents have not yet been submitted for peer review. The authors' contributions are the same as those listed for Chapter 4.